Interrogating Cancer Metabolism using Novel Imaging Techniques

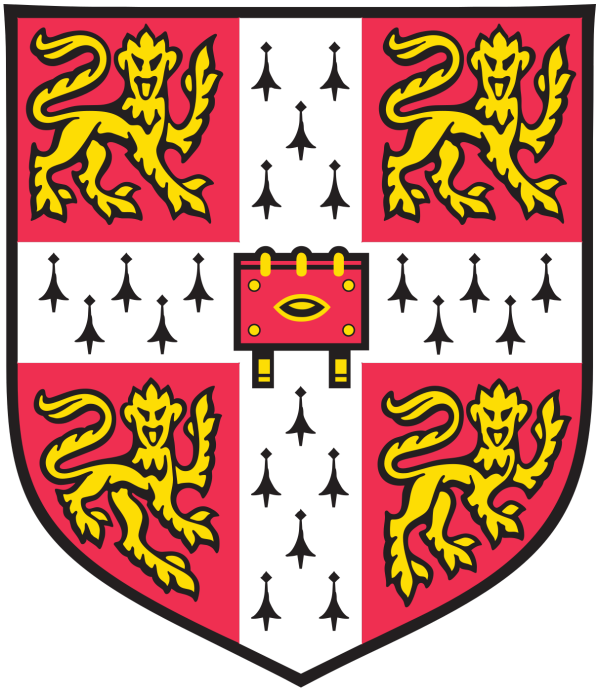

This thesis is submitted for the degree of Doctor of Philosophy

Maria Fala

Gonville and Caius College

Supervisor: Professor Kevin Brindle

September 2020

"Research is to see what everybody else has seen, and to think what nobody else has thought"

Albert Szent-Gyorgyi
1893-1986

Declaration

This thesis is the result of my own work and includes nothing which is the outcome of work done in collaboration except as declared in the preface and specified in the text. It is not substantially the same as any that I have submitted, or, is being concurrently submitted for a degree, diploma or other qualification at the University of Cambridge or any other University or similar institution except as declared in the Preface and specified in the text. I further state that no substantial part of my dissertation has already been submitted, or, is being concurrently submitted for any such degree, diploma or other qualification at the University of Cambridge or any other University of similar institution except as declared in the Preface and specified in the text. It does not exceed the word limit of 60,000 words.

Maria Fala

September 2020

Abstract

Title: Interrogating Cancer Metabolism using Novel Imaging Techniques

Author: Maria Fala

Altered metabolism is one of the hallmarks of cancer and is known to enable the proliferation and survival of cancer cells in changing microenvironments. Metabolic changes can be interrogated using non-invasive metabolic imaging techniques, which enable the investigation of tumour metabolism *in vivo* and the identification of imaging biomarkers. Hyperpolarised ^{13}C Magnetic Resonance Spectroscopic Imaging (MRSI) is a metabolic imaging technique that enables dynamic imaging of isotopically labelled metabolites *in vivo*, with [1-^{13}C]pyruvate being the most widely used substrate in pre-clinical studies and the only substrate used so far in clinical studies. In the first part of this thesis, hyperpolarised ^{13}C pyruvate MRSI was directly compared to mass spectrometry imaging in a murine lymphoma model, cross-validating both methods for providing information on the relative spatial distribution of ^{13}C-labelled lactate.

In the second part, the potential of hyperpolarised [1-^{13}C]Ketoisocaproic Acid as a substrate for hyperpolarised imaging was investigated. Ketoisocaproic acid is a substrate for Branched Chain Aminotransferase 1 (BCAT1), the first enzyme in the catabolic pathway of Branched Chain Amino Acids. This enzyme is upregulated in many cancers and is linked to cancer progression. In this project, the role of BCAT1 in cell proliferation was confirmed in glioblastoma patient derived cells and tumours and BCAT1 was shown to regulate the cells' metabolic and transcriptional profiles through regulation of alpha-ketoglutarate metabolism. *In vivo* imaging of BCAT1 activity is therefore suggested as a potential technique for patient stratification and potentially treatment monitoring. [1-^{13}C]Ketoisocaproic acid was successfully hyperpolarised and showed fast uptake into subcutaneous EL4 lymphoma tumours, healthy rat brain and orthotopic gliomas in rat brain, following intravenous injection. Sufficient ^{13}C leucine signal was generated in the lymphoma tumour models enabling *in vivo* imaging of BCAT activity but the reaction was found to be significantly slower in the healthy rat brain and in the glioma tumours. This was explained by low levels of glutamate, a co-substrate for the reaction, in the glioma tumours, which is a potential limiting factor for this reaction.

Layman Abstract

Cancer is a leading cause of death worldwide and research is aimed at better understanding the disease in order to develop effective treatments. The disease is characterised by a number of features, termed the hallmarks of cancer, that enable cancer cells to not only survive and replicate, leading to tumour growth, but also to develop resistance to many of the therapies that are used to target them. Altered cell metabolism is one of these features, meaning that cancer cells utilise nutrients differently to healthy cells in order to meet the high demand for energy and building blocks needed to enable cell growth and division. Changes in metabolism are often used as targets for cancer treatment and it is therefore essential to develop ways of detecting and measuring these changes in patients, non-invasively.

Hyperpolarised ^{13}C Magnetic Resonance Spectroscopic Imaging (MRSI) is a non-invasive imaging technique that enables measurement of specific aspects of tumour metabolism. In the first part of this thesis, the performance of this technique was evaluated by using hyperpolarised ^{13}C-labelled pyruvate as an imaging agent. Upon injection of pyruvate, a breakdown product of glucose, in tumour-bearing mice, its conversion to lactate was imaged. The lactate images generated by this technique were compared with images generated by another imaging technique, Mass Spectrometry Imaging. The two techniques generated images that were very similar, cross-validating them as techniques for imaging tumour metabolism.

^{13}C-labelled pyruvate is commonly used in hyperpolarised ^{13}C MRSI to image aspects of glucose metabolism, but the metabolism of other nutrients, such as amino acids, is also of great interest in cancer. The second part of the thesis aimed to understand the role that branched chain amino acids, nutrients that we absorb from our diet, and their metabolism, play in brain cancers and to evaluate the potential of ^{13}C-labelled Ketoisocaproate as a novel substrate for imaging this metabolism. The metabolism of branched chain amino acids facilitated the growth and division of cancer cells that were derived from patients with brain tumours. The mechanism by which these amino acids contribute to the aggressiveness of brain cancer and control the rate of division of cancer cells was explored, showing that the ability to image this metabolism in patients will be beneficial for developing new treatments. Hyperpolarised ^{13}C MRSI using ^{13}C-labelled Ketoisocaproate was optimised and shown to perform well in mice with lymphoma tumours, but less so when imaging brain tumours in rats. Investigation of the poor performance of this imaging agent in brain tumours revealed that the tumours had low levels of glutamate, a metabolite that is essential for utilisation of the ^{13}C-labelled Ketoisocaproate. More work needs to be done to develop an agent that can effectively image the metabolism of branched chain amino acids in this particular cancer.

Acknowledgements

Pursuing a PhD in medical sciences has been the most challenging endeavour I have ever undertaken, and it has helped me develop not only as a scientist but also as a person. I have learned the important qualities of perseverance, commitment and critical thinking. More importantly, I have appreciated that having negative data is not necessarily a reflection of the scientist failing, but of the nature of science. We should not be disappointed when a hypothesis is proven wrong, but instead we should reflect on it and keep working until we find the correct hypothesis.

None of this would be possible without the help and support of my supervisor, Professor Kevin Brindle, who has always believed in me, even when I was deeply disappointed by my results. He had a way of boosting my confidence in every single meeting I had with him, and I left his office more determined to find answers to science and with much more optimism. Having discussions about cancer metabolism with him has always been very inspiring and I never ceased to be amazed at the immense knowledge he has and his great understanding of so many disciplines, ranging from magnetic resonance physics and sequence design to biochemical principles and cancer. It has been a privilege to be supervised by such a great scientist.

I was honoured to pursue my PhD in CRUK Cambridge Institute because the core facilities of this institute, and the people running them had a huge contribution towards my training and the results I obtained. In particular, I would like to thank Ian, Loraine, Jane, Manuela and Nicola in the Research Instrumentation and Cell Services core facility for always being willing to train me on experimental techniques and equipment that I had never used before. The genomics and bioinformatics core facilities performed and analysed my RNA sequencing experiment and the Pharmacokinetics and Bioanalytics core facility performed the LCMS analysis for the DNA methylation study. Jodi Miller and the rest of the Histopathology core facility were very helpful in processing my histopathology and immunohistochemistry requests. I am grateful to the staff in Biological Resources Unit for taking care of all the animals and making sure that their welfare was not compromised during our experimental procedures. In particular, special thanks go to Matt, Gemma, Toby, Charlotte and Mike. I am also grateful for the help I obtained from Christian Frezza's lab in the MRC Cancer Unit in performing the metabolomics analysis of my samples.

I should thank everyone in our lab for creating such a welcoming environment. In particular, I would like to thank Richard Hesketh who was my mentor in the lab for the first few months. He let me shadow him during his most busy experimental period, during which he showed me how to operate most of the imaging equipment and also helped me with some of my experiments to start off my project. His advice on experimental planning was instrumental for the rest of my PhD. Jyotsna Rao taught me a lot of the techniques I used in my project and was very supportive and interested in my ideas. She became a good friend and we ended up spending a lot of time together and having numerous conversations about science and life, particularly in the basement, during our long surgical procedures. Susana Ros was very helpful, teaching me the genetic engineering techniques that I used for modulating the expression of my genes of interest and providing me with very helpful and insightful advice during the PhD. Alan Wright has been my MRI go-to person who performed a lot of the imaging experiments with me and helped me understand some of the fundamental MRI principles. De-en Hu taught me important animal handling techniques and helped me every time I struggled with mouse and rat cannulations. His work ethic was inspirational. Sarah McGuire has been the nicest lab manager I could ever wish for. She had answers to all of my questions and was always willing to help me. She was very approachable from the first day I met her, and she became a good friend. We are definitely lucky to have her sit with us in the PhD write-up area.

I also want to thank all my fellow PhD students for being so fun to work with. I have had the fortune to meet a very diverse group of people with very different backgrounds. Over the last three years I met Richard, Robbie, Jiazheng, Lynn, Flaviu, Felix, Rike, Vencel, Anastasia and Ming Li. I want to thank Lynn for being such a lovely person and for looking out for me and making sure I was happy. Vencel and Rike, you have made my last two years in the lab very enjoyable, I will really miss having you around for a nice chat. Rike has been my study buddy for the last months and our virtual study sessions during the coronavirus lockdown period have really helped me go through the thesis writing phase.

I also need to thank the MB/PhD programme, my college and the University for providing me with the opportunity to pursue a PhD in between my medical studies and the Clinical School, CRUK and the Rosetrees Trust for funding my project. One of the greatest parts of the MB/PhD programme was the opportunity to meet a very special group of people who share the same interests as me. I feel extremely lucky to have met Joachim Hanna and Elizabeth Le through this programme because we have become great friends. They both supported me during our

clinical placements and during the PhD, by giving me helpful ideas and input on my project but also by being there for me, celebrating good moments with me and supporting me in difficult times.

Lastly, I owe this PhD, as well as all my other achievements in life until now, to my family. My parents have worked tirelessly for many years to provide me with the best possible teaching opportunities. They are responsible for what I have become, and they have always set the best example for me. I do not tell them often enough that I appreciate everything that they have done for me and I am very grateful for having the best parents in the world. My sister and my brother have also helped me during the PhD by listening to all my complaints and also by helping me with data analysis. My brother even wrote a Python script for me to analyse some of my data. Finally, my fiancé, Yiannis, has changed my world, making me happier every day. He believed in me all along, he heard all of my presentations at least twice when I was practicing, he was very understanding and supportive when I had to stay in the lab late at night and work over the weekends. I love my family and want to thank them for everything that they have done for me.

Completing a PhD is often considered a great achievement for an individual, but the truth is that I would not be able to complete this PhD without the help of all these people.

Table of Contents

List of Abbreviations

2HG	2-hydroxyglutarate
α-KG	alpha-ketoglutarate/2-oxoglutarate
ALL	Acute lymphoblastic leukaemia
AMARES	Advanced Method for Accurate, Robust and Efficient Spectral fitting
AML	Acute Myeloid Leukaemia
ATP	Adenosine Triphosphate
BCAA	Branched Chain Amino Acid
BCAT	Branched Chain Aminotransferase
BCKA	Branched Chain Ketoacid
CNS	Central Nervous System
CSI	Chemical Shift Imaging
DESI	Desorption Electrospray Ionisation
DNA	Deoxyribonucleic Acid
FADH2	Flavin adenine dinucleotide
FBS	Foetal bovine serum
FDG	Fluorodeoxyglucose
FID	Free Induction Decay
FOXM1	Forkhead box protein M1
GBM	Glioblastoma Multiforme
GOT	Glutamic Oxaloacetic Transaminase
GPT	Glutamate Pyruvate Transaminase
GSC	Glioma Stem-like Cell

H&E	Heamatoxylin & Eosin
HIF	Hypoxia inducible Factor
IDH	Isocitrate Dehydrogenase
IHC	Immunohistochemistry
KIC	a-ketoisocaproic acid
KIV	a-ketoisovaleric acid
KMV	a-keto-b-methylvaleric acid
LAT1	Large Amino-acid Transporter
LDA	Limiting Dilution Assay
LGG	Low Grade Glioma
MALDI	Matrix Assisted Laser Desorption Ionisation
MCT1	Monocarboxylate Transporter 1
MCT4	Monocarboxylate Transporter 4
MMP	Matrix Metalloproteinase
MRI	Magnetic Resonance Imaging
MRSI	Magnetic Resonance Spectroscopic Imaging
MSI	Mass Spectrometry Imaging
MSUD	Maple Syrup Urine Disease
mTOR	Mammalian Target Of Rapamycin
NADH	Nicotinamide Adenine Dinucleotide
NADP	Nicotinamide Adenine Dinucleotide Phosphate
PCA	Perchloric Acid
PDGF	Platelet Derived Growth Factor
PDOX	Patient Derived Orthotopic Xenograft

PDX	Patient Derived Xenograft
PET	Positron Emission Tomography
PHD	Prolyl Hydroxylase Domain containing protein
PI3K	Phosphoinositide-3-kinase
qPCR	Quantitative PCR
RF	Radio-Frequency
ROS	Reactive Oxygen Species
SIMS	Secondary Ion Mass Spectrometry
SNR	Signal-to-Noise Ratio
SPECT	Single Photon Emission Computed Tomography
TBS	Tris Buffered Saline
TCA	Tricarboxylic Acid
TE	Echo Time
TET	Ten-Eleven Translocation
TIC	Total Ion Count
TMSP	Trimethylsilylpropanoic Acid
TR	Repetition Time
VEGF	Vascular Endothelial Growth Factor
WHO	World Health Organisation

List of Figures

Chapter 1 - Introduction

1.1 Cancer

Cancer is a leading cause of death worldwide, accounting for more than one in four deaths in the UK[1]. Despite advances in diagnosis, prognosis and treatment of cancer, cancer remains one of the most dreadful diseases for many patients.

In 2000, Douglas Hanahan and Robert Weinberg, described the hallmarks of cancer[2], which were specific characteristics observed in the cells of most types of cancer, that enabled cancer cell survival and proliferation. These hallmarks included: self-sufficiency in growth signals, insensitivity to growth inhibitory signals, evasion of programmed cell death, limitless replicative potential, sustained angiogenesis and tissue invasion and metastasis[2]. Eleven years later, the same authors published a second paper, where they added two more hallmarks; reprogramming of energy metabolism and evading immune destruction[3] (Figure 1).

Figure 1 The revised hallmarks of cancer, adapted from Hanahan and Weinberg[3]

1.1.1 Cancer metabolism

Cancer cells are under high metabolic pressure, due to their high proliferation rate. Cells require a constant supply of nutrients which are used for biosynthetic purposes but also for ATP generation. Also, the high growth rate of cancer cells in a tumour leads to rapid changes in the microenvironment, such as hypoxia, which means that cells need to be metabolically very adaptable in order to survive under these changing conditions. Many metabolic pathways are altered in cancer, enabling favourable energy production, effective redox balance and enhanced biosynthetic activities, all of which provide cancer cells with a selective advantage during tumourigenesis[4,5].

Cancer metabolism refers not only to the metabolic reactions taking place in a cancer cell but also to the ability of cancer cells to acquire essential nutrients from their environment, their ability to use those nutrients efficiently and to use metabolites for various downstream effects[4].

1.1.1.1 Enhanced nutrient acquisition

Two substrates that are avidly used by cancer cells are glucose and glutamine[4]. Both nutrients can be taken up into the cells and can be catabolised to generate intermediates necessary for macromolecule synthesis. Additionally, through the catabolism of these nutrients, reducing power in the form of NADH, $FADH_2$ and NADPH is generated, which is needed to fuel ATP generation, enable biosynthetic reactions and maintain the cell's redox capacity. Glutamine is also a nitrogen donor for the synthesis of nitrogen-containing compounds such as nucleotides and non-essential amino acids. Cancer cells achieve nutrient acquisition through upregulation of cell membrane transporters such as GLUT1, which mediates glucose uptake, but they also utilise other modes of nutrient acquisition such as lysosomal degradation of extracellular proteins which can be taken up by micropinocytosis[4].

1.1.1.2 Reprogrammed metabolic pathways

Other than their ability to acquire nutrients, cancer cells reprogram their metabolic pathways to enable efficient usage of nutrients. One of the first reprogrammed metabolic pathways to be documented in cancer was that of aerobic glycolysis, often referred to as the Warburg effect since it was first observed and documented by Otto Warburg[6]. Many tumours are highly glycolytic, with an increased rate of glucose uptake, consumption and preferential conversion to lactate, regardless of the availability of oxygen. This property of tumours is exploited in the

clinic, where ^{18}F-Fluorodeoxyglucose (FDG), an analogue of glucose, is used as a Positron Emission Tomography (PET) tracer to diagnose and stage cancer[4,7]. The conversion of glucose to pyruvate is much less energy efficient than pyruvate oxidation in the Tricarboxylic Acid (TCA) cycle, which makes the Warburg effect sound counterintuitive. However, even though aerobic glycolysis is less efficient than the TCA cycle in terms of ATP generation, the Warburg effect facilitates the generation of building blocks such as amino acids and nucleosides through generation of NADPH and the donation of carbons which are needed for cell growth and division[8]. Aerobic glycolysis is evident in many cancer types but in certain cancer cells, such as lung cancer stem cells and leukaemic cells there is evidence of higher rates of glucose oxidation in the TCA cycle[9,10].

The TCA cycle is still essential for cancer cells and similarly to glycolysis, it generates numerous intermediates that are used as precursors for macromolecule biosynthesis, such as amino acid and fatty acid synthesis, which happen at a faster rate in cancer cells. In order for TCA cycle flux to be maintained despite the losses of intermediates, a number of anaplerotic pathways are enhanced, which enable entry of TCA cycle intermediates at sites other than acetyl-CoA. Some examples of anaplerotic pathways include glutaminolysis, which generates alpha-ketoglutarate (α-KG) (Figure 2), and pyruvate carboxylation, which produces oxaloacetate from pyruvate[5].

Many tumours show high glutamine consumption[11]. Glutamine is transported across the plasma membrane through several transporters of the SLC superfamily of transporters, including SLC1A5 which enables sodium dependent uptake of glutamine and which is upregulated in many cancers[12]. Glutamine is used to generate intermediates that can enter the TCA cycle, thus maintaining oxidative metabolism, even if pyruvate is converted predominantly to lactate. Glutaminase catalyses the hydrolysis of glutamine, converting it to glutamate[13]. Glutamate dehydrogenase then catalyses the generation of α-KG, which can be used either for generation of NADH and NADPH through the action of IDH3 and IDH1/2, respectively in reverse flux in the TCA cycle to generate citrate, which acts as a precursor of fatty acids or in forward flux in the TCA cycle through the action of α-KG dehydrogenase.

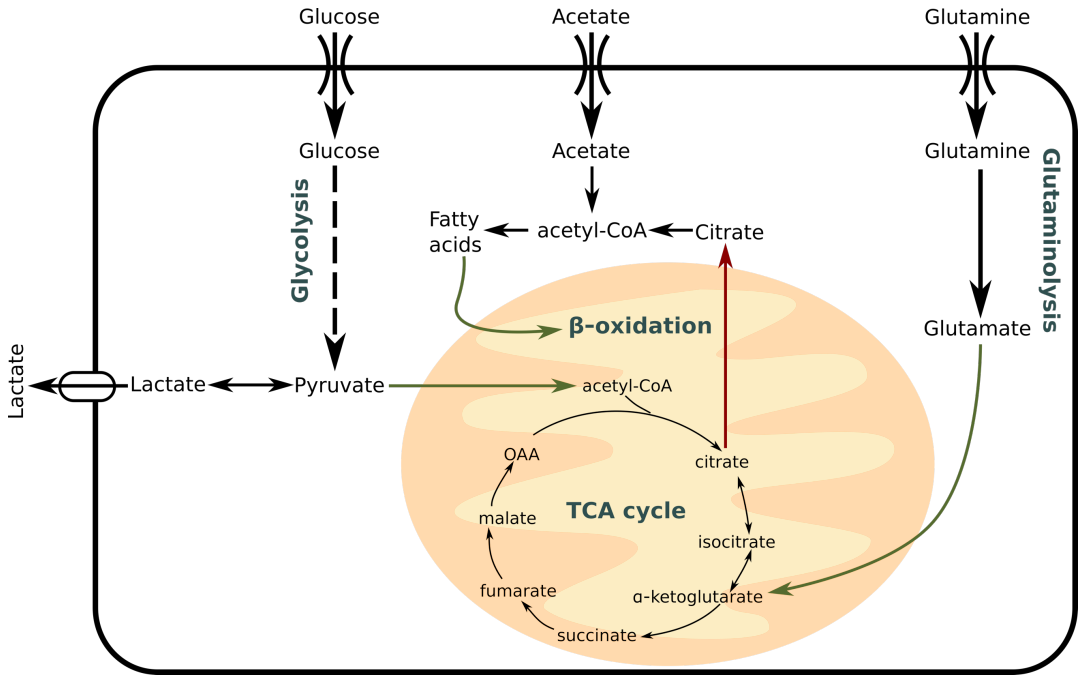

Figure 2 Schematic diagram illustrating cancer cell metabolism. *Glucose, glutamine and citrate are three of the most widely used nutrients by cancer cells. Abbreviations: OAA: oxaloacetate*

1.1.2 Regulation of cancer metabolism

Cancer cells are characterised by their genetic instability, with many genomic alterations, a lot of which are thought to lead to transformation of pre-malignant cells to a cancerous state. The expression of a number of oncogenes, which are genes that facilitate cancer growth, are upregulated through genetic and epigenetic changes. Alternatively, tumour suppressor genes, genes that would normally suppress cancer growth are downregulated through gene deletions and mutations. The genetic makeup of cancer cells is thus very different to normal cells. Many of these genetic changes lead to changes in metabolic processes and hence the reprogrammed metabolism observed in cancer.

One of the most frequently altered pathways in cancer is the PI3K-AKT-mTOR pathway (*Figure* 3). The pathway is activated physiologically when growth factors stimulate Phosphatidylinositol 3-kinase (PI3K) activity through receptor tyrosine kinases. PI3K then activates its downstream targets, AKT and mammalian target of rapamycin (mTOR), which promote the activity of anabolic pathways. In many tumours, PI3K-AKT-mTOR pathway is constitutively active, enabling cell proliferation, even in the absence of growth factor stimulation[5].

Another example of a genetic alteration leading to metabolic changes is increased *MYC* expression resulting from gene amplification, chromosomal translocation and single nucleotide polymorphisms. Increased levels of this transcription factor lead to upregulation of many metabolic genes, including enzymes involved in glycolysis, fatty acid synthesis and glutaminolysis[14].

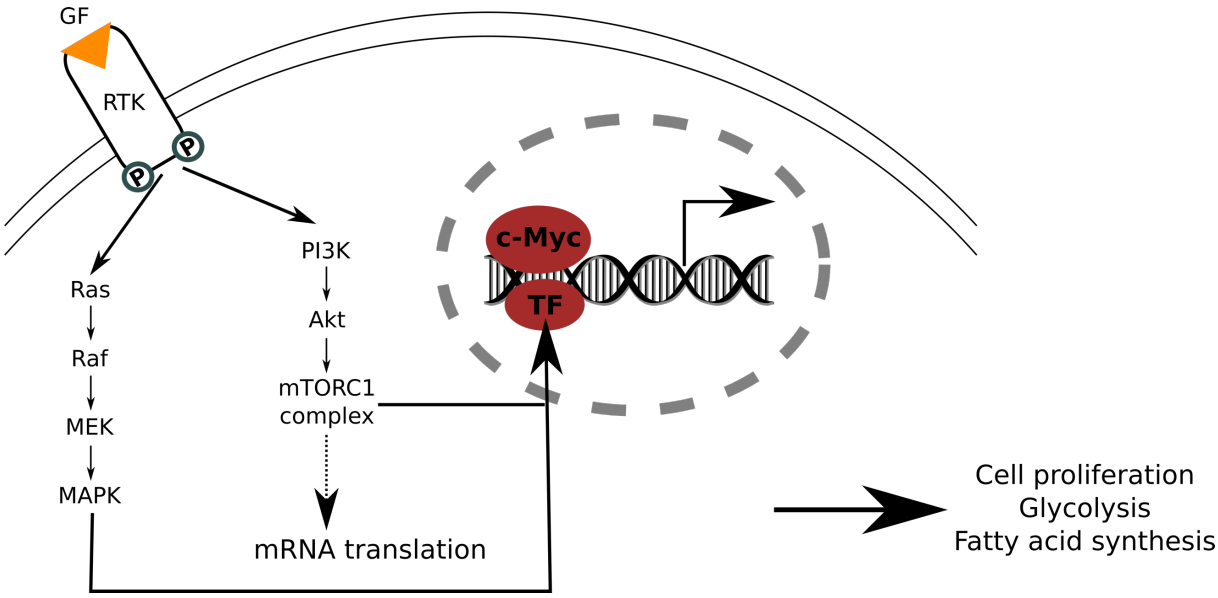

Figure 3 Examples of cell signalling processes that are constitutively activated in cancer, driving metabolic changes in the cell. *The PI3K-AKT-mTOR pathway promotes cell proliferation through increased protein synthesis. Increased expression of c-Myc transcription factor leads to increased glycolysis and fatty acid synthesis, promoting cell proliferation.*

Cancer metabolism is regulated by factors other than genetic alterations, including extrinsic factors that depend on the environment of cancer cells. This is the reason why the metabolism of cancer cells in culture often differs from the metabolism of the same cells in a tumour[15]. For example, lung cancer cells in culture are dependent on glutamine as a TCA cycle fuel, whereas tumours derived from the same cells use glucose as a fuel[16]. Cell lineage can also affect the way metabolism is affected by genetic alterations in different cancers. For example, increased *MYC* expression leads to enhanced catabolism of glutamine in liver tumours but enhanced glutamine synthesis from glucose in lung tumours[17].

1.1.3 Key metabolites in cancer

1.1.3.1 Oncometabolites

Genetic mutations that directly affect specific metabolic enzymes are much rarer in cancer than mutations that indirectly affect metabolic networks via changes in signalling pathways and

transcription factor expression. However, some specific mutations have been characterized in a number of cancers which often lead to the generation of oncometabolites.

An example are the mutations in the active site of Isocitrate Dehydrogenase (IDH), which are present in some cases of Acute Myeloid Leukaemia (AML) and glioblastoma[18,19]. Mutations in this enzyme lead to a neomorphic activity, leading to the generation of the oncometabolite D-2-hydroxyglutarate (D2HG). This metabolite can accumulate to millimolar levels and leads to epigenetic changes due to its inhibitory effect on DNA and histone demethylases[20].

Other examples include mutations of the succinate dehydrogenase complex and fumarase, which lead to the accumulation of succinate and fumarate, respectively[21,22]. Both of these metabolites can act as oncometabolites in a similar manner to 2HG, by inhibiting α-KG dependent dioxygenases[23].

1.1.3.2 α-ketoglutarate

α-KG is an important metabolite in physiology and disease, including cancer [13,24-27]. The metabolite is involved in the generation of ATP, amino acid biosynthesis, signalling and epigenetic regulation[24]. α-KG, also known as 2-oxoglutarate, is a central metabolite of the TCA cycle and is formed from isocitrate by oxidative decarboxylation catalysed by IDH. It can then be converted by α-KG dehydrogenase to succinyl-CoA and NADH[24]. Redox state in the cell determines the amount of α-KG in the mitochondria since an excess of NAD+ leads to more oxidative decarboxylation of α-KG to succinyl-CoA whereas an excess of NADH leads to reductive transamination of α-KG to glutamate via the action of glutamate dehydrogenase.

In addition to its role in the TCA cycle in ATP generation, α-KG also takes part in other metabolic reactions in the mitochondria and in the cytosol. It is transported through the inner and outer membranes of mitochondria through the α-KG/malate antiporter and the voltage-dependent anion channel (VDAC), respectively[27].

Both glucose and glutamine can be used for α-KG production. α-KG can be generated from carbohydrate metabolism, through the TCA cycle and through the action of glutaminase and glutamate dehydrogenase. α-KG also takes part in transamination reactions, catalysed by Glutamate Pyruvate Transaminases (GPT1/2) and Glutamate Oxaloacetate Transaminases (GOT1/2) [27] as well as by Branched Chain Aminotransferases (BCAT) 1 and 2.

1.1.3.2.1 α-ketoglutarate and cell homeostasis

Metabolically, α-KG contributes to the regulation of protein synthesis since it is a substrate for the reversible reaction catalysed by glutamate dehydrogenase, leading to glutamate synthesis, which is then used to produce proline, arginine and glutamine. It can also control L-carnitine biosynthesis and is therefore involved in the regulation of lipid metabolism[27].

α-KG plays an active role in signalling pathways in cellular physiology. For example, it regulates activation of the transcription factor NF-κB by activating PHD1, which leads to activation of inhibitory kB-α[28]. α-KG can also inhibit the mitochondrial ATP synthase, leading to inhibition of mTOR signalling[29].

α-KG also protects the cell against oxidative stress. For example, α-KG takes part in non-enzymatic oxidative decarboxylation, neutralizing hydrogen peroxide[27].

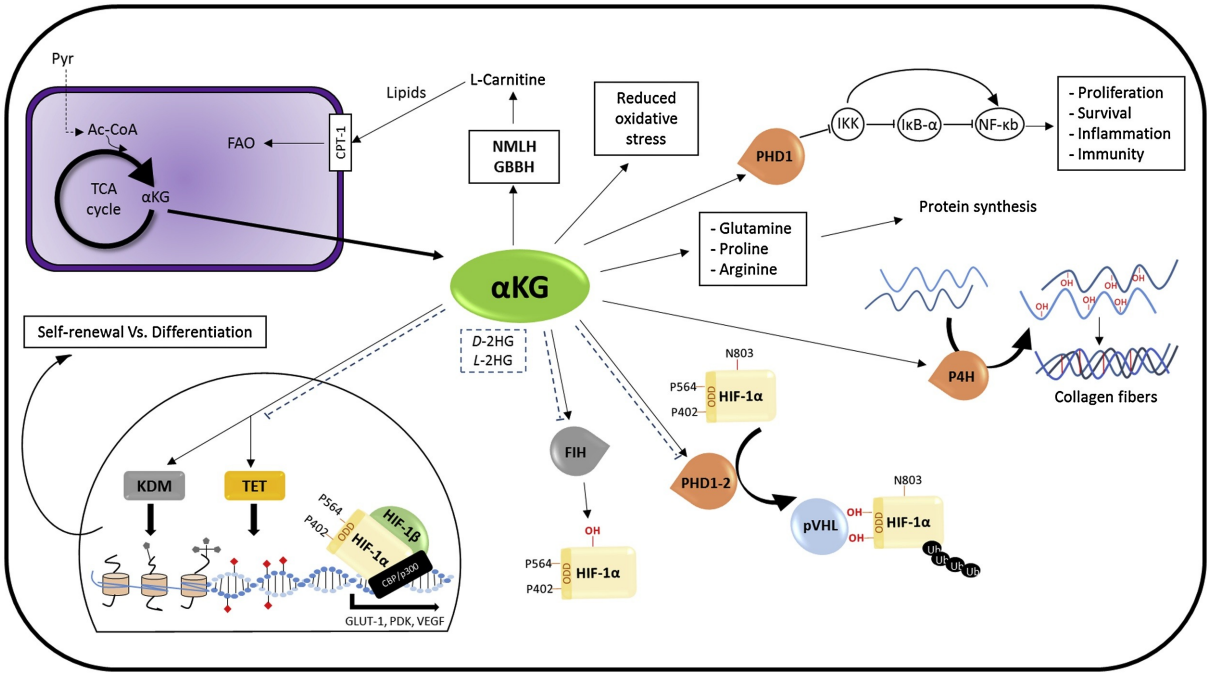

Figure 4 The role of α-KG in cell homeostasis, reproduced from Abla et al[27]*. α-KG controls lipid synthesis by controlling L-carnitine biosynthesis and protein synthesis by controlling glutamine, proline and arginine biosynthesis. It also plays a role in protecting the cell against oxidative stress and is involved in the regulation of transcription factors including NFkB and HIF.*

1.1.3.2.2 α-ketoglutarate and epigenetic regulation

Chemical modifications to chromatin can regulate DNA transcription, repair and replication, therefore regulating the function of the genome. Chromatin modifications include DNA methylation and histone post-translational modifications[24]. Many of the enzymes involved in these reactions belong to the family of 2-oxoglutarate dependent dioxygenase enzymes, which

require α-KG as a co-substrate. These enzymes include histone demethylases such as JmjC domain demethylases (JHDMs) and DNA demethylases such as Ten-eleven Translocation Enzymes (TETs)[30]. Succinate, fumarate and 2-HG have been shown to inhibit TETs leading to enhanced DNA methylation, which may increase carcinogenesis[31-33], while α-KG can reverse this. For example, hypermethylation of promoter CpG islands results in transcriptional silencing of tumour suppressor genes and carcinogenesis in *IDH* mutant gliomas where 2HG inhibits DNA demethylases[34]. DNA and histone methylation status is also important in modulating stemness, depending on the pluripotency state, with high α-KG levels favouring self-renewal in naïve mouse embryonic stem cells but favouring differentiation in primed human or mouse epiblast stem cells[27,29,35].

1.1.3.2.3 Role of α-ketoglutarate as an anti-cancer agent

Altered metabolism is a hallmark of cancer, and α-KG plays an important role in controlling metabolic flux. In cancer cells, α-KG is produced by glutaminolysis and it can then either be oxidised to succinyl-CoA to feed the TCA cycle or undergo reductive carboxylation to citrate, to support lipid synthesis[27].

α-KG as well as its structural analogues succinate and fumarate are known to be involved in the regulation of signalling pathways that are linked to carcinogenesis. PHDs 1-3 regulate the stability of HIF-1α and hence the activity of HIF as a transcription factor. These enzymes are strongly dependent on the concentration of α-KG in the cells, as the K_m for α-KG of many of these enzymes is around 50 μM, similar to the physiological concentration of α-KG, meaning that small changes in concentration can lead to large changes in enzyme activity[36].

Studies *in vitro* and *in vivo* have shown that exogenous α-KG exhibited anti-tumour activity by reducing the levels of HIF-1α in the tumours, thus inhibiting angiogenesis[24] and also by inducing apoptosis via a HIF-independent mechanism, through regulation of PHD3[37]. In a study *in vitro*, addition of 5-50 mM α-KG to three colon adenocarcinoma cell lines, Caco-2, HT-29 and LS-180 led to antiproliferative effects and disruption of the cell cycle by increasing expression of cyclin dependent kinase inhibitors p21 Waf/CIP1 and p27 Kip1[38]. Additionally, α-KG addition to the cells led to reduced cyclin D1 and reduced phosphorylation of Rb leading to cell cycle arrest in G1 phase. The concentrations used in this study are much higher than the physiological concentrations of α-KG due to the low cell membrane permeability for α-KG[24].

Accumulation of endogenous α-KG has also been shown to inhibit cancer progression. For example, α-KG dehydrogenase inactivation in breast cancer leads to accumulation of α-KG, which limits cell migration and EMT[27].

Therefore, α-KG is a promising metabolite for the treatment of cancer, especially in cases where tumourigenesis is associated with inhibition of 2-oxoglutarate-dependent dioxygenases. α-KG is a hydrophilic molecule with low cell permeability, which is why various esters of α-KG have been used to increase the intracellular concentrations of α-KG[39].

1.1.3.3 Glutamine

Glutamine is a non-essential amino acid that plays a crucial role in cancer metabolism, as an energy source for the cell but also as a nitrogen donor. Glutamine is the most abundant amino acid in plasma and many tumours show enhanced glutamine uptake even though glutamine can be synthesised *de novo*[40].

Glutaminolysis, which describes a series of reactions that convert glutamine into substrates that can enter the TCA cycle, is extremely important for maintaining ATP production in cancer cells, especially in cells with high HIF-1α activity leading to inhibition of pyruvate dehydrogenase and thus inhibition of glucose carbon entry into the TCA cycle. In addition to this, glutaminolysis provides nitrogen for nucleotide and amino acid synthesis and leads to NADPH production for lipid and nucleotide synthesis[13].

The first step in glutamine catabolism is its conversion to glutamate, which is catalysed by the glutaminase enzymes, which have been shown to be upregulated and to promote tumour growth in a number of models[40]. Glutamate can then be used in the cell for glutathione synthesis, generation of α-KG and as a donor of amino groups for the synthesis of non-essential amino acids including alanine, aspartate, serine and glycine.

More recently, it has been suggested that the role of glutamine in promoting tumour growth is context dependent. For example, in a panel of non-small cell lung cancer cell lines, variability in the response of cells to glutamine deprivation was observed[41], and *Kras*-driven non-small cell lung cancer tumours were shown to be less dependent on glutamine than cultured cells *in vitro*[16]. Similarly, variability in glutamine dependence was observed in breast cancer cells with basal-type cells showing higher dependence than luminal-type cells[42].

1.1.3.4 Branched Chain Amino Acids

Leucine, isoleucine and valine constitute the group of branched chain amino acids. They are essential amino acids that are preferentially taken up by tumours[43]. Upregulation of the enzymes catalysing branched chain amino acid catabolism has been observed in most cancers. The cytosolic isoform of the enzyme catalysing transamination of the amino acids to their respective ketoacids, Branched Chain Aminotransferase 1 (BCAT1), has been of great interest in the field of cancer metabolism recently as it has been implicated in tumour growth and because in normal cells it is only expressed in the brain, gonadal tissues and activated T lymphocytes, making it an attractive therapeutic target[43].

1.1.3.4.1 BCAT1 is implicated in the progression of different cancers

Over the last decade, BCAT1 upregulation has been shown in a number of cancers, including breast cancer[44], non-small cell lung carcinoma[45], colorectal cancer[46], urothelial carcinoma[47], ovarian cancer[48], gastric cancer[49], leukaemia[50] and glioblastoma[51,52]. In low-malignant potential (LMP) and high-grade (HG) serous epithelial ovarian tumours, BCAT1 upregulation correlated with hypomethylation of a 425 nucleotide CpG-rich region of the *BCAT1* gene[48]. It appears that the enzyme can play different roles in different cancers, and that net flux in the transamination reaction is also dependent on the tissue of origin of the cancer.

1.1.3.4.2 Role of BCAT1 in cell proliferation and migration

BCAT1 was found to be significantly upregulated in early and later stages of nasopharyngeal carcinoma when compared to normal epithelium, as seen on immunohistochemistry. The role of BCAT1 was investigated in nasopharyngeal carcinomas by transfecting cells with BCAT1 shRNA and searching for phenotypic changes. BCAT1 knockdown led to reduced colony formation in clonogenic assays, reduced mobility in migration assays and reduced invasion capability in Matrigel-coated transwell chamber assays[53]. Similar experiments in hepatocellular carcinoma cells revealed very similar results in terms of the role of BCAT1 in cell migration and invasion. In this same study, BCAT1 expression levels were correlated with overall and disease-free survival rates[54]. Zheng et al demonstrated that BCAT1 expression accelerated hepatocellular carcinoma growth *in vivo*, in mice[55] and in the same study, the effects on cell proliferation of BCAT1 overexpression and BCAT1 suppression were explained by changes in cell-cycle distribution, with BCAT1 overexpression reducing the percentage of cells in S phase

and increasing the percentage of cells in G2/M phase. BCAT1 knockdown in ovarian cancer cells also led to cell cycle arrest in S phase[48].

One of the proteins that BCAT1 interacts with and that is involved in tissue remodelling is CD147, also known as basigin and Emmprin (Extracellular Matrix Metalloproteinase Inducer). This is a cell membrane glycoprotein which has been implicated in tissue remodelling[56], since it is released by cancer cells and stimulates fibroblasts and endothelial cells to release MMPs[57]. Inhibition of CD147 expression by siRNA in U251 human glioma cells led to reduced migration and invasion *in vitro*, as measured by scratch-wound assays and Boyden chamber assays, respectively[58]. In human glioblastoma studies, expression of CD147 was shown to be upregulated in glioblastoma tissue and increased CD147 expression was associated with poor overall survival of patients[59]. BCAT1 is proposed to be in a complex with CD147 in the cytosol of human breast cancer cells and suppression of BCAT1 activity in these cells with a specific inhibitor led to suppression of CD147 in conditioned media[60]. This suggests that BCAT1 might play a role in enabling the secretion of CD147 from cancer cells which could be linked to the migratory potential of the cells.

1.1.3.4.3 Role of BCAT1 in chemoresistance

BCAT1 was shown to play a role in rendering hepatocellular carcinoma cells resistant to cisplatin treatment[55]. The proposed mechanism was the enhancement of autophagy in the cells upon BCAT1 overexpression. In contrast, BCAT1 knockdown in ovarian cancer cells had no significant effect on the cells' sensitivity to cisplatin and paclitaxel[48].

1.1.3.4.4 Role and importance of BCAT1 are cancer-type dependent

Although many studies have now linked BCAT1 expression to an aggressive tumour phenotype, it appears that the importance of BCAA metabolism in tumour growth is dependent on the tissue of origin. In a study comparing pancreatic ductal adenocarcinoma and non-small cell lung cancer, both resulting from the same *TP53* and *KRAS* mutations, the dependence of the tumours on BCAA metabolism was very different, with lung cancer cells showing enhanced uptake of BCAAs and incorporation of the nitrogen from these amino acids into protein and non-essential amino acids, while pancreatic tumour cells did not show any differences in BCAA metabolism from healthy pancreatic tissue[61]. In addition, deletion of both *BCAT1* and *BCAT2* genes led to a significantly reduced ability of the lung cancer cells to grow into tumours *in vivo* but not of the pancreatic ductal adenocarcinoma cells in the pancreas[61]. More recently, BCAT2

instead of BCAT1 has been linked to progression of pancreatic intraepithelial neoplasia in mice and BCAT2-mediated catabolism of branched chain amino acids has been shown to be critical for the development of *KRAS* mutation-driven pancreatic ductal adenocarcinoma[62].

1.1.4 Metabolic Heterogeneity in Cancer

Cancer is characterised by a high degree of intertumoural and intratumoural heterogeneity, which is one of the factors contributing to the poor prognosis associated with many types of cancer. Cancer cells are heterogeneous in terms of their genetic make-up, their transcriptional profile and their metabolism. Therefore, even though there are some well-characterised metabolic alterations that commonly occur in cancer, not all of them are present in all cancer cells.

Intratumoural metabolic heterogeneity can arise as a result of the heterogeneity of tumour perfusion, with some areas of the tumour being more vascular than others. This means that cancer cells in different regions of the same tumour experience different conditions in terms of nutrient availability and oxygen concentration. Cancer cells will adapt their metabolic phenotype to maximise survival and proliferation under the conditions where they reside, leading to metabolic heterogeneity within the tumour.

Tumour heterogeneity poses many problems in clinical practice and in cancer research. Specific treatment for tumours works for cells that are sensitive to the treatment but due to the heterogeneity of the tumour, some cells will tend to be resistant to treatment and hence lead to cancer recurrence. Currently, the field of oncology is heavily reliant on tumour biopsies which are often used for staging the disease and for determining the treatment process to follow. However, due to intratumoural heterogeneity, the tumour biopsy sample is not necessarily representative of the whole tumour.

In cancer research, many techniques involve studying tumour models, mainly xenografts in rodents, where the tumour is homogenised, and conclusions are drawn from studying the tumour homogenate. However, any measurements taken from the homogenate represent an average of the cells making up the tumour rather than the measurements of each individual cell. Therefore, techniques that can capture tumour heterogeneity are necessary for cancer research and for guiding treatment in clinical practice.

1.1.5 Targeting metabolism for cancer therapy

Research into cancer metabolism has shown how metabolic changes facilitate cell proliferation and survival. These metabolic changes are sometimes essential for particular cancers, making them potential therapeutic targets. An example is the effective treatment of Acute Lymphoblastic Leukaemia (ALL) using asparaginase[63]. This enzyme reduces the concentration of circulating asparagine in plasma, which is essential for protein synthesis in cancer cells.

Identifying targets for effective cancer therapy is challenging for a number of reasons. Firstly, toxicity can be a problem because metabolic enzymes play important physiological roles in healthy tissue. Secondly, many of the pathways that are reprogrammed in cancer cells are also reprogrammed in normal proliferating cells such as immune cells, therefore targeting those pathways will most likely lead to immunosuppression and other toxic effects[64]. Targets with a good therapeutic window are thus challenging to identify.

Importantly, the high metabolic flexibility possessed by cancer cells as well as their ability to adapt to changing conditions, leads to the problem of resistance to treatment. A very small number of metabolic activities are involved in tumourigenesis, some are required for cancer progression, but many are dispensable in some cases[15]. For this reason, it is crucial to identify true metabolic liabilities of cancer cells, which will most likely require simultaneous targeting of different pathways, in order to effectively suppress tumour growth and significantly slow cancer progression.

Over the last few years, research into cancer metabolism has identified a number of targets for potential therapy. For example, the observation that cancer cells consume high amounts of glucose, has triggered a lot of research into inhibitors of glycolysis. 2-Deoxyglucose, an analogue of glucose that is converted to 2-deoxyglucose-6-phosphate and accumulates in the cells, inhibiting hexokinase, has shown promising results in slowing down the proliferation of cancer cells in preclinical studies, but unfortunately has shown high toxicity in clinical trials[64,65]. In cancer types where specific enzymes are mutated, inhibitors against the mutated enzymes are being developed to target cancer cells. For example, inhibitors of mutant IDH1 and IDH2 enzymes are currently being tested in clinical studies for the treatment of IDH mutant glioblastoma and AML[64].

Further research into cancer metabolism will enable identification of novel metabolic dependencies of cancer as well as potential pathways that can be targeted simultaneously for maximising therapeutic effect. Importantly, methods of characterising the metabolism of individual tumours, such as metabolic imaging will facilitate targeted approaches to therapy which will maximise the chances of survival.

1.2 Metabolic imaging

Metabolic imaging techniques are valuable in cancer research and clinical practice, enabling investigation of cancer metabolism in a spatially dependent manner, thus capturing the metabolic heterogeneity of tumours. Metabolic Imaging techniques include Positron Emission Tomography (PET), Single-Photon Emission Computed Tomography (SPECT), ^{13}C Hyperpolarised Magnetic Resonance Spectroscopic Imaging (MRSI) and Mass Spectrometry Imaging (MSI). All these have shown promising results in pre-clinical and clinical studies in imaging cancer metabolism, characterising the metabolic profile of tumours, and in predicting and measuring treatment response.

1.2.1 ^{18}F-FDG Positron Emission Tomography (PET)

^{18}F-FDG is a positron emitting glucose analogue that has been used extensively in the clinic to detect metastases using PET, hence staging the disease, and for monitoring treatment response. ^{18}F-FDG enters cancer cells through the upregulated GLUT transporters and accumulates in the phosphorylated form through the action of hexokinase. Tumours that are glucose avid show enhanced uptake and accumulation of ^{18}F-FDG. One of the disadvantages of ^{18}F-FDG, other than its radioactive nature, is that it can only provide information on the uptake of glucose but gives no information on glycolytic flux or downstream metabolism.

1.2.2 ^{13}C Hyperpolarised Magnetic Resonance Spectroscopic Imaging (MRSI)

^{13}C Hyperpolarised MRSI is another promising metabolic imaging technique, that enables dynamic imaging of label exchange from a substrate of interest to one or more products of interest *in vivo*. The main principles of Nuclear Magnetic Resonance (NMR) are introduced here, followed by a brief introduction on ^{13}C MRSI and its potential applications.

1.2.2.1 Nuclear Magnetic Resonance (NMR)

NMR is based on the magnetic properties of some atomic nuclei. Several nuclei, including ^{1}H and ^{13}C, possess spin angular momentum, which gives them a magnetic moment. Nuclear magnetic moments are quantized, with nuclei existing in a set number of possible spin states[66]. ^{1}H and ^{13}C nuclei have a spin quantum number of ½ and can only exist in two spin states. When an MR active spin ½ nucleus is placed within an external magnetic field, its magnetic dipole aligns either parallel or antiparallel with the direction of the external magnetic field. These two alignment options represent the two energy levels of the nuclear spin, with the energy difference between the two states being dependent on the magnetic field strength (B_0) and the gyromagnetic ratio (γ) of the nucleus. Usually, there is a small excess of parallel spins (low energy level) relative to antiparallel spins (high energy level), giving rise to a net magnetisation vector[67]. The spins do not align exactly with the external magnetic field but precess about this field (Figure 5) at a frequency, ω, which depends on the identity and chemical environment of the nucleus. The precession frequency, ω, is given by the Larmor equation:

$$\omega = \gamma \times B_{eff}$$

where γ is the gyromagnetic ratio of the nucleus and B_{eff} is the effective magnetic field that the nucleus experiences, which depends on the shielding effect of surrounding electrons[68]. Application of a radiofrequency (RF) oscillating magnetic field (B_1) at frequency ω, so that it is resonant with the precession frequency, results in the absorption of energy, flipping the spins between the two energy levels (Figure 5). Upon removal of the oscillating magnetic field, the excited nuclei realign with the external magnetic field (B_0). Rotation of the decaying net magnetization vector within the x,y plane creates a current in the receiver coil, which represents the signal and is called the Free Induction Decay (FID). Applying the RF oscillating magnetic field in the form of a short pulse covers a range of resonance frequencies and Fourier transform of the resulting FID produces a spectrum of absorbances, from which the chemical structure of a molecule can be inferred.

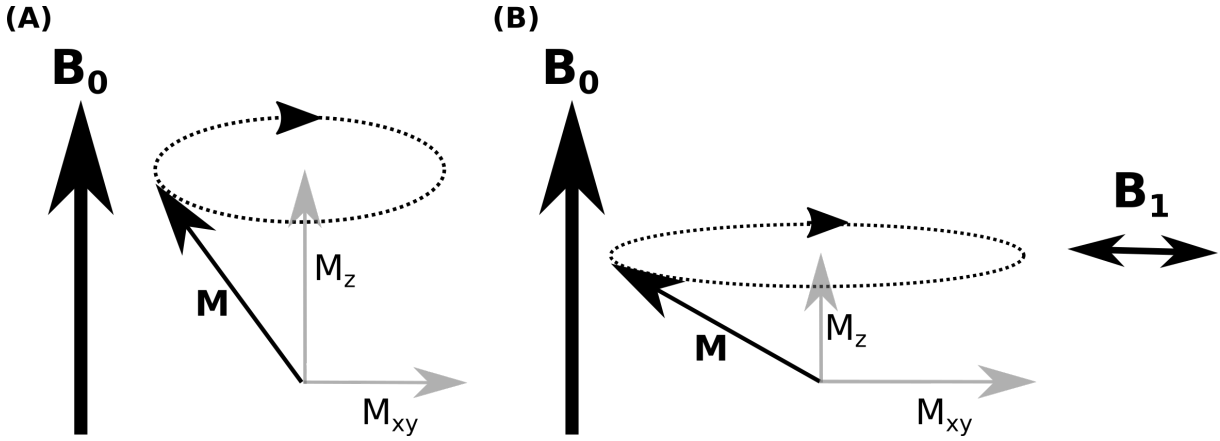

Figure 5 Net magnetisation vector. *(A) When MR active nuclei are positioned in a magnetic field B_0, the magnetisation vectors associated with their nuclear spin precess around B_0 at a characteristic precession frequency, with the net vector aligned with B_0. (B) Upon application of an oscillating magnetic field B_1 in the form of an RF pulse, the net magnetisation vector that lies along B_0 is tilted into the xy plane.*

The most commonly imaged nucleus in MRI is ^{1}H due to the sensitivity of the proton to NMR detection (high γ) and the abundance of water in biological systems. The voxel intensity depends on the proton density of the tissue as well as two tissue-specific parameters: the longitudinal relaxation time, T_1, which is a measure of the time required for the magnetic moments of the excited nuclei to return to equilibrium and the transverse relaxation time, T_2, which is a measure of the time taken for the FID signal to decay in the x,y plane as a result of natural interactions at the atomic or molecular level. However, in real NMR experiments, the observed signal in the x,y plane decays faster than what would be expected by these interactions. Therefore, another time constant, the effective T_2, also known as T_2* is defined, which is mainly the result of inhomogeneities in the magnetic field. Many of the processes leading to T_2* decay are reversible, meaning that if a second RF pulse is applied some time after the initial RF pulse, the dephased spins can be rephased, generating a spin echo (Figure 6). The time between the middle of the first RF pulse and the peak of the spin echo is defined as the echo time (TE). The repetition time, TR, is the time delay between the repetition of the first 90° pulse in the sequence.

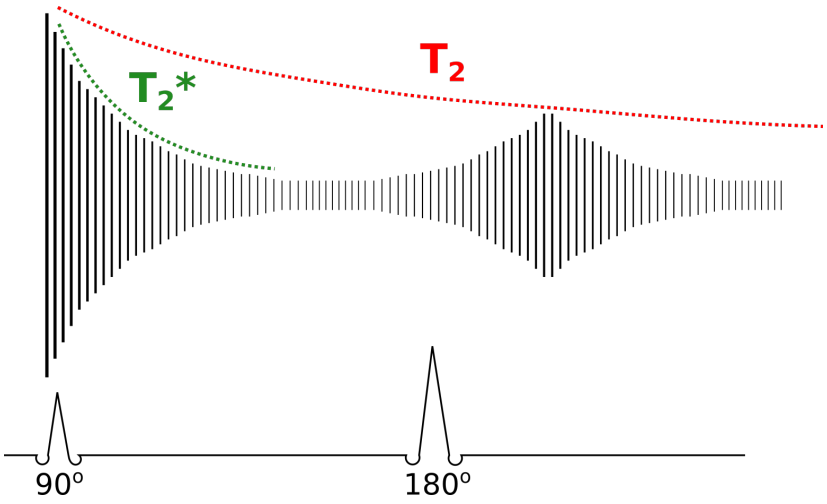

Figure 6 Principle of a spin echo. *After the 90° excitation pulse, the signal decays quickly due to T_2* relaxation processes. In order to eliminate the T_2* related effects, a rephasing 180° excitation pulse is applied which refocuses the magnetisation and generates a second FID, enabling measurement of T_2 relaxation.*

The pulse sequence used for signal acquisition determines the contrast created between different tissues by determining which of the decay parameters will more significantly affect the observed signal. In general, a long TR minimises the effects caused by T_1 relaxation since the spins have enough time to relax before the excitation pulse is repeated. A short TE minimises the T_2 mediated effects because there is not enough time for T_2 relaxation to be observed between the excitation and the echo. Therefore, a pulse sequence with a short TR and a short TE enables T_1 weighted contrast, where the contrast generated will depend on the differences in T_1 constants between the tissues being imaged. For T_2 weighted imaging, a long TR and a long TE are used.

In MRI, magnetic field gradients enable spatial encoding of the FID. The resonant frequency of the detected nucleus is directly proportional to the applied magnetic field, therefore by varying the magnetic field across the sample, the resonant frequency of the nucleus becomes a function of its position in the sample. For encoding in the axial dimension, a magnetic field gradient is added to the constant homogeneous magnetic field, B_0, enabling excitation of a specific slice by modulating the frequency of the RF pulse (Figure 7). For two dimensional in-plane spatial reconstruction, phase encoding (Figure 7) and frequency encoding gradients are implemented. For frequency encoding, a magnetic field gradient is applied during signal acquisition. As a result, nuclei at different locations along the gradient resonate at different frequencies. For phase encoding, the gradient is applied between the excitation and signal acquisition, leading to changes in the precession frequencies of nuclei in different locations and

hence a phase difference at the time of acquisition. This enables three-dimensional localisation of the signal and hence the acquisition of images.

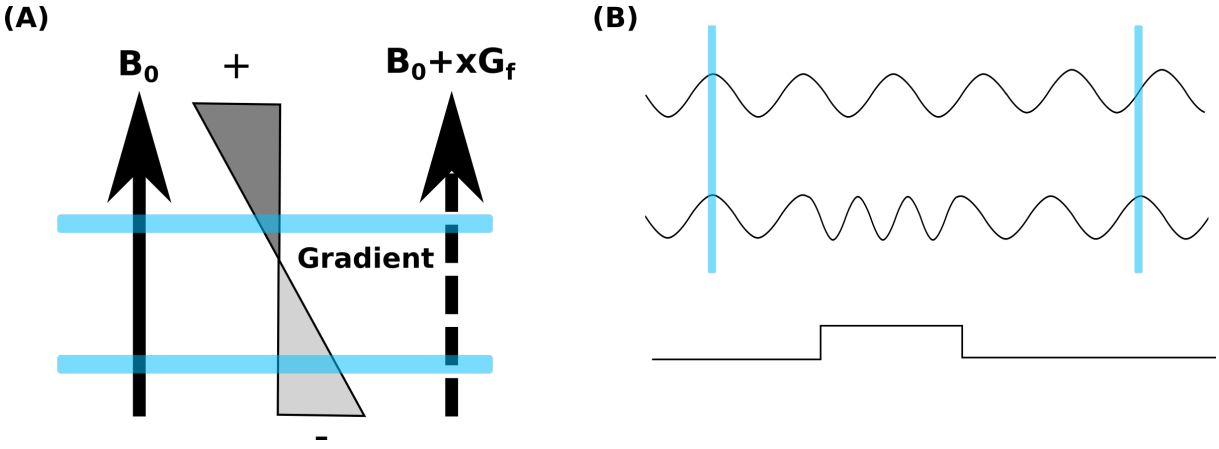

Figure 7 Spatial encoding of NMR signal using gradients*.(A) Slice selection is achieved by frequency encoding. A linear gradient is applied in the direction of B_0, modulating the total magnetic field for each axial slice in the magnet. The Larmor frequency is therefore different for nuclei located at different axial positions, enabling slice selection by excitation with a specific bandwidth. (B) Phase encoding uses gradients in the x or y dimension, after the nuclear spins have been excited. The top trace represents the signal from a reference nucleus and the second trace represents the signal from a nuclear spin subjected to a magnetic field gradient. The gradient causes the nuclear spin to precess at a different frequency and over time this leads to a permanent phase shift.*

Magnetic Resonance Spectroscopic Imaging (MRSI) enables the determination of the spatial distribution of nuclei with a particular resonance frequency, as opposed to conventional MRI, where no distinction is made with regard to the chemical shift of the resonance[68]. By taking advantage of the differences in resonance frequencies of nuclei in different molecules, specific molecules of interest can be imaged, as long as they are abundant enough to generate sufficient signal.

1.2.2.2 Chemical Shift Imaging

Chemical Shift Imaging (CSI) is a pulse sequence that enables MRSI. It applies phase encoding in one, two or three dimensions, to image a column, slice or volume, respectively, before the read phase of the sequence to enable the acquisition of a spectrum for each voxel in the image[69] (Figure 8). More complex versions of this sequence are being developed to maximise the efficiency of the sequence by acquiring maximum signal in minimum time.

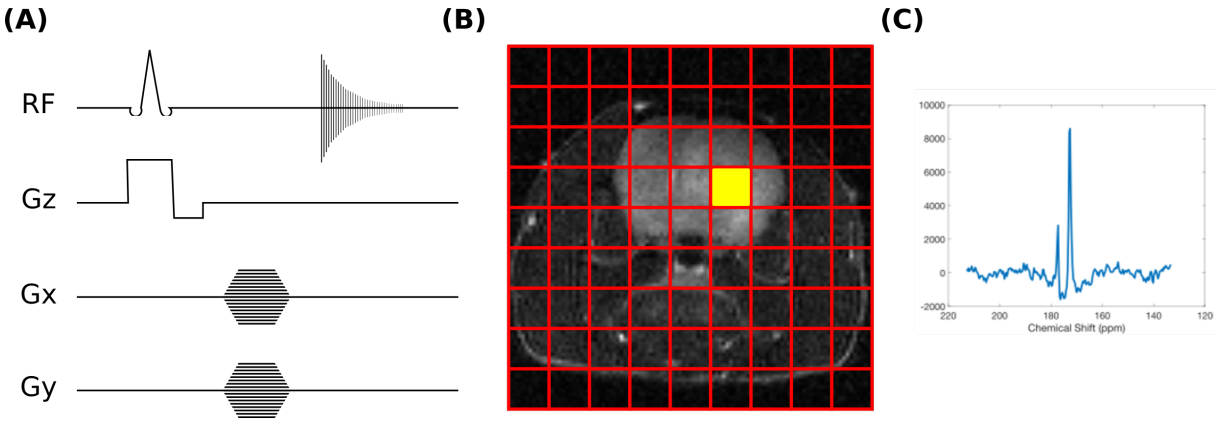

Figure 8 Chemical Shift Imaging (CSI). *(A) For acquisition of spectra from a slice with spatial encoding, a slice selection gradient can be used, along with phase encoding gradients in the x and y dimensions. An FID is acquired for every combination of phase encoding gradients. (B) Spatial encoding splits the slice into a grid whose resolution is determined by the number of phase encoding steps in the x and y dimensions. (C) A spectrum is acquired from each of the voxels in the grid.*

^{13}C is an MR active spin ½ nucleus, therefore carbon spectra could potentially be acquired at different locations in a tissue using MRSI. However, the very low natural abundance of ^{13}C (1.1%) in combination with its small gyromagnetic ratio, renders ^{13}C MRI very insensitive[67]. Therefore, even when multiple scans are acquired and averaged over long periods of time, the ^{13}C spectra acquired would suffer from very low signal-to-noise ratios (SNR)[67].

Hyperpolarisation has been used to increase the SNR of ^{13}C MRI, by increasing the excess of spins aligned with the external magnetic field. Polarisation refers to the number of spins that are aligned parallel to the external magnetic field relative to the total number of spins. Therefore, by increasing the number of spins aligned with the external magnetic field, the percentage polarisation in the sample is increased, and this leads to a larger net magnetisation vector and hence larger signal following an excitation pulse.

Dissolution dynamic nuclear polarization (DNP) is the most commonly used hyperpolarisation method[67]. This technique involves polarising electron spins, which are more easily polarised than ^{13}C nuclear spins, using very low temperatures (~ 1K). The polarisation can then be transferred from electrons to protons using microwave irradiation. A ^{13}C labelled metabolite of interest is dissolved in a suitable solvent, usually containing a stable radical as the source of unpaired electrons, and a glass forming agent[70]. The role of the glass forming agent is to ensure that an amorphous solid is formed upon cooling of the sample, so that the electron spins are homogeneously distributed[70]. This solution is placed in a strong magnetic field at very low temperatures (~1 K), where the electron spins of the free radical are almost fully polarised. This polarisation can then be transferred to the nuclear spins using microwave irradiation at the

electron spin resonance frequency, achieving nuclear spin polarisations of 20% - 40%[71]. Then, to remove the hyperpolarised compound from the polariser, rapid dissolution is performed with a superheated buffer[67]. Upon injection of the hyperpolarised substrate in an animal, the distribution of the substrate and its conversion to different metabolites can be traced, achieving a >10,000-fold increase in the SNR[70].

The limitation, however, of this technique is that the hyperpolarisation is transient, with the lifetime of the hyperpolarisation being dependent on the T_1 relaxation time constant of the hyperpolarised nucleus. Additionally, part of the hyperpolarisation is lost as a result of each excitation pulse. Therefore, long acquisitions cannot be performed[71]. For this reason, very efficient MRI sequences need to be developed to achieve maximum signal acquisition for the duration of the hyperpolarised spin state. The short-lived polarisation also limits the reactions that can effectively be imaged *in vivo*. For a hyperpolarised experiment to be successful, the substrate needs to enter cells and be converted to the product of interest quickly.

Many substrates of interest have been hyperpolarised and used in pre-clinical imaging studies in cancer. These include hyperpolarised ^{13}C-labelled pyruvate, glucose[72], glutamine[73] and glutamate[74]. Hyperpolarised [1-^{13}C]pyruvate has already been translated to the clinic, where it has shown promising results in a number of cancers, including prostate [75] and breast cancer[76]. The ^{13}C label on position 1 of pyruvate does not enable the investigation of the TCA cycle whereas uniformly labelled ^{13}C pyruvate would be more informative. However, only [1-^{13}C]pyruvate has been translated to the clinic owing to its advantageous polarising characteristics[77].

1.3 Glioblastoma

Gliomas constitute a group of tumours of the cerebral hemispheres. They are classified by the World Health Organisation (WHO) into four grades based on histopathological and clinical criteria (WHO I-IV)[78]. WHO I tumours are benign, WHO II and WHO III are low-grade diffuse gliomas (LGG), and WHO IV tumours are highly malignant glioblastoma tumours. Glioblastoma Multiforme (GBM) constitutes the most common and most malignant type of primary tumour of the adult central nervous system (CNS)[79]. The annual incidence of glioblastoma is 5.26 per 100 000 population[78]. Glioblastoma has a very poor prognosis, with a 5-year survival rate of less than 5%, coupled with the poor quality of life and cognitive decline that it can cause[78]. These tumours are highly infiltrative in the surrounding parenchyma but are

typically confined within the CNS. Grade II gliomas have low cell proliferation rates and hence progress more slowly, therefore they tend to show better survival rates (median 12-16 years) compared to Grade IV glioma (median survival less than 17 months)[80].

Multiple genetic changes have been associated with glioma genesis, including mutations, amplifications, deletions and translocations of oncogenes such as *EGFR*, *PI3K* and *KRAS* and tumour suppressors such as *TP53*, *PTEN*, and *NF1*. A subgroup of gliomas also harbour mutations in the isocitrate dehydrogenase genes *IDH1* and *IDH2*[19,81].

The classification of gliomas based on histological features does not provide good prognostic information and cannot guide treatment. Therefore, glioblastoma tumours have also been characterized based on their genomic profiles, leading to the identification of four molecular subtypes of glioblastoma: proneural, neural, classical and mesenchymal[81].

Diagnosis of GBM is usually achieved following clinical presentation of unilateral, progressively more severe headaches, personality changes and occasionally, gait imbalance, which lead to a diagnostic brain MRI examination. These symptoms are the result of oedema and raised intracranial pressure, caused by angiogenesis and blood vessel hyperpermeability, and high secretion rates of excitotoxic glutamate from tumour cells, leading to neuronal cell death[80]. The current treatment guidelines for glioblastoma include surgery if indicated, followed by adjuvant radiotherapy combined with chemotherapy (e.g. temozolomide)[78]. However, treatment is not curative, primarily due to the high invasiveness of the cancer, which means that at the time of treatment initiation, the cancer has already infiltrated the surrounding brain parenchyma. At the time of surgical resection, individual groups of cells can be found at sites as far as 2 cm from the main tumour site and hence escape detection by imaging (MRI) and removal by surgery[80].

1.3.1 Pre-clinical Models of Glioblastoma

Cancer research, including glioblastoma is dependent on pre-clinical models. Pre-clinical models of glioblastoma are usually tumours grown in mouse or rat brains and include cell-based xenografts, patient derived xenografts and genetically engineered mouse models[79].

Commercially available glioblastoma cell lines such as U87 and U251 cells were derived from glioblastoma patients and are commonly grown *in vitro* in culture media which are supplemented with Foetal Bovine Serum (FBS). These cells can also be implanted intracranially

in the brains of immunocompromised rats or mice. They are characterized by high engraftment rates and reproducible tumour growth, but are not representative of human glioblastoma. Some of these cell lines in particular, including U87 and U251 cells, have been in culture for many years and have drifted from the original cells over the years[82]. Genetic profiling and transcriptome analysis of commercially available U87 cells, revealed that these cells were of CNS origin but they did not match the original patient derived cells[83]. Also, recent sequencing of U87 cells revealed many indels, copy number variations and translocations, which have probably been acquired through culturing the cells *in vitro*[84]. Additionally, the histopathological features of xenografts derived from U87 cells are not similar to human glioblastoma[85].

Patient-derived xenografts perform better in terms of maintaining the genetic and histological features of the original primary tumour. These models can be established by directly implanting biopsied tissue into immunocompromised mice, or by culturing patient-derived cells *in vitro* in serum-free media and then injecting these intracranially in mice[84]. The main disadvantage of these models is their poor engraftment rate. Xenografts in immunocompromised rodents, either derived from commercially available cell lines, or directly from patients have the limitation that the immune component of the microenvironment cannot be studied.

Genetically engineered mouse models are established by manipulating gene expression, leading to overexpression or inactivation of particular genes at particular timepoints or in specified cells. These models are useful for identifying genetic alterations causing tumour initiation and progression while preserving the tumour microenvironment[86]. In glioma models, overexpression of certain oncogenic proteins, such as wild type EGFR[87] or mutant IDH1 and PDGF[88] can be used to generate tumours. Limitations of these models include the time and cost associated with generation and maintenance of the transgenic mice. Recently, injection of viral vectors have been used to allow temporal and spatial control of tumour development[87].

1.3.2 Genetic changes associated with gliomas

1.3.2.1 Isocitrate Dehydrogenase (IDH) mutations in gliomas

IDH catalyses the oxidative decarboxylation of isocitrate to α-KG and the concomitant reduction of NAD(P) to NAD(P)H. IDH1 is localised to the cytoplasm and peroxisomes and IDH2 is the mitochondrial isoform of the enzyme. In the human brain, it is estimated that IDH catalysed reactions are responsible for the generation of 65% of cytosolic NADPH, which is

required for the production of scavengers of reactive oxygen species[80]. *IDH1* and *IDH2* heterozygous point mutations have been described in gliomas and acute myeloid leukaemia. In glioma, they are likely to be involved in gliomagenesis[89]. These mutations usually occur on residue R132 of *IDH1* and residue R172 of *IDH2*, which are in the catalytic domains of the proteins. *IDH1* mutations are very common in low-grade gliomas (present in 80% of grade II and III gliomas and secondary glioblastoma) but quite rare in primary glioblastoma (present in 10% of primary glioblastoma)[89]. These mutations lead to a reduced affinity of the catalytic domain for isocitrate and an increased affinity for α-KG as well as a neomorphic function of the enzyme, the reduction of α-KG to 2-hydroxyglutarate (2HG) and the consumption of NADPH[80]. Hence, IDH mutations lead to reduced activity of wild type IDH, reduced formation of α-KG and conversion of α-KG to the oncometabolite 2HG, while consuming NADPH. As discussed earlier in this chapter, 2HG resembles α-KG structurally and as a result it inhibits competitively many α-KG dependent enzymes including the TET (Ten-Eleven-Translocation) family and Jumonji-C-domain containing histone demethylases (JHDMs)[80]. This results in DNA and histone hypermethylation.

Despite the role of *IDH* mutations in gliomagenesis, *IDH* mutations were shown to be independent prognostic markers for improved overall survival and progression free survival in a meta-analysis[89].

1.3.2.2 TP53 mutations in gliomas

The *TP53* gene is a tumour suppressor gene that is commonly mutated in many cancers, including glioblastoma. It encodes the p53 protein, a tetrameric transcription factor. In healthy cells, the levels of p53 are kept low through ubiquitination and degradation and p53 activity is induced in response to stress signals, in particular relating to DNA damage. P53 induction leads to cell cycle arrest, senescence and apoptosis and more recently it has been shown to regulate amongst others, stem cell differentiation and cellular metabolism[90].

The p53 pathway is commonly deregulated in glioblastoma with the highest prevalence of *TP53* mutations being observed in the proneural and mesenchymal molecular classes of glioblastoma. The pathway is also deregulated through changes in other components of the pathway, such as amplification of MDM2 and MDM4 genes and deletion of the CDKN2A/ARF locus, all of which are regulators of p53 activity.

1.3.3 Glioma Stem-like cells (GSCs)

The notion that there is a population of cells within glioblastoma, known as the glioma stem-like cell (GSC) population, has become increasingly popular. These cells, also known as tumour-initiating cells (TICs), share properties with neural stem cells and are believed to be responsible for tumour maintenance and progression[91]. They have also been associated with tumour recurrence and resistance to treatment[92,93]. GSCs are characterised by expression of certain stem cell markers, including Sox2 and CD133 and they are enriched near necrotic regions in the tumour, with low oxygen and nutrient levels[94].

Functionally, GSCs are identified by their ability to form neurospheres, also known as tumourspheres, in cell culture, and also tumours *in vivo*. Limiting dilution assays have been used, both *in vivo* and *in vitro*, to estimate the frequency of glioma stem-like cells in a mixed population of cells. This is achieved by establishing the minimum number of cells in the mixed population that is required for a tumoursphere to form *in vitro*, or a tumour to form *in vivo*. Limiting Dilution Analysis (LDA) is a statistical interpretation of these assays, which assumes a Poisson single-hit model, where the number of glioma stem-like cells, in this case, follows a Poisson distribution and where a single glioma stem-like cell is sufficient to generate a tumoursphere *in vitro* or a tumour *in vivo*[95].

A number of transcriptional and metabolic pathways have been shown to facilitate the maintenance of a stem-like phenotype in cells. For example, Forkhead box protein M1 (FOXM1) is a transcription factor that has been shown to play an important role in the proliferation of GSCs[96,97,98]. ALKBH5 (alpha-ketoglutarate-dependent dioxygenase alkB homolog 5) is upregulated in glioblastoma and is associated with a poor prognosis based on data from The Cancer Genome Atlas (TCGA), R2 and REMBRANDT[92]. Immunohistochemical analysis of human GBM tissue showed ALKBH5 to be co-expressed with SOX2, indicative of stem-like cells. Knockdown of *ALKBH5* in patient-derived cells led to reduced tumoursphere formation frequency and downregulation of SOX2, Nanog and Oct5, which are the transcription factors enabling self-renewal. In the same study, FOXM1 was shown to be a direct downstream target of ALKBH5 in GBM.

Other genes whose expression levels correlated with SOX2 in the TCGA GBM dataset include ABHD4, ANP32E, CENPF, FANCI and FOXM1, suggesting that these might be related to the glioma stem-like cell profile[92].

1.3.4 Epithelial to Mesenchymal Transition in Glioblastoma

The highly invasive nature of GBM has been partly attributed to the migratory capacity of glioma cells, which is thought to result from an epithelial to mesenchymal transition of the cells. Epithelial to mesenchymal transition (EMT) is the process whereby epithelial cells undergo several biochemical processes and gain mesenchymal properties, characterised by weak cell adhesions and enhanced migratory capacity[99]. EMT is a phenotypic switch that is associated with cancer initiation, invasion and metastasis[100]. Three types of EMT have been described, namely Type I, which is involved in embryogenesis and organ formation, Type II, which is involved in wound healing and scar formation and Type III, which is associated with cancer progression and metastasis. EMT is different in glioblastoma, when compared to other cancer types and for this reason, it is sometimes referred to as Glial-to-Mesenchymal (GMT) transition instead. The reason for this is that glial cells originate from neuroepithelial cells, which are different from classical epithelial cells, but nonetheless glioma cells transition into a more mesenchymal-like phenotype.

A number of signalling pathways and transcription factors have been associated with EMT in glioblastoma, including Snai1, ZEB and Twist. Snai1 is a transcriptional repressor which binds to epithelial phenotype promoting genes. It is regulated by a number of signalling pathways, including Wnt, HIF-1α, TGFβ and PI3K/AKT[99]. Similarly, ZEB1 binds to E-boxes in the regulatory regions of genes, leading to repression of epithelial genes and activation of mesenchymal genes. ZEB1 expression has been shown to be inversely correlated with survival in GBM patients and ZEB1 knockdown cells were shown to grow less invasive tumours in mice compared to ZEB1 expressing cells[99].

1.3.5 Cancer cell invasion

The ability of cancer cells, especially glioblastoma cells, to invade through the surrounding normal tissue is closely related to the dismal prognosis of the disease because by the time of diagnosis, enough cancer cells have already invaded normal surrounding tissue, which can lead to relapse following tumour resection. Cancer cells penetrate the basement membrane by forming invadopodia, which are structures enriched with actin filaments, adhesion proteins and proteinases[101].

Cancer cell invasion is dependent on tissue remodelling, involving degradation of the extracellular matrix surrounding the tumour[57]. Tissue remodelling is enabled through the action of matrix metalloproteinases (MMPs), which are mostly produced by stromal fibroblasts within tumours.

1.3.6 Transcription Factors in Glioblastoma

Cancer progression and its ability to adapt to the changing environment is dependent on a number of different transcription factors which regulate gene expression in the cancer cell. Some transcription factors that have been implicated in glioblastoma and more generally in cancer are Hypoxia Inducible Factor (HIF), FOXM1 and c-Myc.

1.3.6.1 Hypoxia Inducible Factor

HIF1 is one of the transcription factors orchestrating the response of cells to hypoxia. It is a heterodimer, consisting of HIF1-α and HIF1-β subunits. HIF1-β is expressed constitutively, but HIF1-α stability is tightly controlled by oxygen availability. Under normoxic conditions, both prolines of the oxygen-dependent degradation (ODD) domain of HIF1-α are hydroxylated by prolyl hydroxylase domain (PHD) – containing proteins, in the presence of iron, α-KG and ascorbate. The best-studied PHD enzyme is PHD2, also known as EGLN1 (Egl-9 family hypoxia inducible factor 1). Proline hydroxylated HIF1-α is recognised by the von Hippel-Lindau tumour suppressor (pVHL) E3 ligase complex leading to its ubiquitination and degradation by the proteasome[102]. PHDs act as oxygen sensors owing to their K_m of around 100 μM for oxygen. Oxygen concentrations in tissues is around 10-30 μM, therefore, oxygen is normally the rate-limiting factor for the activity of PHDs under physiological conditions[27]. Under hypoxic conditions, the activity of PHD is reduced, leading to HIF1-α stabilisation. When HIF-1α is stabilised, it binds to HIF-1β and the heterodimer translocates to the nucleus and binds to the hypoxia-responsive element of target genes, which is located either proximal or distal to the promoter region[103,104].

HIF1 has been shown to play an important role in cancer, not only in enabling survival of cells where oxygen availability is limited, but also in facilitating growth and progression of cancer. It is implicated in glucose metabolic processes, shifting energy metabolism from oxidative phosphorylation to glycolysis[104], extracellular matrix remodelling and EMT[103] and angiogenesis in tumours via upregulation of genes for proangiogenic factors including Vascular

Endothelial Growth Factor (VEGF), Platelet-derived Growth Factor type B (PDGF-B), hepatocyte growth factor, epidermal growth factor and angiopoeietin-2. It also regulates cell proliferation and chemotaxis and is implicated in stem cell maintenance through induction of NANOG, Oct-3/4 and SOX2 expression. Hypoxic tumours have been associated with an increased risk of mortality independently of other prognostic factors[105].

In cancer, HIF-1α is commonly stabilised even in the presence of high O_2 tension, in a process known as pseudohypoxia. Pseudohypoxia can be a result of mutations in succinate dehydrogenase (SDH) and fumarate hydratase (FH), which lead to accumulation of succinate and fumarate, respectively. Both metabolites compete with α-KG for PHD binding thereby inhibiting PHD and leading to HIF-1α stabilisation[102]. In addition, mutations in isocitrate dehydrogenase leading to reduced generation of α-KG and accumulation of 2HG can cause HIF-1α stabilisation.

1.3.6.2 Forkhead box M1 (FOXM1)

FOXM1 is one of the target genes of HIF1[103,106]. It is a member of the Forkhead box protein family and it has been shown to be upregulated in human GBM and is associated with poor prognosis[107]. Additionally, the expression levels of FOXM1 were correlated with glioma grade[107].

FOXM1 is known to regulate the cell cycle in the G1/S transition, G2/M transition and M phase progression[92]. Other than its regulatory role in cell proliferation, FOXM1 has been shown to play many roles in glioblastoma, including cell invasion[108], maintenance of a stem-like phenotype[92], regulation of tumourigenesis through Wnt signalling[97] and radioresistance[96,109,110]. The expression of FOXM1 was shown to be upregulated in irradiated GBM cells *in vitro* and *in vivo*[109]. Conversely, inhibition of FOXM1 radiosensitised cells[109].

1.3.6.3 C-Myc

c-Myc belongs to a family of Myc oncogenes that regulate cell growth and differentiation. These encode DNA-binding proteins that act as transcription factors. C-Myc forms a heterodimer with Max, which can then bind to DNA and promote transcription of target genes. c-Myc is a well-known oncogene, which has been shown to lead to transformation of normal cells in cooperation with an activated RAS oncogene[111].

c-Myc regulates metabolic reprogramming in cancer cells, with target genes involved in glycolysis, glutaminolysis and nucleotide and lipid synthesis pathways[14]. In addition to its role in metabolic regulation, c-Myc is involved in the maintenance of stem-like cells. In transformed human keratinocytes, ectopic overexpression of c-Myc led to an increased stem cell fraction and enhanced tumourigenicity[112]. In gliomas, c-Myc expression correlates with grade of malignancy[113]. In a mouse model of glioblastoma, higher levels were expressed in the glioma cancer stem cell population when compared to the matched non-stem cell population in the same tumour, and c-Myc activity enabled the proliferation and survival of these cells[91]. Conversely, knockdown of c-Myc in stem-like glioma cells abolished tumour formation in mice[91].

1.4 Thesis Overview

The primary aim of this project was to explore the utility of hyperpolarised ^{13}C imaging in non-invasive imaging of cancer metabolism. In the first part of the thesis, hyperpolarised [1-^{13}C]pyruvate imaging was cross validated by comparison with Mass Spectrometry Imaging, another novel metabolic imaging technique. This was achieved by comparing the [1-^{13}C]lactate tumour images that were generated by hyperpolarised ^{13}C MRSI *in vivo* in a subcutaneous murine lymphoma tumour, with [1-^{13}C]lactate images from corresponding tissue sections of the tumours *ex vivo*.

In the second part, the role of branched chain amino acid metabolism in glioblastoma was investigated and the potential of hyperpolarised ^{13}C-labelled ketoisocaproic acid as a novel substrate for imaging BCAT activity in glioblastoma was assessed. The roles of BCAT1 and BCAT2 in the metabolism of patient derived models of glioblastoma were explored and the use of hyperpolarised ^{13}C-labelled ketoisocaproic acid for imaging BCAT activity was evaluated in these same models.

Chapter 2 - Co-registering Mass Spectrometry Images with Hyperpolarised ^{13}C MRI

2.1 Abstract

There has been increasing interest in using Mass Spectrometry Imaging and Hyperpolarised ^{13}C Magnetic Resonance Imaging for interrogating metabolism *in vivo*. However, concerns have been expressed about the validity of the measurements obtained using these two techniques. This study compared dynamic, *in vivo* magnetic resonance images of [1-^{13}C]lactate in a subcutaneous murine lymphoma tumour following a bolus injection of [1-^{13}C]pyruvate with endpoint *ex vivo* mass spectrometry images of [1-^{13}C]lactate in the corresponding frozen sections from the same tumours. A positive correlation was observed when comparing the lactate maps generated by the two modalities. The complementary additional data provided by each modality was used to gain further insight into the dynamics of tumour lactate labelling following injection of [1-^{13}C]pyruvate.

2.2 Introduction

2.2.1 Principles of Mass Spectrometry

Mass Spectrometry is an analytical technique that is used to quantify specific compounds and their isotopic composition. The principle behind the technique is the generation of ionized species, which are separated according to their mass-to-charge (m/z) ratios. Detection of these ions can be used to generate a spectrum whereby the abundance of each ionized species is plotted against its m/z ratio. A mass spectrometer consists of an ion source, which generates the ionised species from the compound or compound mixture to be analysed, a mass analyser, which separates the ions according to their m/z ratio using electromagnetic fields, and a detector, which generates an abundance profile for each species[114].

2.2.2 Mass Spectrometry Imaging

Mass Spectrometry Imaging (MSI) adds another dimension to the data, which is the spatial distribution of the compounds. Ionized species are generated from a surface, such as a tissue section, in a raster scan fashion. The ions are fed into a mass spectrometer and a mass spectrum is generated per pixel analysed, hence the spatial information is preserved (Figure 9). MSI can be applied in an exploratory manner, whereby the molecular patterns of different parts of the tissue, as segmented by histology, are compared and the molecules that are significantly different in the different regions are identified. Alternatively, MSI can be used to visualise the distribution of specific molecules of interest in the tissue section.

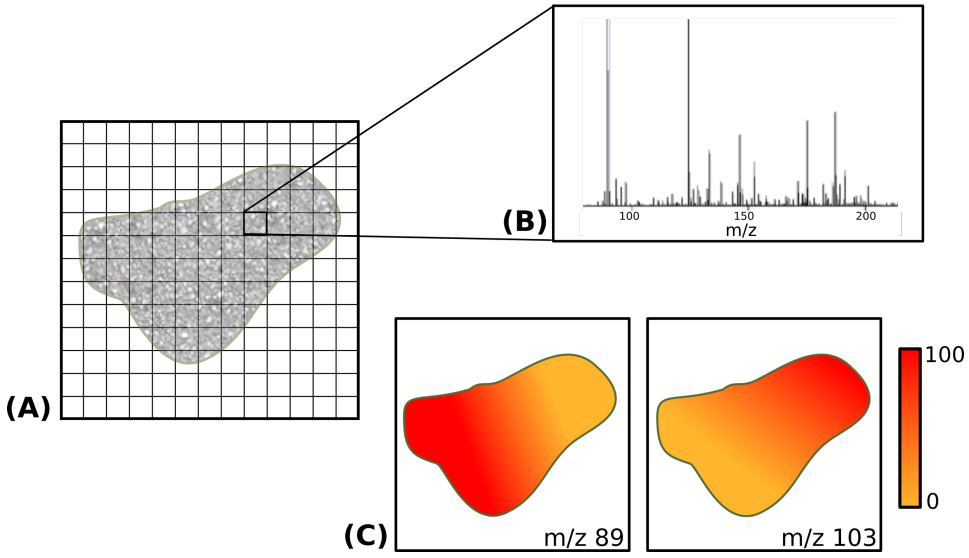

Figure 9 Principles of Mass Spectrometry Imaging. *(A) The surface is scanned in a raster fashion and ions are generated from each pixel, resulting in the acquisition of a mass spectrum per pixel (B). (C) False colour images illustrating the relative intensities of specific metabolites across the surface can be generated.*

2.2.2.1 Ion source

The ionization process in MSI is different to bulk Mass Spectrometric analysis in that the ions need to be generated from each pixel on the surface, therefore the ionizing beam needs to be directed onto the surface and moved with high precision to scan the surface pixel-by-pixel. The methods used in conventional mass spectrometry to extract the analytes and separate them chromatographically cannot be used in this case because the topographic information needs to be preserved and hence novel methodologies have evolved[115]. A number of different ionization techniques have been applied to MSI, which include MALDI (Matrix Assisted Laser Desorption Ionisation), SIMS (Secondary Ion Mass Spectrometry) and DESI (Desorption Electro-Spray Ionisation). The performance of MSI is highly dependent on the efficiency with which the ions are generated from the surface to be analysed[115].

In MALDI, the surface to be analysed is coated with a matrix, usually an organic acid, which forms uniform microcrystals and protects the analytes from being destroyed from the high energy laser beam. For imaging, the section is placed on a stage which moves very precisely (less than 1 µm lateral resolution) and at each pixel the laser beam is directed onto the section, generating ions from a 5 µm diameter circular region[114]. MALDI has the advantage of detecting molecules with a wide range of molecular weights, but the application of a matrix could be seen as a disadvantage since it might affect the spatial distribution of molecules. Another disadvantage of MALDI is that it usually needs to be performed under vacuum[115].

SIMS is another ion generating technique, which utilises a beam of very high energy primary ions to hit the surface to be analysed. The high energy collisions generate secondary ions from the surface very efficiently, which can then be analysed by mass spectrometry. SIMS can produce spatial maps of small molecules with high efficiency. However, due to the high energy of the primary ions, SIMS needs to be performed under vacuum to prevent collisions of the primary ions before they reach the surface[115].

DESI is an ionisation method that can be used in ambient conditions, leaving the sample in its native condition, hence enabling further analysis (e.g. histology) to be performed. In DESI, an electrospray emitter is used, which generates and directs charged droplets of solvent onto the surface to be analysed. In this way, the surface is coated with a thin layer of solvent, which dissolves the compounds on the surface. The charged solvent particles generate secondary ionised droplets from the surface which are then fed into the mass analyser. The secondary droplets, which contain the ionised analyte, can be transported through the air for some distance before entering the mass analyser (Figure 10). This ionisation method has a lower spatial resolution that SIMS and MALDI, with DESI images generally acquired at 180-220 µm, although resolutions of up to 100 µm are achievable[116]. Due to the differences in ionisation mechanisms, these techniques differ in the efficiency with which they ionise particular molecules. For example, lipids are more readily ionised by DESI whereas peptides and proteins are more readily ionised by MALDI[117].

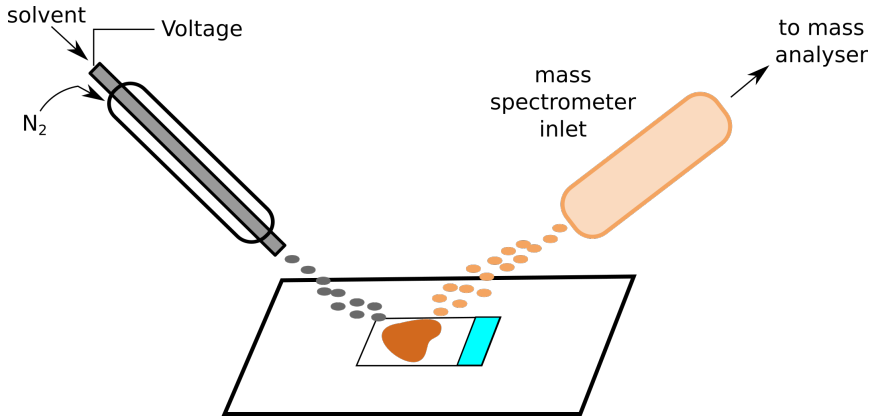

Figure 10 Schematic Diagram of DESI MSI*. An electrospray is guided towards the surface to be analysed. Charged solvent particles hit the surface and dissolve the analytes on it to generate secondary ionised droplets which are fed into the mass analyser. The stage usually moves in a raster scan to generate ionised particles from each pixel.*

2.2.2.2 Mass analyser

The Mass analyser is the component which determines the m/z ratio. Different types of mass analysers have been developed, including quadrupole, ion trap, time-of-flight and Fourier transform analysers[118]. Orbitrap analysers are a type of Fourier transform analyser, where an electric field is used to induce oscillations in the paths of the generated ions. The time-domain signal generated by these oscillations is Fourier transformed to the frequency domain, whereby the axial harmonic frequencies of individual ions are proportional to the m/z ratio. Orbitrap analysers have very good mass resolving power[118].

2.2.3 Applications of Mass Spectrometry Imaging in Medicine

Molecular imaging is of crucial importance to medicine as it enables the gathering of information about the pathology of a tissue, in addition to the morphological information that is obtained using traditional imaging techniques. Biomarkers of disease can be detected using molecular imaging which can then have diagnostic and prognostic importance.

The ability of MSI to perform chemical imaging in a non-targeted and label-free way[119], makes it a good discovery tool in the field of biology and biomedicine[120]. MSI can be performed on biological tissue sections, generating an enormous dataset which can then be analysed according to the purpose of the study. For example, the spatial distribution of particular ions of interest can be imaged. Alternatively, a more explorative approach can be used, where non-supervised clustering analysis can be performed to delineate regions of similar molecular phenotypes. Then, by comparing the mass spectra of different regions, the molecular signatures of particular regions can be identified. The very high spatial resolution of MSI, typically on the subcellular scale, enables direct comparison between the MSI image and histological images of the same or an adjacent section.

MSI has already been applied to the study of cancer, mainly as a way of looking for novel tumour biomarkers or as a way of better visualising tumour margins. For example, in a proof-of-concept study in breast cancer, DESI was used to distinguish between cancerous and healthy breast tissue. The intensities of several fatty acids, such as oleic acid were used to identify tumour margins and the delineation generated by DESI correlated well with histological staining. The authors suggested that this study demonstrates the potential for DESI to be used as a quick intraoperative way of increasing the accuracy of tumour resection[121]. Similarly, DESI

has been used in the operating room during surgical resection of *IDH*^{mut} glioblastoma. In this case, DESI was used to detect the oncometabolite 2-hydroxyglutarate, which correlated with tumour content and thus delineated the tumour margin[122].

Even though MSI seems to be a very promising technique, it comes with some limitations, which have slowed down its translation into clinical practice. One of its limitations includes the strong dependence of the data acquired by MSI on sample collection and preparation, which creates problems with reproducibility. Also, despite the many efforts to obtain quantitative data from this technique, this still proves to be difficult, due to the high dependence of the ion signal on the chemical and morphological environment of the location of interest[123]. This is because the efficiency with which ions of the substrate of interest are generated from the surface depends on the other substrates that are present. It is therefore necessary to include internal standards in any sample, otherwise, no quantitative conclusions can be drawn[123]. Another limitation of MSI is that peak assignment is often solely based on the m/z values, which can sometimes be a problem for distinguishing metabolites with very similar masses. A lot of research is now focusing on developing better protocols to enable the acquisition of reproducible and quantitative data using MSI.

The ability of MSI to detect small molecules could potentially revolutionise the study of metabolomics. For example, MSI could be used to image a section containing a tumour next to healthy tissue and from this, metabolic differences between healthy tissue and cancerous tissue could be derived, leading to a better understanding of tumour metabolism. Additionally, metabolic heterogeneity within the tumour tissue could be explored by utilising the high spatial resolution of MSI.

2.2.4 Hyperpolarised ^{13}C pyruvate imaging

^{13}C MRSI of hyperpolarised ^{13}C-labelled cell substrates enables rapid non-invasive imaging of tissue metabolism in vivo[124]. Exchange of hyperpolarised ^{13}C label between injected [1-^{13}C]pyruvate and the endogenous lactate pool, in the reaction catalysed by lactate dehydrogenase (LDH) has been the most commonly studied metabolic reaction. Hyperpolarised [1-^{13}C]pyruvate has been used clinically, with promising applications, such as disease staging in prostate cancer[125,126], and for detecting tumour responses to treatment[75]. The limitations of ^{13}C MRSI with hyperpolarised substrates include the transient nature of the hyperpolarization, which means that only relatively rapid metabolic reactions can be studied, and the difficulty of

relating signal intensity to concentration, which means that typically only apparent first order rate constants describing the isotope flux are quoted, rather than the metabolically relevant fluxes, expressed for example in mM/min[127].

2.2.5 Aims of the study

The combination of hyperpolarised MRSI with MSI offers new opportunities to investigate the metabolic phenotypes of cancers. Coupling the capability of hyperpolarised MRSI to produce dynamic images of the interconversion of metabolites in three dimensions, with the ability of MSI to acquire information on a very large number of metabolites with high spatial resolution, we will be able to better understand tumour metabolism and interpret the hyperpolarised MRSI data.

The aim of this study was to perform hyperpolarised [1-^{13}C]pyruvate imaging and MSI on the same tumours, to directly compare the data generated by the two techniques as a way of cross validating both methods and as a way of better understanding the factors determining the kinetics of lactate labelling.

2.3 Methods

2.3.1 Optimisation of tumour freezing

For optimisation of the tissue freezing technique, healthy, female C57BL/6 mice were used. The mice were anaesthetised by inhalation of 2% isoflurane gas in air/O_2 (50/50% vol/vol, 2 L/min) and a dorsal incision was made. The two kidneys were exposed and isolated from surrounding tissue. The left kidney was excised and freeze-clamped in liquid nitrogen-cooled tongs, whereas the right kidney was excised and immersed in liquid isopentane that had been pre-cooled in liquid nitrogen. The surgical procedure took around 5 minutes each time. Excision of the kidney and either freeze-clamping or immersion in isopentane were completed in a maximum of 5 seconds. The specimens were then stored at -80^{o}C until extraction.

The kidneys were kept on dry ice during the extraction procedure. They were weighed and homogenised in 10 µl/mg 2M Perchloric Acid (PCA), using a Precellys homogeniser (Birton Instruments). After homogenisation, the samples were kept on ice for 30 minutes and then centrifuged at 13,000g for 2 minutes at 4^{o}C. The homogenate was then neutralised using 2M KOH and then re-centrifuged at 13,000g for 15 mins at 4^{o}C. The samples were then lyophilised before ^{31}P NMR and ^{1}H NMR analysis.

The lyophilised extracts were dissolved in 550 µl Deuterium Oxide and Trimethylsilyl propanoic acid (TMSP) and methylenediphosphonic acid, at 100 nmol/g tissue, were added as chemical shift and intensity standards. Proton decoupled ^{31}P NMR spectra were acquired with an 11µsec pulse with a flip angle of 90^{o} and a repetition time of 7.2 seconds. More than 8000 scans were summed, with a spectral width of 57 ppm (14006 Hz) and 32768 data points. ^{1}H spectra were acquired with an 11 µsec pulse with a flip angle of 90^{o} and a repetition time of 5.3 seconds. 650 scans were summed, with a spectral width of 17 ppm (10000 Hz) and 65536 data points. All spectra were processed using a Gaussian window function of 3 Hz.

2.3.2 Tumour model

A suspension of 5 x 10^{6} EL4 cells in 200 µl Foetal Bovine Serum (FBS) was injected subcutaneously on the right flank of female C57BL/6 mice (Charles River). Tumours were grown for 8-11 days before they were imaged.

2.3.3 ^{13}C pyruvate imaging experiments

[1-^{13}C]pyruvic acid was purchased from Cambridge Isotope Laboratories (MA). 44 mg [1-^{13}C]pyruvic acid was mixed with 15 mM OX063 radical (GE Healthcare) and 1.4 mM gadoterate meglumine (DOTAREM, Guerbet) and loaded in the HyperSense polarizer, where it was polarised for about an hour. The substrate was then dissolved in 6 ml of buffer containing 40 mM Hepes, 94 mM NaOH, 30 mM NaCl and 100 mg/L EDTA and 400 µl of this solution was immediately injected intravenously into the tail vein of the mouse to be imaged.

T_2-weighted axial ^{1}H MR images of the mouse were acquired with a Fast Spin Echo sequence before substrate injection and used for positional reference. These were 16 40 x 40 mm^2 slices with a slice thickness of 1.25 mm. Data were acquired in a 256 x 256 matrix, with a TR of 2 seconds and an effective TE of 48 ms, with 8 echoes acquired. Following intravenous injection of hyperpolarized [1-^{13}C]pyruvate via a tail vein, ^{13}C images were acquired with a single shot 3D volume imaging sequence[128] which used spectral spatial pulses to alternately excite [1-^{13}C]pyruvate and [1-^{13}C]lactate with flip angles of 7^o and 45^o, respectively and a fast spin echo train of 8 adiabatic, non-localised, 180-degree pulses with a stack of spiral acquisitions at the echoes[129]. The 3D volume acquired was 40 mm x 40 mm x 20 mm with a matrix size of 32 x 32 x 16 with a TR of 1s so that each metabolite was imaged every 2s for 90 s. The 8th pair of acquisitions were performed without the phase encoding in the third dimension and were used as a reference scan for this dimension in reconstructing the other time points.

2.3.4 Snap-freezing and sample preparation for Mass Spectrometry Imaging

The whole mouse was snap-frozen in liquid isopentane, pre-cooled in liquid nitrogen, immediately following the MRI acquisition. Ten µm thick sections of animals injected with [1-^{13}C]pyruvate and non-injected control animals were cut on a Leica cryostat and thaw-mounted onto superfrost slides (ThermoScientificTM). To preserve the rapidly changing tissue metabolome, the sections were air-dried, and vacuum packed for storage at -80^{o}C prior to MSI[130]. Adjacent to these sections, sections of 6 µm thickness were also taken, to be used for immunohistochemical staining.

2.3.5 DESI MSI

The slides were shipped to AstraZeneca (The Darwin Building, Cambridge) where they were processed for DESI MSI. Just before DESI MSI, the slides were equilibrated at room

temperature and immersed in chloroform for 1 min 45 seconds. MSI was performed using a Q-Exactive plus mass spectrometer (Thermo Scientific, Bremen, Germany) equipped with an automated DESI ion source (Prosolia Inc., Zionsville, IN, USA). Data were acquired in negative ion mode between m/z 80 and 500. The nominal mass resolution was set to 70,000. The injection time was fixed at 150 ms resulting in a scan rate of 3.8 pixel/s. A home-built DESI sprayer[131] was operated with a mixture of 95 % methanol, 5 % water delivered at a flow rate of 1.5 µL/min and nebulized with nitrogen at a backpressure of 6 bar. The spatial resolution was set to 100 µm. Sections were then stained with Hematoxylin and Eosin (H&E) and imaged on an Aperio (Leica Biosystems, Nussloch) scanner.

2.3.6 Immunohistochemistry (IHC)

For immunohistochemical analysis, 6 µm thick sections were cut and submitted to the Histopathology core in the institute for processing. IHC was run on Leica's Polymer Refine Detection System on the Bond-III platform. For CD31 staining, a rat anti-mouse antibody was used (BD Biosciences, catalogue number 553370), at a concentration of 0.5 µg/ml, followed by a rabbit anti-rat secondary antibody (Bethyl Labs, catalogue number A110-322A).

2.3.7 Data analysis and Statistics

MRSI data were processed using an in-house MATLAB (MathWorks) script[128], for image reconstruction and overlaying the metabolic images on the anatomical ^{1}H MR images. The MSI .raw data files were converted into .mzML files using ProteoWizard msConvert[132] (version 3.0.4043) and compiled subsequently into an .imzML file (imzML converter[133] version 1.3). All subsequent data processing was performed in SCiLS Lab (version 2019c, Bruker Daltonik, Bremen, Germany). The MSI data were analysed following root mean square normalization to compensate for pixel-to-pixel variability and data variation between experiments[134]. For visualization of the relative distribution of [^{12}C] and [1-^{13}C]lactate across the tissue, hotspot removal and weak denoising were applied.

The [1-^{13}C]lactate MS images were co-registered with the ^{1}H MRI anatomical images using a custom MATLAB script. The tumour in the MS image and the corresponding anatomical MR image were contoured manually to yield binary masks, which were first co-registered by affine transformation using the imregister function. The registration was then fine-tuned with the imregdemons function, in order to account for arbitrary shape distortion of the MSI sections

resulting from sample preparation. Non-spatial and spatial statistical techniques were used to quantify the level of association between the co-registered images. For each section, the level of association was defined by means of the Spearman's rank correlation on the raw pixel intensities (estimated by means of the cor function in RStudio software) and the Cohen's kappa coefficient[135,136] on standardized intensities (obtained by categorizing the raw intensities in 20 quantile based levels, estimated by means of the function cohen.kappa of the R package 'psych'). One-sided T-tests were used to assess if the mouse mean association levels were greater than 0 and thus to exclude the null hypothesis that there was negative or no correlation between the two techniques (by means of the t.test R function). Linear mixed models (fitted by means of the function lme of R package nlme) were then used to predict the standardized MSI intensities by means of the MRI intensities, with mice and tumours as hierarchical random effects to take the within-mouse and within-tumour dependence into account and assuming a spherical correlation structure for the residuals[137,138]. Sensitivity analyses considering other spatial dependence structures led to similar conclusions. Significance of the relationship between MRI and MSI was assessed by means of a Wald T-test on the MRI fixed effect parameter estimate. Pearson correlation coefficients were used to assess the correlation between the [1-^{13}C]lactate and [1-^{13}C]pyruvate MR images and between the [^{12}C] and [1-^{13}C]lactate MS images[139].

2.4 Results

2.4.1 Comparison between snap-freezing techniques

In order to optimise the sample processing pipeline before MSI, two freezing methods were compared, namely immersion in liquid nitrogen-cooled isopentane and freeze-clamping in liquid nitrogen cooled tongs. Immersion in liquid nitrogen was not investigated here due to the higher risk of tissue damage upon immersion in liquid nitrogen and the slower freezing rate caused by the vapor barrier created by liquid nitrogen around the immersed solid as discussed in the literature[140]. The comparison was achieved by freezing each of two kidneys of healthy mice by either of the two methods and comparing the ATP:ADP ratios of lyophilised extracts of the frozen samples. ^{31}P NMR analysis on kidney sample extracts suggested that immersion in cold isopentane is comparable to freeze-clamping in terms of preservation of the ATP:ADP ratio (Figure 11). There was a small increase in the preservation of ATP levels with immersion in isopentane when compared to freeze-clamping but the adenylate energy charge[141] measured after freezing with either of the two techniques was very similar. Immersion in cold isopentane also preserves the architecture of the tissue as opposed to freeze clamping, thus enabling co-registration of *in vivo* images to images generated on sections of the frozen tissue. Therefore, for subsequent experiments, the metabolism was effectively stopped by immersion of the whole mouse in liquid isopentane which was pre-cooled in liquid nitrogen.

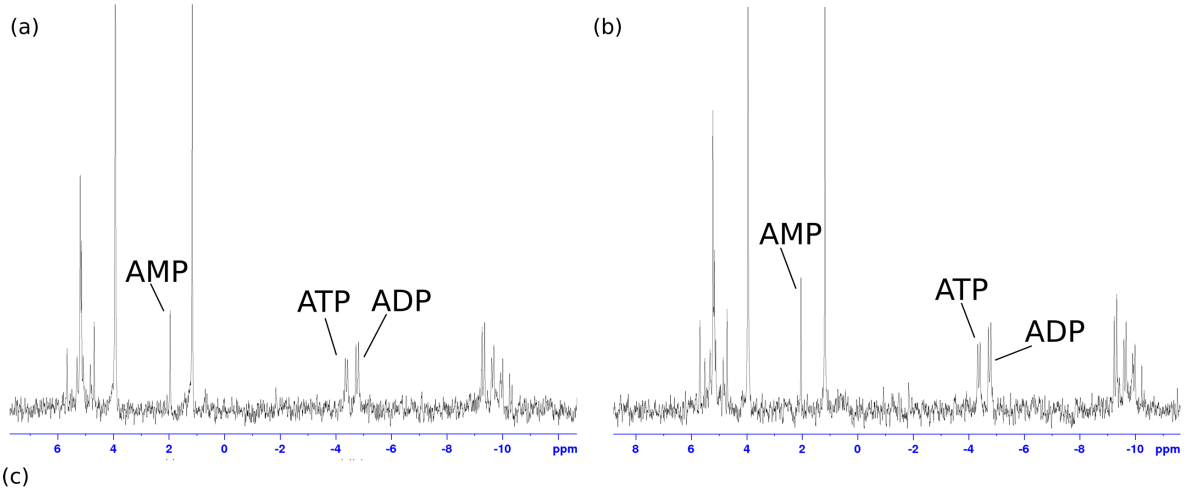

(c)

ATP:ADP ratio		[ATP] (µmol/g)		[ADP] (µmol/g)		[AMP] (µmol/g)		Energy Charge	
Isopentane	Freeze-clamping	Isopentane	Freeze-clamping	Isopentane	Freeze-clamping	Isopentane	Freeze-clamping	Isopentane	Freeze-clamping
0.94	0.81	1.66	1.08	1.76	1.34	1.76	1.34	0.60	0.61
0.82	0.69	1.58	1.28	1.92	1.84	1.92	1.84	0.58	0.60

Figure 11 Comparison of freezing techniques. *The ^{31}P NMR spectrum of an extract of a freeze-clamped kidney (a) is very similar to the spectrum of the extract of a kidney which was immersed in cold isopentane (b), in terms of their relative ATP, ADP and AMP peak areas. The ATP/ADP ratio was calculated from the integrals of the peaks (β-ADP at -4,76 ppm and γ-ATP*

at -4.35 ppm), as measured by TopSpin software (Bruker), and absolute concentrations of ATP, ADP and AMP were estimated by comparing their peak integrals to that of a Methylenediphosphonic Acid standard (at 17.5 ppm). From these, the adenylate energy charge was calculated (c).

2.4.2 Optimised pipeline for direct comparison of hyperpolarised ^{13}C MRSI and DESI MSI

The pipeline followed for this study is outlined in Figure 12. EL4 murine lymphoma cells were implanted subcutaneously in female C57BL/6 mice. Once the tumours reached a diameter of approximately 1.5 cm, the MRI protocol was followed which included T_2-weighted MRI in the axial, sagittal and coronal directions, while [1-^{13}C]pyruvate was being hyperpolarised. For [1-^{13}C]pyruvate imaging, the hyperpolarised substrate was dissolved in superheated buffer and immediately injected into the tail vein of the anaesthetised mouse for the fast ^{13}C imaging acquisition. As soon as the acquisition finished (180 seconds after injection), the deeply anaesthetised mouse was frozen by immersion in liquid isopentane, pre-cooled in liquid nitrogen. Whole mouse axial sections were cut at -20ºC, vacuum packed and stored at -80ºC to maximise the preservation of metabolites until DESI MSI was performed. Following DESI analysis, H&E staining was performed as well as immunohistochemical staining.

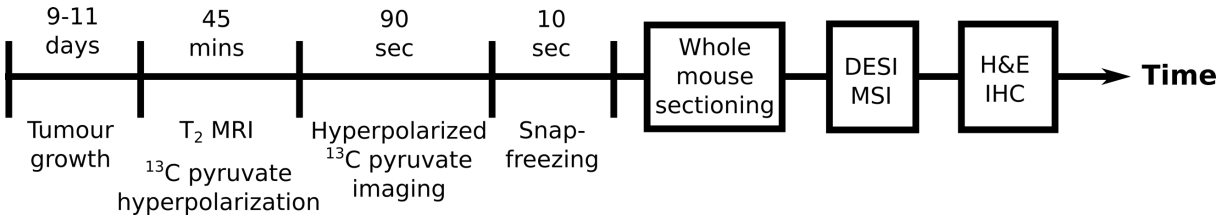

Figure 12 Outline of pipeline used for direct comparison of hyperpolarised ^{13}C pyruvate imaging with mass spectrometry imaging.

2.4.3 Four-dimensional imaging of pyruvate and lactate in tumour bearing mice

Following injection of hyperpolarised [1-^{13}C]pyruvate into EL4 tumour-bearing mice, four-dimensional MRSI was performed using an optimised spectral and spatially selective hyperpolarised ^{13}C MRSI sequence, which was developed by Jiazheng Wang[128]. Axial 1.25 mm thick slices, with an in-plane resolution of 1.25 mm x 1.25 mm, were acquired every second with alternating [1-^{13}C]pyruvate and [1-^{13}C]lactate excitations. The subcutaneous EL4 tumours showed increased pyruvate uptake and conversion to lactate, as expected. A core with high ^{13}C lactate signal intensity closer to the body of the mouse and areas with lower signal intensities were consistently observed (Figure 13). Label exchange between pyruvate and lactate was fast,

with the maximum lactate signal being observed within 20 seconds of the start of acquisition and within 22 seconds of the start of injection (Figure 14).

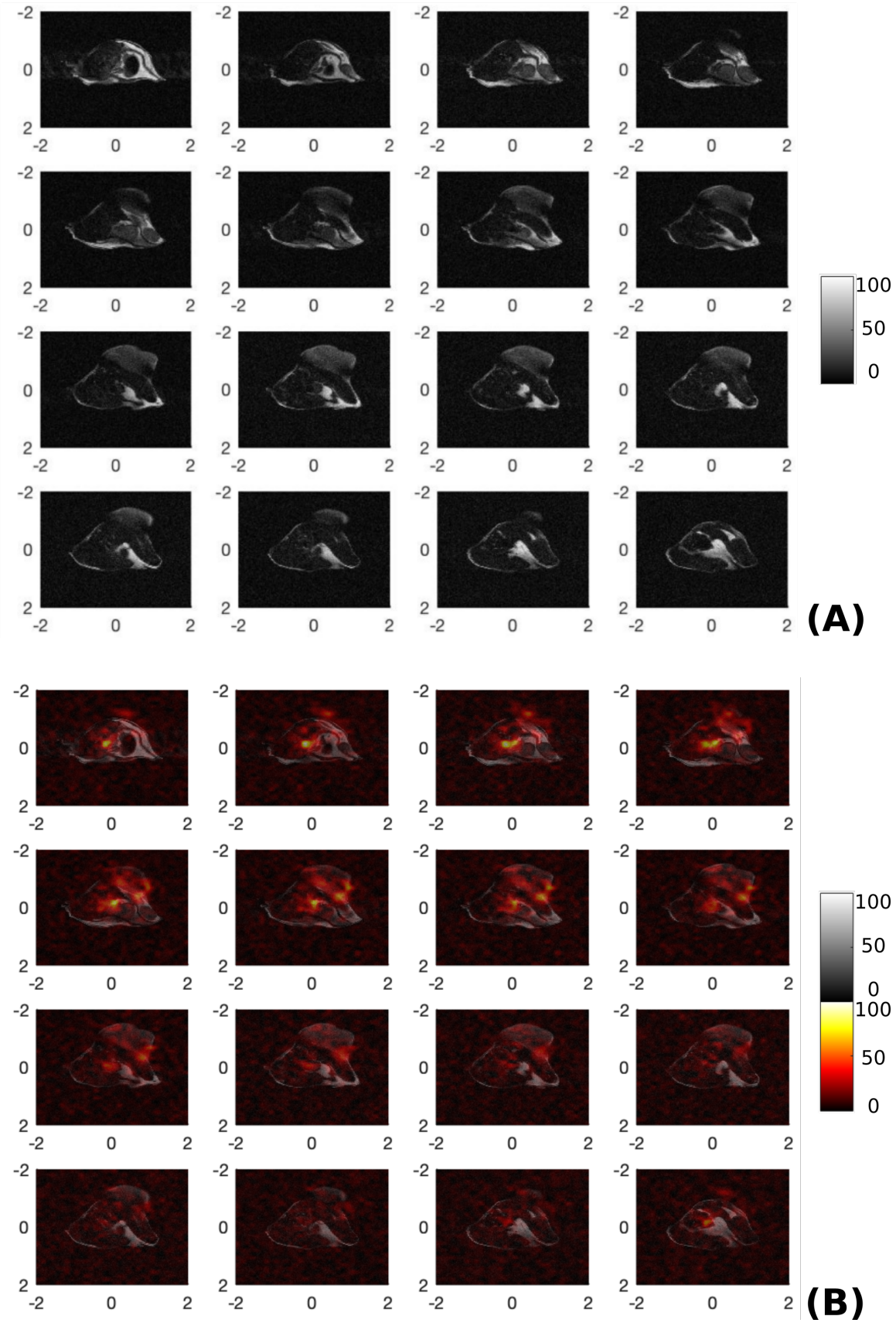

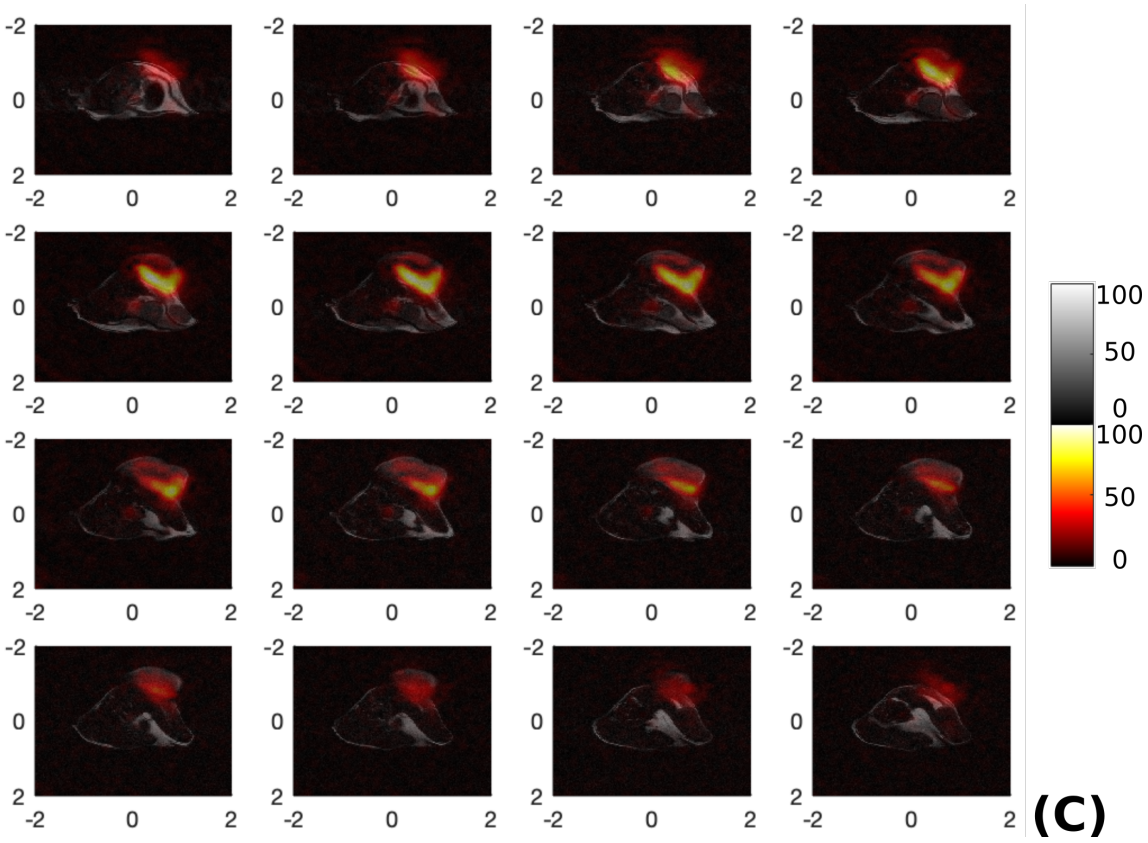

Figure 13 Representative images acquired with hyperpolarized [1-^{13}C]pyruvate in EL4 subcutaneous tumours. *(A) Axial ^{1}H images were acquired before [1-^{13}C]pyruvate injection using a Fast Spin Echo sequence. (B-C) Following injection of pyruvate, a ^{13}C MRSI fast spin echo sequence with spiral acquisition was used to obtain images of [1-^{13}C]pyruvate (B) and [1-^{13}C]lactate (C). False colour images illustrate the summed signal over 14 seconds, overlaid on the grey scale ^{1}H images.*

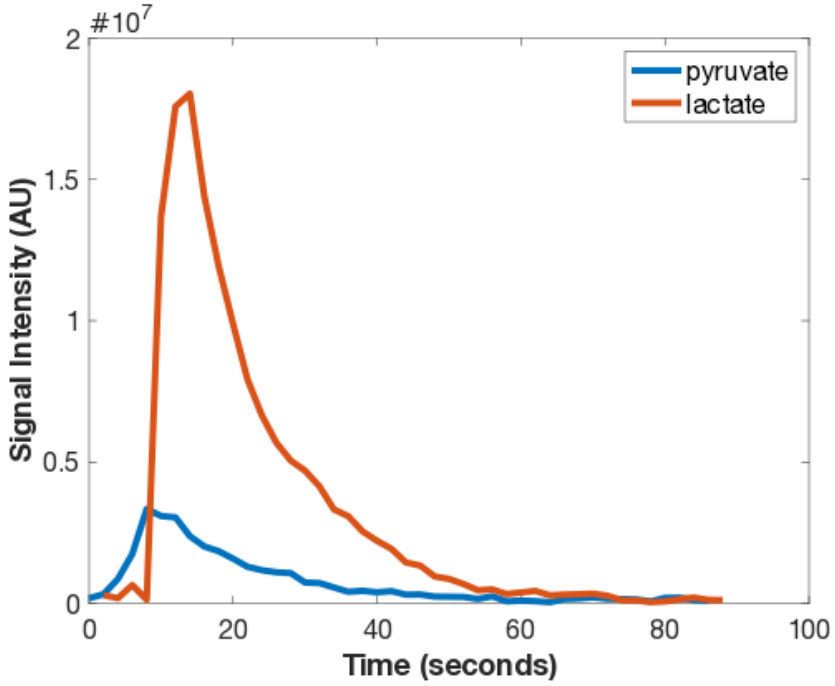

Figure 14 Representative time course of [1-^{13}C]pyruvate and [1-^{13}C]lactate signal intensities. *Each metabolite was imaged every 2 seconds for 90 seconds. The total signal acquired from the tumour region is plotted over time.*

2.4.4 DESI MSI on frozen tissue sections

Immediately after MR imaging, three mice were snap frozen by immersion in liquid isopentane pre-cooled in liquid nitrogen and samples prepared as outlined in the methods section for MSI analysis at AstraZeneca. [1-^{13}C]lactate and [^{12}C]lactate were detected by negative ion mode DESI MSI and metabolic maps were generated from the peak intensities. Control tissue, which consisted of sections of EL4 subcutaneous tumours from mice that were not injected with hyperpolarised [1-^{13}C]pyruvate, was used to confirm the peak assignment for [1-^{13}C]lactate and to control for the natural isotopic abundance of ^{13}C (Figure 15). The natural isotopic abundance from these control tumours was calculated to be 3.3%, as expected. This was not subtracted from the images displayed. Similarly to the MRS images the [1-^{13}C]lactate distribution measured by MSI showed higher signal intensity at the base of the tumour, suggesting that label exchange in those areas is characterised by faster kinetics, which could be a reflection of substrate concentrations, LDH expression or different rates of pyruvate uptake.

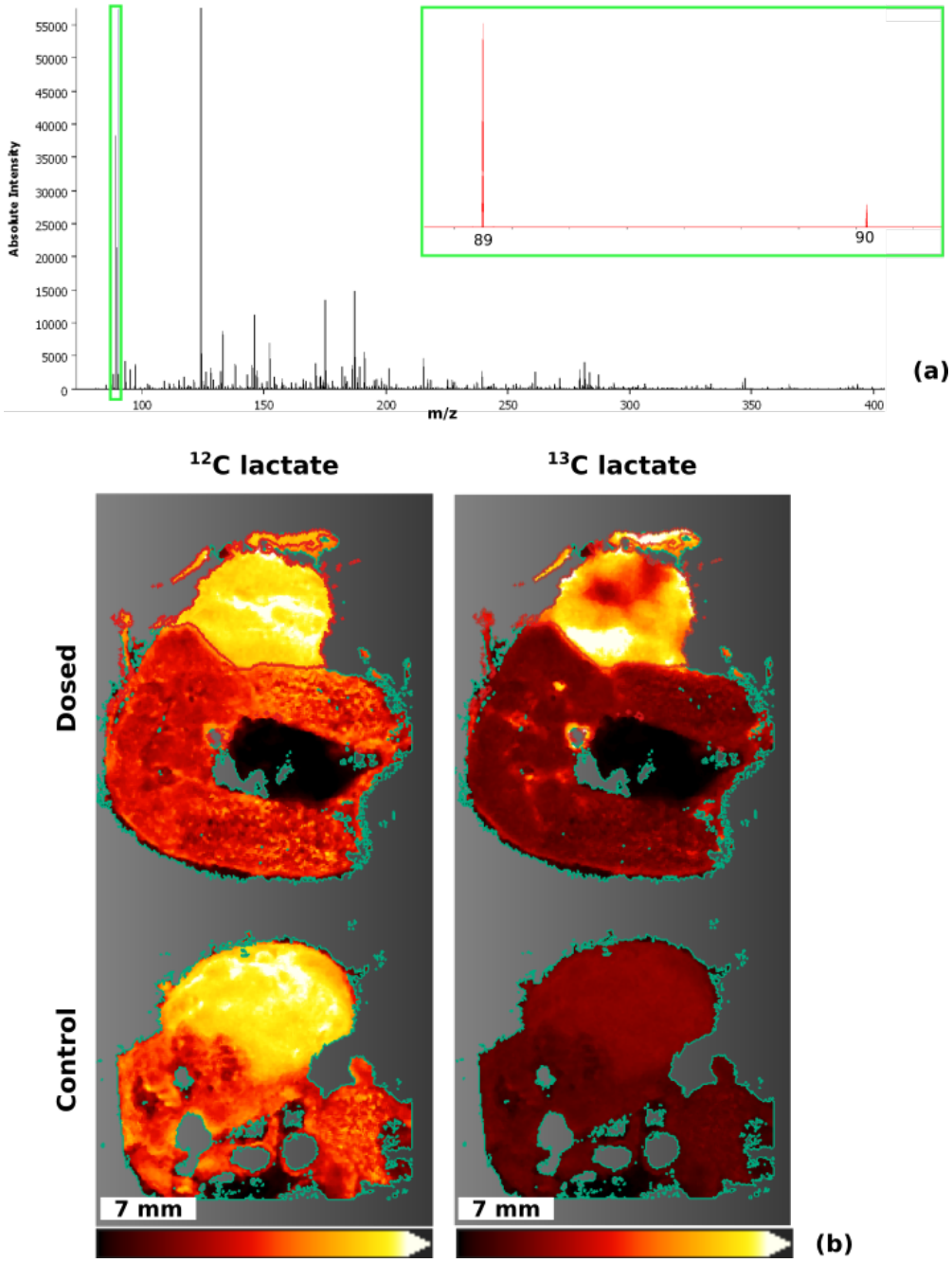

Figure 15 Detection of ^{12}C and [1-^{13}C]lactate by DESI MSI. *(a) The mean mass spectrum across a whole slice is plotted, with the insert showing the peaks corresponding to ^{12}C lactate (89.02 m/z) and [1-^{13}C]lactate (90.03 m/z). (b) Representative slide including a section from a dosed mouse and a section from a control mouse. The distribution of ^{12}C lactate and [1-^{13}C]lactate are shown. ^{12}C lactate shows a homogeneously high distribution in both tumours. The low abundance of [1-^{13}C]lactate in the control tissue confirmed the correct assignment of the m/z peak, and the [1-^{13}C]lactate image from the dosed tissue showed higher labelled lactate nearer the body of the mouse.*

2.4.5 Hyperpolarised ^{13}C MRI and DESI MSI generated positively correlated [1-^{13}C]lactate maps

The ^{13}C MR images of hyperpolarized [1-^{13}C]lactate were compared with the [1-^{13}C]lactate MS images of the corresponding excised tissue sections. Three tumour-bearing mice were used for

the comparison and for each mouse at least three sections were used. The ^{1}H MRI slice corresponding to each MSI section was manually selected using anatomical landmarks within the tumour which were visible on both the H&E images acquired after DESI MSI analysis and on the T_2-weighted MR images (Figure 16).

By visual comparison of the [1-^{13}C]lactate MR images and their corresponding MS images, good agreement was observed between the two techniques (Figure 17A). High [1^{13}C]lactate intensity as measured by both techniques was localised in similar regions of the tumour, which was usually at the base of the tumour. In order to quantify the agreement between the two techniques, the selected slices from the T_2-weighted ^{1}H images, which served as reference images for the ^{13}C MRS images, were co-registered with the MS images using an in-house MATLAB co-registration script, developed by Vencel Somai. The correlation between the lactate MR image, overlaid on the co-registered T_2-weighted ^{1}H images, and the co-registered MS image could then be assessed.

For assessing the agreement between the images generated by the two modalities, Spearman's correlation analysis was used instead of Pearson's correlation analysis because the data were not linearly correlated, due to the different sensitivity and scales of the two modalities. In addition to Spearman's correlation analysis, Cohen's weighted kappa estimates were used to further validate the comparison. Both measures generated similar coefficients that were significantly positive, suggesting that the co-registered images were significantly correlated (Figure 17). Based on the Landis and Koch interpretation of Cohen's weighted kappa coefficients[142], the association in this case is 'fair' on average. This is expected given that the data were generated by different modalities, with different spatial resolutions and more importantly, the comparison was made between intact tissue *in vivo* and frozen tissue sections *ex vivo*. To further validate the significance of the association between the images generated by the two modalities, a linear mixed model - a more powerful parametric analysis able to model the within-mouse, within-tumour and spatial dependence of the MRSI and MSI pixel intensities - was fitted. This showed a highly significant relationship between the MRSI and MSI pixel intensities (p-value of $1.75*10^{-9}$) but a marginal R-squared - fraction of variance of MSI intensities explained by the MRSI ones - of 0.11.

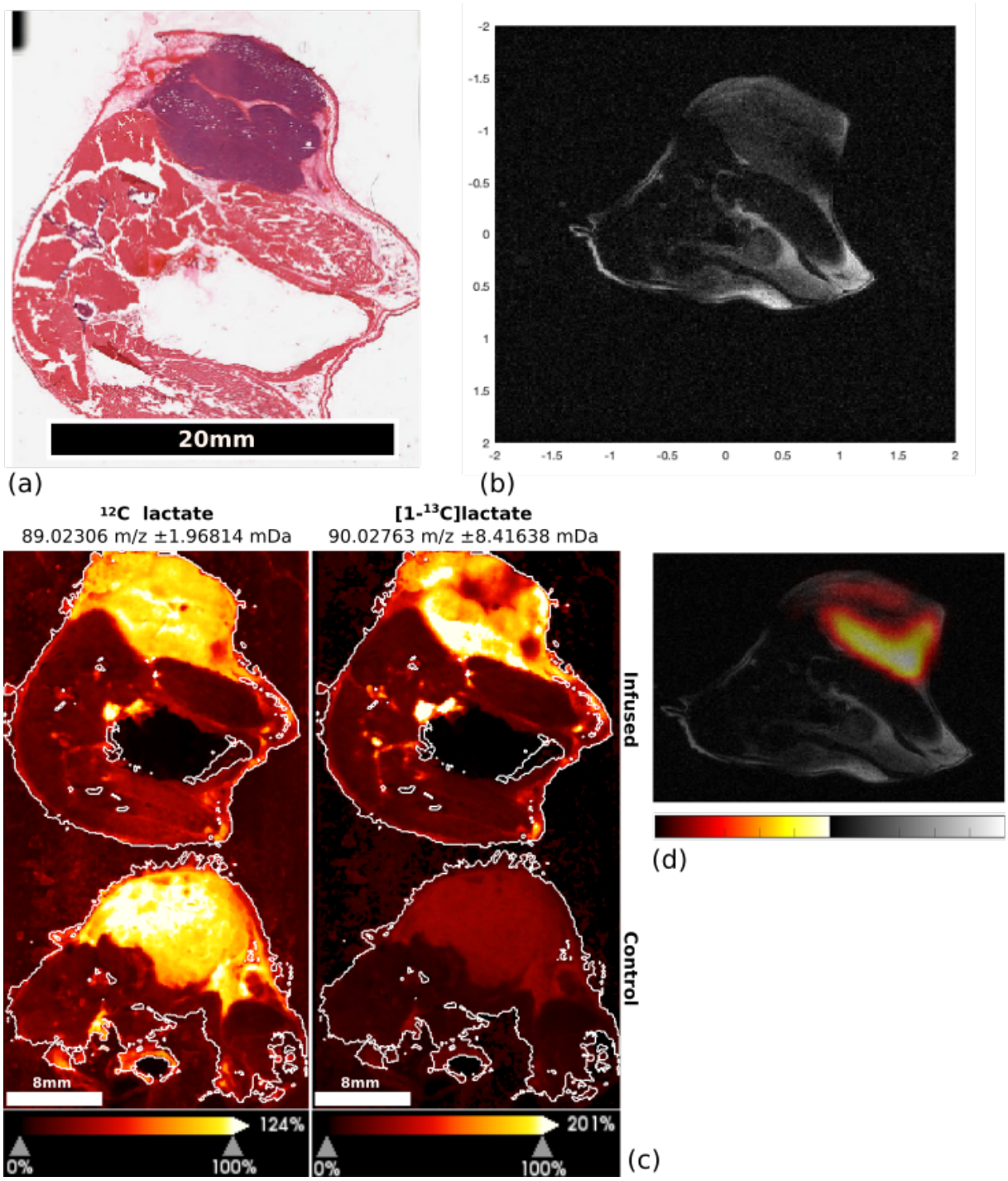

Figure 16 Comparing [1-^{13}C]lactate maps generated in vivo, using hyperpolarised ^{13}C imaging with those generated on sections of the same mouse using MSI*. For registration of the images, the H&E image of the section used for DESI MSI (a) was manually co-registered with one of the 16 T_2-weighted MR image slices (b). This was achieved by matching anatomical landmarks within the tumour as well as overall tumour morphology. (c) DESI MS images showing the same section (top images) as well as a section from a control mouse that was not injected with [1-^{13}C]pyruvate (bottom images). The calculated natural isotopic abundance of ^{13}C lactate in the control tissue was 3.3%. The metabolite abundance is portrayed on a relative scale following application of hotspot removal. Any abundance values over 100% are given the same colour. (d) The hyperpolarised [1-^{13}C]lactate image is overlaid on the T_2-weighted ^{1}H MR image.*

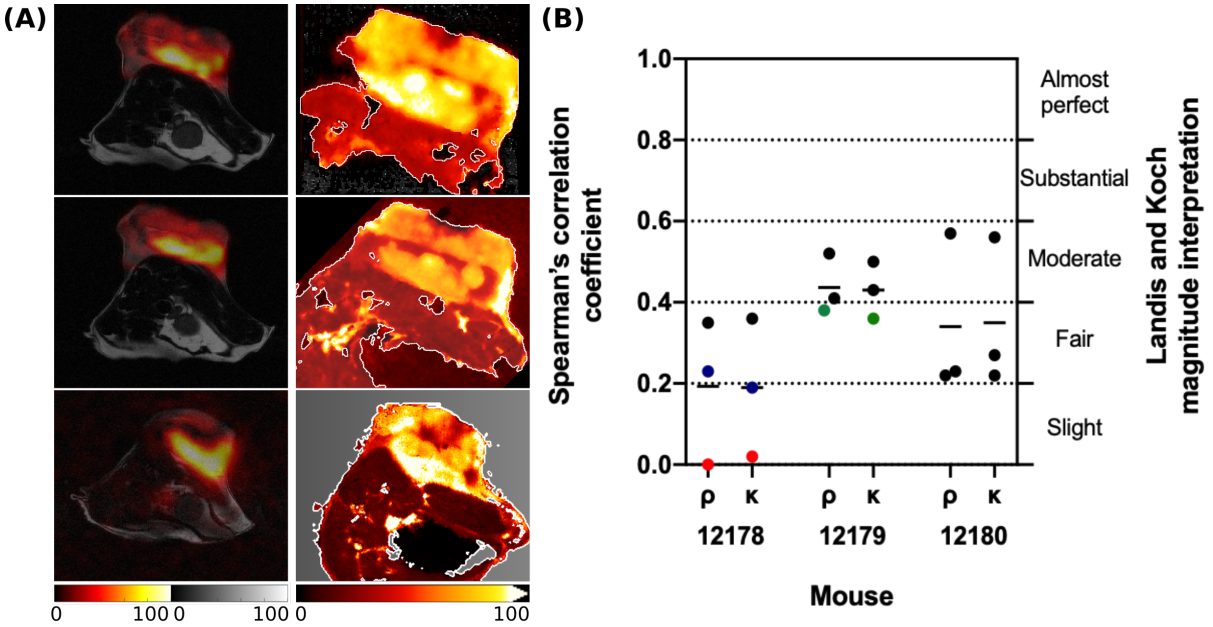

Figure 17 Correlation of metabolic images generated by MSI with images of hyperpolarised [1-^{13}C]lactate generated by ^{13}C MRSI. *(A) Representative paired [1-^{13}C]lactate MRSI slices and MSI sections from two of the three mice used in the study. (B) Correlation of [1-^{13}C]lactate signal intensities in the MS and MRS images, as quantified by pixelwise Spearman's rank correlation (ρ) and Cohen's kappa coefficient (κ) analysis. Each point corresponds to the correlation coefficient calculated from all tumour-containing pixels of each section/slice comparison and the line represents the mean value. The points in blue, red and green correspond to the coefficients calculated from the top, middle and bottom image pairs in (A), respectively. One-sided one-sample t-test on the mean values from different mice on both Spearman's and Cohen's kappa coefficients showed a statistically significant correlation (p=0.02).*

2.4.6 [1-^{13}C]lactate distribution is not correlated with [^{12}C]lactate on the MSI maps

The [^{12}C]lactate distribution, as determined by MSI, was consistently different from the [1-^{13}C]lactate distribution, suggesting that lactate labelling does not simply reflect the endogenous lactate pool. [^{12}C]lactate was generally homogeneously distributed throughout the tumour, whereas [1-^{13}C]lactate showed a more heterogenous distribution (Figure 15, Figure 16 and Figure 18). The Pearson correlation coefficient between [^{12}C]lactate and [1-^{13}C]lactate was calculated for all sections analysed, using Scils software, and this revealed very small positive correlation values, confirming that ^{13}C lactate labelling is not strongly dependent on the endogenous lactate levels in this tumour model (Figure 18) suggesting that the rate of label exchange is almost independent of the endogenous availability of lactate.

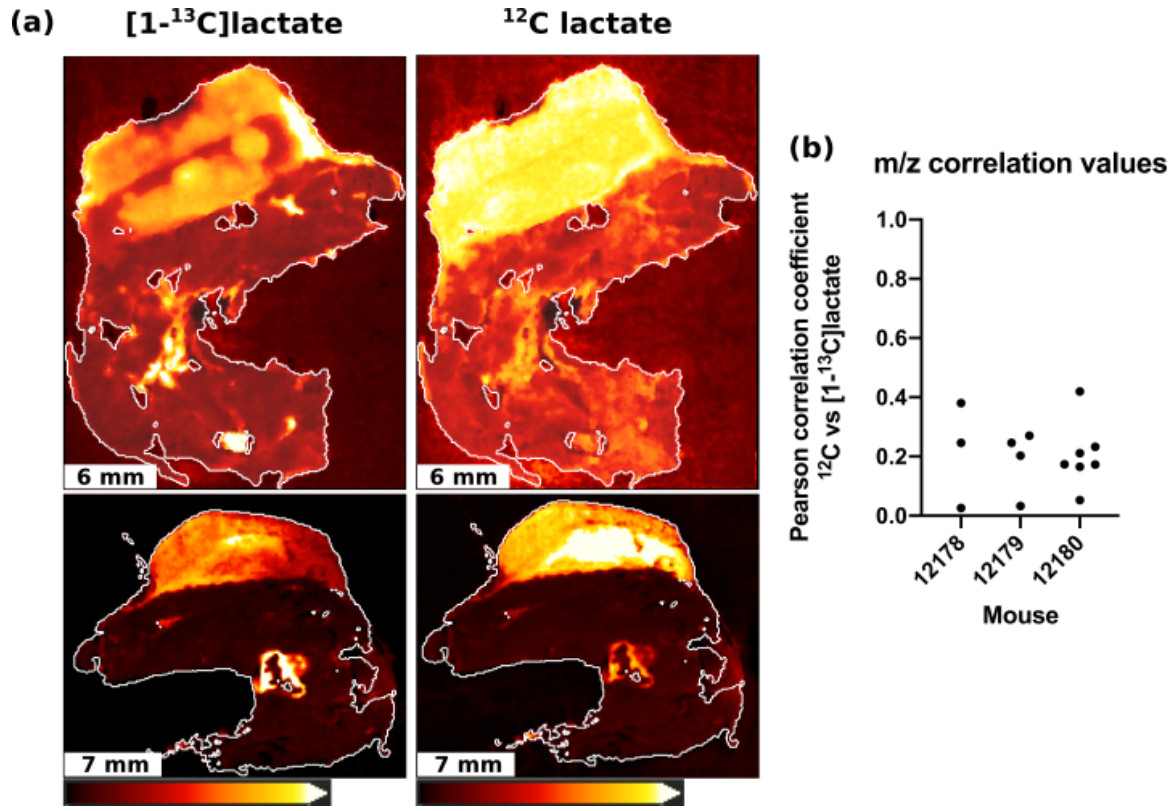

Figure 18 [^{12}C]lactate and [1-^{13}C]lactate show different distributions in EL4 tumours. *(a) [1-^{13}C]lactate (left) and [^{12}C]lactate (right) maps from two representative sections from two different mice, showing the different distributions of the two metabolites. (b) The Pearson correlation coefficients calculated between the [^{12}C] and [1-^{13}C]lactate maps (tumour region only) from all sections of all three mice are plotted, demonstrating the very low positive correlation between the two metabolites.*

2.4.7 [1-^{13}C]lactate distribution is correlated with [1-^{13}C]pyruvate distribution

Similarly to the correlation analysis between [^{12}C] and [1-^{13}C]lactate MS images, the correlation between [1-^{13}C]pyruvate and [1-^{13}C]lactate was assessed on the MRS images. The correlation coefficients in this comparison were higher than between [^{12}C] and [1-^{13}C]lactate, suggesting that ^{13}C lactate labelling is limited principally by the availability of labelled pyruvate in the tumour (Figure 19). Substrate delivery to the tumour depends on perfusion of the tumour as well as the presence of monocarboxylate transporters MCT1 and MCT4 for enabling pyruvate entry into the cells.

Immunohistochemical staining using an antibody against mouse CD31 was performed on sections adjacent to the sections used for MSI, to assess the vasculature throughout the tumour. The staining pattern can be compared to the [1-^{13}C]lactate maps to better understand the limiting factor for lactate labelling in the tumours. CD31 staining showed some heterogeneity across the

tumour, with some areas of the tumour appearing to be more well-vascularised than others, possibly contributing to the heterogeneity in pyruvate delivery (Figure 20).

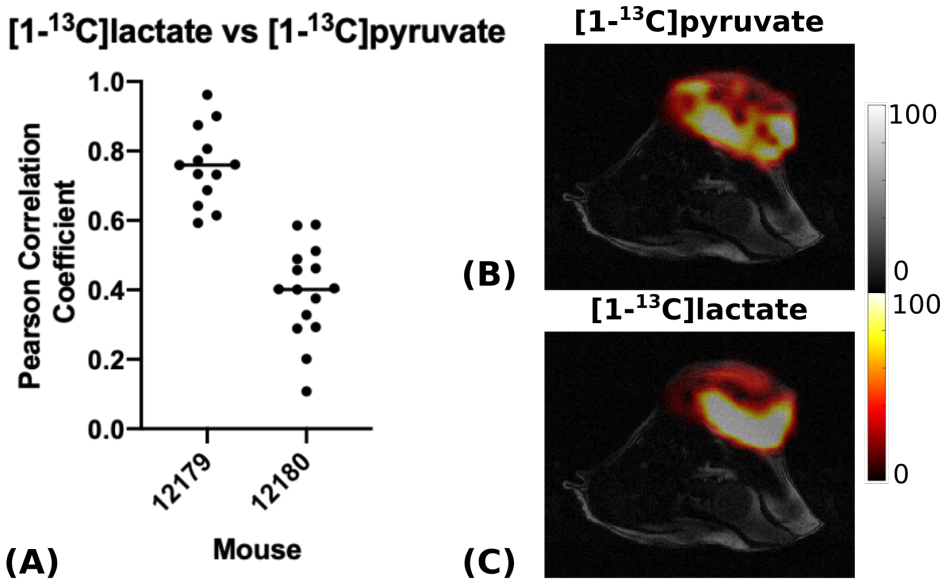

Figure 19 [1-^{13}C]lactate MRS images are well correlated with [1-^{13}C]pyruvate MRS images*. (A) The 2D correlation coefficient between pyruvate and lactate maps was calculated for each slice imaged from two mice using Matlab's corr2 function. Each point on the graph represents the correlation coefficient for each slice. (B-C) Representative examples of images of the summed [1-^{13}C]pyruvate (B) and [1-^{13}C]lactate (C) signal intensities overlaid on the anatomical grey scale ^{1}H image of a slice through one of the mice imaged, demonstrating the good correlation between the two maps.*

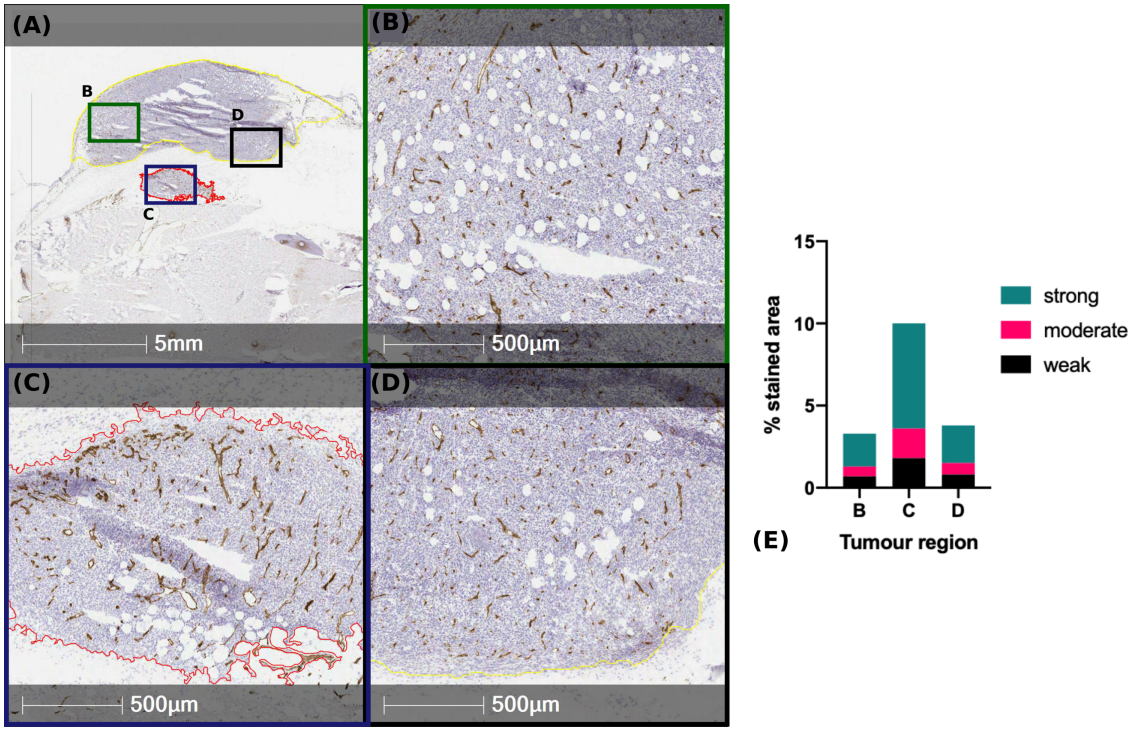

Figure 20 Tissue vasculature is heterogeneous across the tumour. *(A-D)Immunohistochemical staining for CD31 on a frozen section containing EL4 tumour tissue as well as healthy mouse tissue (A). Three areas of the tumour are demonstrated at high magnification (B-D) as labelled on the low magnification image (A). (E) Quantification of the positivity of the tumour regions for CD31 staining was performed using the HALO software (Indica Labs, New Mexico, USA).*

2.5 Discussion

Dynamic ^{13}C MRSI measurements following injection of hyperpolarised [1-^{13}C]pyruvate were used to measure the rate of interconversion of pyruvate and lactate *in vivo*, with a time resolution of 2 seconds, a nominal spatial resolution of 1.25 mm x 1.25 mm x 1.25 mm and an effective spatial resolution of 1.25 mm x 1.25 mm x 4.5 mm, when taking into account the z-direction point spread function[128]. The EL4 tumours showed rapid [1-^{13}C]pyruvate uptake and very fast conversion to [1-^{13}C]lactate, as has been observed previously in this tumour model[72,143]. Sixteen ^{13}C MRSI axial slices were acquired from each of three EL4 tumours and spatial maps of [1-^{13}C]lactate and [1-^{13}C]pyruvate were overlaid on the anatomical T_2-weighted ^{1}H MR images. The [1-^{13}C]lactate signal was largely localised to the tumour and showed a heterogeneous distribution. Inhalation anaesthesia (isoflurane) was used throughout the hyperpolarised MRI experiment which undoubtedly had effects on the measured metabolism as suggested in previous studies[144], but in this case these effects do not pose a problem as comparisons are made between images of the same animals or between different animals that were treated in the same way with isoflurane.

MSI has a much better spatial resolution than MRI, therefore, a more detailed map of labelled lactate could be acquired from tumour sections. However, the lactate images acquired by MSI represent an endpoint measurement, compared to the dynamic metabolism interrogated by hyperpolarised ^{13}C MRSI. The mice were snap-frozen immediately after the end of the MRI acquisition, using an optimised freezing technique in order to preserve metabolite concentrations. For this reason, the [1-^{13}C]lactate MS images were expected to match the maps of summed [1-^{13}C]lactate signal acquired over the time using MRSI. Indeed, there was a good correlation between the MRS and MS images (Figure 17).

Co-registration of MRS tumour images with the MS images of excised tumours proved to be challenging since when the tumour is excised, frozen and then sectioned, the orientation of the tumour with respect to the mouse anatomy was lost and co-registering the sections to the MR slices was impossible. For this reason, the whole mouse was frozen and whole mouse axial sections were taken for MSI. Even then, the changes in morphology due to rapid freezing, the difficulty of taking intact sections through the whole frozen mouse body and the differences in thickness of the MSI sections (10 μm) and the MRSI slices (1.25 mm) meant that the excised sections did not match perfectly the MR images. Anatomical landmarks in the tumour, which

appeared in both the T_2-weighted ^{1}H images and in the images of the H&E-stained sections, were used to facilitate manual alignment of MS images with their corresponding MRI slice. The co-registration MATLAB routines were successful in registering the tumour masks, defined by drawing a region of interest around the tumour, by applying rigid and non-rigid transformations. However, in most cases, the tumour outline was distorted during snap-freezing and during sectioning, thus limiting the accuracy of the registration. Therefore, the magnitude of the correlation between the MS and MRS images is an underestimate of the true agreement between the two imaging modalities. The statistical significance for the correlation between the two modalities was confirmed using spatial and non-spatial statistical tools, enabling the cross-validation of hyperpolarized ^{13}C MRSI and MSI techniques. Both techniques are relatively new and are still undergoing development. Therefore, showing that the two techniques generated similar results in a well-controlled experiment, where we directly assessed the spatial distribution of one metabolite, is encouraging for both methodologies.

There has been a lot of discussion with regard to the ionisation efficiency in MSI and whether ionisation suppression effects in the tissue could affect the accuracy of the spatial maps generated by the technique. Also, due to the small concentrations of ions analysed, tandem mass spectrometry is usually not possible in MSI, therefore, the fractionation pattern of the ions is not investigated. This could mean, that the mass spectra generated are not always specific, since different metabolites could have the same m/z value. Here we show that the accuracy and specificity of DESI MSI for detecting ^{13}C lactate were not compromised. Using negative control tissue which contains [^{13}C]lactate at its natural isotopic abundance, we have shown that the peak we have assigned to [^{13}C]lactate is specific. Also, the good correlation between the [^{13}C]lactate map generated by DESI MSI and ^{13}C hyperpolarised MRSI, suggests that the ionisation efficiency was consistent across the whole tumour and no ionisation suppression effects were visible. The quickly shifting tissue metabolome often presents a challenge in MSI as sample processing can affect the quality of results. In these experiments, an optimised freezing method was used to ensure fast arrest of metabolism and although the samples were brought to room temperature for MSI, processing and storage did not seem to impact the quality of the lactate data, since the MSI data was in agreement with the MRI data.

The exchange of ^{13}C label between pyruvate and lactate in a tumour is dependent on [1-^{13}C]pyruvate delivery, uptake into the tumour cells via the MCT1 and MCT4 transporters, the concentration of LDH and the size of the endogenous tumour lactate pool[145]. The relative

importance of these factors will likely vary according to the tumour type. Previous studies on EL4 cells showed that the activities of the MCTs and LDH are nearly equally important in determining the exchange velocity[145]. Using MSI, we have shown that in EL4 tumours *in vivo*, the size of the endogenous tumour lactate pool, and therefore LDH activity, was poorly correlated with lactate labelling, but that there was a stronger correlation between the [1-^{13}C]pyruvate and [1-^{13}C]lactate signals, suggesting that delivery of labelled pyruvate has the greatest effect on the exchange velocity under these conditions. Additionally, evidence from immunohistochemical staining of tumour sections pointed towards a heterogeneous pattern of vasculature that could affect pyruvate delivery. This does not mean that the activities of the MCTs and LDH are unimportant, but it suggests that under these conditions and in this tumour model, pyruvate delivery is more important. Immunohistochemical staining of the sections for MCT and LDH expression would be very interesting but we were unable to investigate that due to the low specificity of antibodies against these mouse antigens. A recent clinical study in prostate cancer patients, showed positive correlation between MCT1 expression and lactate labeling[125] and it has also been shown previously in the EL4 tumour model that the MCT inhibitor, α-Cyano-4-hydroxycinnamic acid (injected at 150 mg kg^{1}) produced a 40% decrease in label exchange[146].

Another factor that has not been investigated in this study is the contribution of the stroma in label exchange. The combination of MSI with the Imaging Mass Cytometer could enable the involvement of the immune compartment and other parts of the stroma to be imaged[147].

2.6 Conclusion

In this study, hyperpolarised ^{13}C pyruvate imaging and MSI generated positively correlated tumour images of [1-^{13}C]lactate following injection of hyperpolarised [1-^{13}C]pyruvate, thus cross-validating the two techniques. The [1-^{13}C]lactate maps in the tumour were poorly correlated with the endogenous tumour lactate levels but more closely correlated with maps of [1-^{13}C]pyruvate, suggesting that in this tumour pyruvate delivery has the greatest effect on the rate of lactate labelling. This study highlighted the possibility and benefits of combining these two novel metabolic imaging techniques to better understand cancer metabolism. The addition of MSI to the pipeline enabled the visualisation of endogenous metabolites in addition to the labelled metabolites that can be imaged with hyperpolarised MRI as well as a much better resolution.

Chapter 3 - Investigating the role of BCAT1 in Glioblastoma

3.1 Abstract

Upregulation of the cytosolic isoform of Branched Chain Aminotransferase (BCAT1) has been associated with the progression of different types of cancer, including glioblastoma, but its role in cancer pathophysiology is still unclear. The role of BCAT1 in glioblastoma was investigated in cells derived from glioblastoma patients. Differential expression of BCAT1 was observed in a panel of glioblastoma cell lines. Modulation of BCAT1 expression in the A11 line led to changes in cell phenotype, including changes in proliferation, migration and invasion. These effects were not observed in the S2 cell line, which appears to be unaffected by changes in BCAT1 expression. The phenotypic effects of BCAT1 knockdown in A11 cells were not mediated via changes in the levels of Branched Chain Ketoacids (BCKAs), mTOR signalling or changes in glutamate synthesis but by global transcriptional changes, including downregulation of HIF and FOXM1 target gene expression. The levels of 5-hydroxymethylcytosine in DNA were increased in BCAT1 knockdown cells suggesting TET enzyme activation. We suggest that BCAT1 regulates the cells' phenotype through regulation of alpha-ketoglutarate metabolism.

3.2 Introduction

3.2.1 Branched Chain Amino Acid Metabolism

Leucine, isoleucine and valine are Branched Chain Amino Acids (BCAA) with hydrophobic side chains that are essential in the diet and comprise 20-40% of most dietary protein[148]. A high proportion of these amino acids are absorbed through the intestine and are then circulated to the peripheral tissues, where they are incorporated into proteins or catabolised. Interestingly, unlike other amino acids, these amino acids are not metabolised in the liver, due to the absence of the transaminase enzyme which catalyses the first catabolic reaction[149]. Therefore, upon ingestion of a high-protein diet, the circulating levels of BCAA show a dramatic increase, while other amino acids do not show significant changes in their plasma levels, due to their hepatic metabolism[149].

Most of BCAA catabolism takes place in muscle cells, where the enzymes of the catabolic pathways are abundant. The first enzymatic step in the catabolism of BCAAs is a reversible transamination reaction catalysed by Branched Chain Aminotransferase (BCAT). This reaction (Figure 21) uses α-KG as the amino acceptor, leading to transamination of BCAAs leucine, isoleucine and valine to their respective ketoacids (α-ketoisocaproic acid (KIC), α-keto-β-methylvaleric acid (KMV) and α-ketoisovaleric acid (KIV)) and the generation of glutamate[148]. Two isozymes of BCAT have been described in eukaryotes; the cytosolic isozyme, BCAT1, also called BCATc and the mitochondrial isozyme, BCAT2, also called BCATm[150]. These enzymes belong to the Type IV class of Pyridoxal Phosphate-containing enzymes, with catalysis occurring on the pyridoxal phosphate cofactor[151]. The isozymes show differential distribution in the human body, as demonstrated by western blot and enzyme activity measurements. More specifically, BCAT1 seems to be primarily localised in the brain, ovary and placenta, whereas BCAT2 can be found in most tissues[150]. Immunohistochemical studies in rat brain have demonstrated that BCAT1 is primarily expressed in the neurons, whereas BCAT2 is expressed in astrocytes[152].

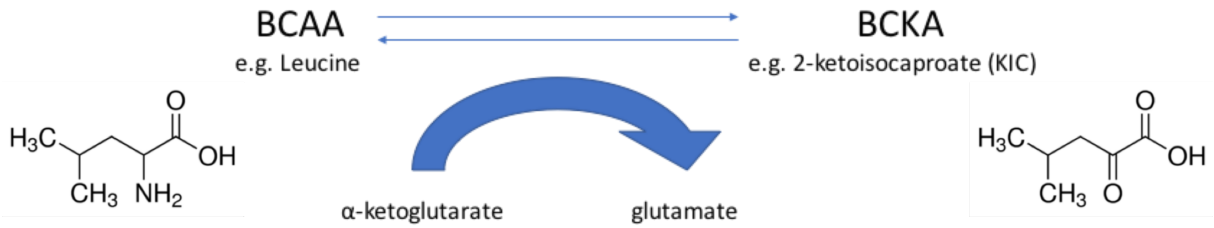

Figure 21 Schematic overview of the reaction catalysed by BCAT. *In the presence of BCAT, BCAAs will be transaminated to their respective ketoacids. α-KG will accept the amino group and will thus be converted to glutamate.*

The ketoacids generated from the transamination reaction are then oxidatively decarboxylated in a reaction catalysed by the branched chain ketoacid dehydrogenase complex, found on the inner leaflet of the mitochondrial membrane[149]. This is an irreversible reaction and represents the rate limiting reaction in the catabolism of the BCAAs. The dehydrogenase activity is modulated by phosphorylation and dephosphorylation events, in response to stimuli such as hormones and cytokines. Further catabolism differs between the ketoacids, with KIC generating acetyl-CoA and acetoacetate, KIV generating succinyl CoA and KMV generating both acetyl-CoA and succinyl CoA[149]. Evidence suggests that BCAA metabolism is self-regulated with high BCAA levels inducing higher catabolic enzyme activities[153]. A number of disorders, including Maple Syrup Urine Disease (MSUD), are caused by dysregulation of these metabolic pathways[148].

An overview of the metabolic fate of BCAAs in the cell is shown in Figure 22.

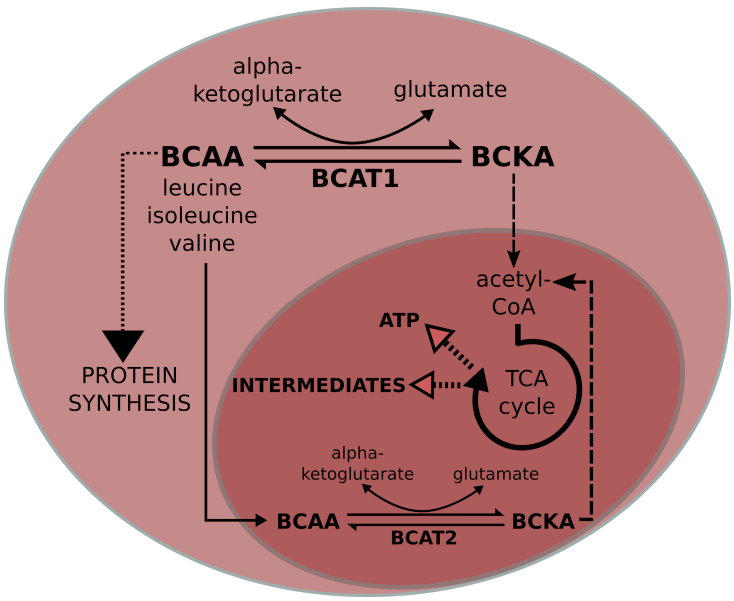

Figure 22 Overview of the metabolic fate of Branched Chain Amino Acids. *They can be incorporated into proteins, or transaminated to their respective ketoacids and further catabolised to acetyl Co-A, which can enter the Tricarboxylic Acid cycle.*

BCAAs play many roles in metabolism. They are essential for protein synthesis. Their metabolism plays a role in energy production but they also act as nitrogen donors for the *de novo* synthesis of other amino acids, including alanine and glutamine[150]. The nitrogen in BCAAs is also used in the Central Nervous System (CNS) for the synthesis of the excitatory neurotransmitter, glutamate[150].

In addition to the metabolic roles of BCAAs, they also take part in signalling, by activating the mammalian target of rapamycin (mTOR) pathway. mTOR is a serine/threonine kinase that regulates numerous cellular processes, which include cell growth, protein synthesis and proliferation. Protein synthesis is controlled by the mTOR complex 1 (mTORC1), which is composed of mTOR and other regulatory proteins. This complex is regulated by amino acids, such as leucine as well as some growth factors and hormones including insulin and leptin[153]. More specifically, leucine acts as an activator of mTORC1 through the enzyme catalysing the ligation of leucine to its transfer RNA (tRNA), leucyl tRNA synthetase, which also acts as a sensor for leucine[153]. Downstream targets of mTORC1 include p70-S6 kinase 1 (S6K1) and eukaryotic initiation factor 4E binding protein 1 (4E-BP1), which are responsible for mRNA translation initiation and protein synthesis. Leucine is also thought to regulate protein synthesis through modulation of the General Control Non-repressible Kinase 2 (GCN2) pathway.

BCAAs are necessary for neurotransmission in the brain. The proposed mechanism for regulation of glutamate synthesis (Figure 23) suggests that BCAAs enter the astrocytes, where they are transaminated to the BCKAs by BCAT2, while glutamate is produced from α-KG[152]. The BCKAs are then released by the astrocytes and taken up by the neurons, where they can be converted to BCAAs by BCAT1 using the amino group of glutamate and returned to the astrocytes, thus forming a cycle between astrocytes and neurons[152]. This is an important mechanism for replenishing the lost glutamate in astrocytes, which is needed for the glutamate/glutamine cycle. The glutamate/glutamine cycle (Figure 23) involves exchange of glutamate and glutamine between neurons and astrocytes. Neurons release glutamate at the synapse, as a neurotransmitter, which is then taken up by the astrocytes. It is converted to glutamine in the astrocyte by glutamine synthetase and the glutamine is then released by the astrocytes to be taken up by the neurons, which use it to produce more glutamate. Some glutamate is oxidised in the astrocytes and is thus lost, requiring the *de novo* synthesis of new glutamate. This role can be fulfilled by the BCAA shuttle, since BCAT2 activity in astrocytes

leads to the generation of glutamate from α-KG[152]. Thus, BCAA metabolism plays an important role in brain physiology.

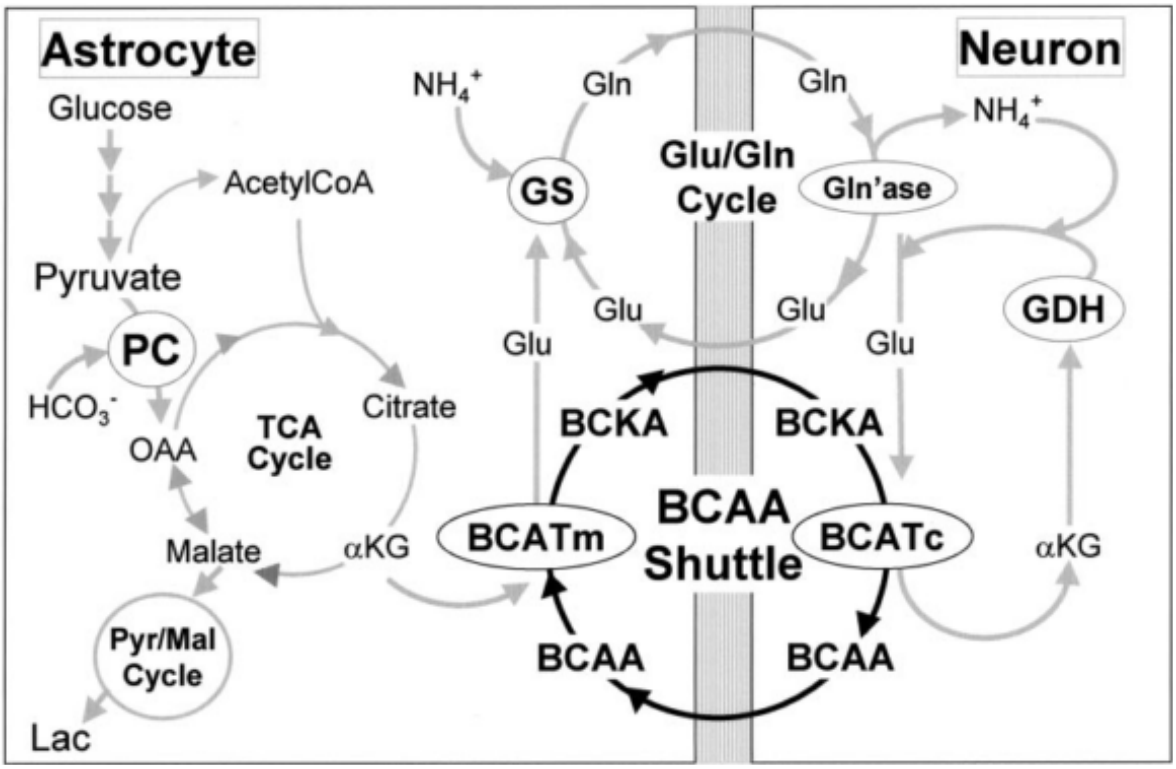

Figure 23 The role of the BCAA shuttle in brain glutamate metabolism, reproduced from Hutson et al[152]. *Glutamate is synthesised from glutamine in the neurons and secreted as a neurotransmitter. Following synaptic transmission, glutamate is taken up by the astrocytes and converted to glutamine. Some of the glutamate is oxidised in astrocytes and replenished by the BCAA shuttle, whereby BCAAs are transaminated to their corresponding BCKAs by BCAT2, generating glutamate from α-KG.*

3.2.2 BCAT1 in glioblastoma

Tonjes et al showed an inverse relationship between *IDH* mutations in glioma and BCAT1 expression, with almost all *IDH* mutant cancers showing low BCAT1 levels. It was also shown that the increase in expression of BCAT1 was the best classifier to distinguish primary glioblastoma from secondary glioblastoma, diffuse astrocytoma and anaplastic astrocytoma[51]. The authors observed expression of three *BCAT1* transcripts (T1, T4, T6) in normal brain and glioblastoma tissues, with T6 being the most predominant transcript in primary gliomas. Treatment of U-87 MG and U-373 MG cells with gabapentin, a leucine analogue that inhibits BCAT1 but not BCAT2, led to intracellular accumulation of BCAAs and reduced glutamate release into the cell media. Additionally, knockdown of BCAT1 using shRNA, led to morphological changes in the cells, which appeared more rounded as well as a reduction in the invasion capacity of the cells, as measured using a microchannel migration assay. Cell proliferation was also impaired upon BCAT1 inhibition using gabapentin and by BCAT1

knockdown. Cell proliferation measured using EdU (5-ethynyl-2'-deoxyuridine) incorporation was reduced and the cells showed partial G1 arrest, which was partially rescued by ectopic overexpression of BCAT1. The effects of BCAT1 knockdown were investigated *in vivo* as well, where mice implanted intracranially with U-87 cells transduced with BCAT1 shRNA grew significantly smaller tumours than those implanted with cells transduced with the non-targeting shRNA.

Taken together, these data suggest that BCAT1 could play a role in glioblastoma development and progression but the mechanism for this is still not well understood. BCAT1 upregulation could lead to enhanced BCAA metabolism, promoting biosynthesis and generation of ATP as well as increased utilisation of nitrogen for glutamate production. Alternatively, since the reaction is reversible, it is also possible that glioma cells take up BCKA and convert them to BCAA for protein synthesis, or even as a mechanism to deal with excess nitrogen. In fact, some of these hypotheses, as well as others have been suggested already and some evidence has been provided for them.

Tonjes et al[51] hypothesised that the catabolism of BCAAs promotes proliferation of glioblastoma cells by providing fuel for the TCA cycle. Silva et al suggested that upregulation of BCAT1 leads to increased BCKA synthesis by glioblastoma cells. Using ultra high-performance liquid chromatography, the *in vitro* intracellular and extracellular concentrations of BCKAs were measured and a very fast accumulation of BCKAs in the media was observed. This accumulation of BCKAs in the cell media was reduced upon shRNA-mediated knockdown of BCAT1. The authors also showed that the efflux of BCKAs is mediated by MCT1 and provided some evidence of specific protein interactions between BCAT1 and MCT1 in U-87 and U-251 cells. The authors suggest that BCKAs released by glioblastoma cells in the tumour stroma are taken up by macrophages and reaminated to their respective amino acids and this results in reduced phagocytic activity. Therefore, upregulation of BCAT1 in glioblastoma might have immunosuppressive effects in the tumour microenvironment[154].

Another potential role that BCAT1 could play in glioblastoma metabolism is the generation of glutamate, which can be used for glutathione synthesis, necessary for resistance to reactive oxygen species[155]. In this study, *IDH1* mutations were shown to inhibit BCAT1 via the production of 2HG. When human glioma cells were infected with a lentivirus expressing mutant *IDH1*, levels of BCKAs and glutamate in the media were reduced while levels of BCAAs were elevated, similarly to when BCAT1 was inhibited, either pharmacologically or genetically.

Using a cell-permeable version of 2HG, the authors showed that 2HG reduced BCAT1 activity *in vitro,* leading to lower intracellular levels of glutamate. The authors suggested therefore that in *IDH*mut gliomas, the cells are highly dependent on glutaminase for glutamate generation, in line with upregulation of a more active glutaminase splice isoform in these tumours. By performing ^{15}N isotope labelling studies in immortalized human astrocytes and human oligodendroglioma cells, the authors showed that half of the nitrogen in the glutamate pool is derived from BCAAs and the rest is derived from glutamine. By expressing mutant IDH1 in these cells, the authors saw reduced flow of nitrogen from ^{15}N-labelled BCAAs to glutathione, suggesting that 2HG-mediated inhibition of BCAT1 in *IDH* mutant gliomas can lead to reduced levels of glutathione. Finally, the authors demonstrated that combining *IDH* mutation with glutaminase inhibition rendered the cells sensitive to oxidative stress *in vitro* and led to reduced tumour growth and increased survival *in vivo* when radiotherapy was used in combination with a glutaminase inhibitor.

Regardless of the mechanism of action, BCAT1 appears to be important in primary *IDH* wild type gliomas and it could potentially be targeted pharmacologically. Gabapentin, a drug used for neuropathic pain relief and seizure control, is known to be a competitive inhibitor of BCAT1 with a K_i similar to the K_m of leucine, while having no effect on BCAT2 activity[156]. Recently, a specific inhibitor of BCAT1, 4-methyl-5-oxohexanoic acid has been described with an IC_{50} of 0.1-1 nM, which has been used *in vitro* to investigate the effect of BCAT1 inhibition in macrophages but also *in vivo*, in the treatment of inflammatory disease[157].

3.2.3 Aims

From the published work on BCAT1 in glioblastoma, it is evident that BCAT1 is upregulated in *IDH* wild type glioblastoma and that it plays a role in the proliferation of glioma cells. Since most of the aforementioned research was primarily based on U87 cells and other conventional human glioblastoma cell lines, known not to represent human glioblastoma, the role of BCAT1 in cell proliferation and other suggested phenotypes was investigated in patient-derived glioblastoma cell lines. The aims of this project were to characterise a panel of patient derived glioblastoma cell lines with regard to their expression profiles and activity levels of BCAT1 and BCAT2 and to assess the role of BCAT1 in the different phenotypes that have been associated with BCAT1 upregulation, including cell proliferation, migration and invasion and radioresistance. The final aim was to understand the mechanism through which BCAT1 enables these phenotypes, which has not yet been elucidated.

3.3 Methods

3.3.1 Cell Culture

All cell lines were mycoplasma tested and Short Tandem Repeat (STR) profiled regularly and prior to freezing any stocks by the Research Instrumentation and Cell Services core facility in the institute.

The cell lines included two rat glioma cell lines (C6 and 9L), two human glioma cell lines (U87 and U251), and four patient derived cell lines (A11, SP20, S2 and A25).

U87, C6 and 9L adherent cells were grown in flasks in high glucose containing DMEM medium (Gibco) supplemented with 10% FBS. U251 cells were grown in low glucose containing DMEM medium (Gibco), which was also supplemented with 10% FBS. Cells were harvested following trypsinisation and washing with PBS.

The patient derived adherent cell lines were grown in serum-free Neurobasal A Media (Gibco) supplemented with B27, N2, 20 ng/ml Epidermal Growth Factor (EGF) (Sigma) and 20 ng/ml Fibroblast Growth Factor (FGF) (Gibco), as well as 2 mM glutamine and Penicillin-Streptomycin antibiotic (100 U/ml) (Gibco) in flasks which were precoated with Extracellular Matrix (Gel from Engelbreth-Holm-Swarm murine sarcoma) (Sigma). Hank's Balanced Salt Solution (HBSS) (Gibco) was used to wash the cells and StemPro Accutase Cell Dissociation Agent (Gibco) to detach them from the flask surface.

Cells were kept in a humidified incubator set at 37°C, 5% CO_2 (Heracell, ThermoFisher).

3.3.2 *In vivo* tumour models

A 5 µl suspension of 10^6 cells (A11, S2, A11shCtrl, A11shBCAT1, A11Strawberry, A11BCAT1 and S2BCAT1) was loaded into a clean Hamilton syringe, which was stabilized on a stereotaxic stage. The rat/mouse was anaesthetized in an induction chamber using 3% isoflurane at 2 L/min air flow, weighed and transferred to the surgery table. Analgesia (Rimadyl and Buprofen) was administered subcutaneously before incision. Temperature was monitored by a rectal thermometer and maintained throughout the procedure using a heat pad. A midline incision was made on the head and a retractor placed to expose the skull. A hole was drilled on the skull at a point 2 mm to the right and 2 mm posterior to the bregma. The Hamilton syringe

was inserted into the brain (4 mm and 3 mm deep for the rat and mouse respectively) and the cells were slowly injected intracranially. The hole on the skull was sealed with bone wax and the skin incision sutured. Surgical glue was applied over the incision site. The animal was then placed in the recovery chamber for about 20 minutes, before it was returned to its cage. Twenty-four and 48 hours after surgery, subcutaneous analgesia (Rimadyl) was administered.

Following implantation, tumour growth was monitored using T_2-weighted MRI scans, which were performed at least monthly.

3.3.3 Cell and tissue protein extraction for western blots

Cells were harvested by centrifugation and the pellets resuspended in about 80 µl per 10^6 cells of cold Pierce RIPA buffer (ThermoFisher Scientific) containing EDTA-free Protease Inhibitor Cocktail (Roche). Excised tissue was snap-frozen in liquid nitrogen and homogenised in 10 µl per mg tissue of the same buffer using a Precellys homogeniser (Bertin Instruments). The solution was then agitated on an end-over-end shaker at 4°C for 30 minutes. The lysed cells and homogenised tissue were then centrifuged at 21,000g for 20 minutes at 4°C. Protein content was quantified using a Direct Detect Infrared Spectrometer (Merck).

3.3.4 Western blots

For the western blots, 30-35 µg protein were mixed with LDS Sample Buffer (4X) (NuPAGE) and Sample Reducing Agent (10X) (NuPAGE). The protein samples were then denatured at 70°C for 10 minutes, before being loaded onto a NuPAGE™ 4-12% Bis-Tris precast polyacrylamide gel (8 x 8 cm) (ThermoFisher Scientific) or onto a Bolt™ 4-12% Bis-Tris Plus Gel (ThermoFisher Scientific), which was run with MES (2-(N-morpholino)ethanesulfonic acid) buffer (2.5 mM MES, 2.5 mM Tris Base, 0.005% SDS, 0.02 mM EDTA, pH 7.3) or MOPS (3-(N-morpholino)propanesulfonic acid) buffer (2.5 mM MOPS, 2.5 mM Tris Base, 0.005% SDS, 0.02 mM EDTA, pH 7.7) at 60 V for 30 minutes and then at 120 V for a further 90 minutes. The protein marker used was the Precision Plus Protein All Blue marker (BioRad).

Following gel electrophoresis, the proteins were transferred onto a nitrocellulose membrane using either dry transfer (iBlot 2 Dry Blotting System (Thermofisher)) or wet transfer (in 10% Methanol containing transfer buffer (NuPAGE)). The membranes were blocked in Odyssey Blocking Buffer (Licor) or 5% Milk for 1 hour with gentle shaking at room temperature. Following blocking, primary antibody diluents were prepared in Odyssey Blocking Buffer

(Licor) with 0.2% Tween-20 or in 5% Bovine Serum Albumin in Tris Buffered Saline with 0.1% Tween-20. The primary antibodies used were:

1. Rabbit BCAT1 Antibody (#12822 CST) at a 1:1000 dilution
2. Rabbit BCAT2 Antibody (#9432 CST) at a 1:1000 dilution
3. Rabbit c-Myc Antibody (#9402 CST) at a 1:1000 dilution
4. Rabbit FOXM1 Antibody (#5436 CST) at 1:1000 dilution
5. Rabbit Hexokinase II Antibody (#2867 CST) at 1:1000 dilution
6. Mouse S6 Antibody (#2317 CST) at 1:1000 dilution
7. Rabbit PS6 antibody (#4858 CST) at 1:2000 dilution
8. Rabbit COX-IV antibody (#4850 CST) at 1:2000 dilution
9. Mouse HIF-1a antibody (ab16066 Abcam) at 1:1000 dilution
10. Rabbit CAIX antibody (NB100-417) at 1:1000 dilution
11. Mouse GAPDH (G8795 SIGMA) at a 1:25000 dilution
12. Mouse beta actin (A5441 SIGMA) at a 1:5000 dilution
13. Rat Beta Tubulin (ab6160-100 Abcam) at 1:2000 dilution

The membrane was incubated with primary antibodies overnight, with gentle shaking, at 4^{o}C and was then washed three times for 5 minutes each time with Tris Buffered Saline (TBS) containing 0.1% Tween 20 before incubation with secondary antibodies.

For fluorescent detection, the membrane was incubated with IRDye 800CW Goat anti-Rabbit IgG (Licor) and IRDye 680LT Goat anti-Mouse IgG antibodies (Licor) for 45 minutes – 1 hour, with gentle shaking, at room temperature. For chemiluminescent detection, the membrane was incubated in Goat Horseradish Peroxidase (HRP) – conjugated secondary antibodies (Cell Signalling Technology and Amersham) for 1 hour. Following three washes, 5 minutes each, with TBS containing 0.1% Tween 20 and a final wash with TBS, the membranes were imaged using a LiCor Clx scanner for fluorescent detection and analysed using Image Studio (Licor). For chemiluminescent detection, Pierce ECL Plus Western Blotting Substrate (ThermoFisher Scientific) was added to the membranes, which were then imaged using a standard film processor. The films were then scanned and analysed on ImageQuant (GE Healthcare Life Sciences).

3.3.5 Immunohistochemistry

For immunohistochemical analysis, rat brains were dissected and fixed in 10% neutral buffered formalin for 24 hours and submitted in 70% ethanol to the Histopathology core in CRUK Cambridge Institute for Formalin Fixed Paraffin Embedded (FFPE) processing. Sections were cut from these blocks at the level of the frontal lobe, where the tumour was visible. IHC was run on Leica's Polymer Refine Detection System on the Bond-III platform. The antibodies used for staining and their respective conditions are summarised in the table below.

Target	Catalogue No.	Dilution/Conc.	Retrieval
BCAT1 (hu)	Proteintech, 13640-1-AP	4.07 µg/ml	Sodium Citrate, 20'
CAIX (hu)	BioScience Slovakia, AB1001	1:1000	Sodium Citrate, 20'
MCT1 (hu)	Atlas, HPA003324	1:500	Tris EDTA, 20'
MCT4 (hu)	Atlas, HPA021451	1:500	Tris EDTA, 20'

3.3.6 Normoxia vs Hypoxia experiments

For investigating the effects of hypoxia *in vitro*, cells were seeded on 100 mm diameter dishes. For normoxia experiments, the cells were incubated in 5% CO_2 at 37°C in a Heracell incubator (Thermofisher). For hypoxia experiments, the cells were incubated in a Tri-Gas incubator set at 1% O_2, 5% CO_2 and 37°C or in a hypoxia chamber set at 0.1% O_2, 5% CO_2 and 37°C for at least 72 hours.

3.3.7 *IDH1* and *IDH2* sequencing

DNA was extracted from cell pellets using the Purelink Genomic DNA Mini Kit (Invitrogen) and eluted in H_2O and quantified using a spectrophotometer. Genomic DNA (1000 ng) from each cell line was used for a PCR reaction, along with 25 µl Taq 2X Master Mix (New England Biolabs), 1 µl of each forward and reverse primers (0.2 µM final concentration) and H_2O to 50 µl total reaction volume. The specific primers used for amplification of *IDH1* and *IDH2* were:

IDH1

Forward: 5'- TGG CAC CAT ACG AAA TAT TCT GG -3'

Reverse: 5'- TCA TAC CTT GCT TAA TGG GTG TAG -3'

IDH2

Forward: 5'- GTG GGA CCA CTA TTA TCT CTG TC -3'

Reverse: 5'- CTG CGG GGA AGT TGT ACA CT -3'

Thermocycling conditions included an initial denaturation step at 95°C for 30 seconds, followed by 40 cycles of 30 seconds at 95°C, 45 seconds of annealing at 51°C and 20 seconds of extension at 68°C. Following a final extension step at 68°C for 5 minutes, the PCR products were cooled to 4°C and stored at -20°C. The PCR products were run on a 2% agarose Size-Select gel (Invitrogen) using E-gel Power Snap equipment (Invitrogen), to confirm the purity of the product. The PCR products were subsequently purified using the ExoSAP-IT PCR Product Cleanup Kit (ThermoFisher Scientific) and were sequenced by GATC (Eurofins Genomics), using the same primers as for amplification.

3.3.8 Cell protein extraction for enzyme assay

For enzyme assays, cells and fresh frozen tissue were used. Cells were harvested by centrifugation. About 80 µl per 10^6 cells of cold lysis buffer (50 mM HEPES, 1 mM EDTA, 0.7 % sodium deoxycholate, 1 % Nonidet P-40, 0.5 M lithium chloride, pH 7.6 with EDTA-free Protease Inhibitor Cocktail (Roche)) was used to resuspend the pellet. Tissue (subcutaneous tumour or brain sample) was resected and snap-frozen in liquid nitrogen. Ten µl of cold lysis buffer was added per mg of tissue and the tissue was homogenised in a Precellys homogeniser.

In both cases, the solution was then agitated on an end over end shaker for 30 minutes at 4°C, followed by centrifugation at 21,000g for 20 minutes at 4°C. Protein content was quantified using a Direct Detect Infrared Spectrometer (Merck), which uses Mid-Infrared Spectroscopy and integrates the amide band in the absorbance spectrum.

3.3.9 Spectrophotometric BCAT Assay

The assay described in Cooper et al[158] was optimised for measuring BCAT activity in cell and tissue extracts. In summary, the reaction contained 5 mM leucine, 5 mM α-KG, 5 mM ammonium sulphate, 0.05 mM NADH, 0.5 mM GTP, 1 mM DTT, 1.9 U leucine dehydrogenase and 5 µl to 20 µl of cell extract in 100 mM potassium phosphate buffer (pH 7.4) in a final volume of 200 µl. All reagents were purchased from Sigma Aldrich except leucine dehydrogenase, which was purchased from Merck. All reagents except α-KG were added to the

wells of a UV transparent 96 well plate (Corning), which was incubated at 37ºC, and the reaction initiated by addition of α-KG. Absorbance at 340 nm was measured every 30 seconds to 1 minute for about 45 minutes at 37ºC in a Pherastar or Clariostar microplate reader (BMG Labtech). For every extract, a control with no leucine dehydrogenase was measured.

3.3.10 Competitive inhibition of BCAT1 *in vitro*

Gabapentin, purchased from Sigma-Aldrich, was dissolved in potassium phosphate buffer (100 mM, pH 7.4) to give a 400 mM stock solution. 4-methyl-5-oxohexanoic acid, purchased from Chemspace, was dissolved in potassium phosphate buffer (100 mM, pH 7.4). The reaction mixture for the BCAT spectrophotometric assay was prepared as described earlier, with slight modifications. Varying volumes of gabapentin or 4-methyl-5-oxohexanoic acid were added to give the required final inhibitor concentrations (0, 5, 10, 20, 40 mM). Appropriate volumes of potassium phosphate buffer were added to each reaction mixture to ensure equal total volumes of 200 µl. The reduction in NADH absorbance at 340 nm was measured.

3.3.11 Reverse Transcriptase Quantitative PCR

RNA extraction of frozen cell pellets was performed using the Qiagen RNA isolation kit (RNeasy Mini Kit). RNA was quantified using the Qubit RNA BR Assay Kit. A mixture of 1 µg of the RNA sample, 2 µl of 50 µM oligo dT solution, 1 µl of 10 µM dNTP solution and the appropriate volume of nuclease free water to make a 17 µl volume, was incubated at 65ºC for 10 minutes. Upon addition of M-MuLV Reverse Transcriptase (NEB) and M-MuLV Buffer (NEB), as stated in the manufacturer's protocol, the solution was incubated at 42ºC for 1 hour, 65ºC for 10 minutes and was then placed on ice. The resulting cDNA solution was stored at -20ºC. For qPCR, the following oligonucleotides were used as primers:

BCAT1 Forward: 5' CTGCCCCAGGTCTTGCTG 3'

BCAT1 Reverse: 5' TGCAATCCTTCATTGTTCCGTC 3'

BCAT2 Forward: 5' GGGCAGATCTGGGCACG 3'

BCAT2 Reverse: 5' GTCTGCAGCCTTGAAACTGG 3'

Beta-Actin Forward: 5' CGCCCTATAAAACCCAGCGG 3'

Beta-Actin Reverse: 5' GCGCGGCGATATCATCATCC 3'

Each reaction contained 10 µl Fast SYBR Green master mix (Applied Biosystems), 200 nM forward and reverse primers, 20 ng cDNA and nuclease free water, in a total volume of 20 µl. The thermal cycling conditions used were an enzyme activation step at 95°C for 20 seconds, followed by 40 cycles of a denaturation step at 95°C for 1 second and an annealing/extension step at 62°C for 20 seconds. Then, for the Melt Curve Stage, the plate was incubated at 95°C for 19 seconds, at 62°C for 1 hour and then at 95°C for 15 seconds. The data were then analysed using the QuantStudio software (Applied Biosystems).

3.3.12 Quantification of Branched Chain Amino Acids in plasma samples

3.3.12.1 Collection of plasma from rats

Rats (healthy and tumour-bearing) were fasted for five hours before blood collection. The rats were restrained manually, the tail vein punctured using a needle and 20-50 µl of blood was collected in an EDTA-coated tube (BD) and immediately placed on ice. The samples were then centrifuged at 2000 g for 10 minutes and the plasma transferred to an Eppendorf tube and stored at -20°C until analysis.

3.3.12.2 Branched Chain Amino Acid assay

For quantification of BCAA concentrations in the plasma samples, Abcam's BCAA Assay kit was used, following the manufacturer's protocol. The kit uses an enzyme assay in which BCAAs are deaminated producing NADH which then reduces a substrate to generate a coloured product which absorbs at 450 nm. Increasing volumes of leucine stock solution were added to wells of a 96-well plate to make 0, 2, 4, 6, 8 and 10 nmol/well standard samples. 5-20 µl of plasma sample was used for the assay and the total volume of the standard and test samples was adjusted with assay buffer to 50 µl. To each well, 50 µl of a mixture of the enzyme and substrates was added. For background subtraction of endogenous NADH and NADPH, samples were also mixed with a background control mixture which lacked the enzyme. The plate was incubated at room temperature for 30 minutes before measuring the absorbance on a plate reader (Clariostar, BMG Labtech).

3.3.13 *In vitro* ^{13}C leucine labelling experiment

[1-^{13}C]leucine (Sigma-Aldrich) was used to quantify the label exchange between leucine and ketoisocaproate. Cells were seeded at 70-80% confluency in T75 flasks in DMEM BCAA-free media. For media formulation, amino acid free DMEM media (Genaxxon) was used and supplemented with glutamine and non-essential amino acids as well as the growth factors B27, N2, FGF, EGF. [1-^{13}C]leucine was added at a final concentration of 0.8 mM. The cells were incubated at 37^{o}C, in 5% CO_2 for 48 hours before metabolite extraction. For metabolite extraction of cell media, the media was collected and added to 20 ml of cold methanol, followed by centrifugation at 21000 g for 5 minutes at 4^{o}C. The extracts were then dried in a nitrogen stream and lyophilised overnight. They were then dissolved in D_2O containing TMSP at a final concentration of 20 mM and proton decoupled ^{13}C NMR spectra were acquired at 14 T using the following parameters: 6000 scans, 249 ppm spectral width, 1.7 sec acquisition time, 12 sec delay time, 90^{o} flip angle.

3.3.14 Extracellular glutamate quantification

For quantification of glutamate levels in the cell media, the Promega GlutamateGlo assay was used, following the manufacturer's instructions. Cells (2 x 10^4) were seeded in each well of a 96 well plate with 100 µl of fresh Neurobasal medium. The cells were incubated for 18 hours, before collecting the media and quantifying the glutamate in it using the GlutamateGlo assay in a white plate.

3.3.15 BCAT1 and BCAT2 knockdowns

3.3.15.1 Lentiviral plasmid generation

Two plasmids were used for the generation of stable BCAT1 knockdowns in the A11 patient-derived glioblastoma cell line. pLKO.1 - TRC cloning vector was a gift from David Root[159] (Addgene plasmid # 10878; http://n2t.net/addgene:10878; RRID:Addgene_10878) and pLKO.1-Tet-OnTet-pLKO-puro was a gift from Dmitri Wiederschain[160] (Addgene plasmid # 21915; http://n2t.net/addgene:21915 ; RRID:Addgene_21915).

The plasmids were digested using AgeI (New England BioLabs) and EcoRI (New England BioLabs), as stated in the manufacturer's protocol. Five µg PLKO.1 vector was digested with 1 µl of each enzyme and 5 µl CutSmart buffer was used in a total volume of 50 µl. Control

reactions with both or either of the two enzymes missing were also performed. The reaction mixtures were incubated at 37°C for 2 hours, followed by an inactivation step at 65°C for 5 minutes.

The restriction digest products were then mixed with DNA Gel Loading Dye (6X) (ThermoFisher Scientific) and run on a 1% Agarose TAE gel containing SYBR™ Safe DNA Gel Stain (ThermoFisher Scientific) at 80V for one hour. The band corresponding to the digested vector backbone was extracted and purified using the PureLink® Quick Gel Extraction Kit (ThermoFisher Scientific) and quantified on a Nanodrop Spectrophotometer.

The shRNA oligos used for BCAT1 knockdown were as described in Tonjes et al[51]:

shBCAT1 Forward:

5' - CCGGCCCAATGTGAAGCAGTAGATACTCGAGTATCTACTGCTTCACATTGGGT TTTT - 3’

shBCAT1 Reverse:

5’ - AATTAAAAACCCAATGTGAAGCAGTAGATACTCGAGTATCTACTGCTTCACA TTGGG - 3’

The shRNA oligos used for BCAT2 knockdown were:

shBCAT2 Forward:

5’ - CCGGACTACAAGTTAGGTGGGAATTCTCGAGAATTCCCACCTAACTTGTAGTT TTTTG - 3’

shBCAT2 Reverse:

5’ - AATTCAAAAAACTACAAGTTAGGTGGGAATTCTCGAGAATTCCCACCTAACT TGTAGT - 3’

In addition to these, for a non-targeting shRNA control the following oligos were used:

shCtrl Forward:

5’ - CCGGCCTAAGGTTAAGTCGCCCTCGCTCGAGCGAGGGCGACTTAACCTTAGG - 3’

shCtrl Reverse:

5’ – AATTCCTAAGGTTAAGTCGCCCTCGCTCGAGCGAGGGCGACTTAACCTTAGG - 3’

The forward and reverse oligos were resuspended in nuclease-free water to give a 100 µM solution. 1 µl of each of the forward and reverse oligos were mixed with 48 µl of annealing buffer (100 mM NaCl in 50 mM HEPES pH 7.4) in Eppendorf tubes, which were placed in a beaker containing boiling water and incubated overnight to cool down slowly.

The annealed oligos were diluted (1:100) in annealing buffer and the ligation reaction between the annealed oligos and the digested vector was set up as follows: 20 ng of the digested vector was mixed with 2 µl ligase buffer (New England BioLabs), 1 µl T4 DNA ligase enzyme (New England BioLabs), 1 µl of the annealed oligos and nuclease-free water in a total volume of 20 µl. The reaction was incubated at room temperature for two hours followed by an enzyme inactivation step at 65^{o}C for 5 minutes.

Thirty µl of One Shot™ Stbl3™ Chemically Competent *E. coli* (ThermoFisher Scientific) were transformed with 1 µl of the ligated product. The bacteria were mixed with ligated product and placed on ice for 15 minutes. They were then heat-shocked for 45 seconds at 42^{o}C and placed on ice for a further two minutes. S.O.C. (Super Optimal Broth with Catabolite repression) medium (250 µl) was added to the bacteria and the mixture was shaken at 37^{o}C for about two hours and then spread on a LB plate containing Ampicillin and incubated overnight.

Colonies from each plate were inoculated in an overnight culture in 5 ml LB Ampicillin (0.1 mg/ml) and the DNA extracted using the QIAprep Spin Miniprep Kit and sequenced by GATC (Eurofins Genomics), using primers:

PLKO.1 Sequencing primer:

5’ CAA GGC TGT TAG AGA GAT AAT TGG A 3’

TetON-PLKO.1 Sequencing primer:

5’ GGC AGG GAT ATT CAC CAT TAT CGT TTC AGA 3’

Colonies with the correct sequence were inoculated in 2 ml LB supplemented with ampicillin (0.1 mg/ml) for 2 hours and then overnight in 200 ml LB supplemented with ampicillin (0.1 mg/ml). DNA was extracted from the bacterial cultures using QIAprep Spin Maxiprep Kit.

3.3.15.2 HEK 293 cell transfections

HEK 293 cells were seeded in 10 cm culture dishes and grown to almost confluency. For each transfection reaction, 80 µl Lipofectamine™ 3000 Transfection Reagent were mixed with 500 µl serum-free DMEM media in an Eppendorf tube. In a second Eppendorf tube, 7.5 µg psPAX2, 2.5 µg D2G and 10 µg of the lentiviral plasmid were mixed with 500 µl serum-free DMEM media. psPAX2 and pMD2.G were gifts from Didier Trono (Addgene plasmid # 12260; http://n2t.net/addgene:12260; RRID:Addgene_12260 and Addgene plasmid # 12259; http://n2t.net/addgene:12259; RRID:Addgene_12259).

The diluted transfection reagent mixture was then added to the plasmid mixture and following brief vortexing, the solution was incubated at room temperature for 30 minutes. The HEK 293 cells were washed with PBS and 4 ml fresh serum-free DMEM media were added. The transfection reagent and plasmid solution were added to the cells, which were then incubated at 37ºC overnight. Five ml fresh DMEM media supplemented with FBS were added to the cell cultures the following morning and incubated for a further 30 hours. The cell medium, containing viral particles, was then collected in 15 ml Falcon tubes and centrifuged at 1500 g for 3 minutes. The supernatant was passed through a 0.45 µm filter to remove any cells and stored at -20ºC.

3.3.15.3 PDX glioma cell infections

A11 PDX cells were seeded and grown to confluency in a 6-well plate. The viral particles were defrosted in a water bath at room temperature. The cells were washed with HBSS and 1 ml of fresh serum-free Neurobasal media (with no antibiotics) was added to each well followed by 8 µl of 5 mg/ml polybrene solution. One ml of the viral particle solution was then added to the cells. The virus containing media were removed 24 hours after the infection and 2 ml fresh serum-free Neurobasal media were added to the cells, which were incubated for a further 24 hours to enable recovery.

The infected cells were selected with puromycin (Gibco™ Puromycin Dihydrochloride), which was added to the media at a final concentration of 2 µg/ml. Fresh puromycin containing media

was added to the cells every 2 days, for 8 days, until the control cells were dead from puromycin toxicity. The selected cells were then grown, and stocks frozen for subsequent experiments.

For induction of BCAT1 and BCAT2 knockdown in the cells infected with the inducible knockdown construct, Doxycycline Hyclate (Sigma) was used at a concentration of 50 ng/ml for time periods ranging from 48 hours to 7 days.

3.3.16 BCAT1 overexpression

The coding region of human *BCAT1* was isolated from a GeneArt plasmid (Thermo Fisher Scientific), by restriction digestion using BamHI (NEB) followed by gel extraction and purification. The BCAT1 coding region was then ligated onto an EF1 plasmid backbone at an insert to vector ratio of 3:1 and the ligated product was used to transform Stbl3 bacteria. The plasmid was isolated from the bacterial culture and sequenced to confirm the presence of the correct coding sequence for BCAT1.

HEK293 cells were transfected as described in section 3.3.2 using pMDL packaging plasmid (Addgene #12251), pCMV-VSV-G envelope vector (Addgene #8454) and pRSV-Rev (Addgene #12253). Lentiviral isolation and infection of GBM cells were performed as described in section 3.3.3.

Cells that were successfully infected with the lentivirus and hence expressed mStrawberry, were FACS sorted into a 6-well plate and expanded to form BCAT1 overexpressing cell lines or luciferase overexpressing control cell lines.

3.3.17 Cell proliferation assays

3.3.17.1 Measuring confluency over time

The rate of cell proliferation was quantified using an Incucyte Live Cell Analysis System (Essen BioScience). Equal numbers of cells were seeded in 6-well, 48-well or 96-well plates in 1000, 250, and 100 µl of growth medium, respectively. The plates were incubated in 5% CO_2 at 37^{o}C in the Incucyte. Phase contrast images were taken every 3 hours until the cells reached 100% confluency. For assessing cell death, Incucyte Cytotox Red Reagent (Essen BioScience) at a final concentration of 250 nM was also added to the medium and dead cells were imaged using the red fluorescence lasers on the Incucyte. Cell proliferation was measured using the %

confluence mask of the Incucyte Cell Analysis software, while cell death was monitored using the Red Object Count per mm^2.

3.3.17.2 Measuring cell number over time

For assessing the proliferation rate of the cells in terms of the increase in cell numbers over time, cells were seeded in 6-well plates at a starting density of 100 000 cells/well with 2 ml of media. Cells were collected at different timepoints and the number of viable cells as well as the percentage viability were measured using the Vi-Cell (Beckman Coulter).

3.3.17.3 Luciferase based assay

A luciferase assay (RealTime Glo, Promega) was performed to monitor the number of live cells over time in a 96 well plate, following the manufacturer's protocol. Briefly, 3000 live cells were seeded per well in an opaque white 96-well plate in 100 µl media containing 1X Nanoluc luciferase enzyme and 1X MT cell viability substrate. In a live cell, the MT cell viability substrate is reduced to the Nanoluc luciferase substrate which will then react in the presence of luciferase to produce a luminescent signal. The plates were incubated at 37ºC for 72 hours and luminescence was read on a plate reader (Clariostar, BMG Labtech) at different timepoints.

3.3.18 Cell Migration and Invasion Assays

3.3.18.1 Scratch Wound Assay for Cell Migration

For investigating cell migration, a scratch wound assay was used. Cells were seeded in a 96-well plate (Essen Bioscience, Image lock plate) at high density (40000-50000 cells per well) and grown to confluence before a scratch wound was made using the WoundMaker (Essen Bioscience). The cells were incubated in 5% CO_2 at 37ºC in the Incucyte and cell migration was monitored over three to four days, by recording images every 3 hours. The initial scratch wound mask was used to calculate relative wound density over time.

3.3.18.2 Scratch Wound Assay for Cell Invasion

For cell invasion assays, a similar setup was used as for cell migration. Once the scratch wound was made, the wound was filled with 50 µl Matrigel Growth Factor Reduced (Corning) and the

plate incubated at 37ºC for 30 minutes for the Matrigel to solidify. Media (100 µl) was then added in each well and the plate placed in the Incucyte.

3.3.18.3 Three-dimensional spheroid invasion assays

For a better representation of glioblastoma invasion, the glioblastoma cells were grown as neurospheres. This was achieved either by using hanging drop cultures, or by seeding the cells in Ultra Low attachment 96-well plates (4000 cells/well), as described in the tumour spheroid invasion assay protocol[101].

For the hanging drops, droplets of 30-50 µl of a 10^6 cells/ml cell suspension were deposited on the lid of a 10 cm dish and incubated for 4 days, for the spheroids to form. The droplets were then collected, centrifuged at 300 g for 5 minutes, resuspended in a 1:1 matrigel: collagen mixture and seeded in a 96- or 48-well plate. The spheroid-containing wells were then imaged on a Zeiss Live cell imaging microscope.

In Ultra Low attachment 96-well plates, glioblastoma cells self-assembled into uniformly sized spheres. The spheres were grown for two days. On the day of the invasion assay, 100 µl of cold Matrigel was added on top of the neurospheres and the plates were incubated at 37 ºC for the Matrigel to solidify. Fresh media was then added on top of the Matrigel layer and the plates were placed in the Incucyte microscope for images to be taken at 3-hour intervals over four days.

For manual image analysis Fiji (ImageJ) software was used to draw regions of interest and measure parameters such as sphere area and diameter, total area covered by cells, distance of invading cells from the sphere at different timepoints. For automated analysis of the Incucyte data, the images were exported and analysed using a Python script. The algorithm used implemented established contrast enhancement (Contrast Limited Adaptive Histogram Equalization), denoising (Non-local means denoising) and thresholding tools. The areas containing cells were identified by measuring the standard deviation within small contiguous regions. To distinguish between the invaded area and the spheroid area, regions of interest around the spheroids were drawn.

3.3.19 Flow cytometry experiments

3.3.19.1 Cell surface expression of CD147

For assessing cell surface expression of CD147, approximately 1 million cells were collected using Accutase (Gibco, StemPro) and stained with Alexa Fluor 647 anti-CD147 antibody (BioLegend) at a dilution of 1:100 in Flow cytometry staining buffer (3% FCS, 0.05% Sodium Azide in PBS) for 30 minutes at 4^{o}C. Following three washes with staining buffer, DAPI (5 µg/ml) or Propidium Iodide (200 ng/ml) were added to the cells, which were filtered and analysed using an LSRII Flow Cytometer. For data analysis FlowJo software was used, where dead cells were excluded and the median fluorescence intensity of live cells bound to CD147 antibody was measured.

3.3.19.2 Cell Cycle Analysis

For cell cycle analysis of the BCAT1 knockdown A11 cells, following 6-day long doxycycline treatment for knockdown induction, approximately 1 million cells were harvested using Accutase, washed with PBS and fixed in 4.5 ml of ice cold 70% ethanol for at least 2 hours at 4^{o}C. The fixed cells were kept at -20^{o}C until stained and analysed.

For synchronizing the cells before fixation, a double thymidine block protocol was used[161]. Equal number of cells (around 500 000) were seeded in 6 well plates and allowed to attach overnight. Cells were then incubated with 2 mM thymidine for 18 hours, fresh media for 9 hours and another dose of 2 mM thymidine for 18 hours. After the second thymidine incubation, the synchronized cells were released and collected at different timepoints for fixation.

For staining, the fixed cells were centrifuged for 5 minutes at 300 g and the pellets were washed with PBS. Following centrifugation, the pellets were resuspended in 600 µl of Propidium Iodide Staining Solution (0.1% Triton X, 2 mg RNAse, 20 mg/ml Propidium Iodide in PBS) and incubated at 37^{o}C for 15 minutes with gentle shaking. The cells were then filtered and analysed on an LSRII (BD) flow cytometer, without any washing steps.

The cell cycle fitting algorithm in the FlowJo software was used to analyse the cell cycle distribution.

3.3.19.3 Cell death assessment

For assessing cell death, cells were harvested using Accutase treatment and washed with HBSS. Following centrifugation at 1000 g for 3 minutes, they were washed once in flow cytometry staining buffer and centrifuged again. The pellets were resuspended in 100 µl Sytox Green (Invitrogen) at 100 nM final concentration and the cell suspension mixed for 10 minutes at 37^{o}C. The cells were then washed in 400 µl flow cytometry staining buffer and finally resuspended in 500 µl buffer for flow cytometry analysis on a FACSymphony (BD) cytometer.

3.3.20 Cell irradiation

For radiotherapy experiments, cells were seeded in 6 well plates and irradiated using a caesium gamma ray irradiator (IBL 637). Irradiation time was varied to adjust the total desired dose in Gy.

3.3.21 Limiting Dilution Assay

For determining the neurosphere formation capacity of GBM cells, a limiting dilution assay was performed. Inducible shScr and shBCAT1 expressing A11 cells were treated with doxycycline for 6 days. They were then harvested by Accutase treatment and centrifugation, washed with PBS, resuspended in 600 µl PBS, filtered and placed in BD Flow Cytometry tubes. DAPI was added to each cell suspension at a final concentration of 5 µg/ml. Live cells were then sorted on an Influx cell sorter (BD) by excluding the DAPI positive cells. For each cell sample, 1, 5, 10 and 20 cells were seeded per well in a 96 well plate containing complete Neurobasal Media with or without doxycycline. The cells were then allowed to grow for 3-4 weeks with no media changes or further doxycycline treatment. At the endpoint, the number of neurosphere-containing wells per group was counted and the data analysed using the Extreme Limiting Dilution Analysis (ELDA) software[95].

3.3.22 RNA sequencing

The inducible BCAT1 knockdown constructs were used to investigate the transcriptional changes upon doxycycline-induced BCAT1 knockdown. A11shBCAT1 and A11shScr cells were treated with doxycycline or were kept as controls for 7 days, before harvesting them and extracting RNA using a RNeasy Mini Kit (Qiagen). RNA was quantified and quality tested using the Agilent 4200 TapeStation system. BCAT1 knockdown was confirmed on qPCR,

before submitting the samples for RNA sequencing analysis in the Genomics Core Facility at CRUK Cambridge Institute. For library preparation, the Illumina Truseq stranded mRNA kit was used, and single read sequencing was performed on a HiSeq 4000 machine (Illumina).

The RNA sequencing results were processed by the Bioinformatics core facility who performed quality checks and generated a list of differentially expressed genes. For gene enrichment analysis, online tools including Metacore (Clarivate analytics) and EnrichR[162,163] were used.

3.3.23 Alpha-ketoglutarate quantification

3.3.23.1 Fluorometric Assay

For quantification of intracellular α-KG the fluorometric Alpha Ketoglutarate assay kit (Abcam) was used and the protocol slightly modified to increase the sensitivity of the assay. Cells were grown to 70-80% confluency in T75 flasks to give a cell number of greater than five million cells per sample. For metabolite extraction, all steps were performed on ice. The flask was placed on ice, the cell media was aspirated, and the cells washed with PBS and any remaining PBS aspirated. Perchloric acid (100 µl, 2M) was added directly on the cells and a cell scraper used to detach the cells. The extract was mixed for 10 minutes at 4°C and centrifuged at 21,000 g for two minutes at 4°C. The pH was then adjusted to 7 by addition of KOH (5M) before the extract was centrifuged again at 21,000 g for 10 minutes at 4°C. The supernatant was then used for analysis using the assay instructions provided by Abcam in a 96 well black plate. In this assay, α-KG is transaminated with the generation of pyruvate which is used to convert a colourless probe to a fluorescent product. Fluorescence was measured using the Clariostar microplate reader (BMG Labtech).

3.3.23.2 Liquid Chromatography Mass Spectrometry

For a more accurate measurement of intracellular α-KG concentration, liquid chromatography mass spectrometry (LCMS) was used. Cells were seeded in 6-well plates and treated with doxycycline or kept as controls for four days. Cell number and cell volume were quantified on the day of the extraction, using one of the wells for each condition on a CASY cell analyser. For metabolite extraction, the plates were placed on ice, the media was aspirated and the cells were washed with PBS twice. Extraction solution (500 µl of 50% Methanol, 30% Acetonitrile, 20% Ultrapure Water, d8-Valine at a final concentration of 5 µM per million cells) was added to each well and the plates incubated on dry ice for 15 minutes. Cells were scraped from the

wells, transferred to pre-cooled Eppendorf tubes and agitated at maximum speed for 15 minutes at 4ºC. The extracts were then incubated for 1 hour at -20ºC, vortexed and centrifuged at 21,000 g for 10 minutes at 4ºC. The supernatant was transferred to autosampler vials, which were submitted for LCMS Analysis at the Frezza Lab (MRC Cancer Unit).

3.3.24 Global DNA methylation analysis

For quantification of relative cytosine, 5-methylcytosine and 5-hydroxymethylcytosine levels in cells, LCMS analysis was performed by the Pharmacokinetics and Bioanalytics core facility in the institute. Cells were harvested using Accutase detachment and centrifugation and DNA was extracted using a Purelink Genomic DNA Mini Kit (Invitrogen) following manufacturers' guidelines. For DNA degradation to 2-deoxynucleosides, up to 1 µg DNA was incubated with 5 units DNA Degradase Plus (Zymo Research) for four hours at 37ºC.

3.3.25 [2-^{13}C,^{15}N]leucine infusion experiment

[2-^{13}C,^{15}N]leucine infusions were performed to investigate the involvement of leucine in the TCA cycle and the fate of nitrogen in the tumours. A11shScr and A11shBCAT1 tumour-bearing mice were fed with a doxycycline-containing diet or vehicle diet for 7-10 days. For the infusion, they were anaesthetised and their tail vein cannulated. The infusion protocol consisted of a bolus injection of 300 mg/g body weight and a continuous infusion of 0.0069 mg/g body weight min^{-1} for 150 minutes using an infusion pump. At the end of the infusion, the mice were sacrificed by cervical dislocation followed by blood collection in EDTA coated tubes, dissection and flash freezing of the tumour and the contralateral hemisphere in liquid nitrogen. The blood samples were processed by centrifugation at 2000 g in Eppendorf tubes for 20 minutes to collect the plasma. Labelled leucine enrichment was measured in metabolite extracts of the plasma, tumour and contralateral brain samples by LCMS.

3.4 Results

3.4.1 Differential expression and activity of BCAT isozymes was observed across a panel of patient-derived glioblastoma cells

3.4.1.1 Protein levels in cell lysates

For studying the role of branched chain amino acid metabolism in glioblastoma, a panel of patient-derived glioblastoma cell lines was used, including: A11, S2, SP20 and A25. The commercially available human glioma cell lines U87 and U251 were also used for comparison, as well as a colorectal cancer cell line, Colo205. Western Blots were performed on whole cell lysates to assess the expression of BCAT1 and BCAT2 across the panel of cell lines with GAPDH or beta actin as loading controls. Differential BCAT1 and BCAT2 expression was observed across the different cell lines (Figure 24).

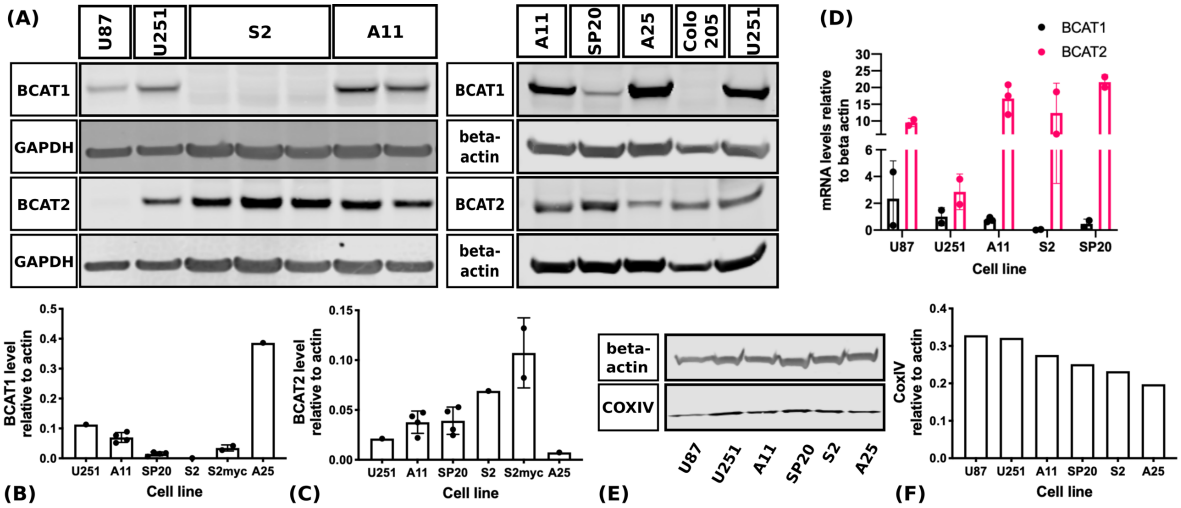

Figure 24 BCAT1 and BCAT2 expression in a panel of GBM patient-derived cells. *(A) Representative Western Blots of BCAT1 and BCAT2 in cell lysates, with GAPDH and beta-actin used as loading controls. Quantitative analysis of BCAT1 (B) and BCAT2 (C) protein expression across the panel of cell lines. Each point on the graphs corresponds to an independent experiment and error bars represent Standard Deviations.(D) BCAT1 and BCAT2 mRNA levels relative to levels of β-actin mRNA from 2 independent experiments. (E-F) Western Blot of CoxIV and beta-actin in cell lysates (E) and quantitative data from it.*

U87 which is an established cell line and was used here as a reference since it was used by Tönjes et al in their investigation of the role of BCAT1 in glioblastoma[51], showed moderate levels of BCAT1 expression and no BCAT2 expression. Of the patient-derived cell lines, A25 showed the highest BCAT1 expression, even higher than U87 and U251. A11 showed moderate BCAT1 expression and SP20 had lower levels of BCAT1 while S2 had the lowest levels of BCAT1, which were not detectable on a western blot.

BCAT2 protein levels showed an opposite pattern. U87 showed no detectable BCAT2. Of the patient-derived cell lines, A25 which had the highest BCAT1 levels showed the lowest expression of BCAT2, whereas S2 had high BCAT2 levels. A similar pattern was observed when measuring mRNA levels of *BCAT1* and *BCAT2*. Interestingly, mRNA levels of *BCAT2* were higher than those of *BCAT1* across all the cell lines and U87 had high levels of *BCAT2* mRNA even though this was not reflected in the levels of the protein.

In order to establish whether the differences in BCAT2 levels between cell lines were a result of different mitochondrial content in the cells, Western Blots for Cytochrome c oxidase subunit 4 (COX IV) were performed. BCAT2 levels were not correlated with mitochondrial content (Figure 24).

3.4.1.2 Protein levels in spheroid culture and xenograft lysates

Since protein expression is often highly dependent on the cell's environment, we assayed BCAT1 protein expression in two more models, which are more representative of human glioblastoma. We performed western blots on lysates of cells grown in spheroid culture, instead of a monolayer, and in lysates of tumours grown following intracranial implantation of the cells in athymic rats. The Western Blots indicated that the pattern of expression across the panel of cell lines persists in spheroid culture and in the orthotopic tumours, as shown in Figure 25. BCAT1 expression is higher in A11 cells grown as neurospheres than in monolayer culture and even higher in the tumours, which might be a result of BCAT1 upregulation in hypoxia as discussed later (Figure 31).

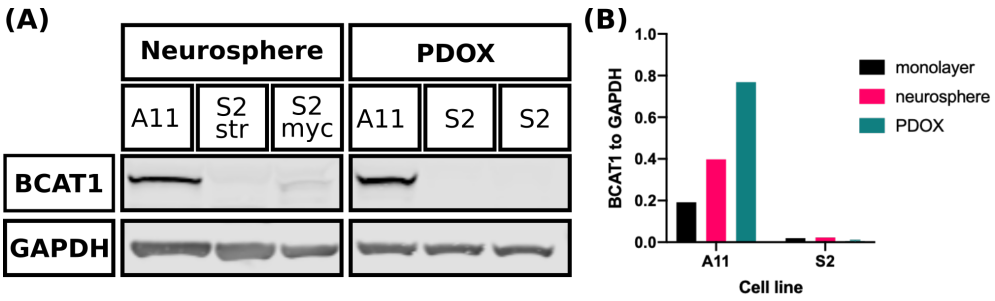

Figure 25 Western Blot of BCAT1 expression in spheroid culture and in orthotopic tumours*. Neurosphere lysates were generated from A11 cells and two genetically engineered clones of S2: S2myc which overexpresses c-Myc and S2strawberry which overexpresses mStrawberry. PDOX lysates were generated from tumours derived from A11 and S2 cells. (A) Western Blot for BCAT1, with GAPDH as a loading control (B) Quantitative expression data for monolayer culture, neurosphere culture and PDOXs derived from A11 and S2 cells. Abbreviations: PDOX: patient derived orthotopic xenograft.*

3.4.1.3 Immunohistochemistry

Immunohistochemical analysis was performed on sections from rat brain containing A11, S2 and SP20 PDOXs in order to observe the expression pattern of BCAT1 in these GBM models. S2 PDOXs showed minimal BCAT1 staining, in accordance with the Western Blot data. A11 and SP20 showed higher BCAT1 staining which was heterogeneous with some cells expressing more enzyme than others (Figure 26). SP20 tumours are highly heterogeneous and invasive and therefore histology on these sometimes reveals tumour cells dispersed through the normal brain parenchyma (Figure 26 G,I) and more rarely, a clear tumour mass containing mostly cancer cells can be seen (Figure 26 H).

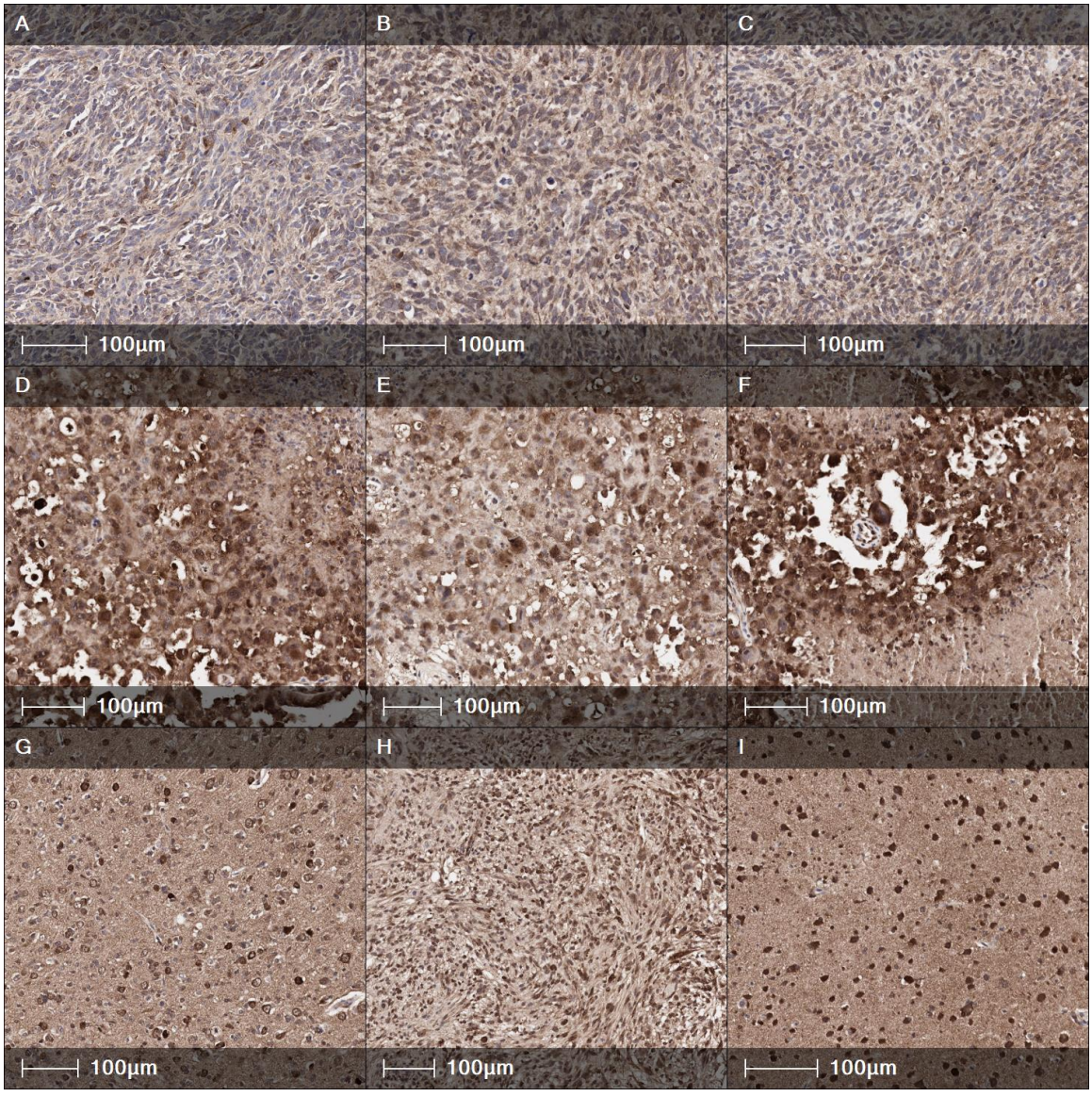

Figure 26 Immunohistochemical staining for BCAT1 in PDOXs in athymic rats. *Representative images of sections from S2 (A-C), A11 (D-F) and SP20 (G-I) tumours. Each image is from a different animal.*

3.4.1.4 S2 cells are IDHwt

BCAT1 has been shown to be downregulated in *IDH*mut GBM and upregulated in *IDH*wt GBM. DNA sequencing for *IDH1* and *IDH2* was performed on DNA extracted from S2 cells, confirming that they do not have *IDH* mutations (Figure 27).

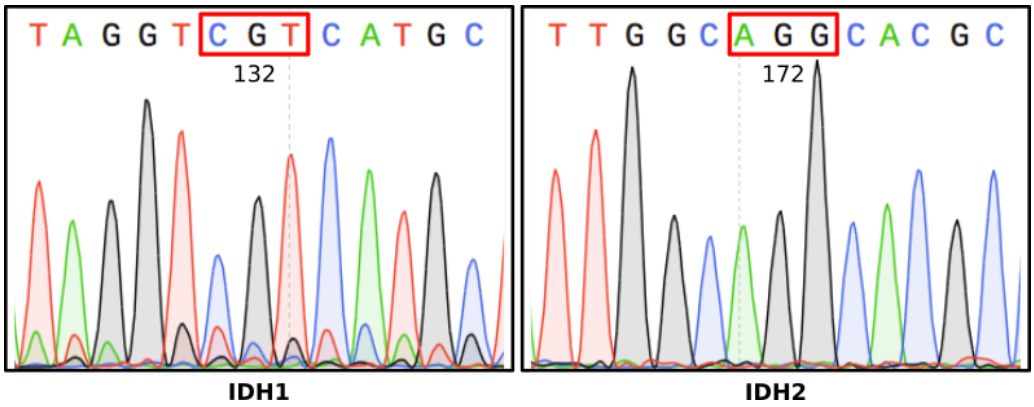

Figure 27 Sequencing of S2 cells revealed no mutation in codons 132 and 172 of the IDH1 and IDH2 genes, respectively.

3.4.1.5 Enzyme activity levels in cell extracts

Using a modified protocol for the coupled spectrophotometric assay developed by Cooper et al[158], the levels of total BCAT activity were measured in whole cell lysates of the glioblastoma primary cell lines and compared with established glioblastoma cell lines, including U87. An overview of the reaction is shown in Figure 28. This assay follows the conversion of L-leucine to its ketoacid, α-ketoisocaproate (KIC), via the transamination reaction catalysed by BCAT1 and BCAT2. In the presence of excess leucine dehydrogenase, any KIC produced will be converted to leucine, oxidising NADH. Therefore, by recording absorbance at 340 nm, which is a measure of the NADH concentration, and measuring the rate of decrease of NADH levels, the BCAT activity can be estimated. The limitation of this assay is the presence of glutamate dehydrogenase in the cell lysates, which can convert α-KG (present in the reaction mixture) to glutamate, also oxidising NADH. Therefore, the measured reduction in absorbance at 340 nm, is actually the result of the combined activities of BCAT1, BCAT2 and Glutamate Dehydrogenase. The addition of the no Leucine Dehydrogenase control, enabled us to measure the contribution of the glutamate dehydrogenase activity to the reduction in NADH levels[158]. By subtracting the rate of NADH oxidation in the reaction without Leucine Dehydrogenase from the rate of NADH oxidation in the full reaction, an estimate of the combined BCAT1 and BCAT2 activities in each cell lysate were obtained. These are illustrated in Figure 29.

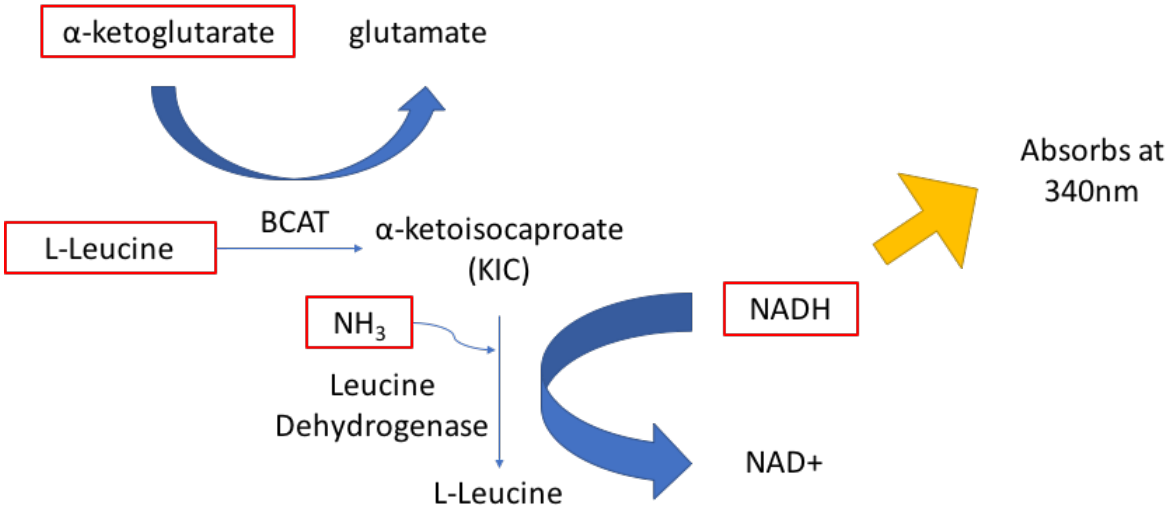

***Figure 28 Overview of the spectrophotometric assay**. In the presence of BCAT in the cell lysate, leucine will be converted to KIC while α-KG is converted to glutamate. An excess of leucine dehydrogenase will convert the KIC produced to leucine, using NADH. Decreases in NADH concentration are measured from the decrease in absorbance at 340 nm.*

The total BCAT activity was similar across most of the cell lines, at approximately 8 nmol NADH/minute/mg protein. A25 cells, which showed very high levels of BCAT1 on the western blots, had much higher total enzyme activity compared to the other cells.

To distinguish between the relative contribution of BCAT1 and BCAT2 towards the total activity measured by the spectrophotometric assay we used gabapentin, which is a competitive and selective inhibitor of BCAT1 but not BCAT2. Gabapentin was added at increasing concentrations (0 mM to 40 mM) to the assay in order to eliminate the activity of BCAT1 and thus enable measurement of the remaining BCAT2 activity. The decrease in NADH absorbance at 340 nm in the control samples, which is a measure of glutamate dehydrogenase activity, was not affected by gabapentin.

Figure 29B demonstrates inhibition of BCAT1 by increasing gabapentin concentrations in enzyme extracts. The pattern of enzyme activities measured across the panel of cell lines showed good agreement with the protein levels measured by Western Blot, indicating that the protein level is a good measure of the activity levels in the cells. For example, A25 cells, which showed the highest BCAT1 expression (Figure 24), also showed the highest reduction in enzyme activity following gabapentin treatment. S2 cells, on the other hand, which showed no BCAT1 expression on the western blot showed no reduction in the total activity upon gabapentin treatment. In addition, U87 cells showed no BCAT2 expression on western blot, which was confirmed by the very small residual BCAT activity upon BCAT1 inhibition with 40 mM gabapentin.

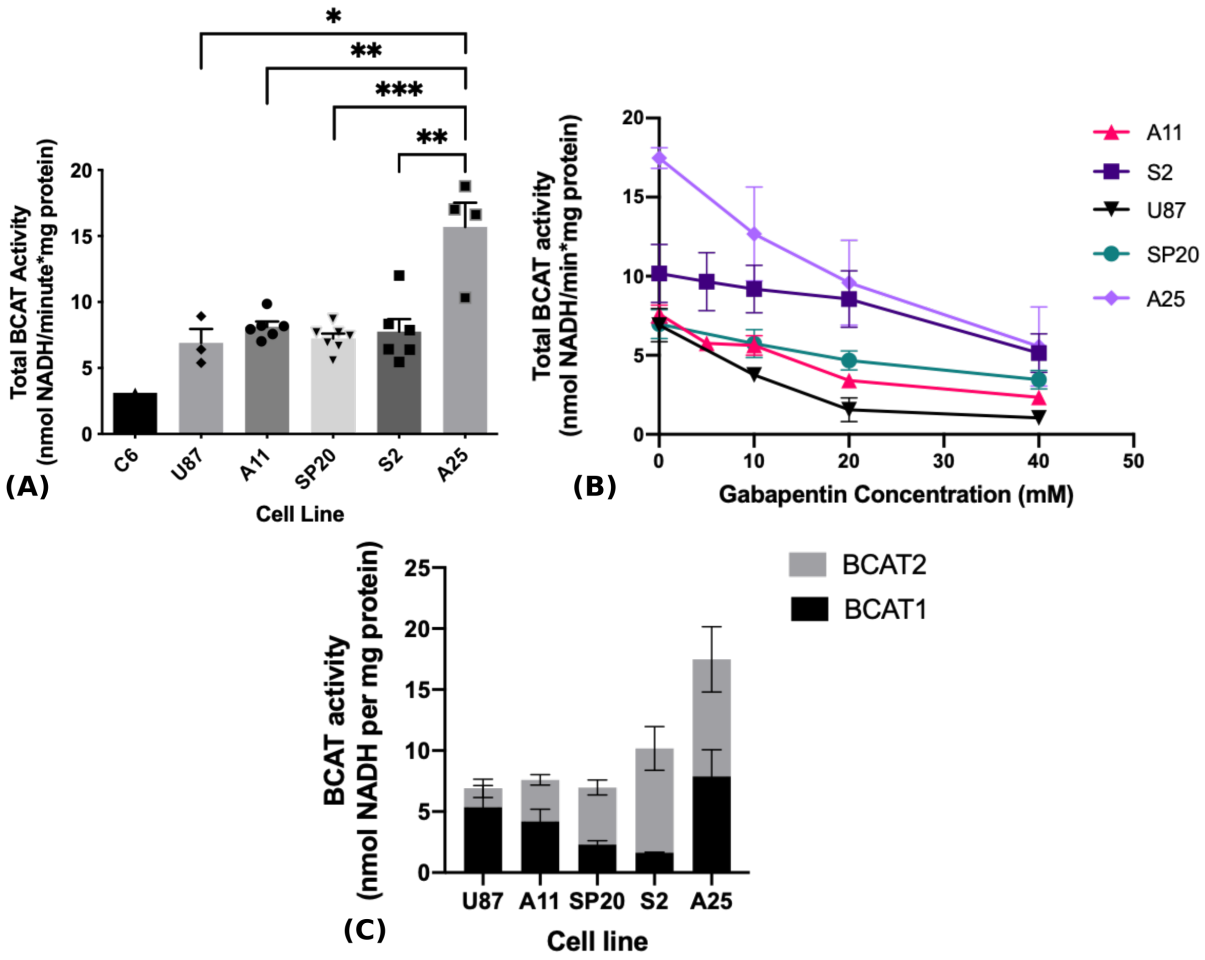

Figure 29 Measurement of BCAT activity in cell lysates using a spectrophotometric assay. *(A) The combined BCAT1 and BCAT2 activities were compared across the panel of patient-derived primary cells as well as the established human cell line, U87 and the rat cell line, C6.* Each point represents a different biological replicate. T*wo-tailed t-tests were performed to compare the total activities of different cell lines. *p<0.05, **p<0.01, ***p<0.001 (B) Total BCAT activity in cell lysates in the presence of increasing concentration of gabapentin. (C) The activity measured in the presence of 20 mM gabapentin is plotted as BCAT2 activity and the difference between the activity measured in the absence of gabapentin and the presence of 20 mM gabapentin is plotted as BCAT1 activity. Error bars represent Standard Error of the Mean (SEM).*

3.4.2 BCAT1 expression is regulated by c-Myc and hypoxia

3.4.2.1 c-Myc regulates BCAT1 expression

It has been suggested that c-Myc regulates BCAT1 expression[53]. To confirm this and to investigate the effect of c-Myc on BCAT2 expression, a genetically engineered clone of the S2 cell line, which overexpresses c-Myc, was used. Overexpression of c-Myc was confirmed in lysates of these cells by western blot (Figure 30). Although S2 cell lysates showed no BCAT1 protein, the lysates of S2myc cells, showed BCAT1 expression on western blots (Figure 30), confirming that BCAT1 expression is regulated by c-Myc, as suggested in the literature[53]. BCAT2 levels, on the other hand, were not affected by c-Myc overexpression (Figure 30). This is explained by the presence of a c-Myc binding element in its 5' unstranslated region and the

absence of c-Myc binding elements on BCAT2[164,165]. BCAT1 and BCAT2 are located on different chromosomes and while BCAT1 is known to play an important role in embryogenesis, organogenesis and in proliferating cells, BCAT2 is not documented to play the same role[164].

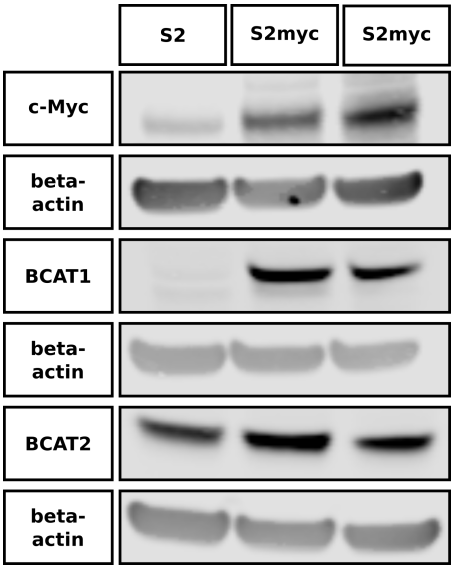

Figure 30 c-Myc affects BCAT1 but not BCAT2 expression in S2 cells*. Western Blots of BCAT1, BCAT2 and c-Myc as well as their beta-actin loading controls are shown for S2 and S2myc cell lysates.*

3.4.2.2 The effect of hypoxia on BCAT1, BCAT2 and c-Myc expression

The first intron of the human *BCAT1* gene includes a hypoxia response element and it has been suggested that expression of BCAT1 is regulated by HIF-1α[166]. To investigate the role of hypoxia in regulation of BCAT1 expression in glioblastoma, U251, A11 and SP20 glioblastoma cell lines were grown in hypoxia (1% O_2) and normoxia in 100 mm dishes and then harvested for protein extraction. Western blots of whole cell lysates of U251, A11 and SP20 demonstrated elevated levels of BCAT1 in cells grown under hypoxia compared to cells grown under normoxia (Figure 31). On the other hand, S2 cells grown at oxygen concentrations as low as 0.1% continued to show no BCAT1 expression (Figure 32). Hypoxia did not have an effect on BCAT2 levels, as shown by western blot (Figure 33). The western blots of c-Myc in A11 cells showed a significant reduction in c-Myc levels in A11 cells grown under hypoxia, compared to the cells grown under normoxia (Figure 33). No such effect was evident in the SP20 cell lysates, but these have lower baseline levels of c-Myc and quantitation was more difficult.

Therefore, the regulation of BCAT1 by HIF-1α has been confirmed in A11 and SP20 cells and the regulation by c-Myc has been confirmed in S2 cells. The dependence of A11 and SP20 cells

on c-Myc has not been investigated and the relative effects of c-Myc and HIF-1α in the cells are unknown.

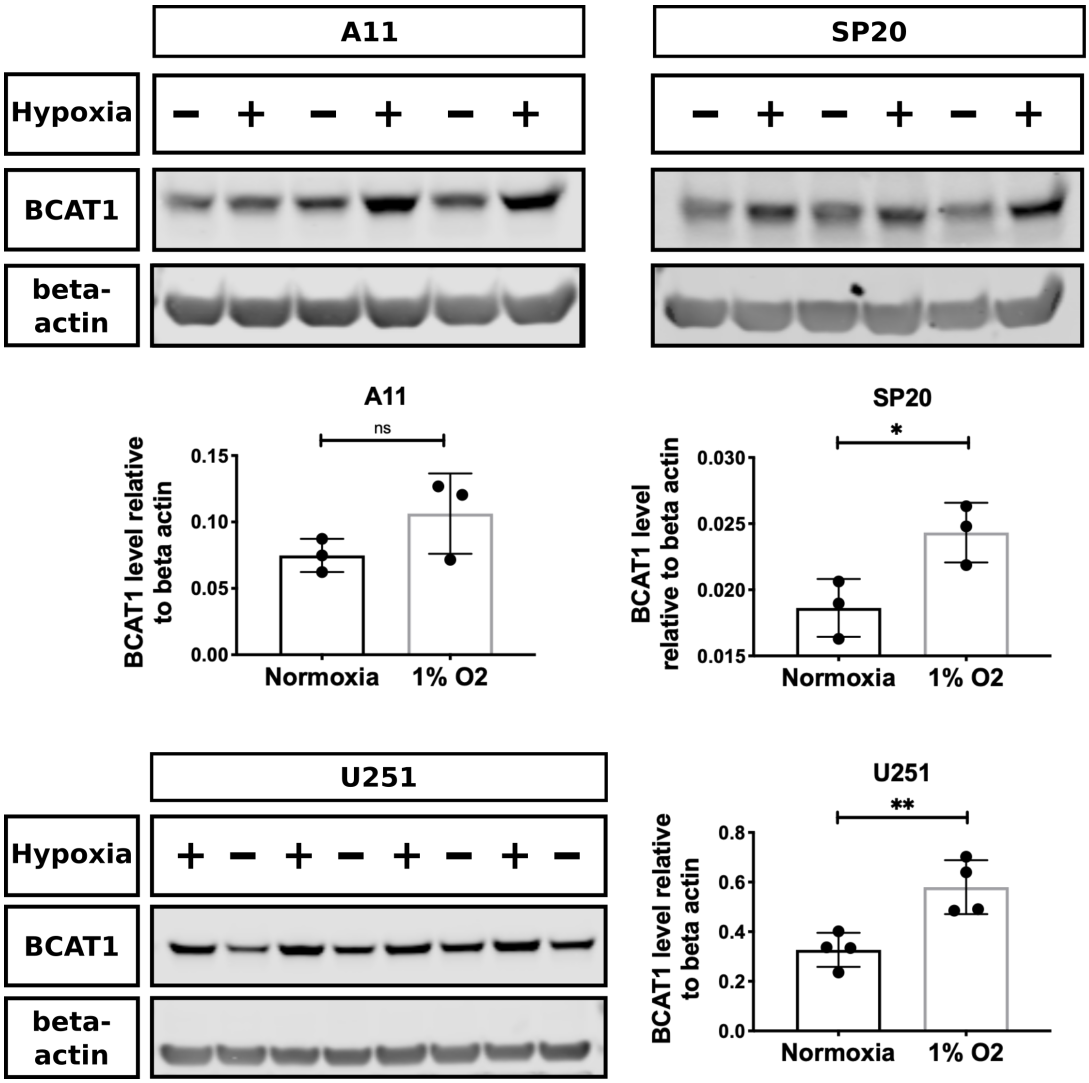

Figure 31 Hypoxia-induced BCAT1 overexpression in U251, A11 and SP20 cells*. Western blots of BCAT1 and beta actin loading control for three or four replicates of lysates from cells (U251 cell line as well as A11 and SP20 patient-derived cell lines) grown in normoxic and hypoxic conditions (1% Oxygen) for 72 hours and quantitation of band intensities normalised to beta actin. Error bars represent the Standard Deviations. Two-tailed unpaired t-tests were used to compare the normoxia and hypoxia groups for each cell line. ns p>0.05, *p<0.05, **p<0.01*

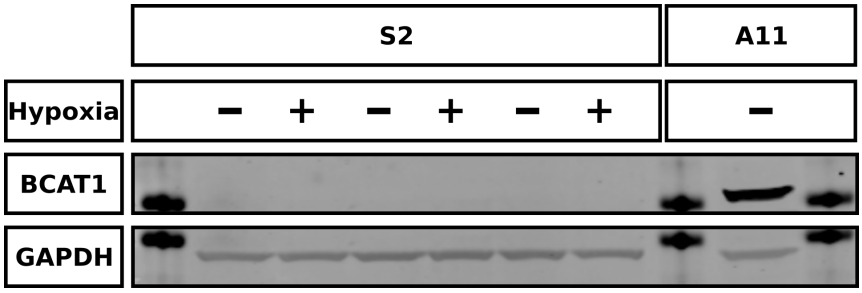

Figure 32 S2 cells showed no BCAT1 expression under hypoxic conditions. *Western blot of lysates from 3 biological replicates of cells grown in normoxic conditions and cells grown in a hypoxia chamber at 0.1% O_2 concentration. GAPDH was used as a loading control. An A11 cell lysate was run on the same gel as a positive control for BCAT1 expression. The bands on either side of the A11 lane and in the first lane are from a 37 kDa marker.*

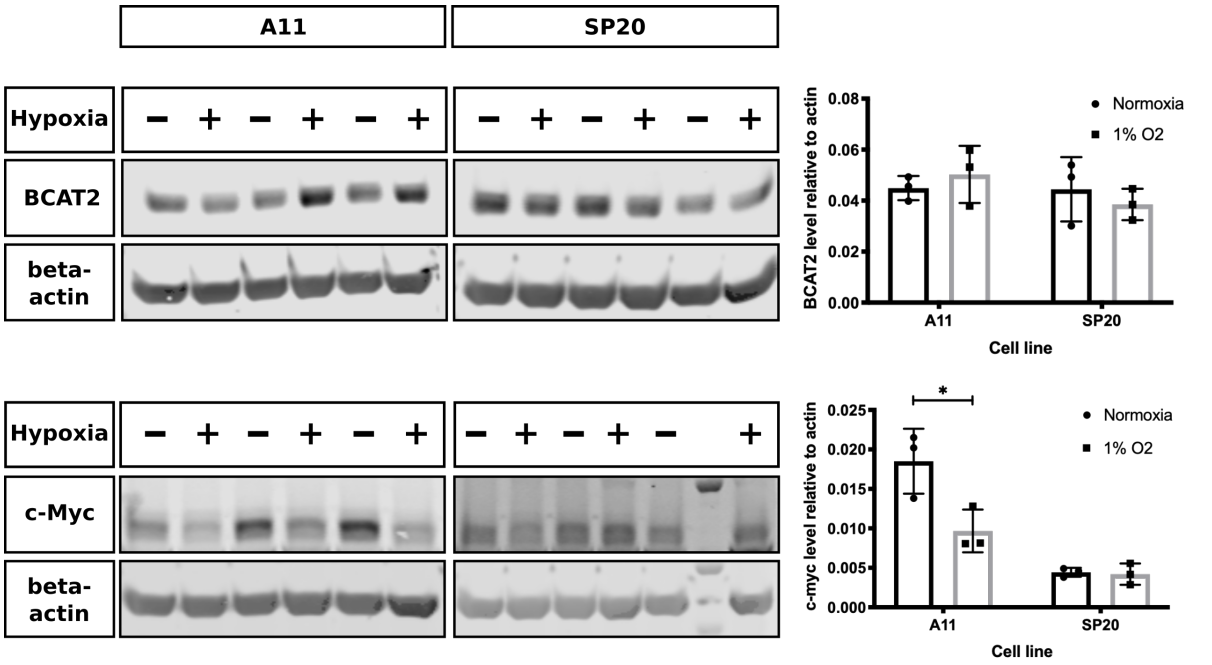

Figure 33 Effect of hypoxia on BCAT2 and c-Myc protein levels in A11 and SP20 cells. *Western blots of BCAT2 and beta-actin in A11 and SP20 cells under normoxic and hypoxic conditions. Quantitation of BCAT2 band intensities relative to beta-actin are shown in the top panel. Western blots of c-Myc and beta-actin in A11 and SP20 cells under normoxic and hypoxic conditions. Quantitation of c-Myc band intensities relative to beta-actin are shown in the bottom panel. Error bars represent the Standard Deviations from three biological replicates. Two-tailed t-tests were performed to compare the expression levels in normoxia and hypoxia. *p<0.05.*

3.4.2.3 Constitutive BCAT1 knockdown in A11 cells persists over multiple passages

Based on previous literature suggesting an important role for BCAT1 in glioblastoma, the following experiments were performed to further investigate the mechanistic role of BCAT1.

In order to investigate the phenotypes associated with BCAT1 expression in glioblastoma cells, BCAT1 levels were modulated in A11 and S2 patient derived cells using constitutive and inducible lentiviral plasmids expressing BCAT1. Constitutive knockdowns have the limitation of compensation effects, while inducible knockdowns can avoid those effects enabling the investigation of short-term knockdown mediated effects. However, the limitation of the inducible knockdown system is the induction with doxycycline, in this case, which can itself have confounding effects on the cells, including cell metabolism effects[167,168].

Transfection of the A11 cells with the constitutive shBCAT1 expressing lentivirus led to good BCAT1 knockdown, which was sustained with repeated passages, as shown in Figure 34.

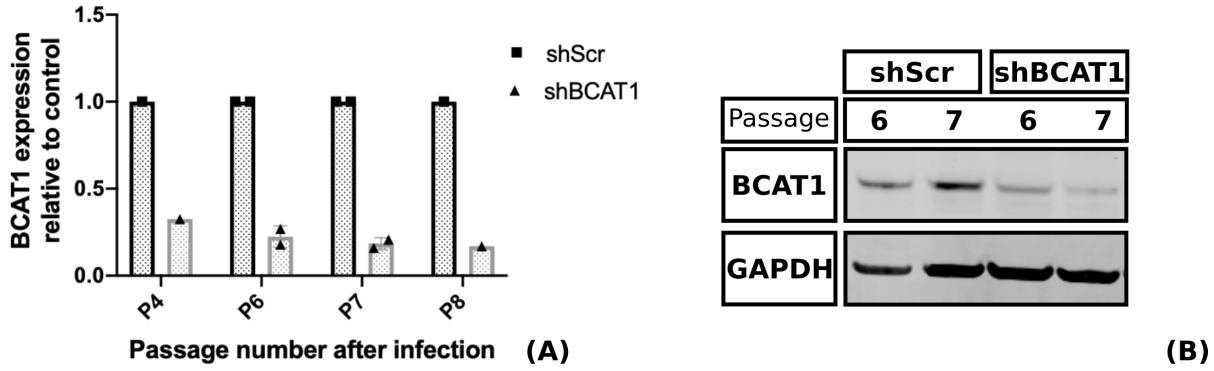

Figure 34 Western blot of BCAT1 and GAPDH confirmed BCAT1 knockdown persists with repeated passages*. (A) Quantitative analysis of BCAT1 protein expression in shBCAT1 expressing cells relative to the shScr expressing controls. (B) Representative Western Blot of BCAT1 and GAPDH loading control in cell lysates.*

3.4.2.4 Optimisation of inducible BCAT1 knockdown

For inducible BCAT1 knockdown in A11 cells, increasing doxycycline doses (10, 50 and 100 ng/ml) were used to determine the optimal dose. All three concentrations produced a sufficient knockdown (Figure 35), and for further experiments, 50 ng/ml was used. Time course experiments were performed to determine the time needed for BCAT1 knockdown to be established. Fifty ng/ml doxycycline was used for varying time periods (48, 72 and 96 hours) to investigate the kinetics of shRNA expression and subsequent knockdown of the protein. BCAT1 protein levels were sufficiently reduced after 72 and 96 hours of doxycycline treatment and the doxycycline treatment itself did not seem to have a significant effect on BCAT1 expression. However, the A11shScr construct had baseline differences in BCAT1 expression when compared to the A11shBCAT1.

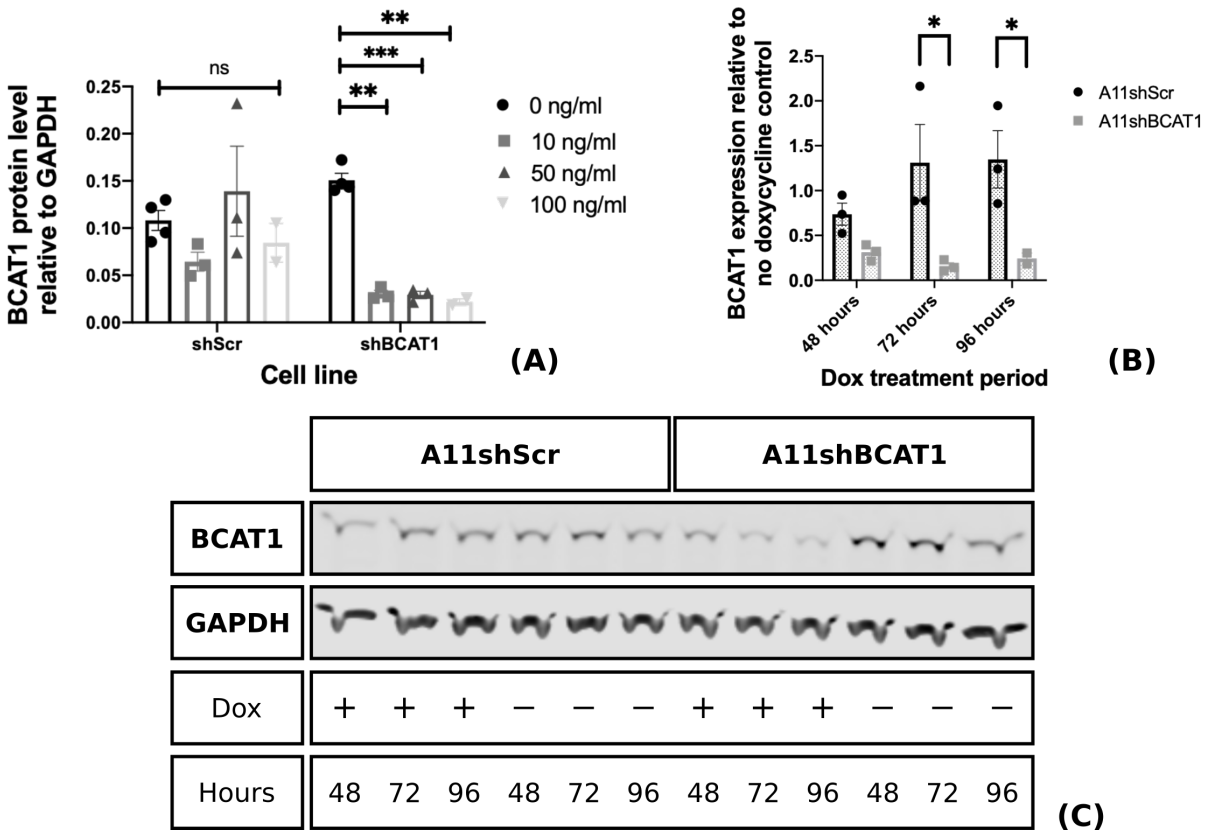

Figure 35 Optimisation of BCAT1 knockdown by doxycycline induction. *(A) Levels of BCAT1 relative to GAPDH loading control in shScr and shBCAT1 cell lysates treated with increasing concentrations of doxycycline. (B) Quantitative Western Blot data from 3 independent experiments of the time course experiment, showing BCAT1 expression relative to the no doxycycline treatment control, with error bars representing SEM. Two-tailed t-tests were performed to compare the levels of BCAT1 across different conditions. ns: p>0.05, *p<0.05, **p<0.01, ***p<0.001 (C) Representative Western Blot showing BCAT1 expression and GAPDH loading control for A11shScr and A11shBCAT1 cells treated with doxycycline for 24-96 hours as well as no treatment controls.*

3.4.2.5 BCAT1 Knockdown leads to reduced BCAT activity in cell lysates

Total BCAT activity in lysates of A11shBCAT1 and A11shScr cells was compared to the activity of lysates of control cells which had not been induced with doxycycline, using the BCAT spectrophotometric assay. Total BCAT activity of BCAT1 knockdown cells was significantly reduced compared to control lysates (Figure 36A). To directly compare BCAT1 enzyme activity between BCAT1 knockdown and control cell lysates, gabapentin was added to the spectrophotometric assay. The reduction in the total activity measured with increasing concentrations of gabapentin was lower in the knockdown cells compared to the control cells, demonstrating that BCAT1 activity levels were reduced upon BCAT1 knockdown. The remaining activity at 40 mM gabapentin was unchanged, demonstrating that BCAT2 activity was unchanged (Figure 36B and C). When directly comparing BCAT1 protein levels and total BCAT activity in the same lysates, the change in BCAT1 protein was greater than the change in activity levels (Figure 36D), suggesting that post-translational modifications of the enzyme

might compensate for the reduced levels of protein expression. Both isoforms of BCAT have a redox-active CXXC motif, which can undergo oxidation by H_2O_2, nitrosation and glutathionylation, all of which lead to modulation of enzymatic activity[169-171].

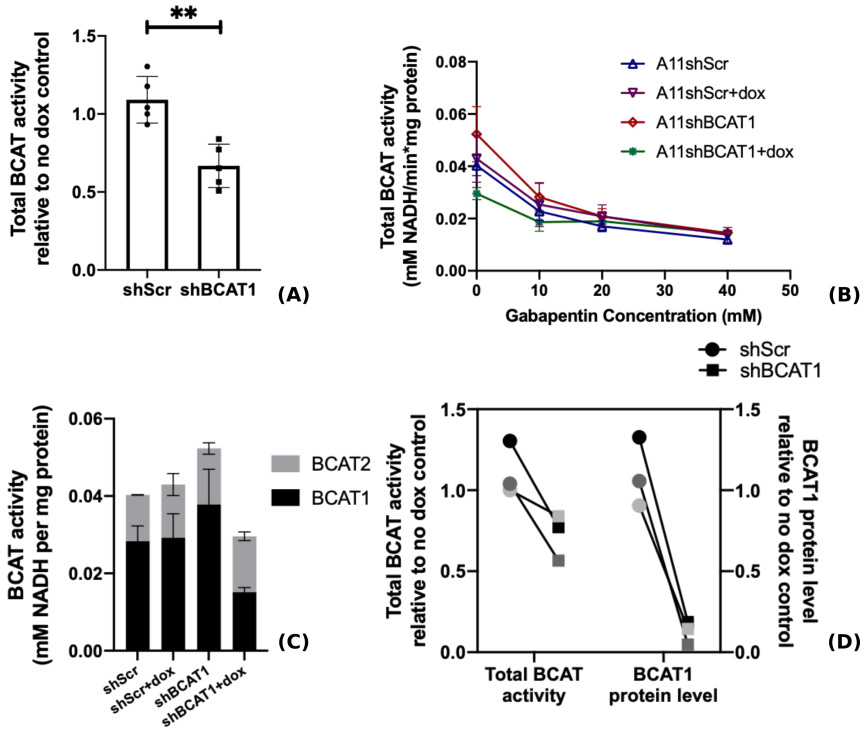

Figure 36 Measuring BCAT activity in BCAT1 knockdown and control lysates using the BCAT spectrophotometric assay. *(A) Lysates of cells expressing a control shRNA (shScr) and shBCAT1, untreated and treated with doxycycline, were assayed for total BCAT activity. The activity in the doxycycline-induced cells relative to the activity in the non-induced cells is plotted for every biological replicate (n=5) and the error bars represent the Standard Deviations. A two-tailed t-test was performed to compare the activity levels between the two groups. **p<0.01 (B) Increasing concentrations of gabapentin were used in the spectrophotometric assay to selectively inhibit BCAT1 in the BCAT1 knockdown cell lysates and their controls. Error bars represent SEM from 2 independent experiments. (C) The activity measured at 40 mM gabapentin was plotted as BCAT2 activity and the difference between the total BCAT activity at 0 mM gabapentin and BCAT2 activity was plotted as BCAT1 activity. Error bars represent SEM for two independent experiments. (D) The change in total BCAT activity of the shScr control cells and BCAT1 knockdown cells when induced with doxycycline is compared to the change in protein levels of BCAT1 in the same lysates.*

3.4.2.6 BCAT1 overexpression in S2 and A11 cells leads to increased levels of the protein as well as a fusion protein

For BCAT1 overexpression experiments, a vector containing the mStrawberry sequence and the BCAT1 coding sequence, separated by an E2A sequence was used. For control cells, the BCAT1 sequence was replaced with a Luciferase sequence. BCAT1 overexpressing cells are labelled as A11 BCAT1 and S2 BCAT1 for A11 and S2 cells, respectively. Control cells, which express mStrawberry and Luciferase are referred to as A11Str and S2Str.

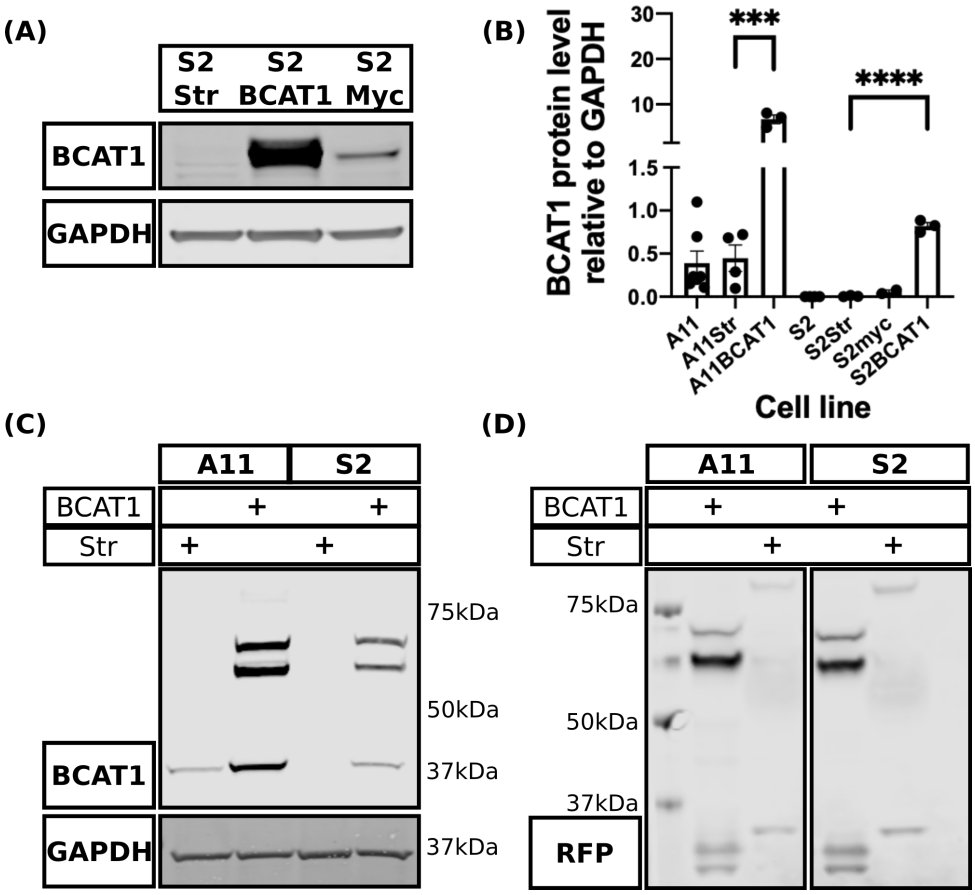

Figure 37 Western Blot analysis of BCAT1 overexpressing A11 and S2 cells and their luciferase-expressing controls. *(A) Representative Western Blot of BCAT1 and GAPDH loading control in different clones of S2 cells. S2Str: Strawberry and Luciferase expressing control, S2BCAT1: BCAT1 overexpressing clone, S2myc: cMyc overexpressing clone. (B) Quantitative data from Western Blots showing BCAT1 expression relative to GAPDH for the different cell lines. Error bars represent SEM. Two-tailed t-tests were used to compare between the Str controls and BCAT1 overexpressing cells. ***p<0.001, ****p<0.0001 (C) Western Blot of BCAT1 and GAPDH for A11 and S2 BCAT1 overexpressing cells and controls. The band at 40kDa represents BCAT1. The 2 bands at 65-70 kDa only appear in the BCAT1 overexpressing cell lysates. (D) The same bands at 65-70 kDa also appear in Western Blots when blotting for Red Fluorescent Protein (RFP).*

Western blots of A11 and S2 BCAT1 overexpressing cells showed higher BCAT1 protein expression compared to the luciferase expressing controls, and also showed mStrawberry protein expression (Figure 37). Two more bands (65-70 kDa) also appeared on the BCAT1 Western Blot as well as on the Red Fluorescent Protein (RFP) Western Blot suggesting that it represents fused mStrawberry and BCAT1 proteins. This is probably the result of using a construct containing two genes separated by an E2A sequence, where ribosome skipping is unsuccessful, leading to read-through translation of a fused protein[172].

3.4.2.7 Overexpression of BCAT1 in A11 and S2 cell lines leads to increased BCAT activity

The effect of BCAT1 overexpression on enzyme activity was investigated in lysates of the original cell lines as well as the control clones and the overexpressing clones (Figure 38). BCAT activity in the control clones did not differ from those in the lysates of the original cell lines. Lysates of the BCAT1 overexpressing clones showed a tenfold increase in total BCAT activity, when compared to the control clones, in accordance with the increase in BCAT1 protein levels seen on Western Blot, suggesting that the overexpressed protein is active. When gabapentin was added to the reaction, BCAT1 inhibition observed in lysates from overexpressing cells was less than expected, and the measurable activity at 40 mM gabapentin concentration was much higher than the expected BCAT2 activity. This can be explained by the high Ki of gabapentin for BCAT1[173], whereby there is still about 13% residual BCAT1 activity at a gabapentin concentration of 40 mM.

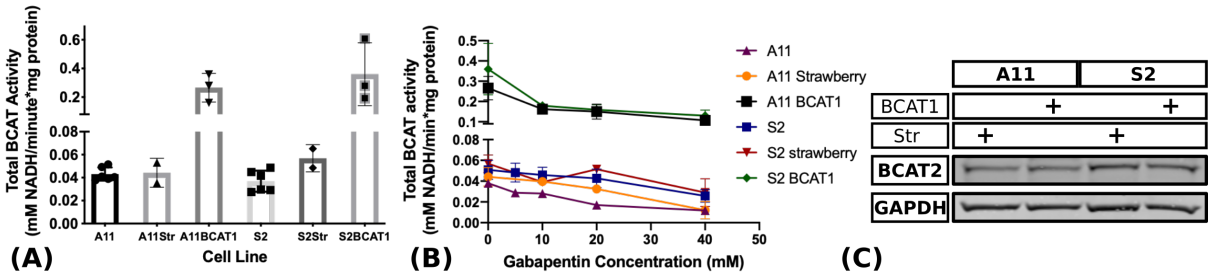

Figure 38 BCAT1 overexpression in A11 and S2 cells led to increased BCAT activity as measured by the spectrophotometric assay. *(A) Bar chart showing total activity levels measured in independent experiments for the parental cell lines (A11, S2) as well as the controls (A11Str, S2Str) and the BCAT1 overexpressing cells (A11BCAT1, S2BCAT1). (B) The total BCAT activity measured at different concentrations of gabapentin, demonstrating inhibition of BCAT1 with increasing gabapentin concentration. (C) Western Blot of BCAT2 and GAPDH loading control from lysates of A11 and S2 BCAT1 overexpressing cells and their respective controls.*

3.4.3 The reaction favours transamination of BCAAs to BCKAs

3.4.3.1 BCAT1 overexpression leads to higher ^{13}C-labelled KIC generated from ^{13}C-labelled leucine in culture

Since the transamination reaction catalysed by BCAT1 is reversible, it was important to understand which reaction was favoured, forward or reverse, which is greatly dependent on the relative concentrations of the substrates of the reaction.

Labelling experiments with [1-^{13}C]leucine were performed to investigate the net flux in the reaction and assess the changes in the rate of amino acid transamination to its respective ketoacid, KIC, upon BCAT1 overexpression. Cells were incubated with BCAA-free DMEM media and supplemented with [1-^{13}C]leucine at a concentration of 0.8 mM for 48 hours. The [1-^{13}C]KIC to [1-^{13}C]leucine ratio in the media was measured using ^{13}C NMR and normalized to the protein content determined after the metabolite extraction. BCAT1 overexpression in both A11 and S2 cells led to an increased ratio of [1-^{13}C]KIC to [1-^{13}C]leucine in the media compared to the controls. In addition, A11 control cells transaminated leucine at a faster rate than S2 control cells (Figure 39A). These results suggest that in cell culture, BCAT1 favours the forward reaction, generating BCKAs that are released into the media.

3.4.3.2 BCAT1 knockdown leads to reduced secretion of glutamate in cell culture

Further evidence for the forward reaction being favoured in cultured GBM cells was provided by quantifying glutamate released into the culture medium of A11 BCAT1 knockdown cells and control cells. This was achieved using a spectrophotometric assay, which couples glutamate oxidation and NADH production, by glutamate dehydrogenase with a bioluminescent detection system, where a luciferin pro-substrate is reduced to the active luciferase substrate.

Following induction of BCAT1 knockdown with doxycycline, equal numbers of viable cells were seeded in a 96 well plate with fresh media in order to control for the effects caused by proliferation differences. Quantification of the glutamate in cell media revealed a significant decrease in glutamate secretion by cells upon BCAT1 knockdown (Figure 39B). This effect could be a direct result of BCAT1 knockdown leading to reduced glutamate production from α-KG, or an indirect effect of BCAT1 knockdown on the expression of glutamate transporters or on glutamate metabolism in the cell. For further investigation of this effect, tracing experiments with [^{15}N]leucine would be necessary.

3.4.3.3 Glioblastoma tumours consume Branched Chain Amino Acids

BCAAs differ from other amino acids in that they are poorly metabolised during the first pass through the liver, due to the low levels of BCAT1 and BCAT2 expression in hepatocytes. Therefore, changes in circulating levels of BCAAs can be used as markers for several pathologies, including insulin resistance[149,174]. In cancer, it appears that changes in plasma

levels of BCAAs is context dependent, with elevated levels of BCAAs being observed in mice with early pancreatic ductal adenocarcinoma[45] and in patients with breast cancer[44] but reduced levels of BCAAs observed in mice with non-small cell lung cancer[45]. In order to investigate the systemic effect of glioblastoma on BCAAs, the concentration of BCAAs was measured in blood plasma samples that were taken from healthy rats and tumour-bearing rats. Rats with a visible tumour on T_2-weighted MRI scans had reduced concentrations of BCAAs in their plasma samples when compared to rats which did not show signs of tumour growth (Figure 39C). No differences were seen between different Patient Derived Orthotopic xenografts (PDOXs), suggesting that the systemic effects of glioblastoma on BCAA metabolism were not dependent on BCAT1, since S2 PDOXs, which show no BCAT1 expression also led to reduced circulating BCAA levels. From three rats that were sampled at different time points during tumour progression, we observed greatly reduced plasma BCAA concentrations when the tumour first appeared on MRI and as the tumour size increased, the plasma concentrations of BCAAs then increased (Figure 39D). Even though the reduction in plasma levels of BCAAs can be attributed to many factors including uptake and consumption in the tumour for catabolism or protein synthesis as well as other effects of the tumours on systemic BCAA metabolism, it suggests that there is no net generation of BCAAs from BCKAs by the tumours.

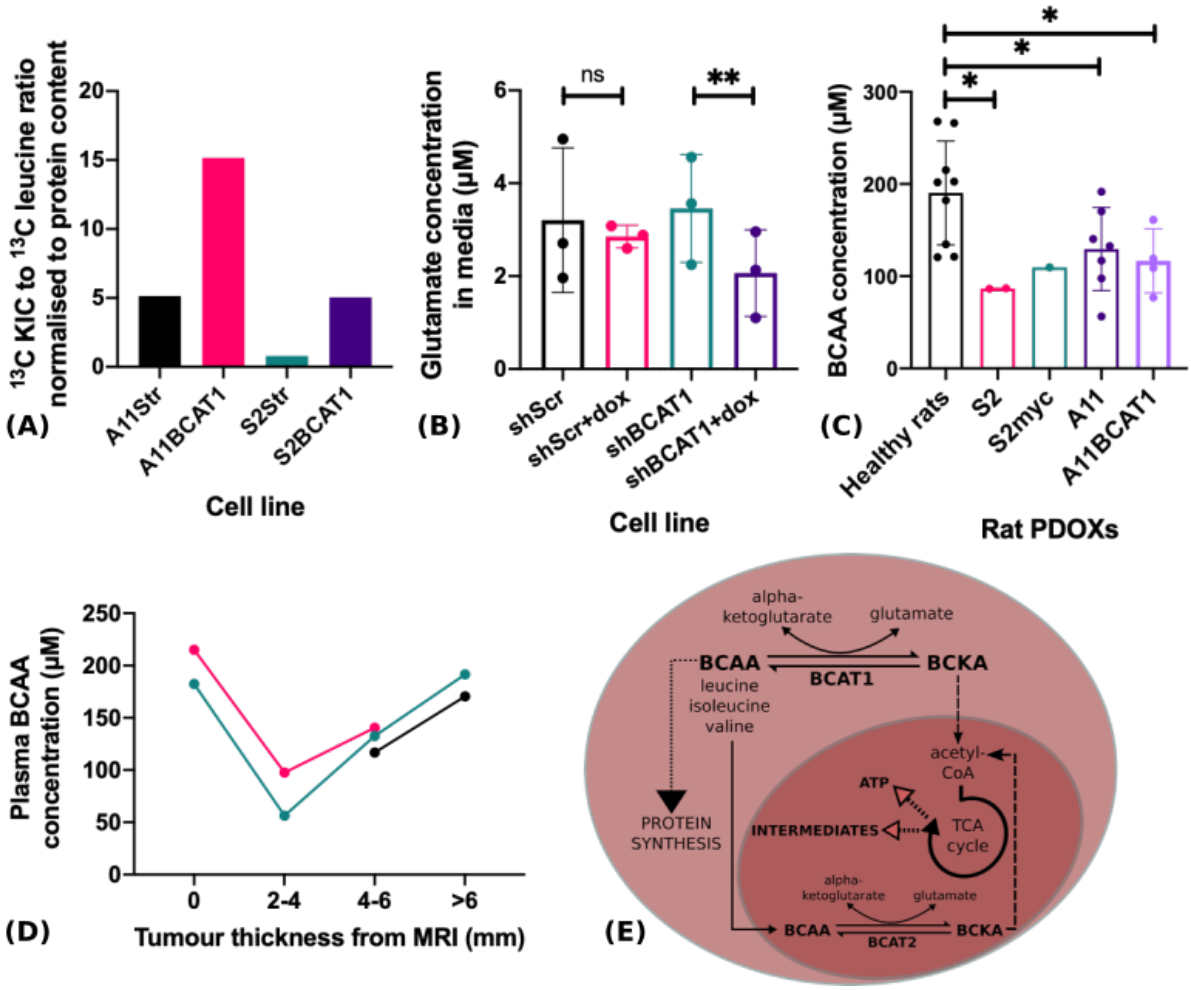

Figure 39 BCAT1 favours transamination of BCAAs to BCKAs in glioblastoma. *(A) The ^{13}C-labelled KIC to leucine ratio in cell media normalised to the amount of protein. Cells were incubated with labelled leucine for 48 hours and the concentrations of labelled leucine and KIC measured using ^{13}C NMR. (B) The concentration of glutamate in cell media as measured using a spectrophotometric enzyme-based assay. Each point represents the mean of technical replicates from each independent experiment (n=3) and the error bars represent the Standard Deviations. Two-tailed paired t-tests were performed to compare the glutamate concentration between the doxycycline treated and untreated cells. ns: p>0.05, **p<0.01 (C) Plasma BCAA concentrations in rats, with healthy rats representing a pool of non-implanted rats as well as rats that were implanted but did not show signs of tumour growth on MRI. A11 includes rats implanted with A11shScr and A11shBCAT1 cells but in which the shRNA expression was not induced with doxycycline. Each point represents a measurement from a different rat or from repeated samples from the same rat. Two-tailed t-tests were performed to compare the plasma BCAA concentration of healthy rats with tumour-bearing rats. *p<0.05 (D) Rats that were repeatedly sampled over time revealed a reduction of circulating BCAAs with initial tumour growth with recovery of the BCAA plasma concentration over time. (E) Illustration of BCAA metabolism in the cytoplasm (pink) and mitochondrion (dark red) of the cell.*

3.4.4 BCAT1 activity affects proliferation of A11 cells but not S2 cells

BCAT1 has been shown to be involved in the proliferation of commercially available glioblastoma cell lines[51]. To confirm whether BCAT1 plays a role in cell proliferation in the patient derived glioblastoma cells used here, pharmacological inhibition and genetic manipulation of BCAT1 expression were used. Pharmacological inhibition of BCAT1 by high doses of gabapentin and 4-methyl-5-oxohexanoic acid led to reduced cell proliferation in the panel of patient derived cells, but these effects appeared to be non-specific. However, BCAT1

knockdown and BCAT1 overexpression in A11 cells led to significant reduction and increase, respectively, in cell proliferation rate. BCAT1 overexpression in S2 cells did not result in increased cell proliferation.

3.4.4.1 Inhibition of BCAT1 by gabapentin led to reduced proliferation rate

Gabapentin has been used in many studies to investigate the role of BCAT1 *in vitro*, as it competitively inhibits BCAT1 but has no effect on BCAT2. Cell proliferation assays were performed for the panel of patient derived GBM cell lines in the presence of increasing concentrations of gabapentin to investigate the effect of BCAT1 inhibition on cell proliferation. Twenty mM gabapentin led to a significant reduction in the proliferation rate of A11, SP20, S2myc and U87 cells but less so in S2 cells (Figure 40A-F). Twenty mM gabapentin also led to morphological changes in the cells, resulting in a more rounded shape (Figure 40J). The low potency of gabapentin was observed in the spectrophotometric assay of BCAT activity, where 20 mM gabapentin was needed to maximally inhibit BCAT1. This high concentration needed to significantly inhibit cell proliferation raises a concern about possible off-target effects. For this reason, BCAT1 inhibition by a more specific inhibitor, 4-methyl 5-oxohexanoic acid (MOHA) was used to investigate proliferation effects in A11 cells (Figure 41). A similar reduction in proliferation rate was observed using this inhibitor at 10 mM. However, increased staining with Incucyte Cytotox red reagent suggests the inhibitor had cytotoxic effects, which at this concentration might be off-target effects (Figure 41D).

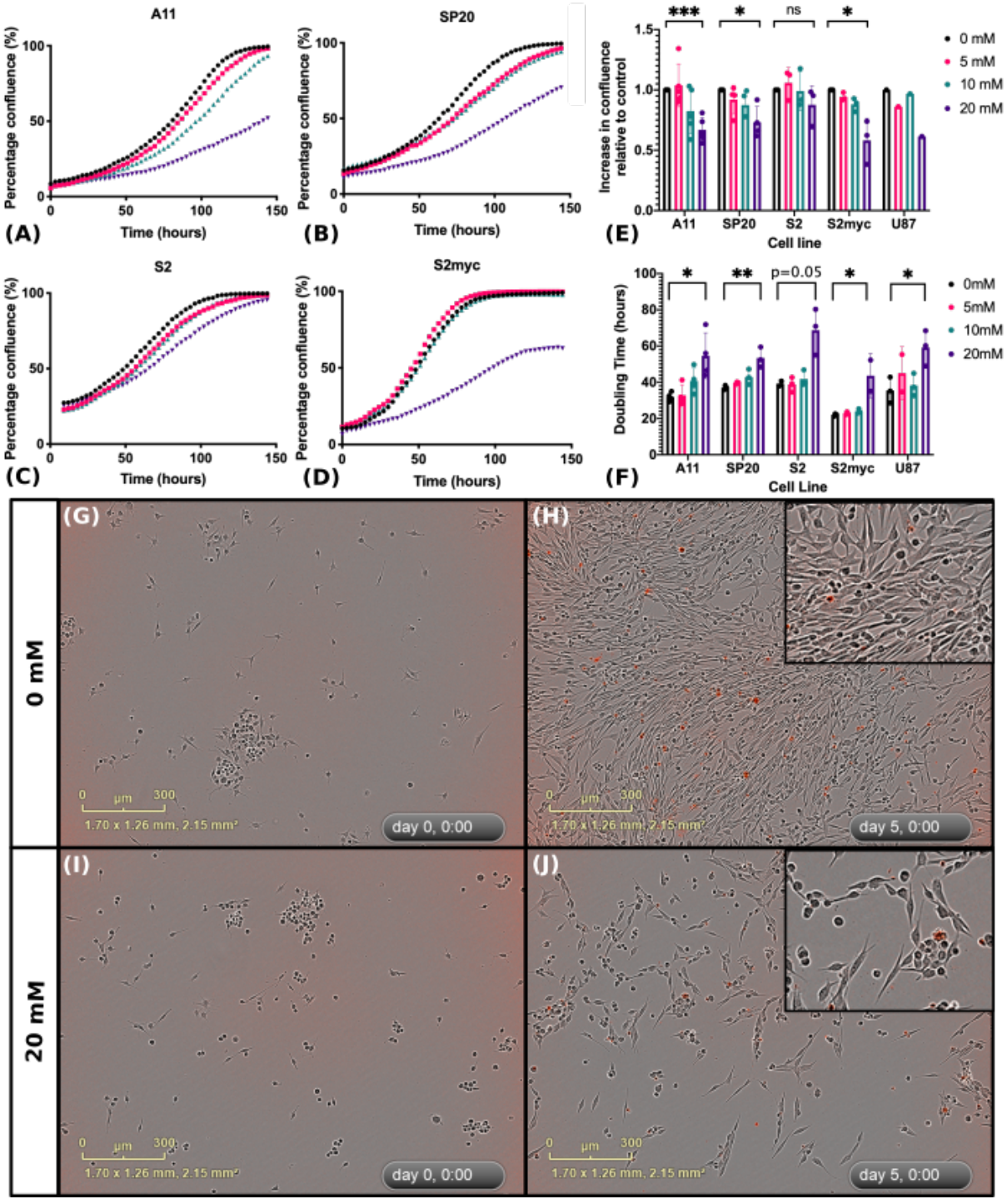

Figure 40 Effects of gabapentin on glioma cell proliferation. *(A-D) Representative growth curves showing mean percentage confluence over time, as measured by the Incucyte Software (Essen Biosciences) for glioma patient-derived cell lines A11(A), SP20(B), S2(C) and S2myc(D). (E,F) The data from five independent experiments are summarised as the increase in percentage confluence relative to the untreated controls (E) as well as the doubling times obtained following exponential curve fitting performed in Prism (GraphPad) (F). The error bars represent the Standard Deviation. Two-tailed t-tests were performed to compare the untreated control cells to the gabapentin treated cells. ns: p>0.05, *p<0.05, **p<0.01, ***p<0.001 (G-J) Representative images of A11 cells at the point of seeding (G,I) and 5 days later (H,J) after treatment with 0 mM and 20 mM gabapentin, illustrating the inhibition of proliferation caused by gabapentin. Incucyte Cytotox Red reagent (Essen Bioscience) was used at a 1:4000 dilution to stain for cell death, showing that the inhibition of proliferation does not result in increased cell death.*

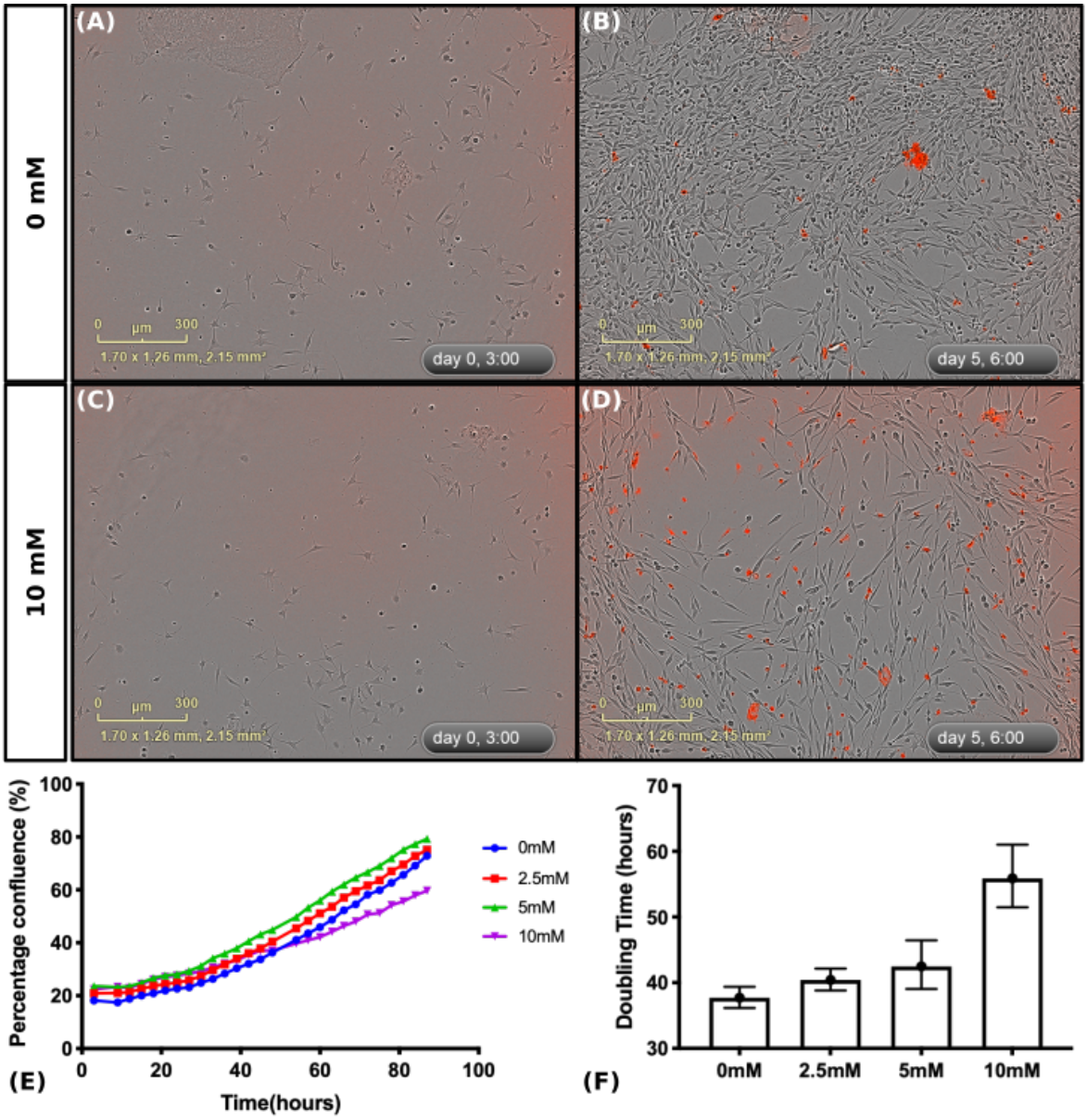

Figure 41 Effects of 4-methyl-5-oxohexanoic acid on A11 cell proliferation. *(A-D) Representative Incucyte 10X images of A11 cells 3 hours after seeding (A,C) and 5 days later (B,D) after treatment with 0 mM (A-B) or 10 mM (C-D) inhibitor. Incucyte Cytotox Red reagent (Essen Bioscience) was used at a 1:4000 dilution to stain for cell death, showing that the inhibitor is cytotoxic. (E) Growth curves plotted for the mean of 3 replicate wells of A11 cells incubated with increasing concentrations of 4-methyl-5-oxohexanoic acid. The doubling time calculated from fitting the curve to an exponential function is plotted in (F), illustrating the dose dependent increase in doubling time with inhibitor concentration.*

3.4.4.2 Knockdown of BCAT1 but not BCAT2 inhibits proliferation of A11 cells

To further investigate the role of BCAT1 in cell proliferation and exclude any off-target effects of drug treatment, we made BCAT1 knockdown constructs for the A11 patient-derived cells. Both inducible and constitutive BCAT1 knockdown constructs were used. Constitutive BCAT1 knockdowns showed reduced proliferation rates compared to the shScr controls at early passage numbers but regained their original growth rates at later passages, even though the knockdown

was maintained, suggesting that the cells had compensated for the loss of BCAT1 expression, potentially through altered flux through other metabolic reactions (Figure 42). Treatment with gabapentin (0-20 mM) as well as the more specific inhibitor 4-methyl-5-oxohexanoic acid (0-20 mM) had very similar effects in the BCAT1 knockdown late passage cells and the control cells, suggesting that the proliferation effects seen upon pharmacological treatment are, at least partly, off-target effects (Figure 42).

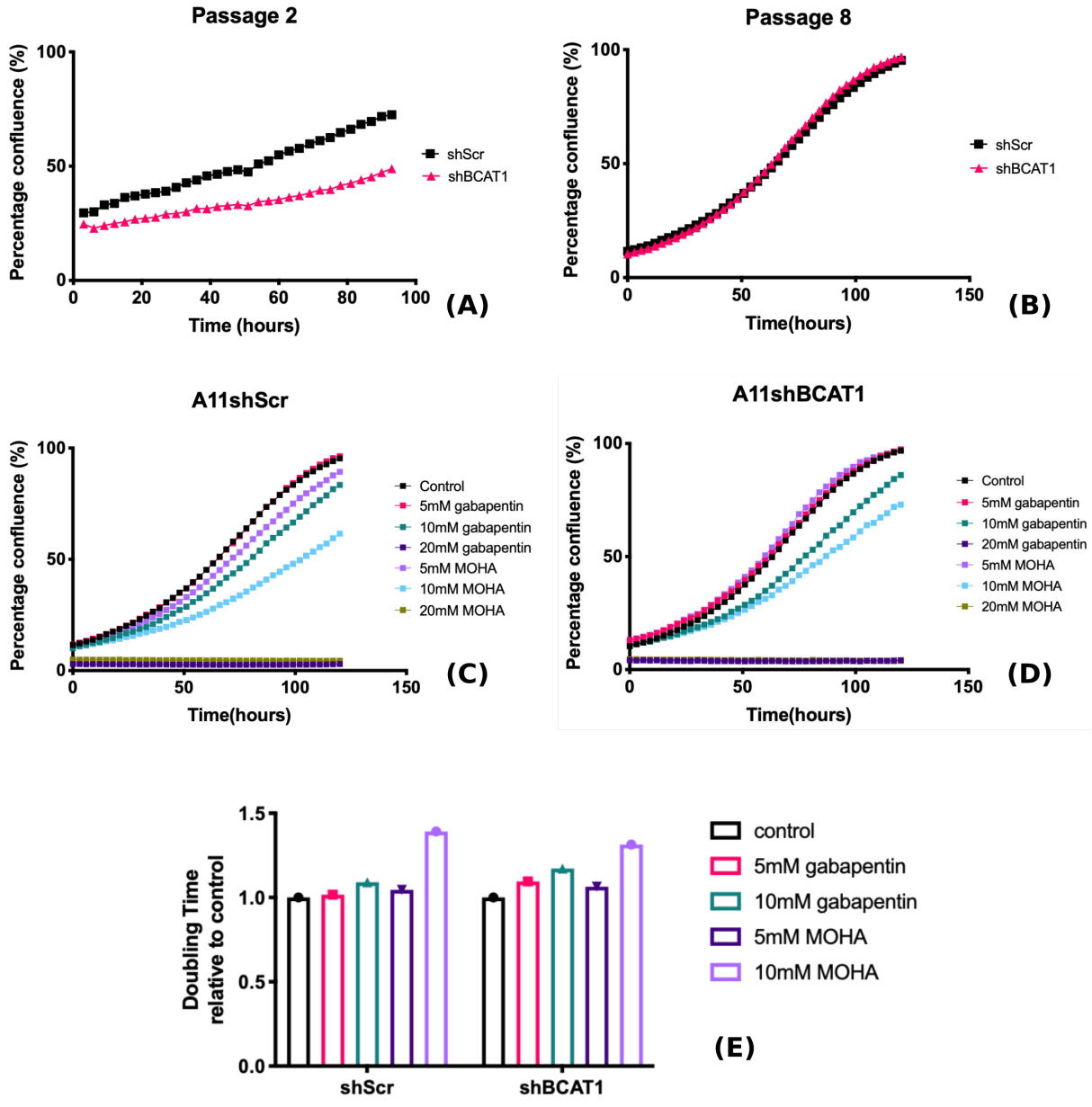

Figure 42 Cell proliferation following constitutive BCAT1 knockdown in A11 cells. *The proliferation rate of A11 cells following constitutive shBCAT1 expression and expression of a control shRNA (shScr) were compared, demonstrating inhibition of proliferation following BCAT1 knockdown (A) which was reversed in later passages (B). The points on the growth curves represent the mean confluence of three wells from one experiment . (C-D) Growth curves of A11 cells expressing shScr (C) or shBCAT1 (D) and treated with gabapentin or 4-methyl-5-oxohexanoic acid (MOHA). (E) The doubling time of the cells, calculated by fitting an exponential curvel to the growth curves, relative to their respective untreated control are plotted for the two cell lines.*

Induction of BCAT1 knockdown with doxycycline also led to a reduced proliferation rate, but the effect was smaller than that seen with gabapentin treatment, also suggesting that at least part of the effect seen following gabapentin treatment was non-specific (Figure 43). To further confirm inhibition of proliferation following induced BCAT1 knockdown, proliferation was also assessed by measuring number of viable cells over time using Trypan Blue dye exclusion cell counting (Vicell) and using a Luciferase based proliferation assay (RealTime-Glo MT Cell Viability Assay (Promega)). In the latter assay, a cell permeable pro-substrate is reduced by the viable cell to produce a luciferase substrate which diffuses out of the cell and is used by NanoLuc luciferase to produce a luminescence signal. The inhibition of proliferation caused by knockdown of BCAT1 was clear and reproducible when measured with the luciferase-based assay (Figure 44). Using the same assay, we investigated whether branched chain keto acid (BCKA) supplementation could reverse the BCAT1 knockdown effects. Addition of BCKA at concentrations up to 0.8 mM of each of α-ketoisocaproate, α-ketoisovalerate and α-keto-β-methylvalerate did not lead to an increase in the proliferation rate of the BCAT1 knockdown cells and it led to a slight inhibition of control cell proliferation (Figure 44).

BCAT2 knockdown in the same cells as well as in S2 cells did not cause a proliferation defect similar to BCAT1 knockdown as measured by the RealTime Glo assay, suggesting that the two BCAT isoforms play different roles in the cell (Figure 45).

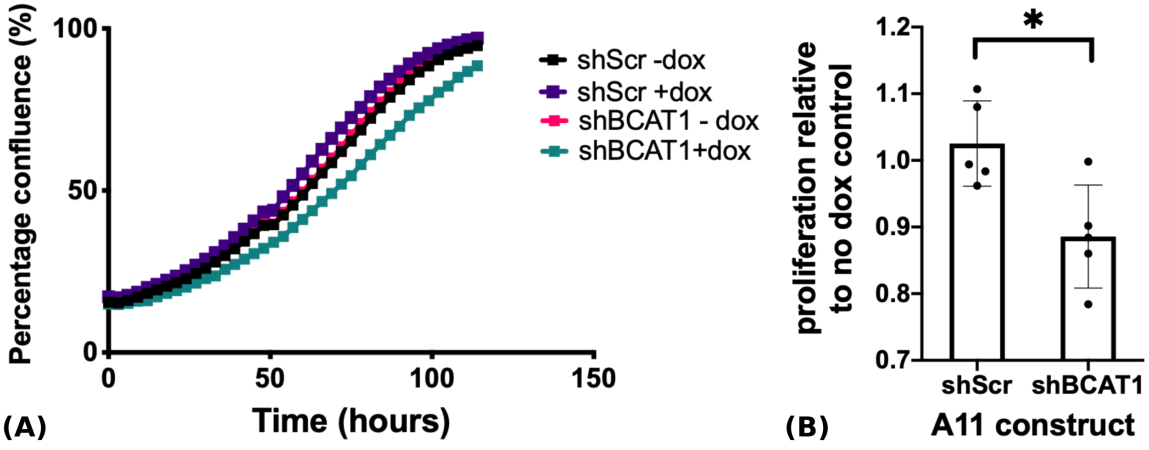

Figure 43 Cell proliferation following doxycycline-induction of BCAT1 knockdown. *(A) Growth curves of A11 cells expressing shScr or shBCAT1 and induced or non-induced with doxycycline (50 ng/ml). The points represent the mean confluence from three independent experiments. (B) The proliferation rate, in terms of fold-increase in cell confluence from the initial timepoint to the final timepoint normalised to the increase in the respective non-induced control cells (n=5). A two-tailed t-test was performed to compare the two cell lines. *p<0.05*

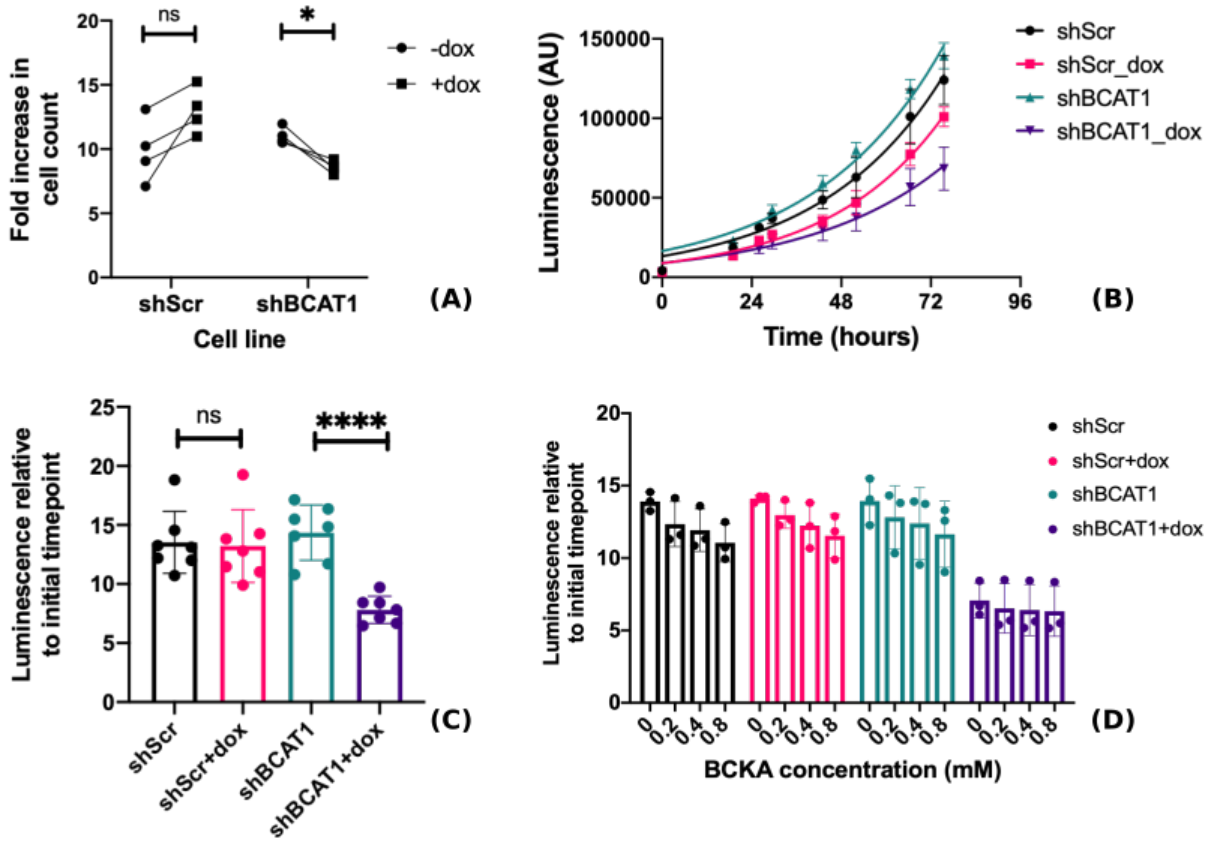

Figure 44 Inducible BCAT1 knockdown leads to reduced cell proliferation as measured by a Trypan Blue dye exclusion assay and a luciferase-based assay. *(A) Equal numbers of inducible A11shScr and A11shBCAT1 cells were seeded in 6 well plates and were treated with doxycycline (50 ng/ml) or were untreated. The number of viable cells over time was measured using the ViCell instrument and the fold increase in cell numbers over a period of three days was plotted for the four conditions. Each point on the graph represents the fold change in independent experiments (n=4). Two-tailed t-tests were performed to compare the proliferation in doxycycline induced and non-induced cells. ns: p>0.05, *p<0.05 (B-D) A luciferase-based assay was used to measure cell viability in control cells and BCAT1 knockdown cells over time. (B) is a representative example of the growth curves plotted when measuring luminescence over time and in (C) the fold-change in luminescence over two days is plotted, with each point representing the mean of three technical replicates for each independent experiment (n=7). The error bars represent the Standard Deviations. Two-tailed t-tests were performed to compare the proliferation in the different groups. ns: p>0.05, ****p<0.0001 (D) Cells were supplemented with increasing concentrations of BCKA (0 mM – 0.8 mM of each ketoacid). Each point represents the mean of three technical replicates from an independent experiment (n=3) and the error bars represent the Standard Deviations.*

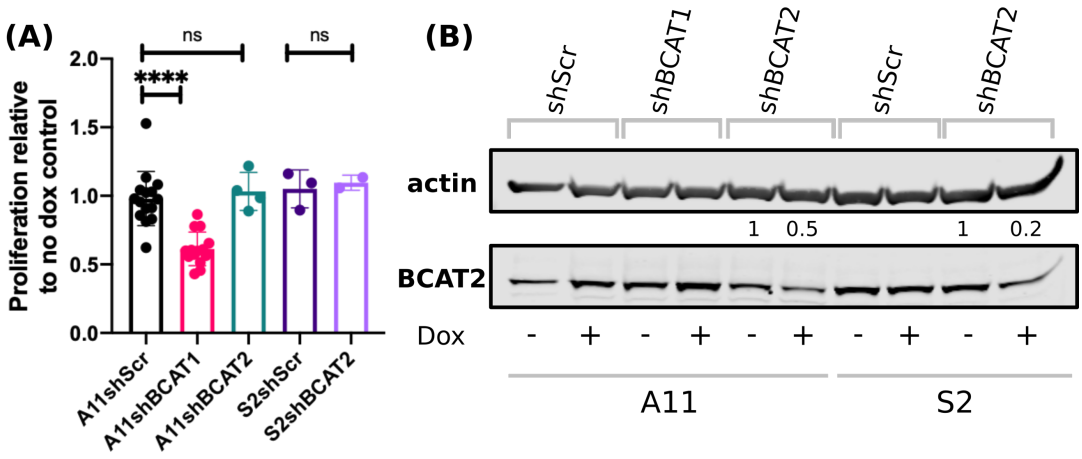

Figure 45 BCAT2 knockdown does not have a significant effect on the proliferation rate of A11 and S2 cells. *(A) Summary plot showing the proliferation rate of doxycycline treated cells relative to the untreated controls for A11 and S2 cells transfected with the shScr, shBCAT1 or shBCAT2 lentiviral vectors. Each point corresponds to the mean proliferation from an independent experiment and error bars represent Standard Deviation. Two-tailed t-tests were performed to compare the BCAT1 and BCAT2 knockdown cells to their respective shScr controls. ns: p>0.05, ****p<0.0001. (B) Western Blot of BCAT2 and actin loading control to confirm the knockdown of BCAT2 in A11 and S2 cells. The quantitative expression level of BCAT2 relative to the non-doxycycline treated control is shown for A11 and S2 cells.*

3.4.4.3 The reduced proliferation rate of A11 BCAT1 knockdown cells is explained by partial cell cycle arrest

The reduced proliferation rate of A11 cells upon BCAT1 knockdown could be a result of cell cycle arrest. In order to identify cell cycle changes, the cells were fixed and permeabilized with ethanol and their nuclear DNA stained with propidium iodide. Cell cycle analysis was performed on cells that had been synchronised using a double thymidine block protocol as well as on non-synchronised cells. In non-synchronised cells, BCAT1 knockdown resulted in a higher proportion of cells in G1 phase and smaller proportions in G2 and interphase (Figure 46). When synchronized, control cells progressed through the cell cycle phases while the BCAT1 knockdown cells largely remained in G1 (Figure 47).

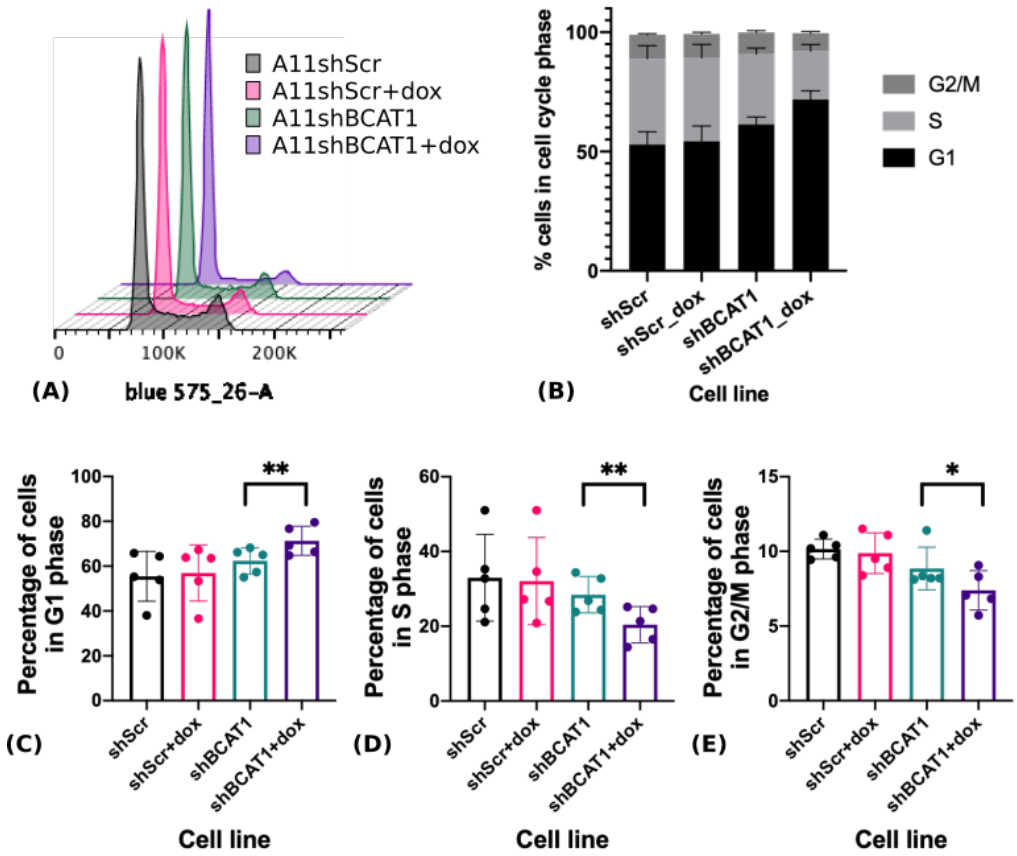

Figure 46 Cell cycle analysis of A11 cells reveals partial G1 cell cycle arrest upon BCAT1 Knockdown. *A11shScr and A11shBCAT1 cells were treated with doxycycline or were untreated for at least four days before they were fixed and permeabilised for DNA staining. (A) Representative example of propidium iodide staining for the four cell conditions with the y-axis normalised to the mode of each histogram. (B) Quantitative cell cycle analysis using the FlowJo cell cycle package from five independent experiments showing the distribution of cells in the cell cycle phases. Error bars represent SEM. (C-E) The mean percentage of cells in each of the three cell cycle phases with error bars representing Standard Deviations of five independent experiments. For statistical analysis, two-tailed paired t-tests were performed to compare doxycycline-induced cells to non-induced cells. *p<0.05, **p<0.01.*

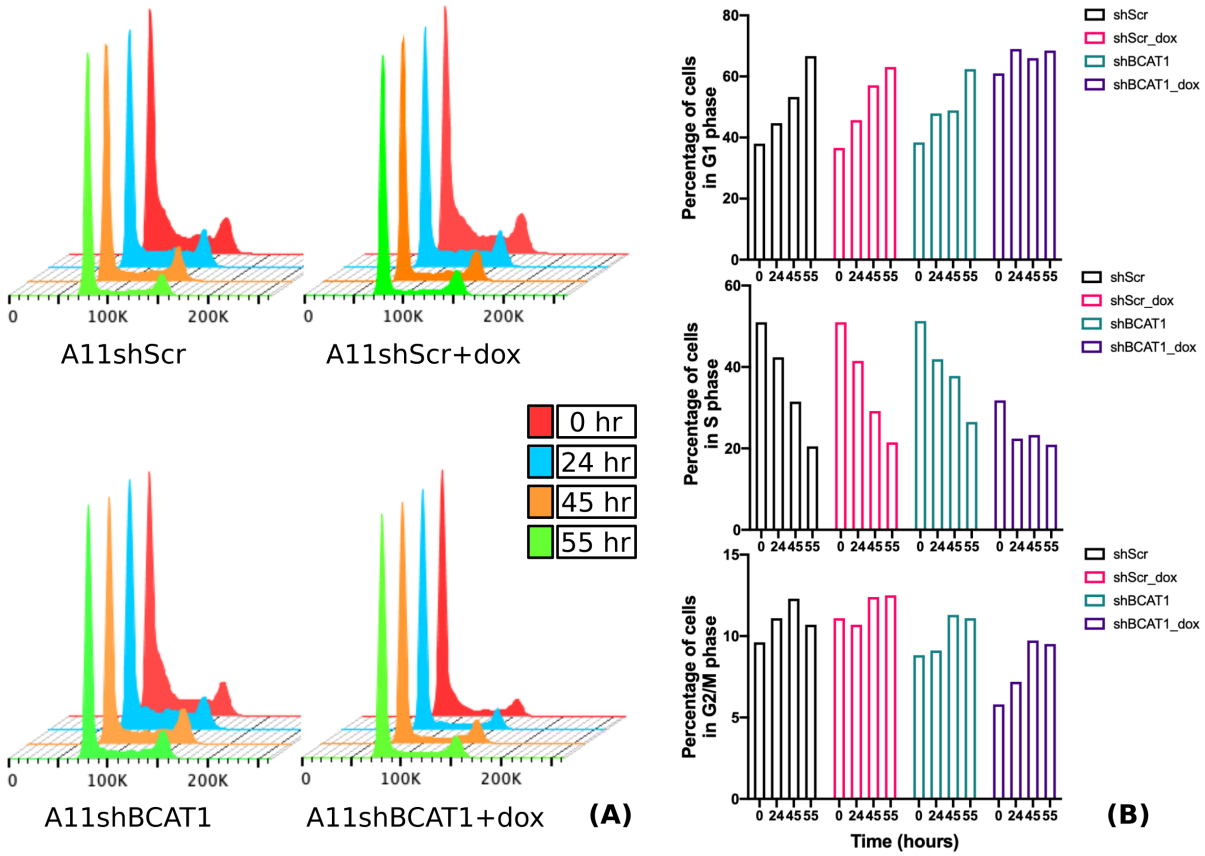

Figure 47 Cell synchronisation revealed that BCAT1 knockdown caused partial cell cycle arrest. *(A)Histograms showing propidium iodide staining, normalised to the mode of each distribution, for four timepoints following release of the cells from thymidine block. (B) Distribution of cells in the cell cycle phases.*

3.4.4.4 BCAT1 overexpression results in increased proliferation of A11 but not S2 cells

A11 cells showed moderate baseline levels of BCAT1 protein whereas S2 cells had no detectable BCAT1 on western blots. We hypothesized that if BCAT1 plays such an important role in cell proliferation, as suggested in the literature, then overexpression of the protein could potentially increase the proliferation rate of the cells. Constitutive overexpression of BCAT1, as detected by spectrophotometric assays of enzyme activity in cell lysates, led to an increased proliferation rate of A11 but slowed the proliferation of S2 cells (Figure 48).

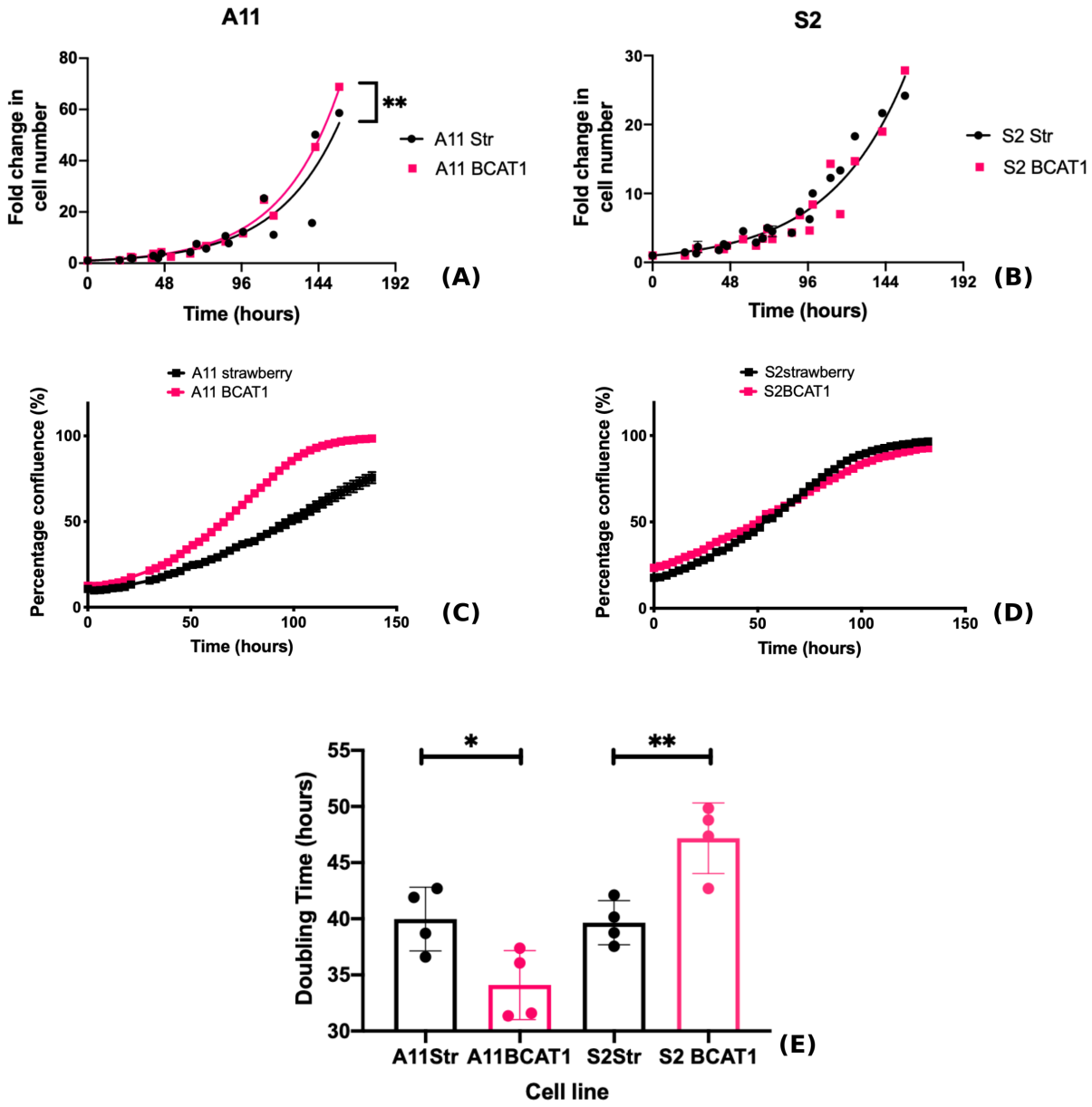

Figure 48 Proliferation rates of cells overexpressing BCAT1 and Luciferase-expressing controls. *(A,B) Increase in cell counts was measured using the ViCell instrument. The cell numbers measured from five independent experiments were pooled and nonlinear regression analysis was performed to fit exponential growth curves for the different cell lines. A comparison between the growth rate constant revealed significantly different rate constants between A11 BCAT1 overexpressing cells and luciferase and mStrawberry expressing controls ($p<0.01$) (A), but no statistically significant differences between S2 BCAT1 and controls ($p>0.05$) (B). (C-E) Cells were seeded in 6-well plates and incubated in the Incucyte microscope to measure increase in cell confluence over time. Representative growth curves of A11 BCAT1-overexpressing cells and their control cells (C) and S2 BCAT1-overexpressing cells and their respective control cells (D) are plotted. (E) Exponential curves were fitted to the growth curves of the cells in four independent experiments and the doubling times for the cells are plotted with error bars representing Standard Deviations.Two-tailed t-tests were performed to compare the Str cells and the BCAT1 overexpressing cells. *$p<0.05$, ***$p<0.001$*

3.4.5 BCAT1 plays a role in the invasive phenotype of A11 cells but not S2 cells

3.4.5.1 BCAT1 knockdown leads to reduced A11 cell migration and invasion

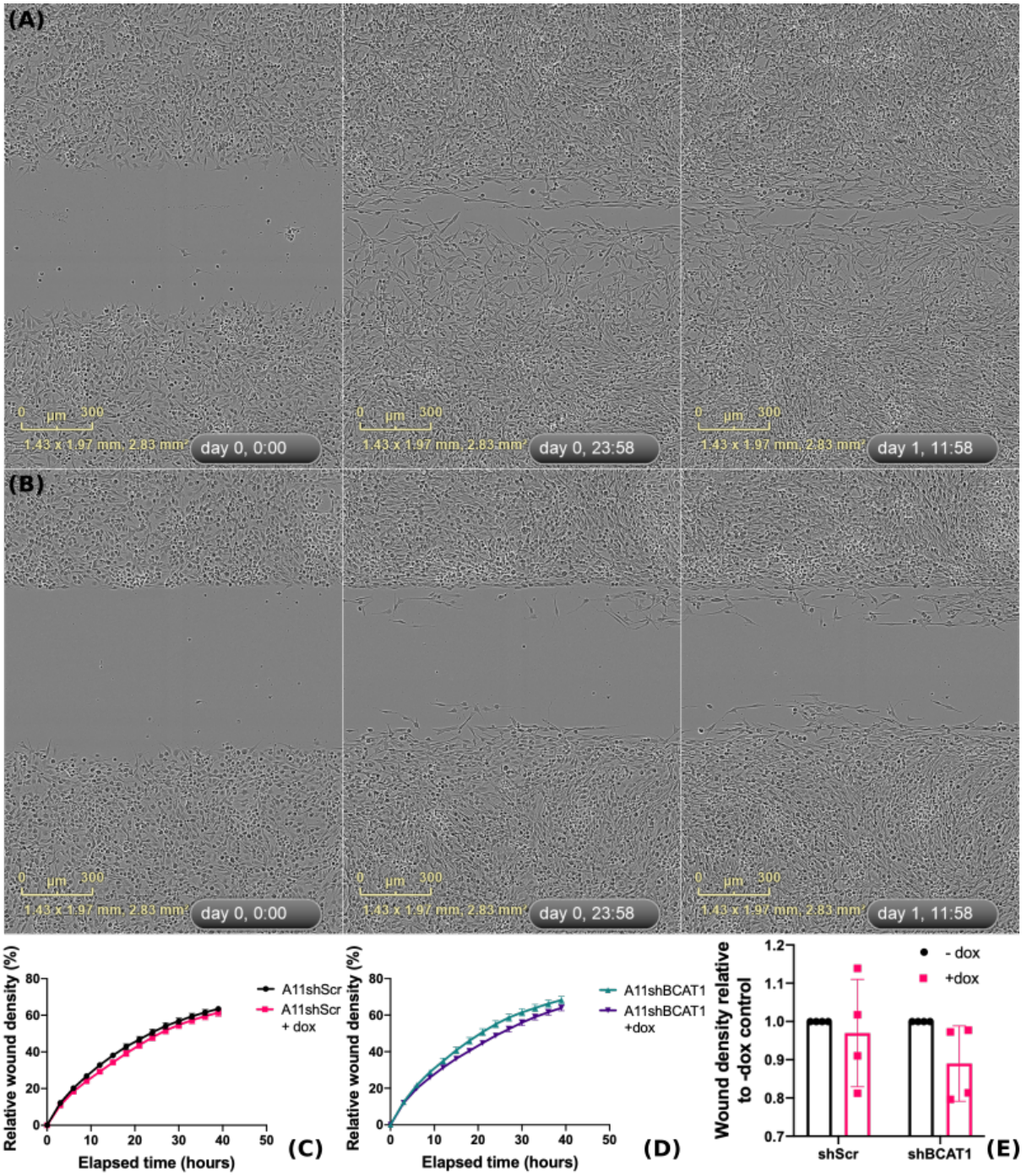

Figure 49 Inducible BCAT1 knockdown in A11 cells led to a small reduction in the ability of the cells to migrate across a scratch wound. *(A-B) Incucyte images showing the migration of A11shBCAT1 cells without doxycycline treatment (A) and following doxycycline treatment (B) over 36 hours after the formation of the scratch wound. The relative wound density from pooled data from five independent experiments is plotted over time for A11shScr (C) and A11shBCAT1 (D) cells, showing a small reduction in the migration of BCAT1 knockdown cells. (E) The relative wound density at 33 hours after the scratch*

wound, relative to the no doxycycline control is plotted for each of four independent experiments. Error bars represent Standard Deviation.

The effect of inducible BCAT1 knockdown on the capacity of cells to migrate on plastic and invade through Matrigel was investigated using the Scratch Wound assay. A small reduction in both migration (Figure 49) and invasion (Figure 50) were observed in A11 cells upon BCAT1 knockdown. The cells differ in their morphology in the two assays, with the migrating cells maintaining their original morphology (Figure 49) while the invading cells are much more elongated (Figure 50).

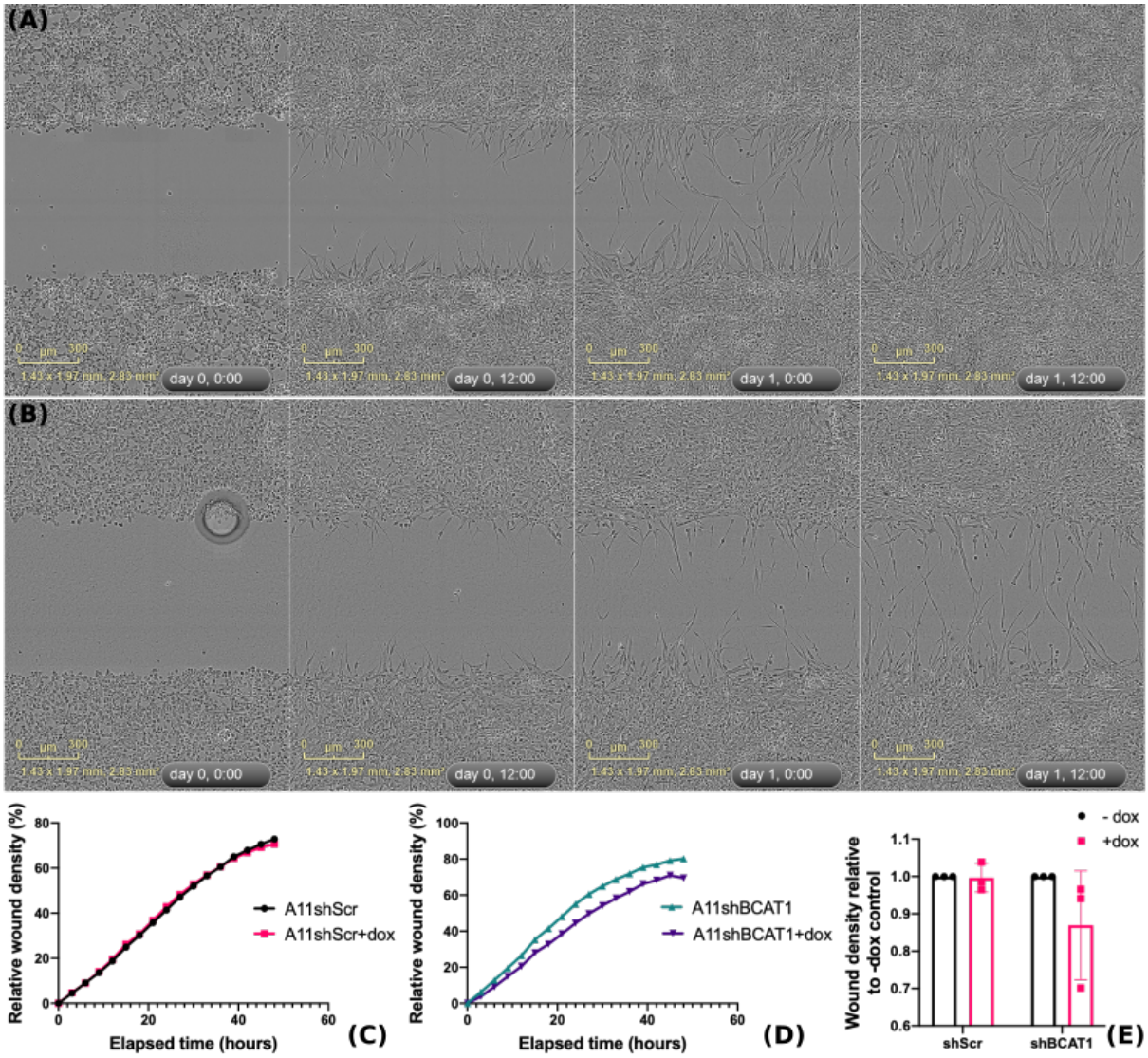

Figure 50 Inducible BCAT1 knockdown in A11 cells led to a reduction in the ability of the cells to invade through a Matrigel layer in the scratch wound assay. *(A-B) Representative images showing the invasion of A11shBCAT1 cells, without doxycycline induction (A) and with doxycycline induction (B), through the Matrigel layer, which was deposited in the scratch wound, over a period of 36 hours. (C-D) Relative wound density over time of pooled data from three independent experiments for A11shScr (C) and A11shBCAT1 (D) cells. (E) Wound density at 33 hours post scratch wound formation, relative to control cells that were not induced with doxycycline for A11shScr and A11shBCAT1 cells. Error bars represent Standard Deviation.*

3.4.5.2 Constitutive overexpression of BCAT1 leads to higher migration and invasion capacity in A11 cells but no change in S2 cells

In order to further define the role of BCAT1 in the invasive phenotype of GBM cells, A11 and S2 cells constitutively overexpressing BCAT1 were compared with their respective strawberry and luciferase expressing controls in a scratch wound migration assay and in a scratch wound invasion assay, similarly to the BCAT1 knockdown experiments, as well as in three-dimensional neurosphere Matrigel assays.

We observed a trend towards increased migration and invasion of A11 cells overexpressing BCAT1 but no change in the S2 cells, as measured in a scratch-wound assay (Figure 51). Three-dimensional invasion assays were set up to investigate the invasion properties of the cells in a more biologically relevant setting[101]. In these experiments, patient-derived glioblastoma cells were grown as spheroid cultures, with the 3D structure mimicking the tumour micro-environment. The neurospheres were then embedded in Matrigel and imaged in the Incucyte microscope every 3 hours for four days, while the cells were in the process of invading through the Matrigel. Upon BCAT1 overexpression, more cells could be seen leaving the sphere and invading the basement membrane, whereas A11 control neurospheres grew uniformly with less activity on their surface. To quantify these changes, a Python script was used to measure the area covered by cells, including and excluding the neurosphere. The area covered by cells, excluding the neurosphere, is the invaded area, which when normalised to the area of the neurosphere, shows an increased invasion capacity in the BCAT1-overexpressing A11 cells when compared to the control cells. S2 cells, on the other hand, showed no significant changes upon BCAT1 overexpression (Figure 52). S2 cells are able to proliferate and invade in the absence of baseline BCAT1 expression, and the absence of any significant changes upon BCAT1 overexpression in these cells suggest that their phenotype is independent of BCAT1.

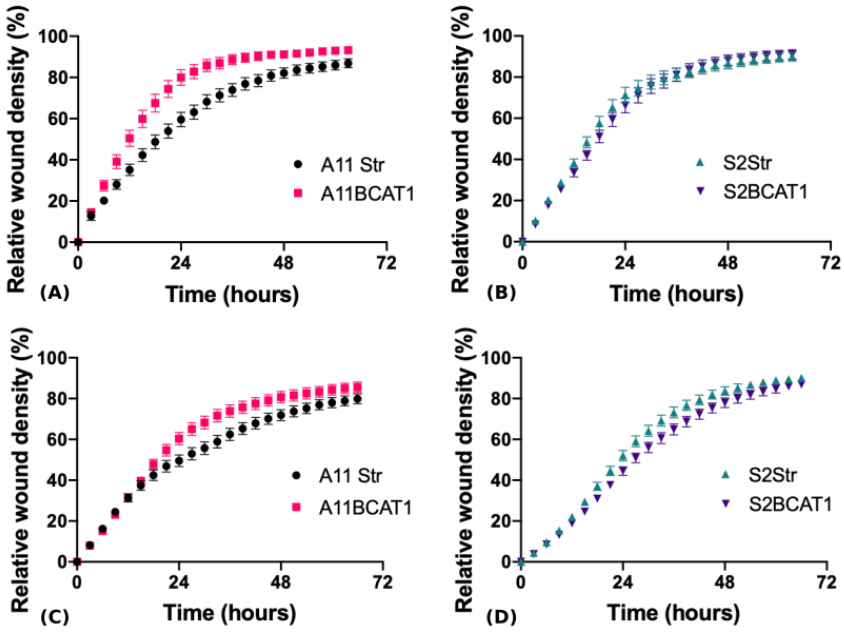

Figure 51 BCAT1 overexpression leads to slightly increased migration and invasion in A11 cells but not in S2 cells. *The mean relative wound density from 15 technical replicates of one independent experiment are plotted over time in a migration scratch wound assay for A11 (A) and S2 (B) cells overexpressing BCAT1 or luciferase as a control. Similarly, the mean relative wound density from 15 technical replicates of one independent experiment are plotted over time in a two-dimensional scratch wound Matrigel invasion assay for A11 cells (C) and S2 cells (D).*

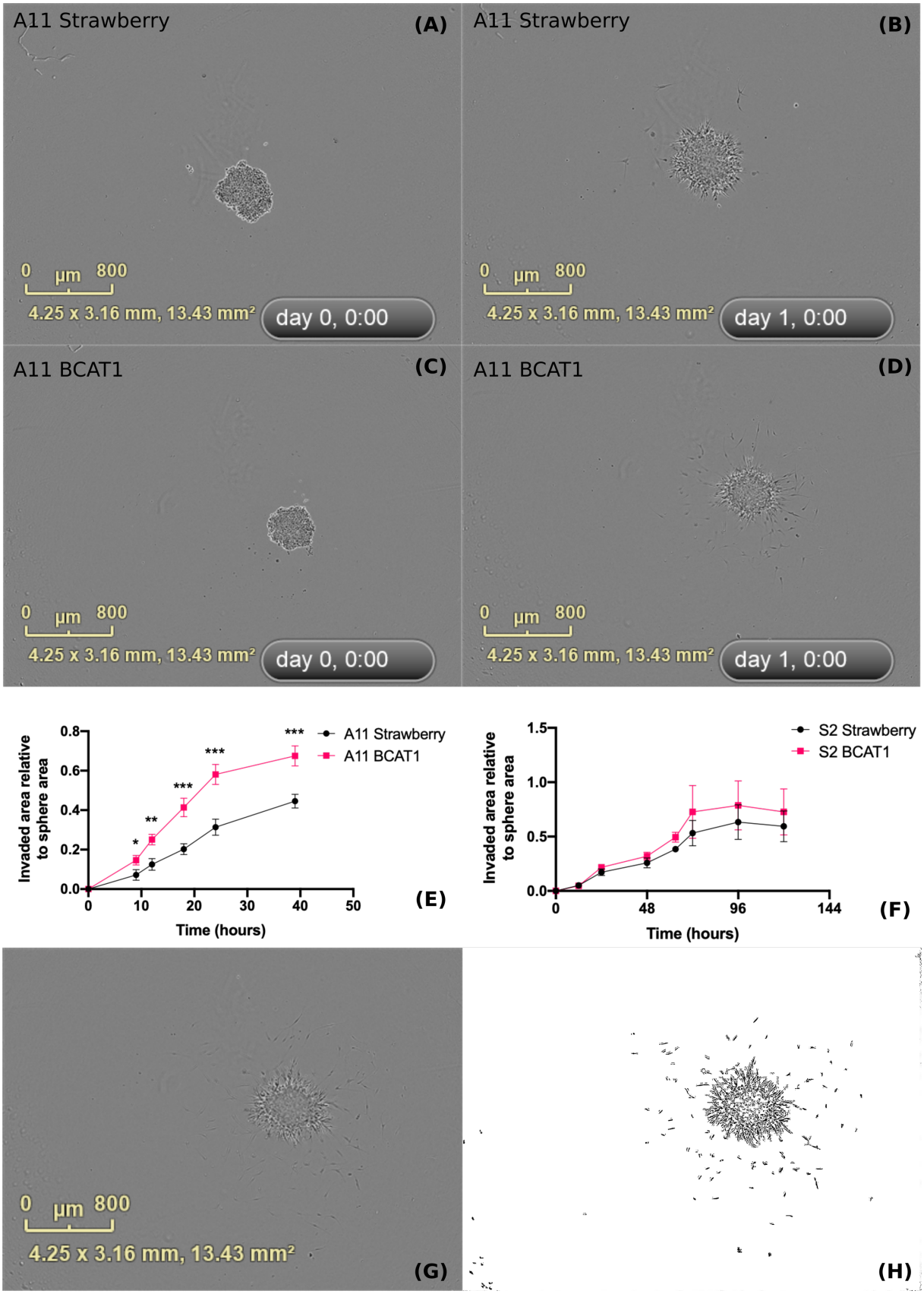

Figure 52 Investigation of the invasion capacity of cells following BCAT1 overexpression in three-dimensional invasion assays. *(A-D) Representative images from a three-dimensional invasion assay at the start of the experiment, where the spheroid is embedded in matrigel (A,C) and 24 hours later (B,D) for A11Str cells (A,B) and A11 BCAT1 overexpressing cells (C,D). The BCAT1 overexpressing cells cover a larger area over time compared to the control cells. (E) The area invaded by the cells*

*over time was quantified and normalised to the area of the sphere for six replicates in each of three independent experiments and the mean of biological replicates is plotted for A11 Str and A11 BCAT1 cells (E), as well as S2 Str and S2 BCAT1 cells (F), with error bars representing SEM. Multiple t-tests corrected for multiple comparisons using the Holm-Sidak method were performed to compare the Str and BCAT1 overexpressing cells. *p<0.05, **p<0.01, ***p<0.001. (G,H) Illustration of the cell detection algorithm, with the original image in (G) and the detected cells in (H).*

3.4.5.3 Cell surface expression of CD147 may be linked to the changes in invasion profiles

To investigate whether CD147, which has already been implicated in cell migration and invasion might be involved in the mechanism through which modulation of BCAT1 expression leads to changes in cell invasion, the cell surface expression of CD147 was compared between cell lines. BCAT1 knockdown in A11 cells led to significantly higher levels of CD147 surface expression while BCAT1 overexpression in A11 cells had the opposite effect. BCAT1 overexpression in S2 cells had a smaller effect (Figure 53).

The changes in the amount of cell surface expressed CD147 may reflect changes in the secretion of the protein, suggesting that BCAT1 knockdown leads to less CD147 secretion which could contribute to the effects on cell migration and invasion. It has been suggested that CD147 exists in both soluble and membrane-bound forms and that through secretion of CD147 by cancer cells, the surrounding stromal cells upregulate matrix metalloproteinases leading to tissue remodelling[57,175]. Measurement of secreted CD147 in media would enable further investigation of this hypothesis.

The co-localisation of CD147 with MCT1 and MCT4 transporters and the role of CD147 in facilitating the expression of the transporters on the plasma membrane raise more hypotheses regarding this observation which would be interesting to further investigate[176].

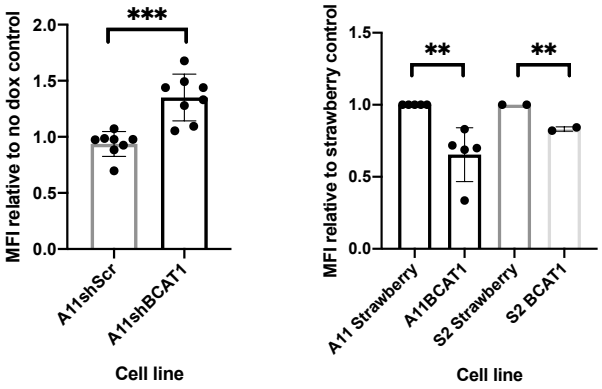

Figure 53 Expression of CD147 on the surface of GBM cells is increased upon inducible knockdown of BCAT1 and is reduced upon constitutive BCAT1 overexpression. *The surface expression of CD147 in A11shScr and A11shBCAT1 cells was measured by flow cytometry and the Median Fluorescence Intensity (MFI) of cells treated with doxycycline was plotted relative to untreated control cells (left). The MFI of A11 and S2 BCAT1 overexpressing cells is plotted relative to their Strawberry-Luciferase controls (right). Each point represents a biological replicate in an independent experiment. Two tailed t-tests were perfomed to compare the MFI between samples. **p<0.01, ***p<0.001*

3.4.6 Modulation of BCAT1 expression in A11 and S2 cells led to small changes in resistance to radiotherapy

BCAT1 has been suggested to play a protective role against reactive oxygen species in glioma, via glutamate synthesis, which is required for glutathione synthesis[155]. More specifically, glutaminase inhibition in *IDH* mutant glioma cells, where 2-hydroxyglutarate was shown to inhibit BCAT activity, led to reduced glutathione synthesis and sensitisation of glioma cells to radiation *in vitro* and *in vivo*. We thus hypothesised that modulation of BCAT1 expression might have an effect on the cells' resistance to radiotherapy. Cells were irradiated in 6-well plates at 16 and 20 Gy. The effects of radiotherapy were assessed with either flow cytometry and Sytox green staining or using the Vicell machine to quantify cell death using Trypan blue staining. BCAT1 knockdown in A11 cells led to a small increase in the sensitivity of cells to radiotherapy (Figure 54) while BCAT1 overexpression in both A11 and S2 cells led to a small increase in resistance to radiotherapy (Figure 55).

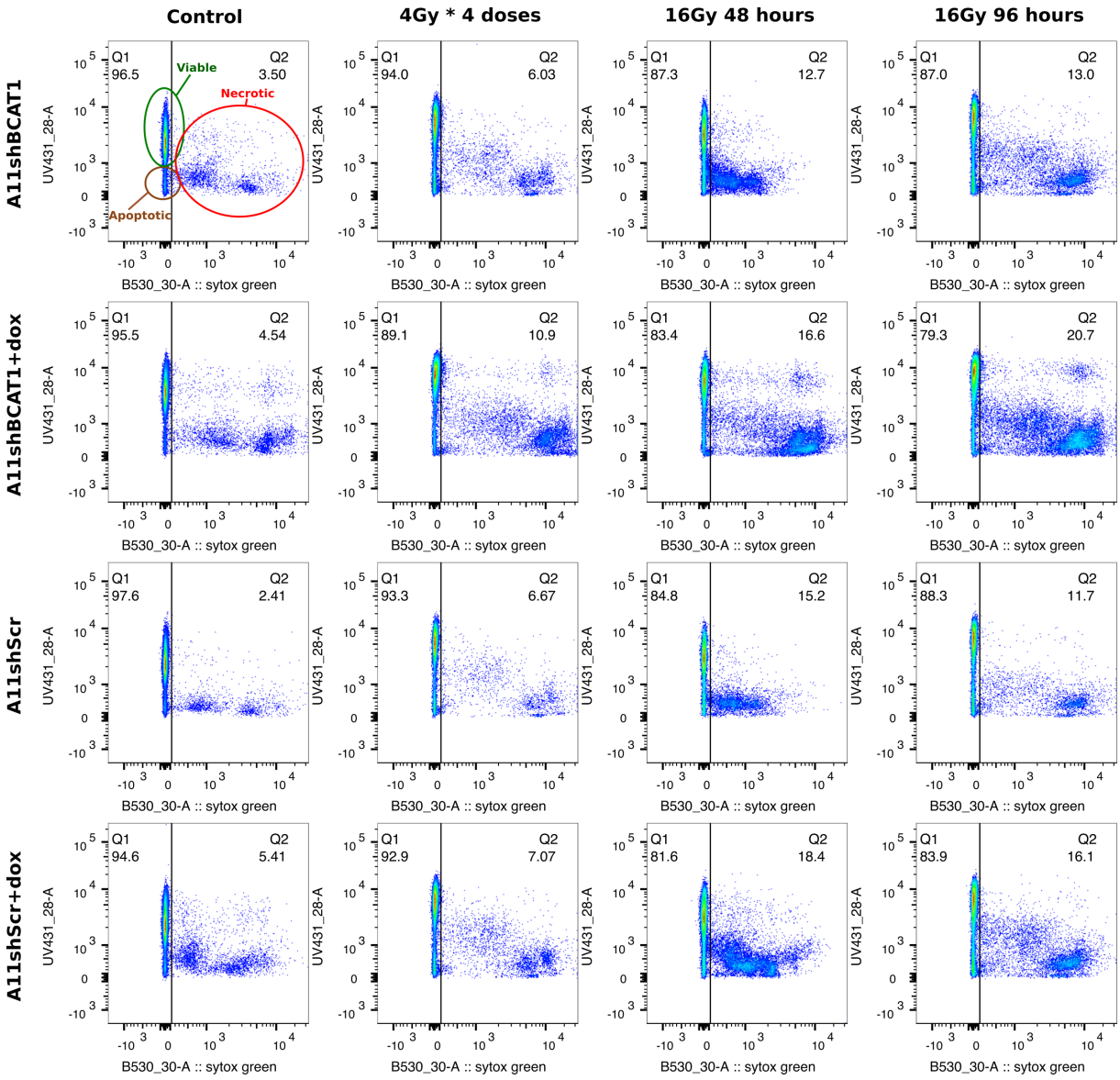

Figure 54 Cell irradiation leads to increased cell death in BCAT1 knockdown cells. *Flow cytometry dot plots showing Sytox Green staining on the x-axis and NADH levels, as measured by the UV detector on the y-axis, where the percentage of necrotic cells (Sytox positive) is shown in Q2. Four conditions were tested, control cells that were not irradiated, cells that were irradiated with 4 Gy every day for four days, cells that were irradiated with 16 Gy 48 hours before measuring cell death and cells irradiated with 16 Gy 96 hours before measuring cell death.*

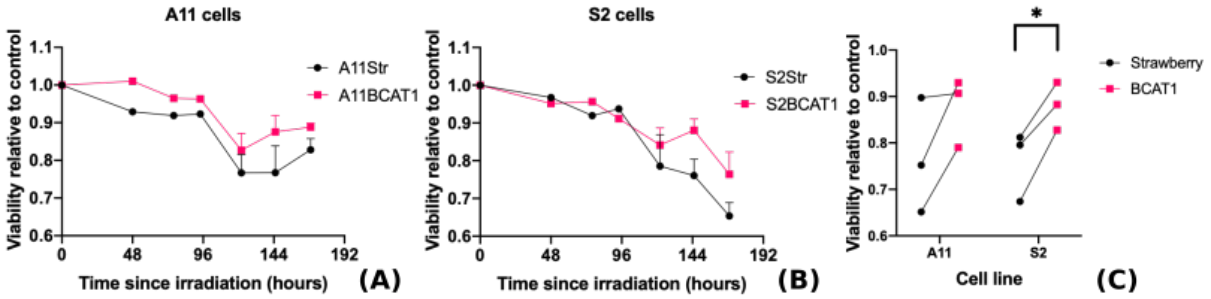

Figure 55 BCAT1 overexpression leads to increased radiotherapy resistance in both A11 and S2 cells. *Cells were treated with a single dose of 20 Gy using an irradiator and cell viability was measured using Trypan Blue dye exclusion in the Vicell and normalised to the viability of control untreated cells. Two-tailed t-tests were used to compare the Str control cells and BCAT1 overepxressing cells. *p<0.05*

3.4.7 BCAT1 knockdown leads to changes in the transcriptional profile of A11 cells

To further investigate the mechanism through which BCAT1 expression promotes cell proliferation, RNA sequencing analysis was performed to compare the transcriptional profiles of A11 BCAT1 knockdown and control cells. RNA sequencing under four different conditions (A11shScr and A11shBCAT1 with and without doxycycline treatment), followed by pairwise distance clustering of the groups, revealed that the BCAT1 knockdown samples clustered together and were significantly different to the other three control groups. The replicates of the three different control groups all clustered together, suggesting that the only transcriptionally different group was the BCAT1 knockdown group (Figure 56).

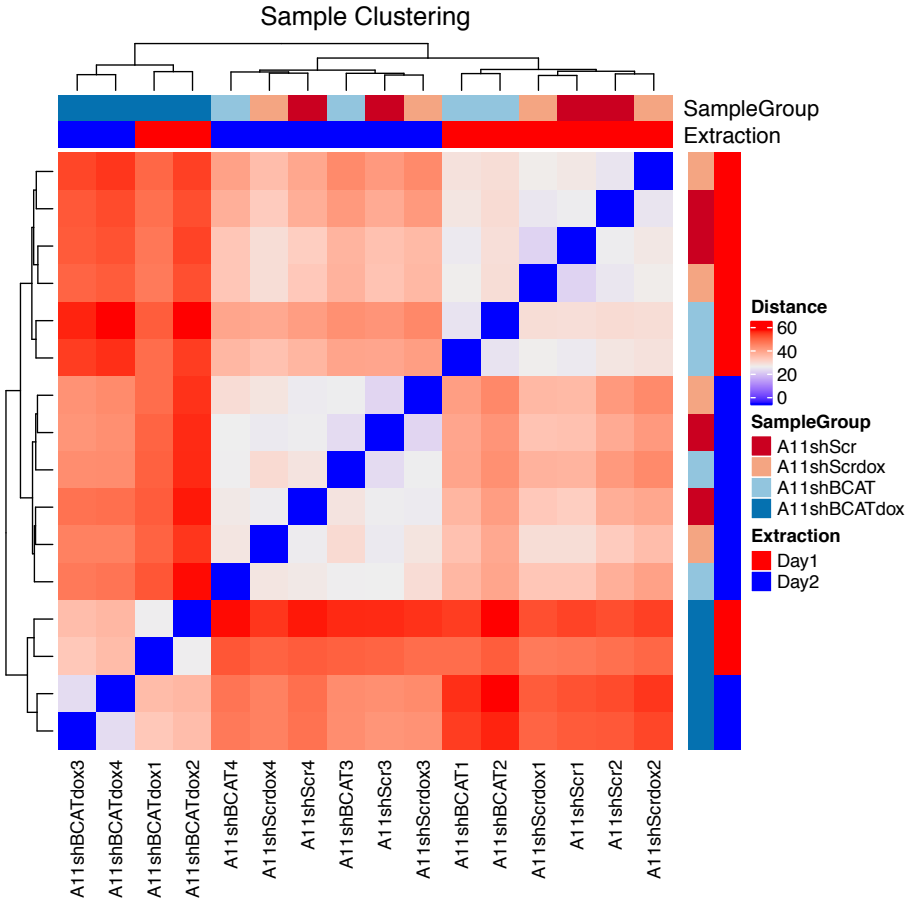

Figure 56 Clustering heat map, based on the pairwise distance between samples, considering read counts at all annotated features. *The four BCAT1 knockdown samples clustered together and away from the other three control groups.*

Principal Component Analysis (PCA) of the variance-stabilizing transformed raw counts based on the top 500 most variable features showed that most of the variance in the samples was attributed to BCAT1 knockdown. Data analysis also revealed that the day of sample extraction

contributed to some variance across the samples, which was accounted for in subsequent analyses (Figure 57).

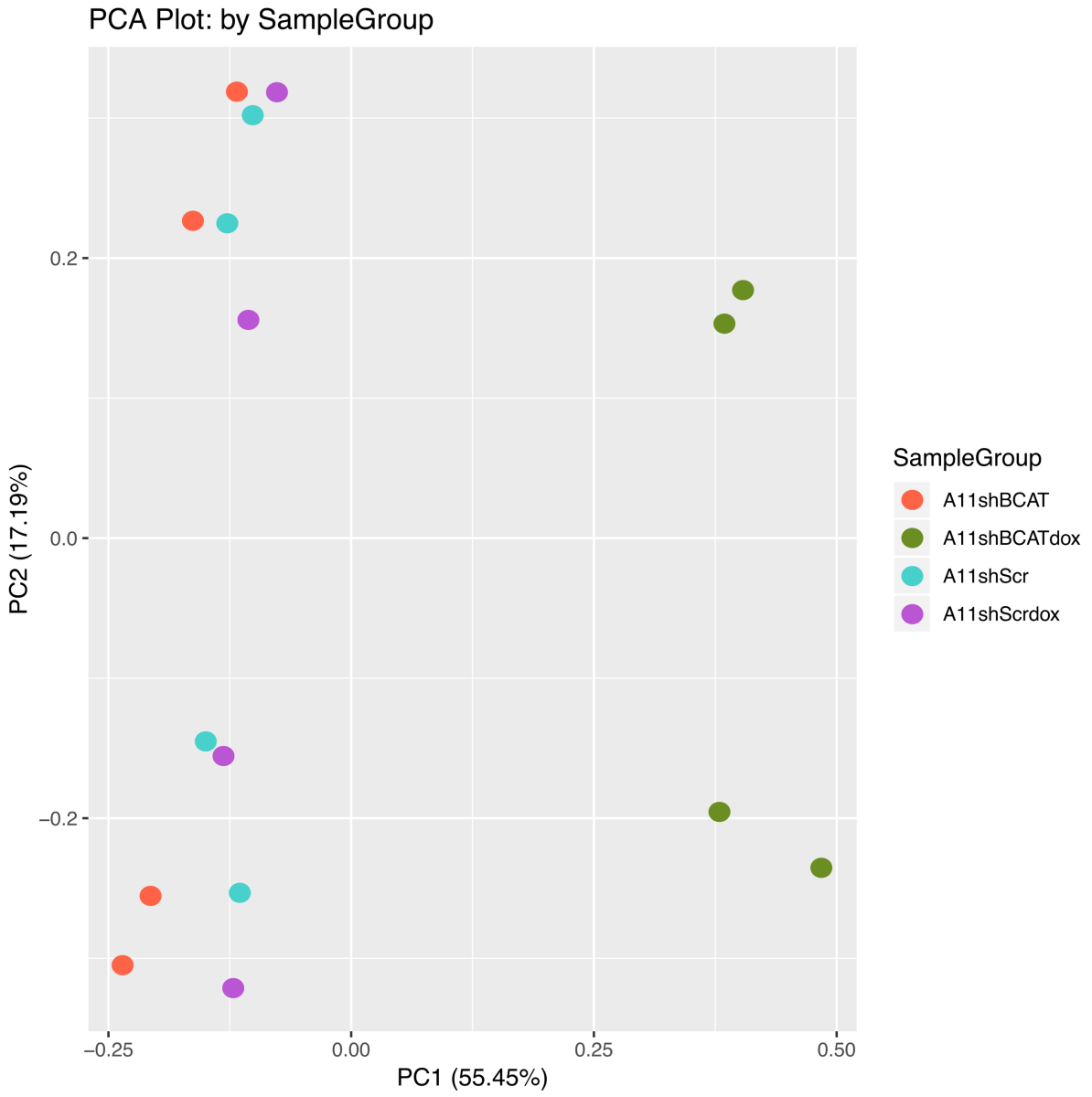

Figure 57 Principal Component Analysis of the variance-stabilizing transformed raw counts based on the top 500 most variable features from the pairwise analysis between A11shBCAT1 induced and non-induced samples. *The first component, which is responsible for most of the variance in the samples, separated the BCAT1 knockdown sample and the second component illustrates the effects of extraction on different days.*

Pairwise comparisons between all the test groups were made and each comparison yielded a list of differentially expressed genes. As expected from the clustering analysis and PCA, comparing the shBCAT1 + dox treatment group against any of the other three control groups yielded many more differentially expressed genes than any other comparison. Interestingly, very few differentially expressed genes appeared when comparing any of the three control groups (Figure 58). The presence of no statistically significant differentially expressed genes

between shScr cells with doxycycline treatment and shScr cells with no doxycycline treatment, suggested that doxycycline treatment did not have major transcriptional effects on the cells. This suggested that using the comparison between shBCAT1 cells with and without doxycycline for investigating transcriptional effects upon BCAT1 knockdown was valid. Also, there was a large overlap between the differentially expressed genes when comparing BCAT1 knockdown cells with any of the three control groups, further validating the experiment (Figure 59).

Numerator	Denominator	Upregulated	Downregulated
A11shScrdox	A11shScr	0	0
A11shBCATdox	**A11shBCAT**	**2994**	**3548**
A11shBCATdox	**A11shScr**	**2872**	**3251**
A11shBCATdox	**A11shScrdox**	**2801**	**3191**
A11shBCAT	A11shScr	114	60
A11shBCAT	A11shScrdox	164	99

Figure 58 Numbers of significantly upregulated and downregulated genes between different comparison groups*. A11 BCAT1 knockdown sample group compared with any of the other 3 control groups yielded a high number of differentially expressed genes, whereas the three control groups were very similar to each other, yielding small numbers of differentially expressed genes.*

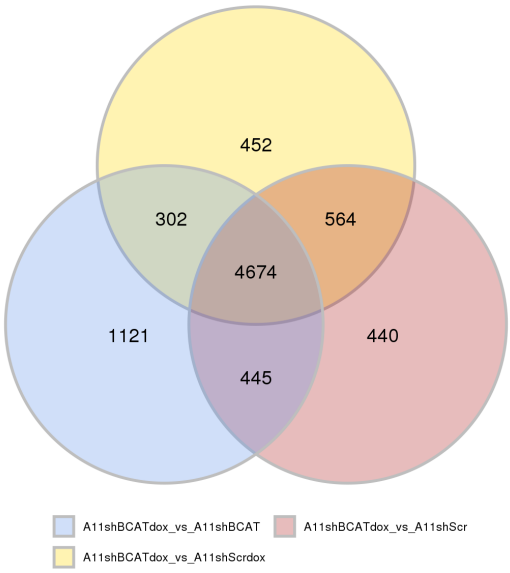

Figure 59 Illustration of the overlap between the differentially expressed genes when comparing BCAT1 knockdown samples against the three control groups. *The numbers shown in the Venn diagram include both upregulated and downregulated genes. Most of the differentially expressed genes were found in the intersection of all three comparisons suggesting that they are truly an effect of the knockdown of BCAT1.*

When directly comparing A11shBCAT1 cells which were induced with doxycycline versus A11shBCAT1 cells that were not induced, the transcriptional profile of the cells was

significantly different with thousands of upregulated and downregulated genes. Focusing on the top 200 most significantly differentially expressed genes, the BCAT1 knockdown cells showed a clear distinction from all other test groups (Figure 60).

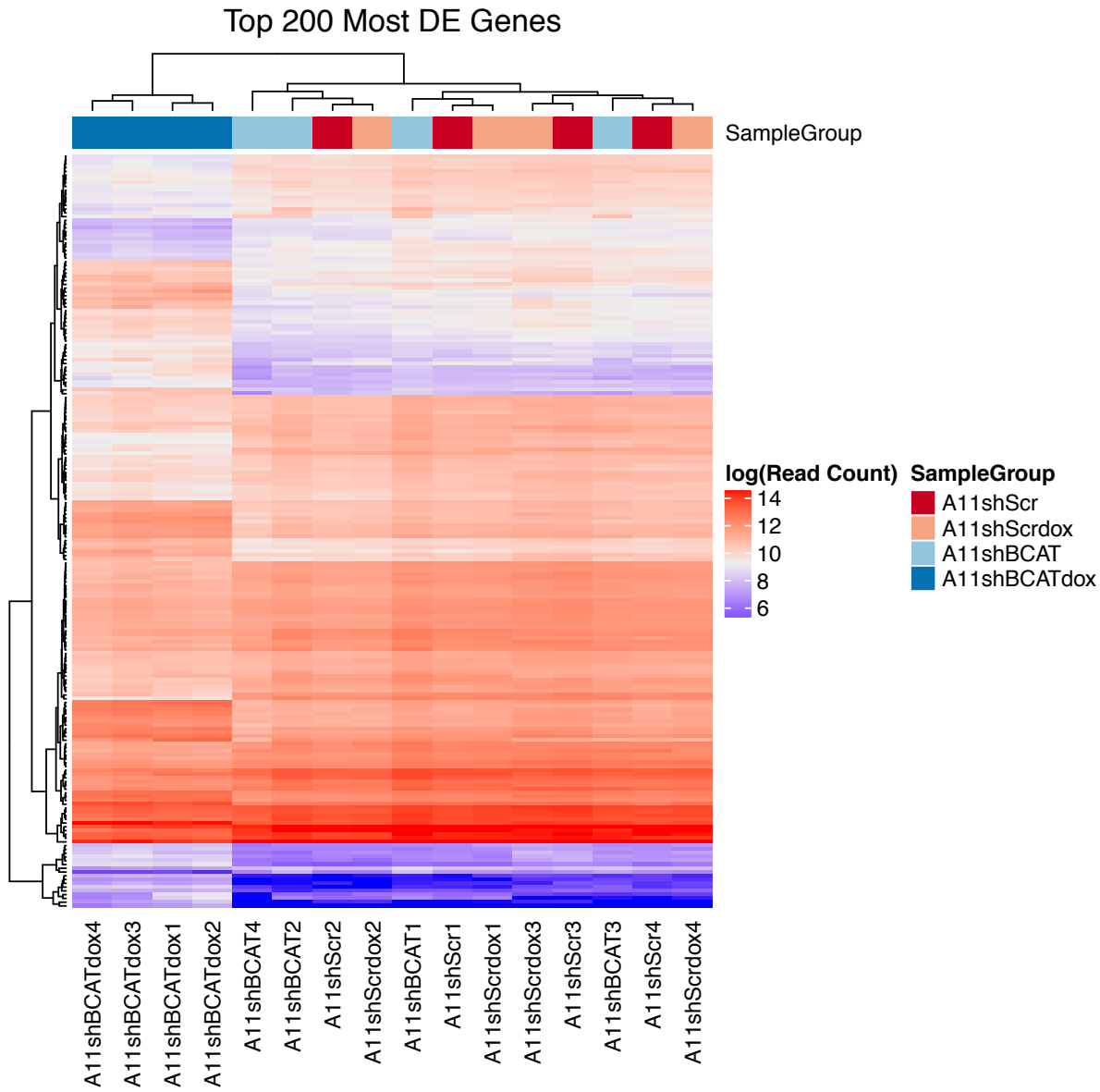

Figure 60 Heat map showing how the top 200 most significantly differentially expressed genes in the pairwise analysis of A11shBCAT1 induced and non-induced clustered across all test samples.

3.4.8 Gene enrichment analysis revealed a connection between BCAT1 expression and HIF stabilisation

To further investigate the transcriptional changes upon BCAT1 knockdown, gene enrichment analysis was performed using the list of genes that were differentially expressed in the BCAT1 knockdown cells versus the control cells. This showed that a number of pathways and cellular

processes were affected upon BCAT1 knockdown (Figure 61). Many of the processes being affected were related to cell cycle progression, with many cyclins and cell cycle checkpoint proteins being downregulated (Figure 62), which is in agreement with the partial cell cycle arrest observed in the cells upon BCAT1 knockdown (Figure 46 and Figure 47).

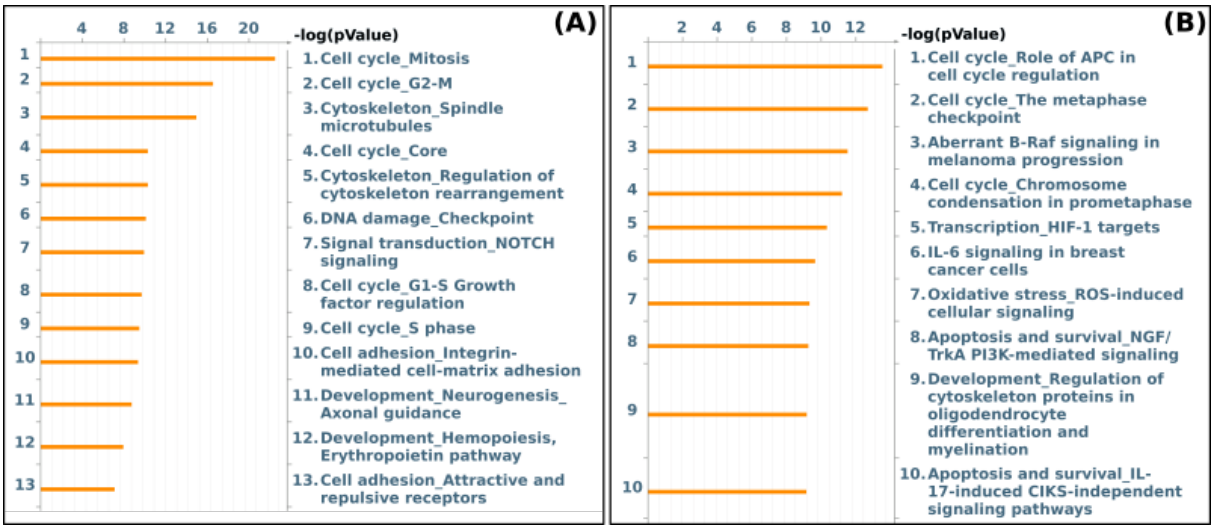

Figure 61 Gene enrichment analysis results using Metacore (Clarivate Analytics) tool*. The list uploaded to the tool included the genes that were differentially expressed in both comparisons of A11shBCAT1+dox transcripts with A11shBCAT1 without dox and A11shScr+dox transcripts. The top process networks (A) and pathway maps (B) that were enriched in the gene list are plotted here against their respective -log(pValue).*

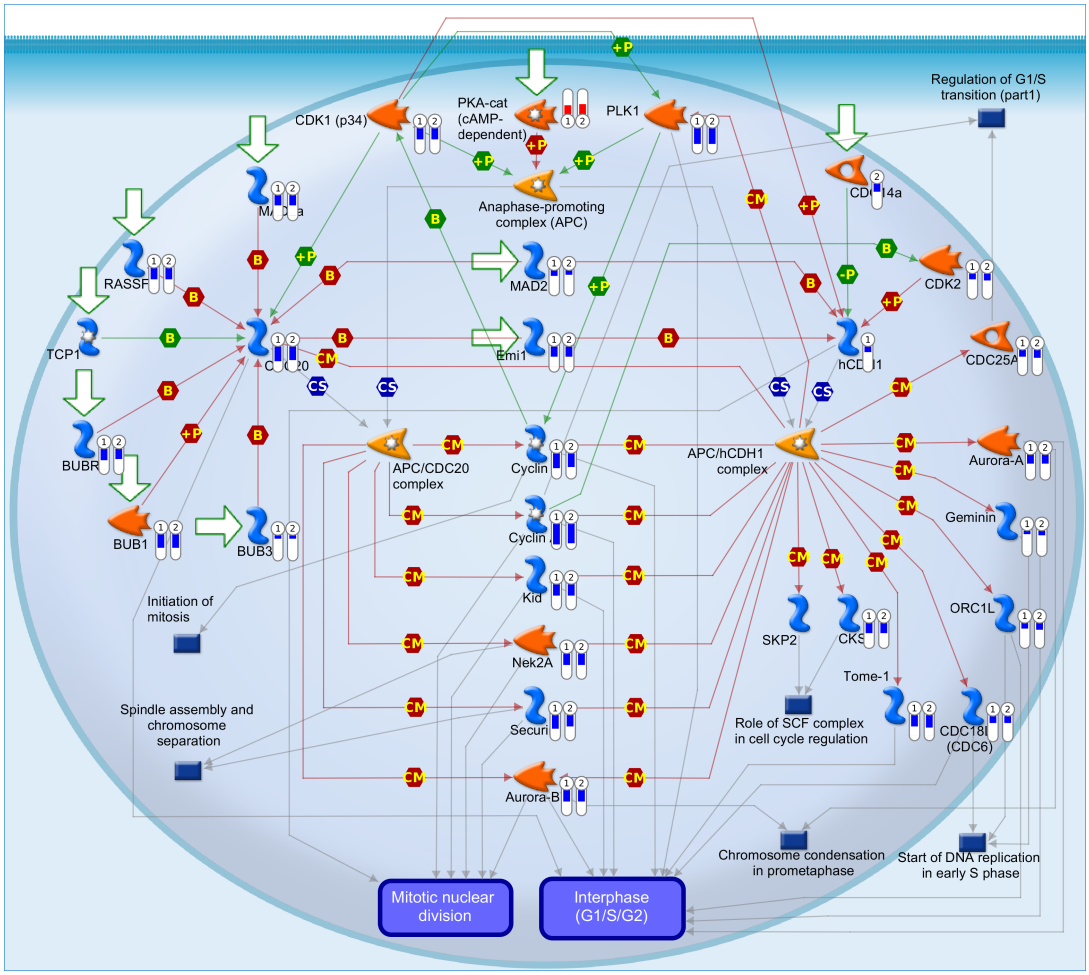

Figure 62 BCAT1 knockdown leads to downregulation of the processes controlling G1/S cell cycle transition. *Imagemap of the regulation of G1/S cell cycle transition, generated using Metacore. The differentially expressed genes from both A11shBCAT1+dox vs A11shBCAT1 and A11shBCAT1+dox vs A11shScr+dox comparisons are shown next to the protein name, numbered 1 and 2, respectively, with blue representing downregulation and red representing upregulation.*

In addition to cell cycle changes, the HIF-1α pathway was in the top enriched pathway maps from gene enrichment analysis. The downregulation of the HIF pathway upon BCAT1 knockdown was validated *in vitro* and *in vivo*, by blotting for HIF-1α as well as the products of HIF1 target genes, Carbonic Anhydrase IX (CAIX) and Hexokinase II (HKII) in cell lysates and in PDOX tumour lysates. Induction of BCAT1 knockdown with doxycycline led to reduced levels of HIF-1α and reduced levels of HKII and CAIX. Doxycycline treatment of control cells also led to reduced levels of HIF-1α but the effect upon BCAT1 knockdown was bigger (Figure 63). The effect of BCAT1 on CAIX levels was also confirmed in BCAT1 overexpressing cells which had higher CAIX levels compared to their controls. Additionally, immunohistochemical staining of patient derived orthotopic xenografts established in rats following injection of A11 cells, showed co-localisation of high BCAT1 staining with CAIX, MCT1 and MCT4 staining, all of which are targets of HIF (Figure 64).

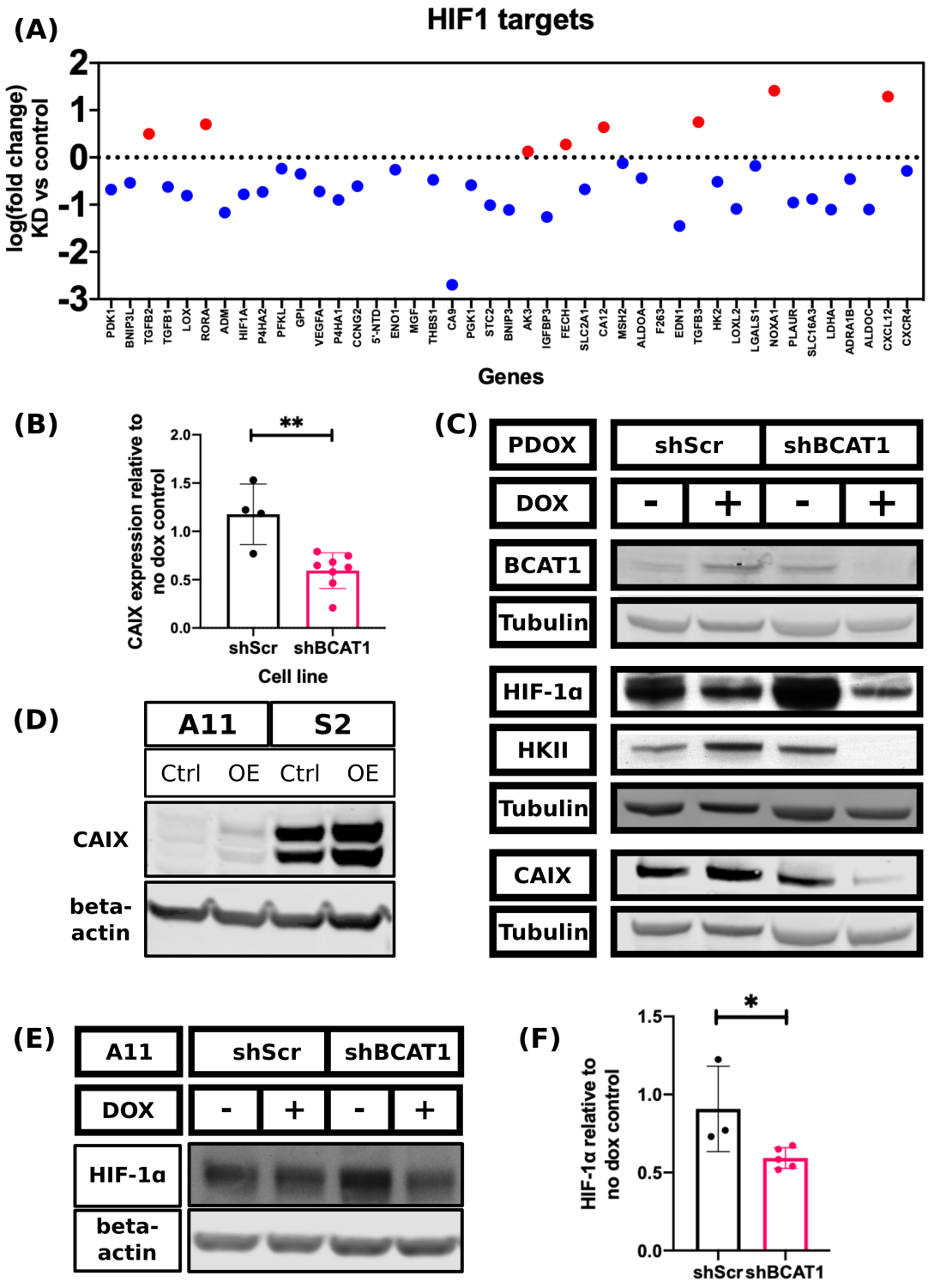

Figure 63 BCAT1 controls HIF transcriptional activity in GBM models. *(A) The log(fold change) in expression when comparing A11shBCAT1 cells induced with doxycycline versus cells not induced is plotted for every HIF target that was revealed in the enrichment analysis by Metacore. (B) Quantitative data from western blots for CAIX expression from lysates of A11shScr and A11shBCAT1 cells treated with doxycycline relative to the non-doxycycline induced controls. Each point represents a measurement from an independent experiment and the error bars represent Standard Deviations. A two-tailed t-test was performed to compare the two groups. **p<0.01 (C) Western blots for BCAT1, HIF-1a, HKII, CAIX and β-tubulin loading control from lysates of A11shScr and A11shBCAT1 PDOXs. (D) Western blots for CAIX and beta actin loading control from cell lysates of control and BCAT1 overexpressing A11 and S2 cells. (E-F) For measurement of HIF-1a levels in A11 control and BCAT1 knockdown cells, cells were incubated at 1% O_2 for 8 hours, before cell lysis and protein extraction. A representative western blot of HIF-1a and beta-actin loading control is shown in (E) and the densitometric data from all independent experiments are summarised in (F). A two-tailed t-test was performed to compare the two groups. *p<0.05*

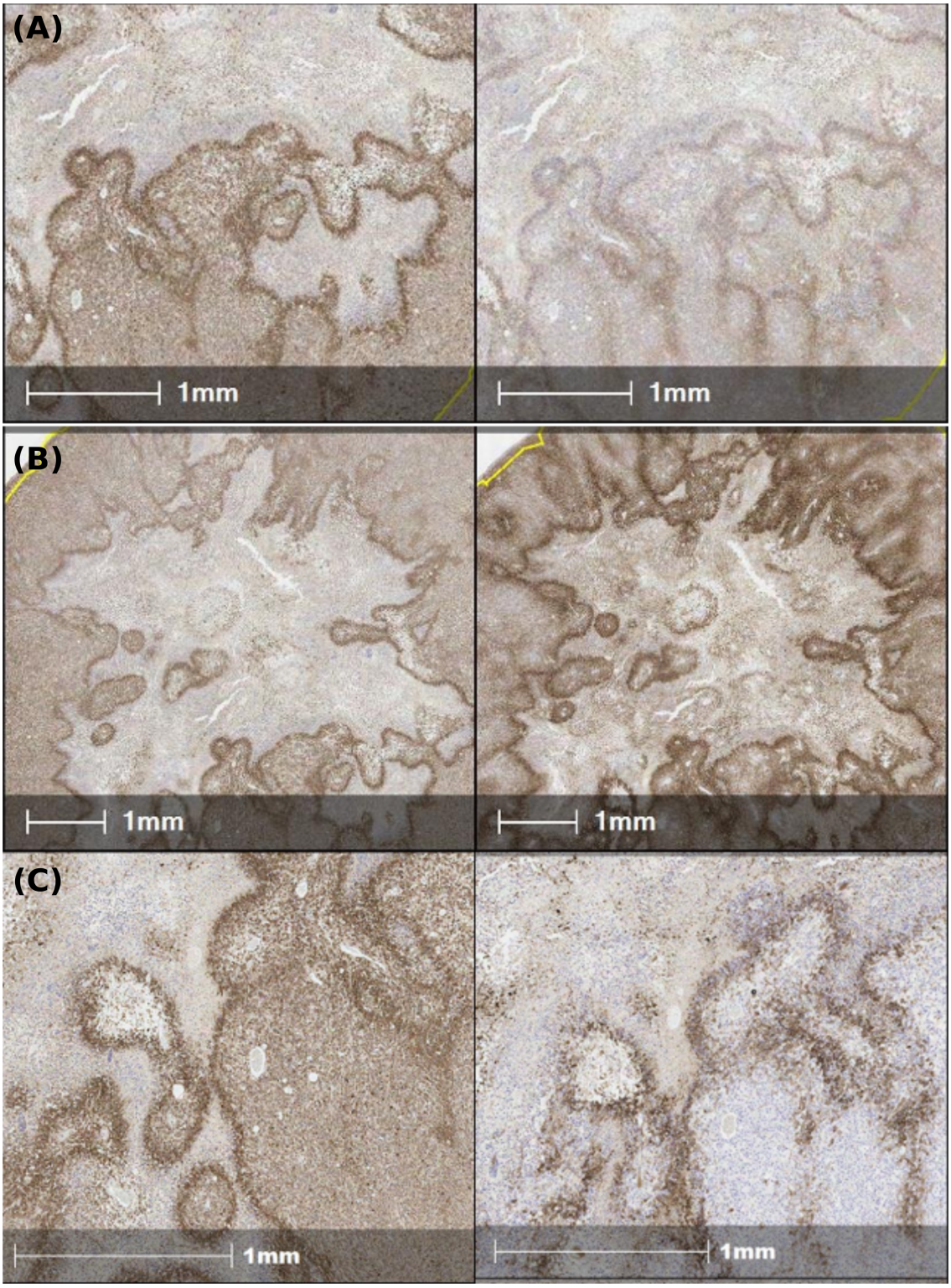

Figure 64 Immunohistochemical staining showing co-localisation of BCAT1 with MCT1, MCT4 and CAIX. *Representative examples of IHC images from sections of a rat brain containing an A11 tumour, stained for BCAT1 on the left and MCT1 (A), MCT4 (B) and CAIX (C) on the right. The images are from a representative tumour and only the tumour (with its necrotic core and the periphery) is visible in the Field of View.*

FOXM1 is a transcription factor that has been documented to play multiple roles in glioblastoma[96-98,109,110]. FOXM1 is a direct target of HIF, with HIF binding sites found in the

FOXM1 promoter region[106]. Analysis of the RNA sequencing data revealed that FOXM1 as well as many of its target proteins were downregulated upon BCAT1 knockdown. FOXM1 downregulation was confirmed *in vitro* in lysates of A11 BCAT1 knockdown cells and control cells as well as *in vivo* in PDOX in mice (Figure 65).

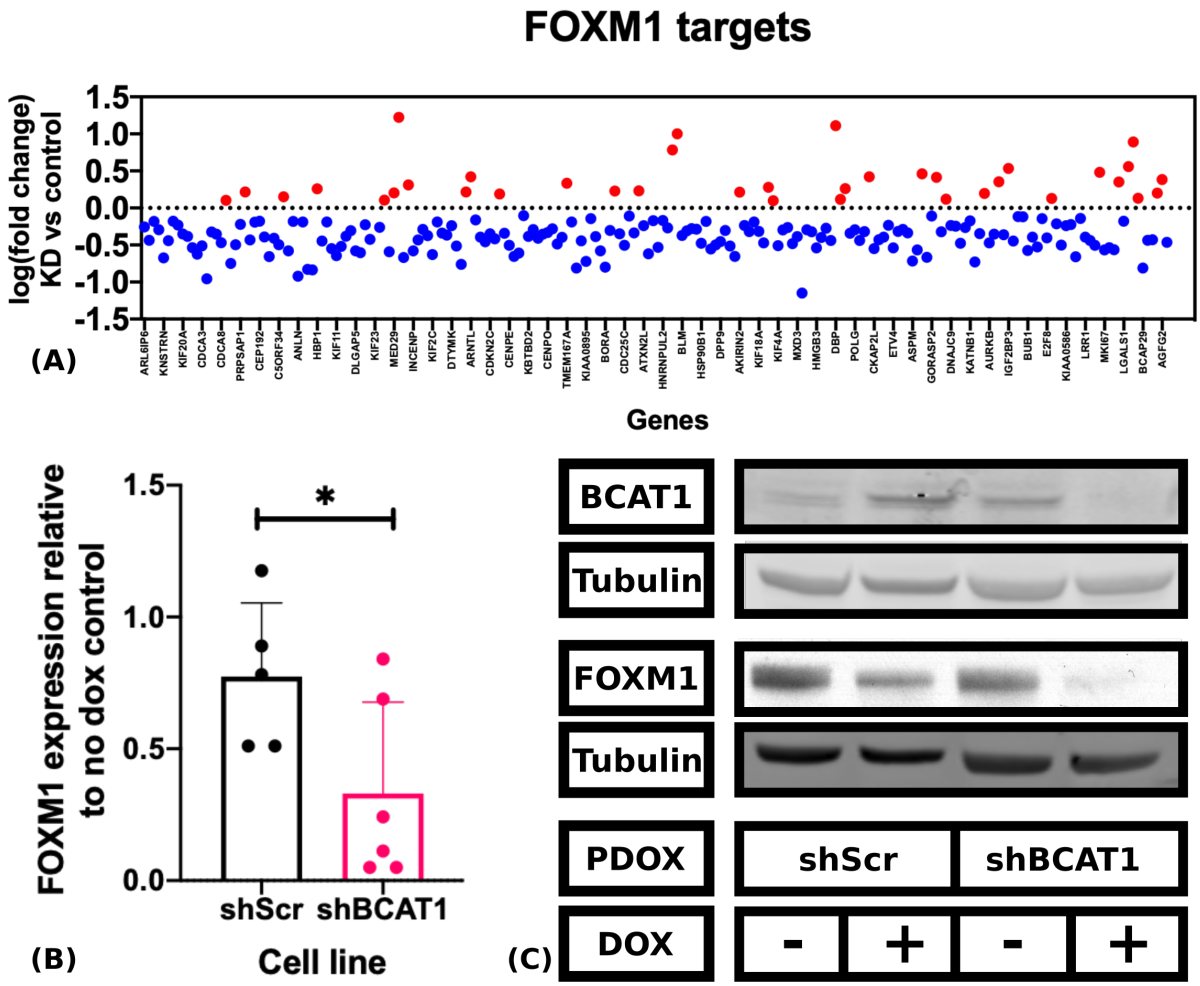

Figure 65 FOXM1 transcription factor and its targets are downregulated upon BCAT1 knockdown in A11 cells. *(A) The mean logarithmic fold change in transcript numbers when comparing A11shBCAT1 cells that were induced with doxycycline and those that were not induced is plotted for each target gene of FOXM1, showing significant enrichment of FOXM1 transcriptional targets in the differentially expressed genes upon BCAT1 knockdown. The target genes of FOXM1 were acquired from Pathway Enrichment analysis using EnrichR online tool. (B) Quantitative data from Western Blots of cell lysates showing the expression of FOXM1 relative to the non-induced cells for shScr and shBCAT1 cells. Each point represents a measurement from an independent experiment and the error bars represent the Standard Deviations. Two-tailed t-test analysis was performed to compare the two cell lines (n=5). *p<0.05 (C) Western blots of BCAT1, FOXM1 and β-tubulin loading control in lysates of dissected brain tumours from mice. To induce BCAT1 knockdown, mice were fed with doxycycline-containing diet for 10 days.*

RNA sequencing analysis showed that a number of genes that have been associated with glioblastoma stem-like cells were significantly downregulated upon BCAT1 knockdown in A11 cells, including *ALKBH5, ANP32E, CENPF, FANCI* and *FOXM1*. A neurosphere formation assay was performed and Extreme Limiting Dilution Analysis (ELDA) was used to

compare A11 BCAT1 knockdown cells with control cells. Knockdown of BCAT1 was induced in the cells by incubating with doxycycline for seven days before sorting 1, 5, 10 and 20 cells in each well of a 96-well plate. Doxycycline treatment was discontinued following seeding of the cells in the plate and the cells were incubated for at least three weeks before the number of sphere-containing wells was measured. Therefore, the effect of BCAT1 knockdown on cell proliferation had minimal contribution to the phenotype measured. Instead, the frequency of cells capable of replication at the time of seeding determined the number of neurospheres being formed. From three independent experiments, a significant reduction in stem cell frequency was observed upon BCAT1 knockdown in A11 cells, suggesting that BCAT1 knockdown reduced the neurosphere-forming potential of the cells (Figure 66).

Group	Dose	Tested	Response
A11shScr	1	12	0
	5	12	2
	10	12	4
	20	12	12
A11shScr+dox	1	12	0
	5	12	1
	10	12	6
	20	12	11
A11shBCAT1	1	12	0
	5	12	4
	10	12	10
	20	12	12
A11shBCAT1+dox	1	12	0
	5	12	0
	10	12	4
	20	12	8

(A)

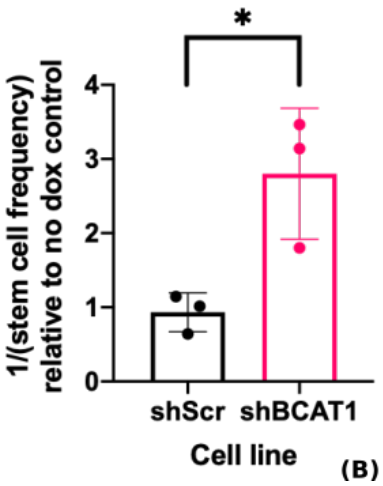

(B)

Figure 66 BCAT1 knockdown led to a reduction in the capability of A11 cells to form neurospheres. *(A) Representative example of data from a Neurosphere formation assay used as input for the Extreme Limiting Dilution Analysis (ELDA), where 'dose' represents the number of live cells seeded in the well, 'tested' represents the number of technical replicates and 'response' represents the number of wells with observable spheres at the endpoint. (B) Bar graph showing 1/stem cell frequency calculated by ELDA for A11shScr and A11shBCAT1 cells treated with doxycycline relative to their respective no doxycycline controls, with each point representing an independent experiment and error bars representing Standard Deviations. A two-tailed t-test was performed to compare the two cell lines N=3, *p<0.05*

EMT, or glial-to-mesenchymal transition (GMT) for glioblastoma, is associated with the migratory ability of cells. BCAT1 knockdown led to reduced cell invasion and BCAT1 overexpression led to increased cell invasion in A11 cells (Figure 49 to Figure 52). Important markers of GMT were differentially expressed in RNA sequencing analysis of A11 BCAT1 knockdown cells and controls. These include *Snai1* and *ZEB1*, which are transcriptional regulators of GMT and were downregulated to 40% and 51%, respectively, in A11shBCAT1 cells treated with doxycycline when compared with the untreated cells. This suggests that the reduced invasion of A11 cells observed upon BCAT1 knockdown might be because the cells become more glial-like and less mesenchymal-like.

3.4.9 α-KG accumulation as a potential mechanism for HIF destabilisation upon BCAT1 knockdown

Supplementation of BCAT1 knockdown cells with BCKAs did not rescue the cells from the proliferation defect caused by BCAT1 knockdown suggesting that the primary role of BCAT1 in GBM cells is not the generation of BCKAs for entry into the TCA cycle (Figure 44). Knockdown of BCAT2, the mitochondrial isoform of the transaminase found in a complex with BCKDC, which catalyses the rate-limiting oxidation of BCKA, in A11 and S2 cells had no significant effect on the proliferation of the cells, suggesting that the two BCATs play different roles in glioblastoma and that generation of TCA cycle intermediates is not the main role of BCAT1 (Figure 45).

Other potential mechanisms of action of BCAT1 that have been suggested in the literature are generation of glutamate, which is required for glutathione synthesis[155], and regulation of mTOR activity[44,177]. However, LCMS analysis of A11 BCAT1 knockdown and control cell extracts, revealed that both glutamate and glutathione levels were increased in cells in which BCAT1 was knocked down compared to the control cells, suggesting that BCAT1 knockdown does not impair the cells' ability to synthesise glutathione. Additionally, intracellular levels of BCAAs were not significantly changed upon BCAT1 knockdown, suggesting that leucine mediated control of the mTOR pathway is not affected. In addition, western blots of lysates of A11 control and A11 BCAT1 knockdown tumours revealed no difference between the levels of P-S6 relative to total S6, suggesting that mTOR signalling is not affected by BCAT1 knockdown (Figure 67).

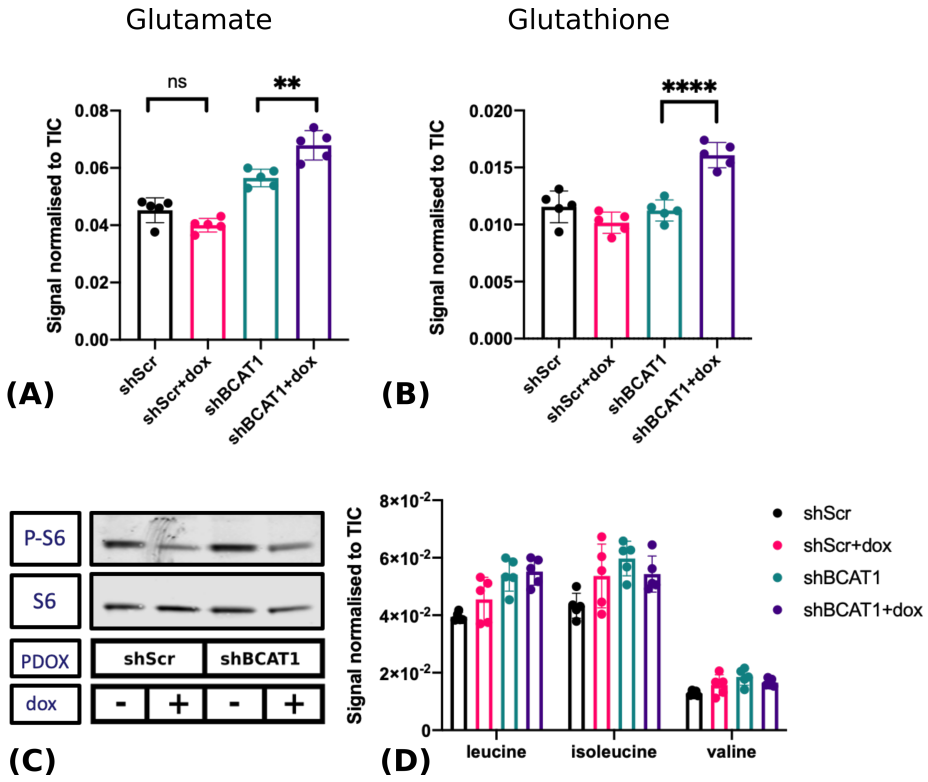

Figure 67 BCAT1 knockdown does not inhibit glutathione synthesis or mTOR signalling. *LCMS analysis of glutamate (A) and glutathione (B) in extracts of A11 cells expressing shScr or shBCAT1. Error bars represent Standard Deviations. T-tests were performed to assess the differences between the doxycycline-induced and non-induced cells (n=5). Ns: p>0.05, **p<0.01, ****p<0.0001 (C) Western blot analysis of total S6 and phosphorylated S6 in lysates of an A11 PDOX. (D) LCMS analysis of leucine, isoleucine and valine concentrations in cell extracts. Error bars represent Standard Deviation.*

The global changes in the transcriptional profile of A11 cells upon BCAT1 knockdown as well as the destabilisation of HIF-1α point towards a mechanism with multiple downstream effects. BCAT1 knockdown leads to reduced cytosolic transamination of BCAAs into BCKAs but also reduced conversion of α-KG to glutamate. A potential mechanism for the effects seen upon BCAT1 knockdown could be the increased availability of α-KG in the cytoplasm that can then lead to HIF-1α destabilisation through increased activity of PHD (Figure 68).

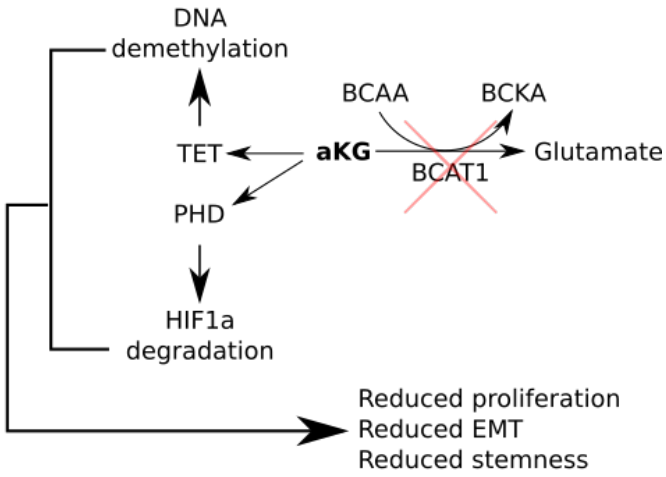

Figure 68 Increased availability of α-KG could explain the effects seen upon BCAT1 knockdown. *Increased availability of α-KG leads to activation of enzymes including TET demethylases, leading to DNA demethylation as well as the prolyl hydroxylases, such as PHD2, leading to HIF-1a degradation. These effects could lead to the phenotypic changes seen upon BCAT1 knockdown.*

α-KG-mediated effects would also include an increase in DNA demethylation resulting from the increased activity of TET enzymes. Indeed, A11 BCAT1 knockdown cells showed a significant increase in the relative level of 5-hydroxymethylcytosine reflecting increased TET activity (Figure 69).

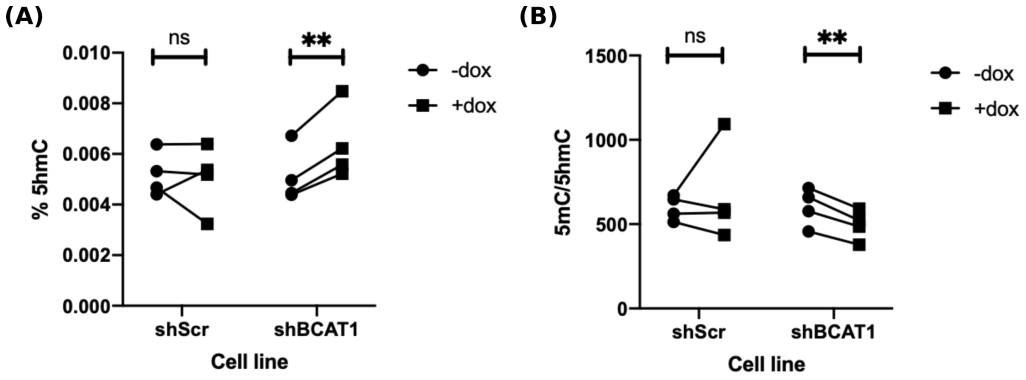

Figure 69 BCAT1 knockdown leads to activation of TET DNA demethylase enzymes. *(A) Proportion of 5-hydroxymethylcytosine in DNA extracted from A11shScr and A11shBCAT1 cells following doxycycline treatment compared to the untreated controls. (B) The ratio of 5-methylcytosine to 5-hydroxymethylcytosine in DNA extracts. Each point represents a biological replicate. A paired two tailed t-test was performed to assess the statistical significance of the differences between groups. N=4 for all groups, ** $p<0.01$, ns: $p>0.05$*

α-KG acts as a co-substrate in the prolyl hydroxylase reactions, while fumarate and succinate have been shown to act as inhibitors of these reactions[31]. Supplementation of A11 cells with dimethyl α-KG, a membrane-permeable analogue of α-KG, phenocopied the effects of BCAT1 knockdown, in terms of reduced cell proliferation (Figure 70). Conversely, addition of Diethyl Succinate, a membrane permeable analogue of succinate and 3-nitropropionic acid, an inhibitor of succinate dehydrogenase which causes succinate accumulation, both led to reversal of the

BCAT1 knockdown effects. A competitive inhibitor of all α-KG dependent dioxygenases, dimethyloxalylglycine (DMOG), also rescued the BCAT1 knockdown effects, suggesting that the proliferation defect observed upon BCAT1 knockdown is probably mediated via increased activity of α-KG dependent dioxygenases, even though DMOG has been documented to also cause non-specific effects[178]. Taken together, these data suggest that BCAT1 knockdown leads to reduced proliferation via an increase in the concentration of α-KG and consequently the activity of α-KG-dependent dioxygenases, including the TET and Prolyl Hydroxylase enzymes and not via reduced flux through the TCA cycle.

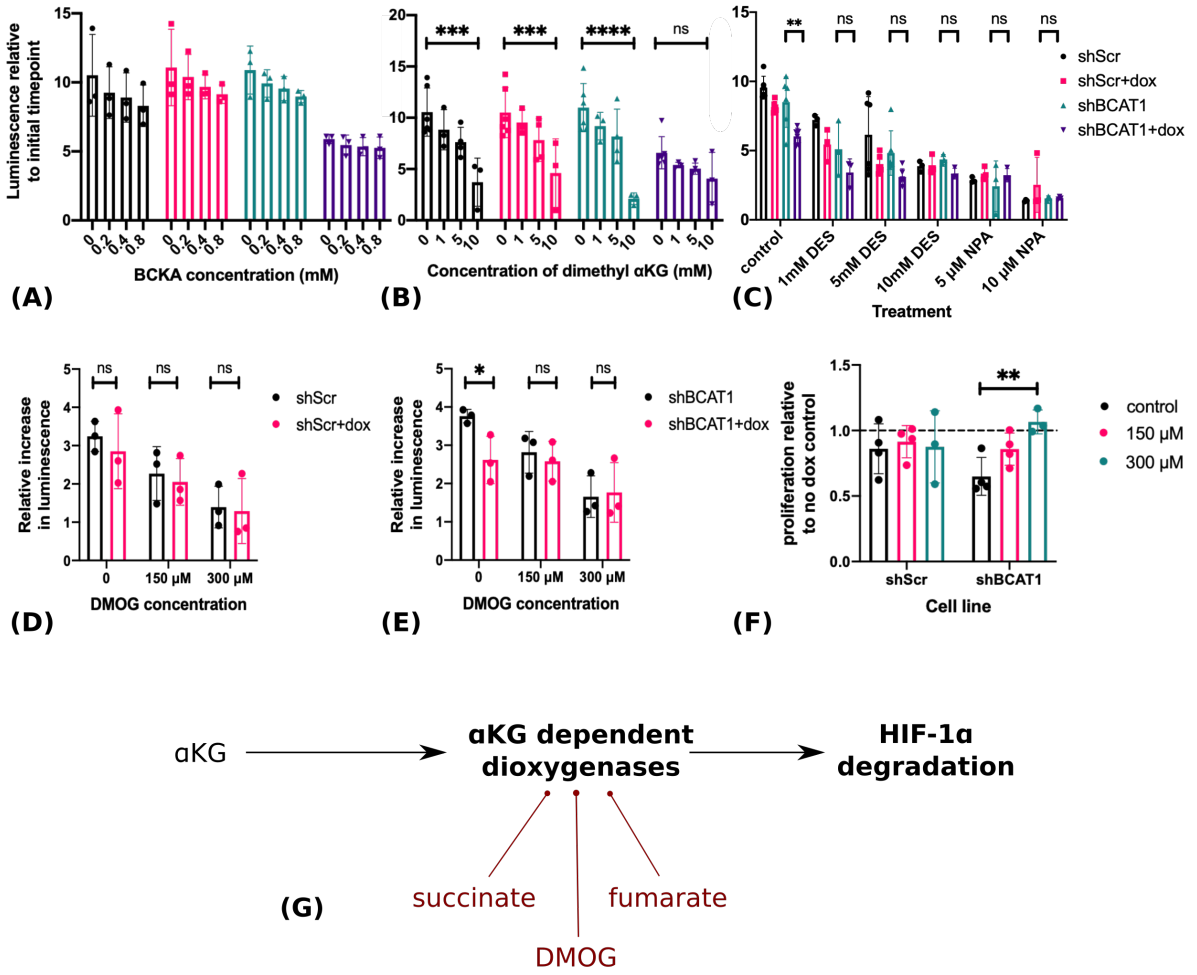

Figure 70 α-KG accumulation is responsible for the effect of BCAT1 knockdown on the proliferation of A11 cells. *A luciferase-based assay was used to assess the proliferation rate of A11 BCAT1 knockdown and control cells. The effects of increasing concentrations of BCKAs (A), dimethyl α-KG (B) and diethyl succinate (DES) and Nitropropionic Acid (NPA) (C) were investigated. Each point represents the mean from three technical replicates of each independent experiment and error bars represent Standard Deviations. Two-tailed t-tests were performed to compare the different groups. (D-F) A11 BCAT1 knockdown and control cells were supplemented with 150 μM and 300 μM Dimethyloxalylglycine (DMOG). The relative increase in luminescence for A11shScr (D) and A11shBCAT1 (E) cells induced with doxycycline are plotted next to the untreated controls. Each point represents the mean from technical replicates of each independent experiment (n=3) and error bars represent Standard Deviations. (F) Cell proliferation rate relative to the control cells that were not treated with doxycycline with each point representing a biological replicate (n=3-4). Two-tailed t-tests were performed to compare the groups.(G) Schematic summary of the effects of α-KG, fumarate, succinate and DMOG on the activity of α-KG-dependent dioxygenase enzymes. ns: p>0.05, *p<0.05, **p<0.01, ***p<0.001, ****p<0.0001*

Additionally, α-KG supplementation of cells for 24 hours led to greatly reduced HIF-1α levels when the cells were grown at 1% oxygen for 8 hours, mimicking the effect of BCAT1 knockdown and providing further evidence that increasing availability of α-KG in the cells leads to greater HIF-1α degradation (Figure 71). High concentrations of α-KG were used in this experiment because of the low cell membrane permeability of α-KG and therefore, even though there was no evidence of cytotoxicity, the reduced levels of HIF-1α could also be a reflection of early stages of cell death.

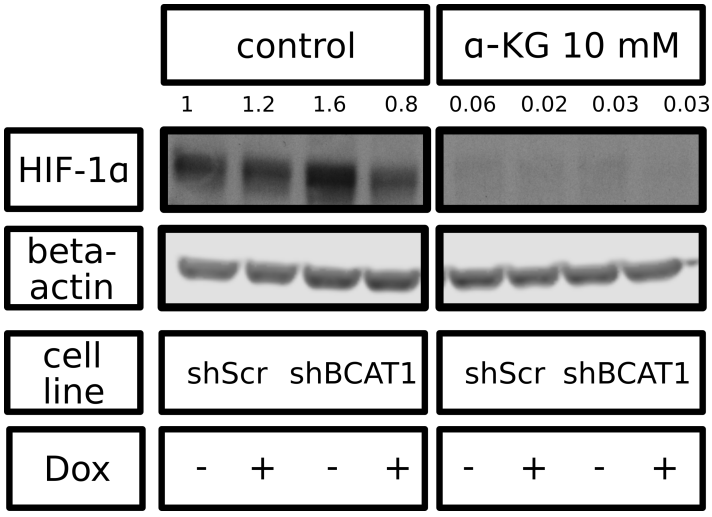

Figure 71 α-KG supplementation of A11 cells leads to reduced HIF-1α levels measured on Western Blot. *Representative western blots of HIF-1α and beta actin loading control in A11shScr and A11shBCAT1 cells, treated with doxycycline and their non-treated controls. Cells were supplemented with 10 mM α-KG for 24 hours and were incubated in 1% O_2 for eight hours before cell lysis, in order to enable measurement of HIF-1α levels. The numbers above the Western Blot bands represent the densitometric quantitation relative to the first band, A11shScr control cells.*

Intracellular α-KG concentrations were measured using a fluorometric assay and LCMS to determine whether BCAT1 knockdown in A11 cells led to the accumulation of α-KG. In addition, the relative concentrations of α-KG from orthotopic tumour tissue extracts were measured using LCMS. However, no significant differences in α-KG levels were measured by either method (Figure 72), although the intratumoural levels of α-KG were slightly higher in BCAT1 knockdown tumours induced with doxycycline diet when compared to the vehicle diet controls. Both methods quantify the total intracellular pool of α-KG, therefore there could still be an increase in the cytosolic levels of α-KG that is masked by changes in the mitochondrial levels. There was a trend toward increased BCAT2 expression upon BCAT1 knockdown (Figure 73). This increased BCAT2 activity could potentially lead to increased consumption of α-KG in the mitochondria, which could mask any increase in the cytoplasm and thus no detectable changes would be measured in the total intracellular pool of α-KG.

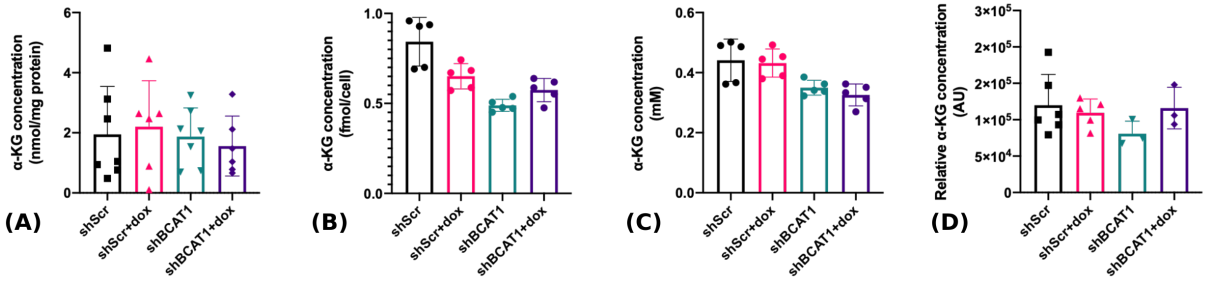

Figure 72 Quantification of α-KG levels showed no significant changes upon BCAT1 knockdown. *(A) α-KG concentration in nmol/mg extracted protein, as measured by a fluorometric assay. Each point represents the calculated concentration value from an independent experiment. (B-C) α-KG concentration measured by LCMS and normalised to cell count (B) or cell volume (C). (D) Relative α-KG concentration of mouse orthotopic xenograft tissue lysates as measured on LCMS. Error bars represent Standard Deviations.*

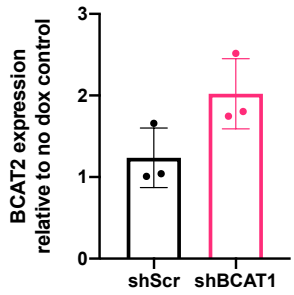

Figure 73 BCAT2 upregulation following BCAT1 knockdown in A11 cells. *Quantitative analysis of BCAT2 western blots of lysates of A11shScr and A11shBCAT1 cells induced with doxycycline relative to the untreated controls. Error bars represent Standard Deviations. Each point represents one of three independent experiments. A two-tailed t-test was performed to compare the two cell lines p=0.07.*

3.5 Discussion

BCAT1 upregulation has been documented in several types of cancer, including glioblastoma[51], breast[179], ovarian[48] and hepatocellular[180] cancer as well as Acute Myeloid Leukaemia[50]. However, different studies have attributed different potential roles to BCAT1 in terms of its contribution to cancer progression. Indeed, it has been suggested that the role of BCAT1 is largely dependent on the tissue of origin[45]. In glioblastoma, BCAT1 upregulation has been demonstrated in *IDH* wild type tumours when compared to healthy brain. BCAT1 inhibition as well as knockdown in the long established U87 human glioblastoma cell line led to reduced proliferation *in vitro* and reduced tumour growth *in vivo*[51] and it was suggested that upregulation of BCAT1 promotes cell proliferation through enhanced generation of TCA cycle intermediates.

Here the role of BCAT1 in glioblastoma has been explored using patient derived cells that better recapitulate aspects of the human disease than U87. Differential expression of BCAT1 was observed across a panel of patient derived *IDH* wild type glioblastoma cells with BCAT1 being expressed in all cells with the exception of S2 cells. This was unexpected, since S2 cells were derived from a primary human GBM tumour and BCAT1 has been identified as the best classifier to distinguish primary GBM from secondary GBM, diffuse astrocytoma and anaplastic astrocytoma[51]. The possibility that these cells might be *IDH*mut was explored, but the cells did not have the common *IDH* mutations. To validate the role of BCAT1 expression in cell proliferation, gabapentin was used as a selective inhibitor for BCAT1, as well as a more specific inhibitor, 4-methyl-5-oxohexanoic acid. Although changes in cell proliferation were observed *in vitro* upon treatment with both agents, concentrations of at least 10 mM were needed in order to see an effect and, in some cases, cytotoxic effects were also observed. Concentrations of 10-50 mM gabapentin have been used in other cancer related BCAT1 studies in order to achieve BCAT1 inhibition and this was attributed to the fact that gabapentin competes with leucine for binding to BCAT1 and leucine is present in the mM range in the cytoplasm of cancer cells[173]. However, when treating A11 BCAT1 knockdown cells and control cells with the two inhibitors, similar effects were observed in both cells, suggesting that the inhibitors were causing off-target effects. Similar non-specific effects were observed upon gabapentin treatment of colorectal carcinoma cells, which lack BCAT1 expression[173]. This suggests that many of the effects observed upon gabapentin treatment in cancer cells are not necessarily BCAT1 specific.

The role of BCAT1 in promoting cell proliferation was validated in A11 cells, where BCAT1 knockdown led to reduced proliferation *in vitro* as well as partial cell cycle arrest. BCAT1 overexpression on the other hand, led to increased cell proliferation *in vitro*. Smaller effects on migration, invasion and resistance to radiotherapy were also observed, in accordance with the literature on glioblastoma and other cancer types[51,53,54,179,181]. Conversely, S2 cells, which showed no baseline BCAT1 expression, showed no significant changes upon BCAT1 overexpression, suggesting that the phenotype of these cells is not affected by BCAT1 expression and activity. S2 cells and A11 cells have a very different mutation status, with A11 cells harbouring mutations in *NF1*, *PIK3R1* and *PTEN* while S2 cells harbour mutations in *TP53*, *STAG2, NF1, RB1, TERT* and *PTEN*. Orthotopic tumours derived from A11 cells and S2 cells, labelled in the referenced paper as GB4 and GB1, respectively, have shown differential lactate labelling in hyperpolarised ^{13}C pyruvate imaging, suggesting that these tumours are metabolically different[182]. Therefore, it is possible that the metabolic and genomic differences between the two cell lines render them more or less dependent on BCAT1 expression.

We have shown upregulation of BCAT1 by overexpression of c-Myc in S2 cells, which is in agreement with the literature which has shown that the BCAT1 promoter contains a c-Myc binding site[47,53,183]. We have also observed upregulation of BCAT1 in hypoxia in all the tested cell lines (A11, SP20 and U87), with the exception of S2 cells, where incubation at an O_2 concentration of 0.1% did not lead to observable BCAT1 expression. In previous studies, HIF-1α and HIF-2α have been shown to bind to the hypoxia response element in the first intron of the human BCAT1 gene and HIF-1α has been shown to be responsible for hypoxia-induced BCAT1 expression in U251 and U87 GBM cells[166]. A potential explanation of the inability of S2 cells to respond to hypoxia could be a mutation in the hypoxia response element on the BCAT1 gene in these cells.

In most cancers, including breast cancer and hepatocellular carcinoma, BCAT1 upregulation was shown to lead to increased transamination of BCAAs to their respective BCKAs, while in pancreatic ductal adenocarcinoma, elevated levels of BCAAs were observed in plasma[45] and in chronic myeloid leukaemia, increased expression of BCAT1 led to increased generation of BCAAs from BCKAs[50]. In the patient-derived glioblastoma models, the reaction appears to favour the forward direction, since BCAT1 overexpression in cells *in vitro* led to increased labelling of [1-^{13}C]KIC from [1-^{13}C]leucine and BCAT1 knockdown led to reduced glutamate secretion. In addition, the plasma levels of BCAAs were reduced upon growth of orthotopically

implanted patient derived xenograft tumours, similarly to a previously published study in non-small cell lung cancer models[61] suggesting that the tumour is consuming the amino acids or initiating systemic effects leading to increased BCAA consumption (Figure 39).

The mechanism by which BCAT1 facilitates cell proliferation in glioblastoma remains unclear. A number of hypotheses have been proposed for the role of BCAT1, including the generation of BCKAs which can be further catabolised to generate TCA cycle intermediates[51] and also the generation of glutamate, which is required for the synthesis of glutathione[155]. Additionally, upregulation of BCAT1 in glioblastoma has been shown to lead to increased secretion of BCKAs through MCT1 into the tumour microenvironment. BCAT1 and MCT1 were found to be located in close proximity, suggesting possible functional interaction between the two proteins. The secreted BCKAs can be taken up by macrophages and reaminated to BCAAs leading to reduced phagocytic activity[154].

In this study, the proliferation defect of A11 cells was not rescued by supplementation of BCAT1 knockdown cells with increasing concentrations of BCKAs, suggesting that reduced generation of BCKAs to feed the TCA cycle is not the mechanism mediating the reduced proliferation rate. The uptake of BCKAs upon supplementation in the media was not confirmed by LCMS, but good uptake was expected given the high expression of MCT transporters in the cells and given the *in vivo* data in Chapter 4, where injection of [1-^{13}C]Ketoisocaproate in A11 glioma bearing rats led to uptake of the substrate and conversion to [1-^{13}C]leucine. Additionally, knockdown of the mitochondrial isoform of the enzyme, BCAT2, which is part of the metabolon catalysing BCAA catabolism[184], did not affect the cells' proliferation rate. Disassociation of BCAT1 activity from the generation of TCA cycle intermediates has been documented in other cancers as well as glioblastoma, suggesting that even though BCAT1 catalyses the first step in the catabolic pathway of BCAAs, the BCKAs produced from BCAAs might not always be committed for further catabolism. For example, in hepatocellular carcinoma, transcriptomic, enzymatic and metabolomic analyses revealed that the pathway of BCAA catabolism, with the exception of BCAT1 and BCAT2, was suppressed when compared to adjacent healthy liver tissue[185]. Nevertheless, BCAT1 upregulation promoted cell proliferation and chemoresistance to cisplatin[55], suggesting that the role of BCAT1 in promoting proliferation and chemoresistance may be independent of the rest of the catabolic pathway of BCAAs.

To understand the mechanism responsible for reduced proliferation upon BCAT1 knockdown in A11 cells, RNA sequencing analysis was performed, which revealed that BCAT1 is a regulator of the transcriptional activities of HIF and FOXM1, with BCAT1 knockdown leading to reduced levels of HIF-1α, downregulation of HIF targets such as CAIX and HKII and reduced levels of FOXM1, both *in vitro* and *in vivo*. Conversely, BCAT1 overexpression led to upregulation of CAIX. The importance of HIF in GBM progression has already been established, with high HIF-1α activity being implicated in tumour progression and maintenance of a tumour stem cell phenotype[186]. Therefore, the effects of BCAT1 knockdown, including reduced cell proliferation and migration can be explained by reduced HIF activity. The frequency of cells with self-renewal capacity was assessed using a neurosphere formation assay, where BCAT1 knockdown cells had a significantly lower frequency of cells with the potential to form a neurosphere when compared to controls.

The association of BCAT1 levels with HIF-1α activity in GBM cells has not been described before, however BCAT1 mediated stabilisation of HIF-1α has been documented in Acute Myeloid Leukaemia (AML) cells[187]. In this study, the authors performed isotope labelling experiments with ^{13}C-labelled BCAAs and showed an absence of ^{13}C-labelled TCA cycle intermediates in both control and BCAT1 knockdown cells, suggesting that BCAT1 catalysed transamination of BCAAs does not contribute to TCA metabolism via generation of BCKAs. Instead, they report increased incorporation of BCAA nitrogen into non-essential amino acids and nucleotides. Furthermore, they suggest that BCAT1 acts primarily as a regulator of intracellular α-KG levels. They showed that the effects of BCAT1 knockdown were phenocopied by addition of dimethyl α-KG, a cell permeable variant of α-KG, suggesting that BCAT1 knockdown leads to cell proliferation changes through an increase in α-KG concentration. Additionally, exogenous administration of an octyl derivative of α-KG led to downregulation of HIF-1a, phenocopying BCAT1 knockdown effects, while overexpression of HIF-1a in BCAT1 knockdown cells led to rescue of the proliferation and survival defects. A significant increase in intracellular α-KG concentration was reported upon induction of BCAT1 knockdown in three AML cell lines as well as in the MDA-MB-231 breast cancer cell line and U87 and U251 GBM cell lines. Conversely, BCAT1 overexpression in leukaemia cells led to a reduction in intracellular α-KG levels.

α-KG homeostasis has been shown to be essential in cancer cells, due to the role of α-KG as a co-substrate for a number of α-KG-dependent dioxygenases including EGLN1 and the TET

family of DNA demethylases. Owing to its central role in metabolism, the concentration of α-KG can be regulated by many reactions and enzymes, one of which is BCAT1. Here, we saw downregulation of HIF and its targets, an increase in the amount of 5-hmC in DNA, reduced proliferation and reduced frequency of cancer stem cells upon BCAT1 knockdown in A11 cells, all of which would be the effects of an increase in α-KG levels in the cell cytosol. Also, supplementation of A11 cells with dimethyl α-KG led to reduced cell proliferation, phenocopying the effects of BCAT1 knockdown. Conversely, supplementation of cells with diethyl succinate and 3-nitropropionic acid, both of which lead to succinate accumulation and thus inhibition of the α-KG dependent dioxygenases, led to an elimination of the BCAT1 knockdown effect. The same effect was observed upon treatment of the cells with DMOG, an inhibitor of α-KG dependent dioxygenases. Supplementation of the cells with dimethyl α-KG did not lead to HIF downregulation, but instead, dimethyl α-KG led to stabilisation of HIF-1a as seen by the increased levels of CAIX. This has been documented previously by Hou et al, where dimethyl α-KG led to a transient stabilisation of HIF-1a via inhibition of PHD2[102]. However, supplementation of the cells with 5 mM and 10 mM α-KG led to destabilisation of HIF-1a, phenocopying the effects of BCAT1 knockdown.

Measurement of intracellular α-KG levels upon BCAT1 knockdown, however, failed to show that the effects of BCAT1 knockdown are mediated via an accumulation of α-KG, since no consistent increase in α-KG levels was measured. However, the central role of α-KG in cellular metabolism renders it a tightly controlled metabolite, meaning that increased flux of α-KG in various reactions, including its conversion to succinate, catalysed by α-KG dehydrogenase, to isocitrate, catalysed by IDH, and to glutamate, catalysed by glutamate dehydrogenase, as well as its consumption in hydroxylation reactions and transamination reactions could very quickly compensate for an increase in concentration caused by BCAT1 knockdown. Raffel et al in their studies on AML cells quote specific timepoints for cell harvest after doxycycline induction of BCAT1 knockdown when measuring changes in α-KG concentration, which differ between cell lines, for example 12 hours for SKM-1 cells but 48 hours for HL-60 cells and 96 hours for MDA-MB-231 cells[187]. In A11 cells, we saw some reduction in BCAT1 levels on Western Blot at 48 hours after initiation of doxycycline treatment with maximum BCAT1 knockdown being reached by 72 hours of doxycycline treatment. Therefore, the levels of α-KG at 96 hours after initiation of doxycycline treatment might already be compensated for by increased flux in other reactions. Additionally, the total intracellular pool of α-KG is measured, whereas the expected changes would occur in the cytosolic pool. BCAT1 knockdown in the A11 cells will possibly

lead to increased BCAA transamination in the mitochondria by BCAT2, leading to increased consumption of mitochondrial α-KG masking the reduced consumption in the cytoplasm. This might not have been the case in the U87 cells investigated by Raffel et al[187] owing to the absence of BCAT2 expression, as shown in Figure 24.

BCAT2, the mitochondrial isoform of the transaminase, is not often investigated in studies on BCAT1. No changes in BCAT2 mRNA levels were found between *IDH*wt and *IDH*mut tumours in the study by Tonjes et al[51]. However, in a later study, BCAT2 upregulation was documented in *IDH* wild type glioblastoma and low expression of BCAT2 correlated with improved patient survival[188]. We observed here an inverse relationship between BCAT1 and BCAT2 expression in a panel of patient derived glioblastoma cells, with S2 cells showing the highest levels of BCAT2 protein expression and no BCAT1 protein expression and A25 cells showing the highest BCAT1 and lowest BCAT2 expression. The differences in BCAT2 expression were not a reflection of differences in mitochondrial content. More work needs to be done, however, to understand whether the two isoforms can complement each other and share similar roles in the cells. However, evidence presented here points towards different roles for BCAT1 and BCAT2 in cancer cells. We showed that BCAT1 but not BCAT2 expression was regulated by c-Myc and hypoxia and that BCAT1 knockdown but not BCAT2 knockdown led to reduced proliferation rate in A11 cells. In addition, we have shown that BCAT1 knockdown did not lead to any significant changes in the intracellular levels of BCAAs. BCAT2 was shown to be bound to the E1 decarboxylase enzyme of the Branched Chain Ketoacid Dehydrogenase Complex (BCKDC), forming a metabolon that enables coupling of the first two steps of BCAA catabolism[184]. Therefore, it is likely that BCAT2 plays the main catabolic role in the mitochondria of cells, with BCAT1 enabling metabolic regulation in the cytoplasm. In BCAT1 knockdown cells, the rate of BCAT2-mediated BCAA transamination is likely to increase owing to the higher substrate availability, which might explain the absence of any significant changes in the total intracellular pool of α-KG and BCAAs.

3.6 Conclusion

A panel of patient derived cells has been characterised with regard to expression of BCAT1 and BCAT2. The role of BCAT1 was further investigated with a focus on A11 cells which express moderate levels of BCAT1 and BCAT2. Knockdown of BCAT1 led to phenotypic changes in these cells, with the most significant effect being observed on the cell proliferation rate. This was not rescued by exogenous supplementation of BCKAs. The BCAT1 knockdown effects are mediated by HIF-1α destabilisation and increased DNA demethylation, most likely resulting from cytoplasmic accumulation of α-KG.

Chapter 4 - *In vivo* imaging of BCAA metabolism using Hyperpolarised ^{13}C Magnetic Resonance Spectroscopic Imaging

4.1 Abstract

Hyperpolarised ^{13}C imaging is a metabolic imaging technique which has been used pre-clinically and clinically to investigate altered metabolism. Hyperpolarised [1-^{13}C]Ketoisocaproic acid is a substrate that can be used to image Branched Chain Amino Acid Metabolism in cancer, and more specifically to assay upregulation of BCAT1 in different types of cancer. We have investigated here the potential of hyperpolarised [1-^{13}C]Ketoisocaproic Acid to image BCAT1 activity in a subcutaneous murine lymphoma tumour model and in Patient Derived Orthotopic Xenograft models of glioblastoma. The substrate performed well in the lymphoma but in the orthotopic glioblastoma tumours exchange of label between [1-^{13}C]Ketoisocaproic and endogenous leucine was limited by the availability of the glutamate co-substrate, and therefore could not be used for the direct assessment of BCAT1 activity.

4.2 Introduction

BCAA metabolism plays an important role in normal physiology and cancer pathophysiology. As discussed in Chapter 3, the transamination reaction catalysed by BCAT1 is essential for the maintenance of rapidly proliferating glioblastoma cells. Therefore, it would be beneficial to be able to image BCAA metabolism *in vivo*, for diagnostic and prognostic purposes as well as for guiding treatment. Hyperpolarised ^{13}C MRSI has already been used in rodents to image conversion of a ^{13}C-labelled BCKA ([1-^{13}C]Ketoisocaproate (KIC)) to its respective BCAA ([1-^{13}C]leucine)[189,190].

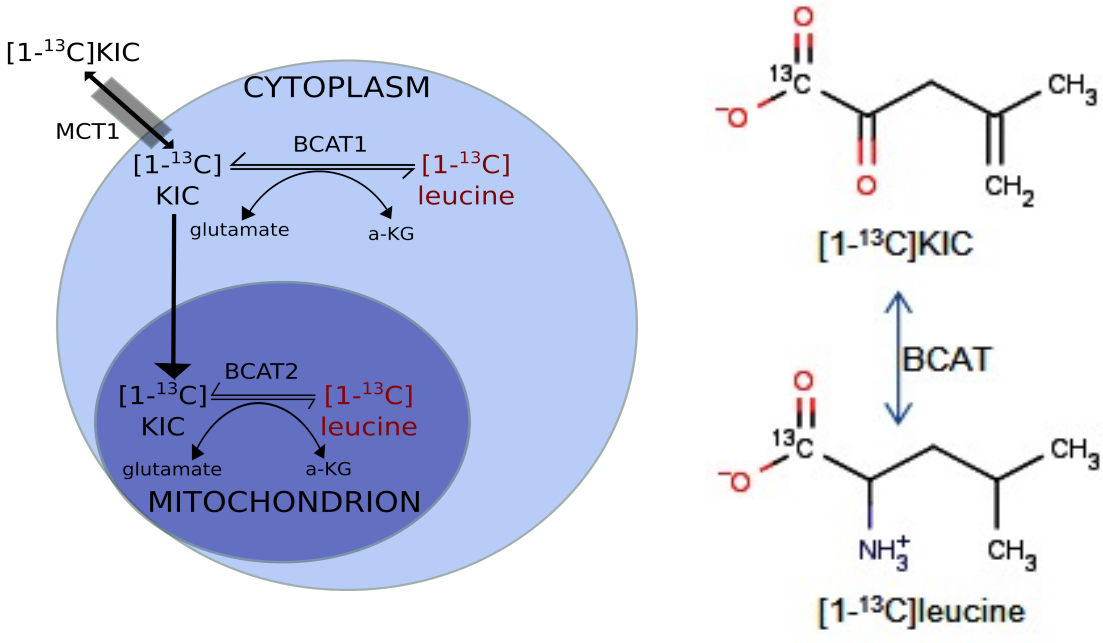

Figure 74 Imaging the first step of BCAA metabolism using hyperpolarised [1-^{13}C]KIC. *The substrate enters the cell through Monocarboxylate Transporters, such as MCT1 and MCT2, and can be converted to [1-^{13}C]leucine in the cytosol, in the reaction catalysed by BCAT1 and in the mitochondria, by BCAT2.*

By using hyperpolarised [1-^{13}C]KIC, and measuring its conversion to [1-^{13}C]leucine, Karlsson et al[189] and Butt et al[190], used MRI to image the activity of BCAT in tumours and in healthy brain, respectively. The ^{13}C resonance of [1-^{13}C]KIC is at 172.6ppm and that of [1-^{13}C]leucine at 176.8ppm, enabling the metabolites to be distinguished. When ^{13}C labelled KIC was injected into EL4 tumour-bearing mice, [1-^{13}C]leucine was detected, with good contrast between the tumour and surrounding healthy tissue[189]. When the same technique was applied to a rat breast cancer model, R3220AC, however, minimal leucine was detected, owing to the much lower levels of BCAT activity[189]. This suggests that some cancers, including lymphoma, overexpress BCAT, but that this is not a general feature of neoplasms. In the normal healthy brain, Butt et

al observed that the hippocampal regions demonstrated increased BCKA transamination when compared to the rest of the brain[190]. In the same study, hyperpolarised [1-^{13}C]pyruvate and [1-^{13}C]KIC were injected simultaneously. The distribution and signal intensities of the two substrates were similar, suggesting that KIC was able to successfully cross the blood brain barrier. MCT2, which is the main transporter in the rodent brain has high affinity for pyruvate, KIC and lactate[190]. KIC is also a substrate for MCT1, with a K_m of 0.67 mM compared to a K_m for pyruvate of 1 mM[190,191]. In both tumour and normal brain studies, maximum leucine signal was observed between 20 and 35 seconds following injection of the substrate.

More recently, Suh et al used hyperpolarised ^{13}C KIC imaging to assess BCAA metabolism *in vitro* and *in vivo* in a rat glioma model, F98[192]. Interestingly, reduced transamination of hyperpolarised ^{13}C KIC to ^{13}C leucine was measured in the glioma compared to normal brain. Conversely, increased $H^{13}CO_3^-$ was measured in the tumours compared to the contralateral healthy brain. When assessed *in vitro* for BCAT enzyme activity and protein expression, these tumours were seen to have similar total BCAT activity levels to the contralateral normal appearing brain. However, the tumours showed lower BCAT1 and higher BCAT2 levels compared to the normal brain, which is not representative of the upregulation of BCAT1 in human *IDH*wt glioblastoma. In fact, the tumour model used in this study is a rat cell line which has been grown since 1971, therefore its resemblance to human glioblastoma is unknown.

In this study we hypothesised that hyperpolarised ^{13}C KIC imaging *in vivo* in patient derived orthotopic xenograft models of glioblastoma that express high BCAT1 levels would show faster conversion to leucine and hence higher leucine signal in the tumours when compared to the contralateral healthy brain.

4.3 Methods

4.3.1 Cell culture

EL4 murine lymphoma cells (ATCC) were grown in suspension in RPMI medium (Gibco) supplemented with 10% Foetal Bovine Serum (FBS) and 2 mM glutamine. Cells were harvested by centrifugation and washed with Phosphate Buffered Saline (PBS).

Glioblastoma cells were grown as described in Chapter 3.

4.3.2 Establishment of tumour models

4.3.2.1 Implantation of subcutaneous lymphoma tumours in mice

A suspension of 5 x 10^6 EL4 cells in 200 µl Foetal Bovine Serum (FBS) was injected subcutaneously in the right flank of female C57BL/6 mice (Charles River). Tumours were grown for 8-11 days before they were imaged.

4.3.2.2 Patient Derived Orthotopic Xenograft implantations

For intracranial implantations of glioma cells in rats, the procedure described in Chapter 3 was used.

4.3.3 Magnetic Resonance Imaging and Spectroscopy in vivo

Animals were placed in a 7.0 T magnet (Agilent). For the mouse imaging experiments, a 42 mm diameter ^{1}H and ^{13}C transmit volume coil was used as well as a 20 mm diameter ^{13}C receive-only surface coil, which was placed over the tumour. For the rat imaging experiments a 72 mm diameter volume coil was used for ^{1}H and a 20 mm diameter transmit and receive surface coil for ^{13}C, which was placed over the rat's head, with the rat in a prone position, unless otherwise stated. The rats and mice were anaesthetised by inhalation of 2-3% isoflurane in air/O_2 (75/25% vol/vol, 2 L/min). Respiration and body temperature were monitored over the course of the imaging experiment. The body temperature of the animal was maintained with a stream of warm air.

4.3.3.1 Substrate hyperpolarisation

[1-^{13}C]Ketoisocaproate and [1-^{13}C]pyruvate were hyperpolarised using a HyperSense DNP polarizer (Oxford Instruments, Abingdon, UK) at 1.2 K in a magnetic field of 3.35 Tesla (T), with micro-wave irradiation at 94.1 GHz.

4.3.3.1.1 [1-^{13}C]Ketoisocaproate

[1-^{13}C]sodium ketoisocaproate was purchased from Cambridge Isotope Laboratories (MA) and converted to [1-^{13}C]ketoisocaproic acid using the following procedure: [1-^{13}C]ketoisocaproic acid, sodium salt was placed in a 10-ml round bottom flask and dissolved in water. The solution was stirred at 0^{o}C and acidified using 1 ml of concentrated Hydrochloric Acid. After 2 hours of stirring at 0^{o}C, the aqueous layer was extracted with diethyl ether (3 × 3 mL). The combined organic layers were dried with anhydrous magnesium sulphate, filtered, and concentrated under nitrogen gas to give [1-^{13}C]KIC as a colourless oil. The purity of [1-^{13}C]KIC acid was confirmed by ^{1}H NMR.

For hyperpolarisation of [1-^{13}C]KIC, the recipe was modified from previous literature[189,190,193] as follows: 63 mg [1-^{13}C]KIC was mixed with OX063 radical (GE Healthcare, Amersham, UK) (15 mM final concentration) and gadoterate meglumine (DOTAREM, Guerbet, Roissy, France) (1.5 mM final concentration) and hyperpolarised for about an hour. The hyperpolarised substrate was dissolved in 6 ml of buffer containing 40 mM Hepes, 94 mM NaOH, 30 mM NaCl and 100 mg/L EDTA. For the mice 400 µl and for the rats 2 ml of this solution were injected intravenously via a tail vein.

4.3.3.1.2 [1-^{13}C]pyruvate

[1-^{13}C]pyruvic acid was purchased from Cambridge Isotope Laboratories (MA). 44 mg [1-^{13}C]pyruvic acid was mixed with 15 mM OX063 radical (GE Healthcare) and 1.4 mM gadoterate meglumine (DOTAREM, Guerbet) and loaded in the HyperSense polarizer, where it was polarised for about an hour. The substrate was then dissolved in 6 ml of buffer containing 40 mM Hepes, 94 mM NaOH, 30 mM NaCl and 100 mg/L EDTA and 400 µl of this solution was immediately injected intravenously into the tail vein of the mouse to be imaged.

4.3.3.2 Hyperpolarised ^{13}C KIC MRI experiments

4.3.3.2.1 Subcutaneous tumour imaging in mice

For T_2-weighted proton anatomical images of the mice, a Fast Spin Echo sequence was used. For this, 15 axial slices with a Field-of-View (FOV) of 40 mm x 40 mm and 2 mm thickness were acquired with a matrix size of 256 x 256, TR of 2 s and an effective TE of 48 ms, with 8 echoes acquired.

For acquisition of the time course of hyperpolarized [1-^{13}C]KIC metabolism in EL4 tumours, signal was acquired from a 10 mm thick slice (40mm x 40mm FOV) containing the tumour, for 180 seconds from the start of hyperpolarized ^{13}C KIC injection. The ^{13}C spectra were acquired with a 600 μs 10^o flip angle pulse, with a TE of 0.5 ms, TR 1 second. 1024 spectral points were acquired, covering a spectral width of 6010 Hz.

For two-dimensional chemical shift imaging in a 16 x 16 matrix, an 8 mm thick slice was selected (FOV 40 mm x 40 mm), based on the T_2-weighted proton images, that contained the tumour. The image was acquired with a TR of 47 ms, TE of 0.85 ms and a 600 μs pulse with a flip angle of 10^o. 256 spectral points were acquired covering a spectral width of 6010 Hz. For higher resolution imaging of EL4 tumours, a 6 mm thick slice was imaged in a 32 x 32 matrix, with a TR of 30 ms, TE of 0.85 ms, and a 600 μs pulse with a flip angle of 10^o. 128 spectral points were acquired covering a spectral width of 6010 Hz. In both cases, the k-space was acquired from the centre, spiralling outwards with repeated excitation pulses.

4.3.3.2.2 Brain imaging in rats

For T_2-weighted proton anatomical images of the rat brain, a Fast Spin Echo sequence was used. For this, 15 axial slices with a FOV of 40 mm x 40 mm and 2 mm thickness were acquired with a matrix size of 128 x 128, TR of 1.8 s and TE of 50 ms, with 8 echoes acquired.

For Chemical Shift Imaging in rat brain, signal was acquired from a slice of 8-10 mm thickness, in a 16 x 16 matrix, with a TR of 47 ms, TE of 0.75 ms and a 600 μs pulse with a flip angle of 75^o, unless otherwise stated. 256 spectral points were acquired covering a spectral width of 6010 Hz. The k-space was acquired from the centre, spiralling outwards with repeated excitation pulses.

4.3.3.3 ^{1}H Spectroscopy Experiments

Proton magnetic resonance spectra were acquired using a 9.4T spectrometer with a Bruker console from two 2.5×2.5×3 mm voxels, one placed inside the tumour and one in contralateral normal appearing brain tissue, using a PRESS acquisition and CHESS water suppression[194] pulse sequences. A 72 mm diameter volume coil for transmit (RAPID Biomedical) and a surface coil placed over the rat's head for receive (Bruker). Spectra were acquired with an echo time (TE) of 30 ms, a repetition time of 2 s and 256 averages. Water reference spectra were acquired with an identical pulse sequence and timings using 16 averages. A basis set of model metabolite spectra was simulated using NMRSIM with the timings of the experimental PRESS sequence but idealised 90˚ and 180˚ pulses. Simulated spectra were based on published chemical shifts and coupling constants[195] for alanine, aspartate, choline, creatine, gama-aminobutyric acid, glucose, glutamine, glutamate, glycine, glutathione, myo-inositol, lactate, N-acetyl-aspartate, N-acetyl-aspartyl-glutamate, phosphoethanolamine and taurine. Data and simulated spectra were transferred to MATLAB (The Mathworks, Natick, MA, USA) for spectral fitting. Raw in vivo FIDs were QUALITY[196] corrected for frequency, phase and lineshape using the water reference spectrum with line broadening set to a consistent 24 Hz with a gaussian window function before Fourier transformation. The real part of the spectral regions were fitted with the model spectra with 24 Hz Gaussian lineshapes, a cubic spline baseline and 8 simulated broad singlets for fatty-acid resonances (dialylic bounded methylene at 2.8 ppm, methylene adjacent to a carboxyl at 2.3ppm, methylene adjacent to an allyl at 2.1 ppm, three methylenes around 1.3 ppm and two methyls at 0.9 ppm). A trust-region reflective least squares fitting was used to fit the real part of each spectrum between 4.2 and 0.6 ppm and quantified assuming the water reference peak was 46 M[197] with no correction for T_1 or T_2 relaxation.

4.3.4 *Ex vivo* measurements of BCAT activity

For measuring total BCAT activity and the contribution of BCAT1 and BCAT2 activities to the total activity, the tissues were dissected immediately after sacrificing the animals and snap-frozen in liquid nitrogen. Tissue was homogenized and assayed using the spectrophotometric assay, as described in Chapter 3.

4.3.5 *Ex vivo* measurements of metabolites by ^{1}H NMR

For measuring BCAA levels in healthy brain and in A11 orthotopic xenografts, tissue was snap frozen in liquid nitrogen. Metabolites were extracted using a methanol/chloroform/water extraction method[198]. Around 250 mg frozen tissue was homogenised in 4 ml cold methanol using the Precellys homogeniser. The homogenate was incubated on ice for 15 minutes and then 4 ml cold chloroform was added. The methanol/chloroform mixture was vortexed and incubated for another 15 minutes on ice before 4 ml of H_2O were added. The mixture was incubated at -20^{o}C overnight, followed by centrifugation at 21000 g for 40 minutes at 4^{o}C for separation of the layers. The aqueous phase was dried using a stream of nitrogen gas and lyophilised, while the protein in the interphase was extracted using RIPA buffer for protein quantification.

For ^{1}H NMR, the lyophilised extracts were dissolved in D_2O containing 10 mM TMSP standard. ^{1}H spectra were acquired on a 600 MHz spectrometer (Bruker) with an 11 μsec pulse with a flip angle of 90^{o} and a repetition time of 5.3 seconds. 512 scans were summed, with a spectral width of 17 ppm (10000 Hz) and 65536 data points. All spectra were processed using a Gaussian window function of 3 Hz.

4.4 Results

4.4.1 BCAT activity can be imaged with hyperpolarised [1-^{13}C]KIC in EL4 subcutaneous tumours

In a surface coil-localised ^{13}C spectroscopy experiment, signals from both [1-^{13}C]KIC (at 172.6 ppm) and its transamination product, [1-^{13}C]leucine (at 176.8ppm), were acquired following intravenous injection of hyperpolarised [1-^{13}C]KIC into an EL4 tumour-bearing mouse (Figure 75). Following fitting of the individual spectra using the AMARES (Advanced Method for Accurate, Robust and Efficient Spectral fitting) algorithm in the OXSA Matlab toolbox[199], the time course data was observed. The signal obtained from [1-^{13}C]KIC peaked at around 10 seconds after injection and declined quickly thereafter, disappearing completely by 50 seconds, whereas the signal from [1-^{13}C]leucine peaked later, at about 30 seconds, and lasted longer, as it was still observed 1 minute after the injection.

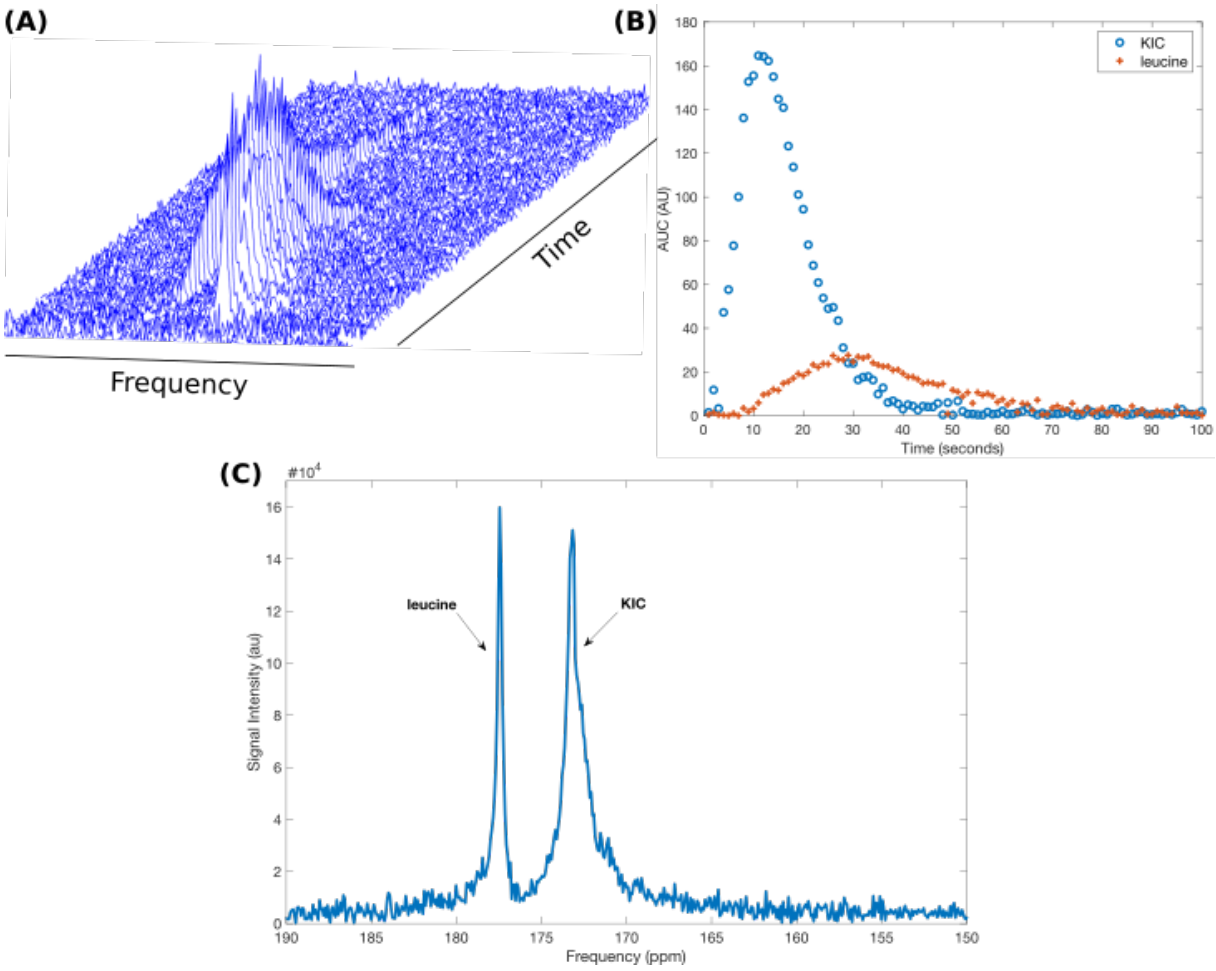

Figure 75 Transamination of hyperpolarised ^{13}C KIC to ^{13}C leucine in vivo measured using ^{13}C Magnetic Resonance Spectroscopy. *For the ^{13}C excitation, a 10º flip angle pulse, with a TR of 1 second was used. 1024 spectral points were acquired, covering a spectral width of 6010 Hz. (A) A stack of spectra acquired every second between 1 and 80 seconds after injection, showed that the ^{13}C KIC signal (peak on the right) peaked first and then declined quickly, while its transamination product, ^{13}C leucine (peak on the left) built up over time and lasted longer. (B) The spectra were fitted using the AMARES algorithm and the peak area for the fitted KIC and leucine peaks was plotted over time. (C) The absolute values of the summed spectra for the entire duration of the experiment (180 seconds). The chemical shift of leucine is 176.8 ppm and that of KIC is 172.6 ppm.*

Chemical Shift Imaging (CSI) was then performed in EL4 tumour bearing mice. A low resolution (16 x 16 matrix for a 40 x 40 mm^2 slice) imaging experiment (Figure 76) demonstrated that it was possible to image the metabolism of hyperpolarized [1-^{13}C]KIC to [1-^{13}C]leucine *in vivo* in this subcutaneous tumour, in agreement with previously published data[189]. The highest [1-^{13}C]leucine signal was observed near the edges of the tumour, although [1-^{13}C]KIC was more homogeneously distributed throughout the tumour.

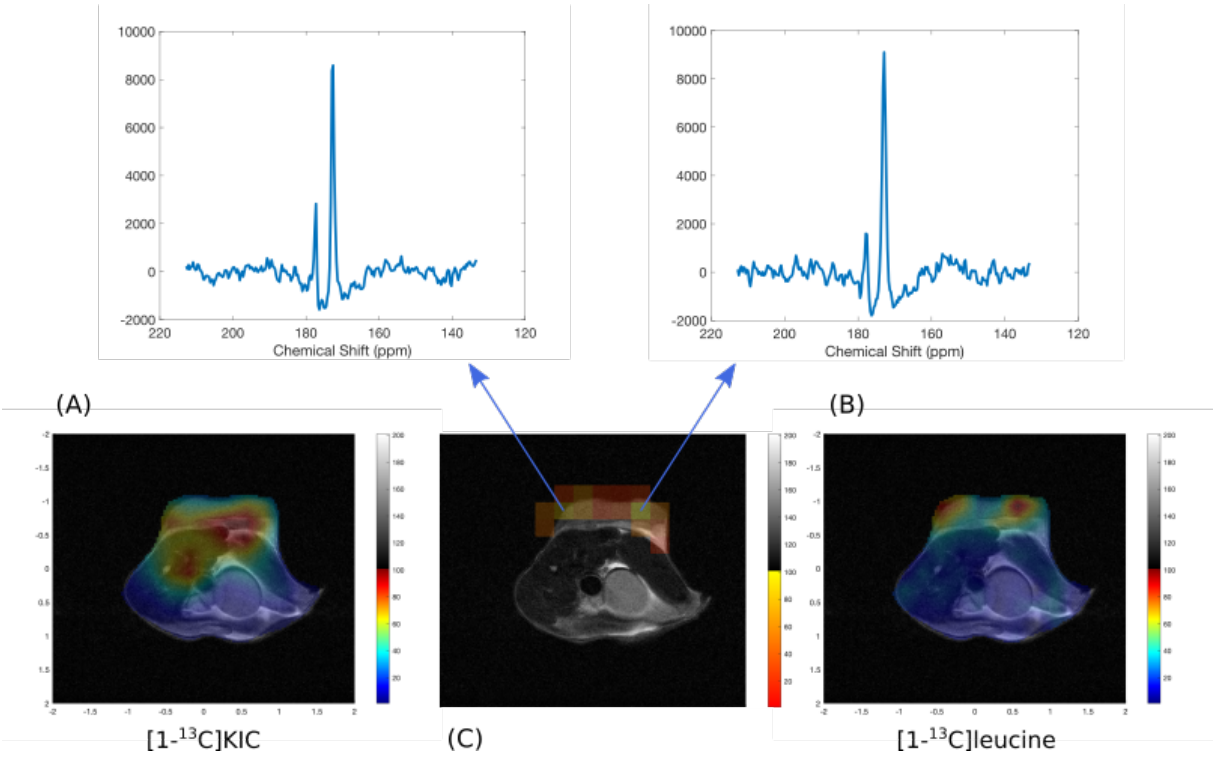

Figure 76 2D ^{13}C CSI in a murine EL4 tumour. *The axial ^{1}H reference image was acquired using a Fast Spin Echo Sequence. Twenty five seconds after the start of injection of 400 µl of hyperpolarised [1-^{13}C]KIC via the tail vein of the mouse, a chemical shift imaging sequence with TR 47ms, TE 0.85ms and a 600 µs 10^{o} flip angle pulse was used to acquire a 16 x 16 matrix of ^{13}C spectral information. A false colour image of [1-^{13}C]KIC (A) and [1-^{13}C]leucine (B) signal in the mouse, normalised to the maximum signal in the image. The signal was interpolated from a 16 x 16 matrix to a 128 x 128 matrix and the image is overlaid on the reference anatomical ^{1}H image. (C) The false colour image depicts the non-interpolated leucine signal in the tumour, normalised to the maximum signal in the mouse. The spectra from the two voxels with the highest leucine signal intensity are shown.*

Higher resolution CSI was performed in EL4 tumour-bearing mice, to compare ^{13}C KIC imaging to ^{13}C pyruvate imaging. Mice were imaged on two consecutive days with the two substrates. In these imaging experiments, pyruvate was mostly seen in the large vessels 20 seconds after the start of injection of the substrate, while lactate was distributed across the tumour. In some tumours lactate labelling was seen evenly throughout the tumour (Figure 77B) whereas in other tumours the labelling was more focal (Figure 77F). The distribution of [1-^{13}C] leucine in these tumours was similar to the distribution of [1-^{13}C]lactate. High [1-^{13}C]KIC signal was also observed in the tumours, in contrast to the ^{13}C pyruvate signal, suggesting that label exchange between KIC and leucine is slower than the exchange between pyruvate and lactate.

In order to investigate the dependence of ^{13}C labelling of leucine on BCAT1 activity, a mouse was imaged on consecutive days with and without gabapentin administration. Gabapentin administration one hour before imaging with hyperpolarised [1-^{13}C]KIC led to a decreased ^{13}C leucine signal in the tumour compared to the signal observed in the same tumour the previous

day (Figure 77D,J), despite the very similar ^{13}C KIC distribution on both days (Figure 77C,I). This suggests that BCAT1 inhibition leads to decreased label exchange between KIC and leucine. Some leucine was still detectable in the tumour, which could be from uninhibited BCAT2 activity or residual BCAT1 activity.

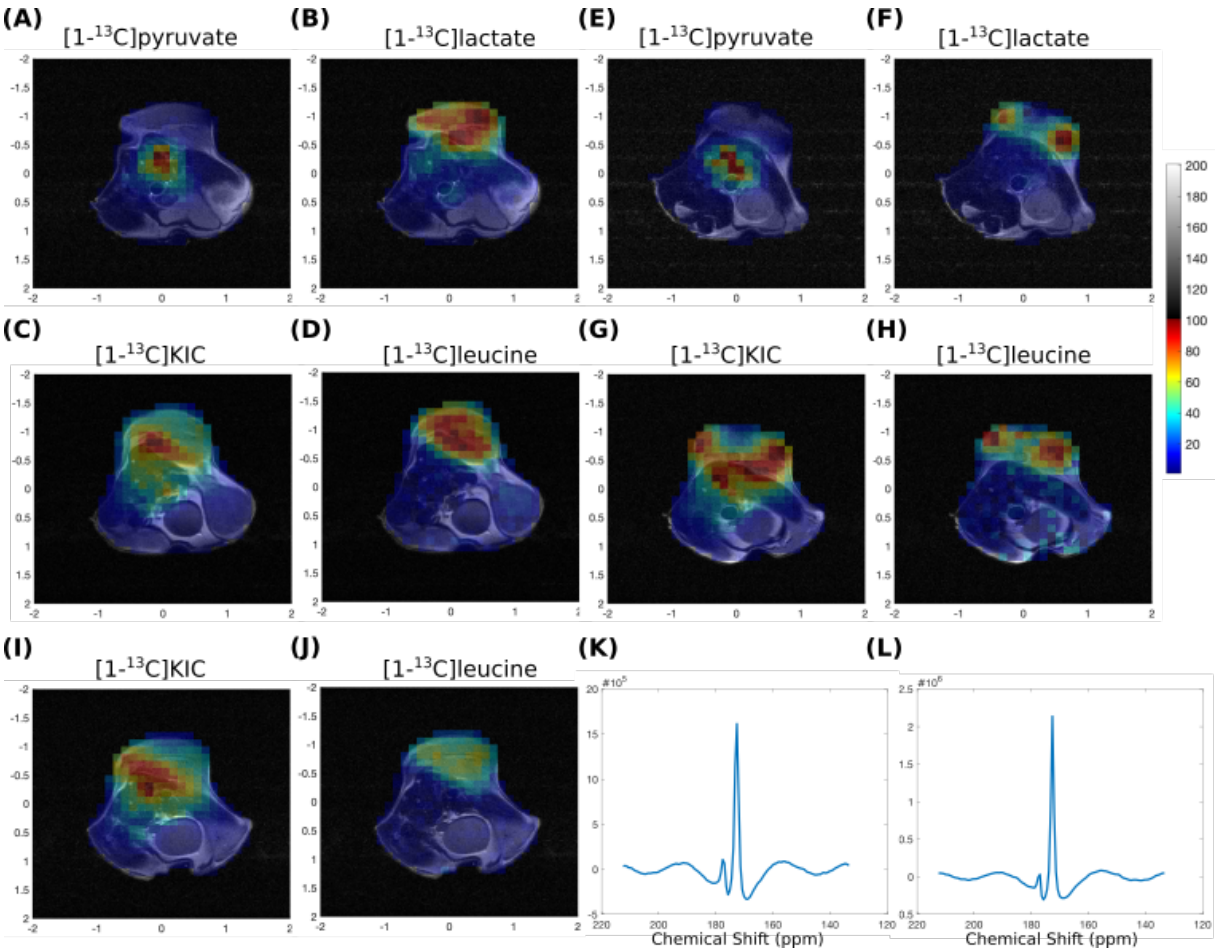

Figure 77 Chemical shift imaging of hyperpolarised ^{13}C pyruvate and ^{13}C KIC in EL4 tumour-bearing. *Hyperpolarised ^{13}C pyruvate and ^{13}C KIC were compared by imaging the same mice on consecutive days. Images (32 x 32 matrix size) were acquired from a 6 mm thick slice in both cases, using a 10º, 600 µs excitation pulse. For pyruvate imaging, the acquisition was started 20 seconds after the start of injection and for KIC imaging after 25 seconds. ^{13}C-labelled pyruvate, lactate, KIC and leucine false colour images are shown for two mice (A-D first mouse, E-H second mouse). The images were normalised to the maximum signal in the image. (I-L) The same mouse imaged using hyperpolarised ^{13}C KIC on the third consecutive day, 1 h after an intravenous injection of gabapentin solution (300 µl of 30 mg/ml solution). (I,J) False colour images represent the intensity of ^{13}C KIC (I) and ^{13}C leucine (J), normalised to the maximum signal in images (C) and (D), respectively, to enable direct comparison. (K,L) Summed spectra from all tumour containing voxels showing the KIC and leucine peaks in the images acquired before (K) and after (L) gabapentin administration. The spectra were normalised to the signal-to-noise ratio to enable direct comparison. The KIC to leucine ratio in (K) is 0.173 and in (L) it is 0.097.*

4.4.2 BCAT activity can be imaged with hyperpolarised [1-^{13}C]KIC in healthy rat brain

Both BCAT isoenzymes have been shown to be expressed in healthy brain in humans and rats[200]. Conversion of [1-^{13}C]KIC to [1-^{13}C]leucine was detected in healthy rat brains in CSI

experiments (Figure 78). The leucine to KIC ratio calculated from summed spectra of brain-containing voxels was lower than from summed spectra of EL4 tumour-containing voxels. This may be caused by multiple factors, including different circulation kinetics in rats compared to mice, rate of delivery of the substrate to the subcutaneous tumour compared to the brain, MCT expression, BCAT1 and BCAT2 activities and the endogenous glutamate and leucine pool sizes.

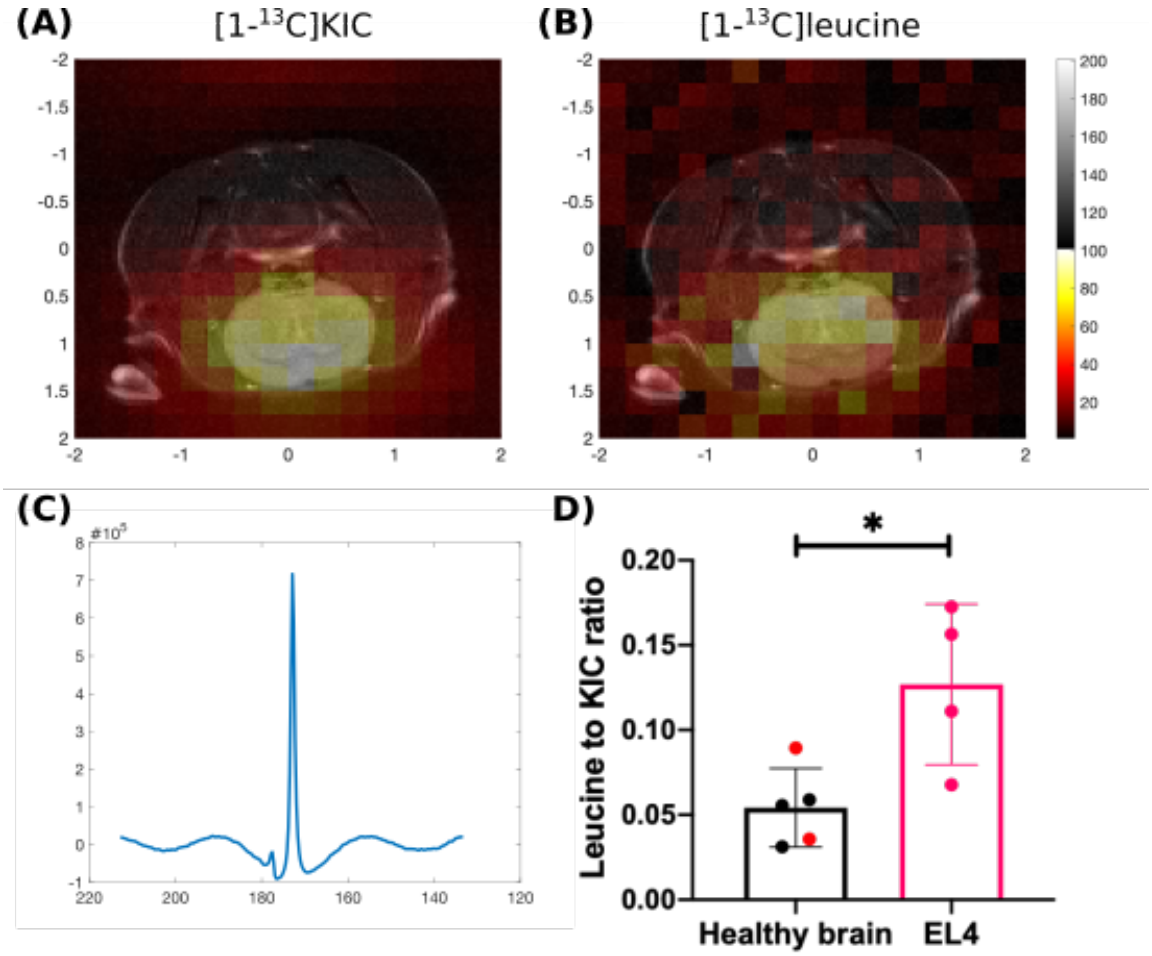

Figure 78 Hyperpolarised ^{13}C KIC imaging in healthy rat brain. *[1-^{13}C]KIC (A) and [1-^{13}C]leucine (B) images overlaid on reference ^{1}H images of the brain of a healthy rat. For the reference ^{1}H image, 15 axial slices of thickness 2 mm and 40 mm x 40 mm field of view were imaged using a Fast Spin Echo sequence. For the ^{13}C CSI, signal was acquired from a 10 mm thick slice using a 700 µs long excitation pulse with a 53° flip angle. The acquisition was started 20 seconds following the start of injection of hyperpolarised ^{13}C KIC. The original voxel size is shown (16 x 16 matrix) and the signal was normalised to the maximum signal in the image. (C) Representative summed spectrum across brain voxels showing the ^{13}C KIC peak (172.6 ppm) and the ^{13}C leucine peak (176.8 ppm). (D) The leucine to KIC ratio in healthy rat brain is smaller than the ratio in subcutaneous EL4 tumours. Ratios were calculated by dividing the area of the leucine peak by the area of the KIC peak in the summed spectra from the brain and tumour voxels. Each dot represents a measurement from a different animal. For healthy brain, black dots represent CSI acquisitions performed 20 seconds after the start of injection of hyperpolarised KIC with rats in a supine position and red dots represent CSI acquisitions performed 35 seconds after the start of injection of hyperpolarised KIC with rats in a prone position. A two-tailed t-test was performed to compare the two groups. N=5 for healthy brain, N=4 for subcutaneous EL4 tumours, *p<0.05 .*

4.4.3 *In vivo* measurements of BCAT activity in Patient Derived Orthotopic Glioblastoma Xenografts

To investigate the capability of hyperpolarised ^{13}C KIC imaging to measure BCAT activity *in vivo* in glioblastoma, athymic nude rats implanted with patient derived glioblastoma cells were used. The cells used for implantation were the A11 cells as well as the genetically engineered clones including the inducible A11shBCAT1 and A11shScr clones, the A11 BCAT1 overexpressing cells and the A11 Luciferase overexpressing cells, all of which were described in Chapter 3. The leucine to KIC ratios measured by CSI in the A11 tumour containing regions of the brain were comparable to those generated in the contralateral normal appearing brain (Figure 79A,B) and much lower than those produced in the subcutaneous EL4 tumours. ^{13}C KIC images showed homogeneous substrate uptake in normal appearing brain and in tumour regions. In order to investigate whether BCAT activity in the tumours was limiting, rats were implanted with A11 BCAT1 overexpressing cells. BCAT1 overexpression led to lower leucine to KIC ratio measured upon hyperpolarised ^{13}C KIC imaging (Figure 79B). Measurement of total BCAT activity in tissue lysates revealed that the A11 glioma had lower total BCAT and BCAT1 activities than healthy brain. However, BCAT1 overexpression led to a three-fold increase in the tumour BCAT activity. Therefore, enzyme activity does not seem to be limiting label exchange.

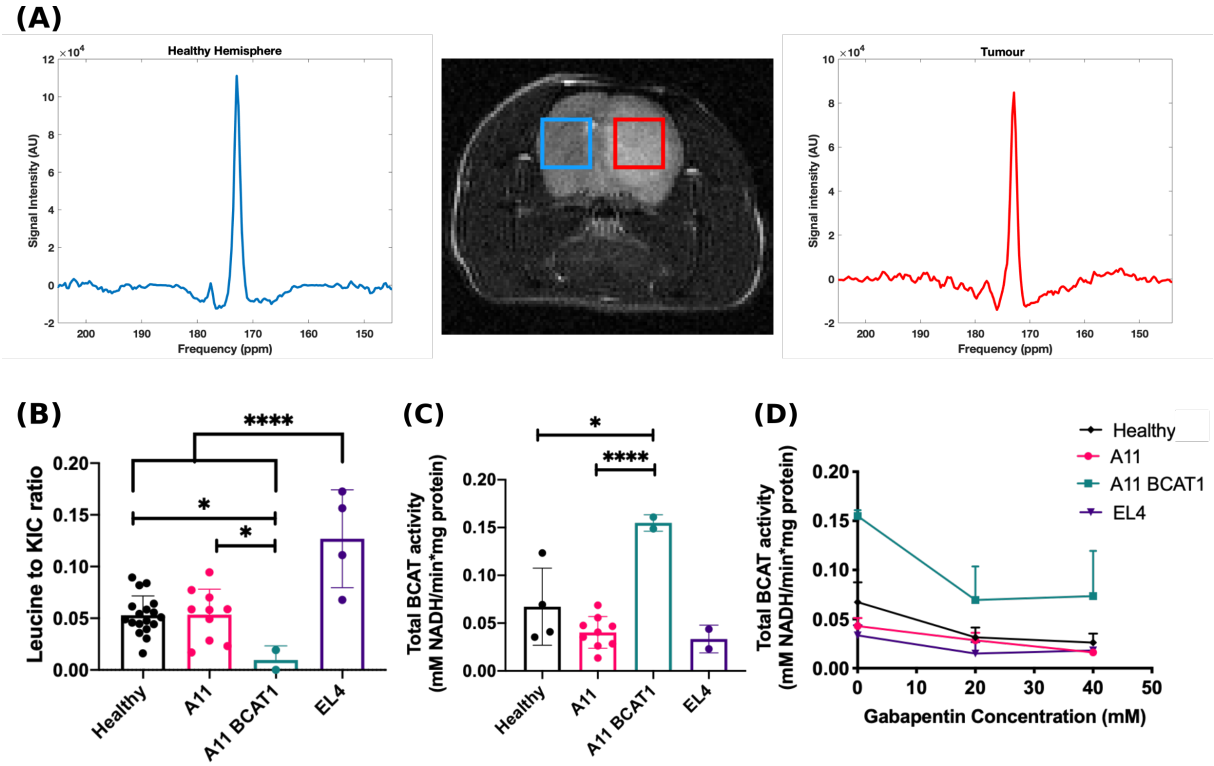

Figure 79 Hyperpolarised ^{13}C KIC imaging in PDOXs. *(A) T_2-weighted MR image of an axial slice showing the healthy left hemisphere and tumour in the right hemisphere. The boxes indicate the voxels from which the summed spectra shown on each side of the image were acquired. Leucine is at 176.8 ppm and KIC is at 172.6 ppm. (B) The leucine to KIC ratio calculated for each imaging experiment from the summed spectra from healthy brain and tumour voxels. Each point represents a measurement from an independent imaging experiment. For A11 tumours, rats implanted with doxycycline-inducible A11shScr and A1shBCAT1 cells and that had not been fed doxycycline in the diet were pooled together. Error bars represent Standard Deviations. (C) Total BCAT activity in tissue lysates measured using a spectrophotometric assay. Each point represents an independent measurement. A11 contains pooled data from doxycycline-inducible A11shScr and A11shBCAT1 tumours in animals that had not been fed with doxycycline. Error bars represent Standard Deviations. (D) Total BCAT activity measured in the spectrophotometric assay with increasing concentrations of gabapentin. Error bars represent SEM. Two-tailed t-tests were performed to compare the mean leucine to KIC ratio and total enzyme activity across different tumour types. *p<0.05,**p<0.01, ***p<0.001, ****p<0.0001*

While the activity measured using tissue lysates in the spectrophotometric assay is the activity in the presence of high substrate concentrations, the activity measured *in vivo* with hyperpolarised [1-^{13}C]KIC is dependent on the concentrations of glutamate and ^{13}C KIC as co-substrates that could be limiting. In addition, the endogenous leucine pool will also affect the rate of label exchange. Delivery of [1-^{13}C]KIC to the tumours appeared equally rapid in the A11 tumours and the contralateral normal appearing brain, as determined by CSI experiments (Figure 80A-B). Additionally, the A11 gliomas express both MCT1 and MCT4 transporters that enable KIC uptake into the cells (Figure 80C-D).

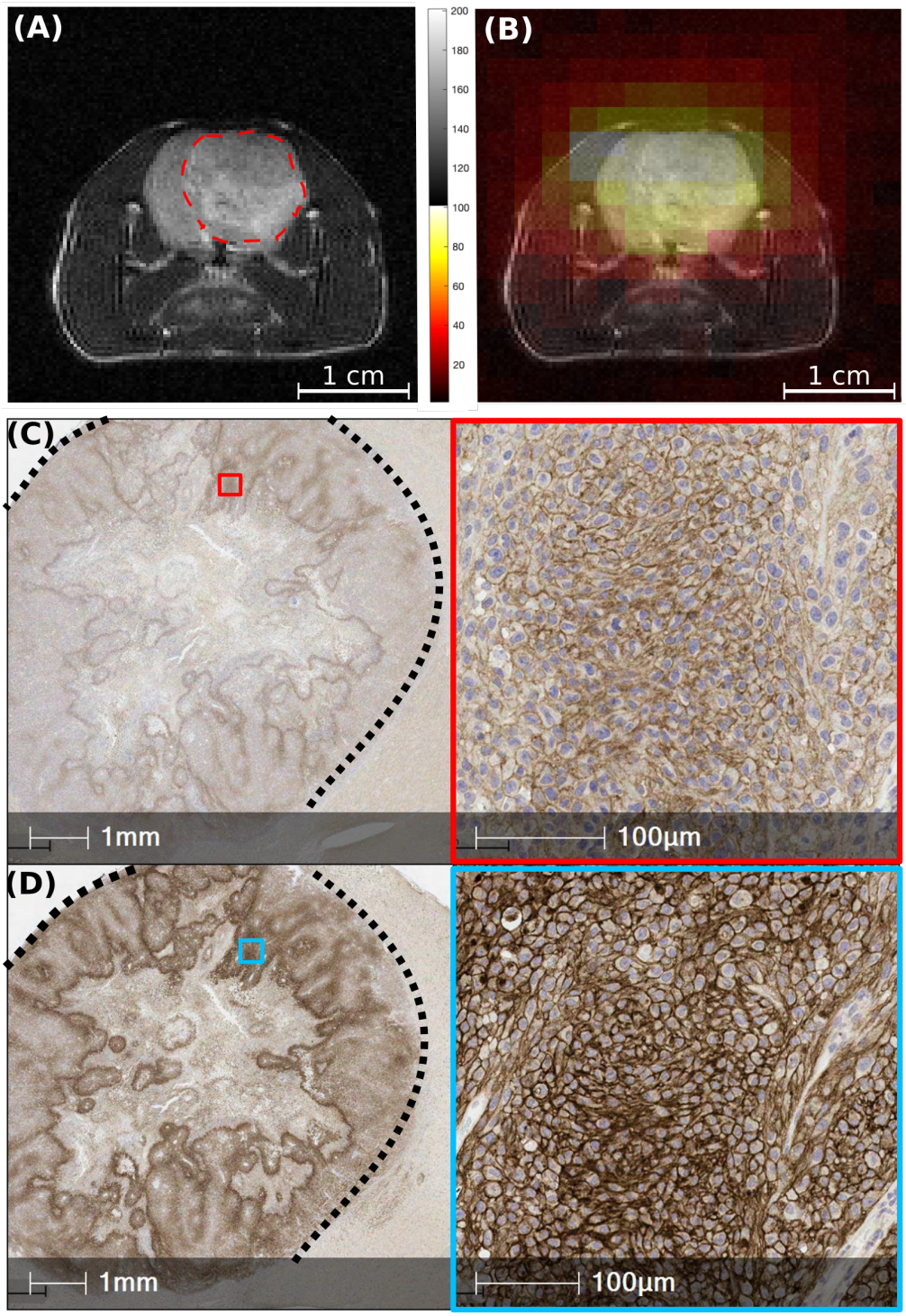

Figure 80 Hyperpolarised ^{13}C KIC delivery and uptake into the tumour does not limit leucine labelling. *Representative example of a T_2-weighted ^{1}H image of an orthotopic A11 glioma (A), with the dashed line delineating the tumour region, overlaid with the [1-^{13}C]KIC signal (B). (C-D) Immunohistochemical staining of an orthotopic A11 tumour for MCT1 (C) and MCT4 (D).*

Gliomas show enhanced uptake of branched chain amino acids through the upregulated Large Neutral Amino Acid Transporter (LAT1)[201]. ^{1}H NMR measurements on extracts of A11 tumour and normal appearing brain confirmed that A11 tumours have a larger pool of endogenous branched chain amino acids, including leucine, when compared to the contralateral normal

appearing brain (Figure 81A-C). Therefore, label exchange is unlikely to be limited by the endogenous leucine pool in these tumours.

Conversely, glutamate levels in the tumours could potentially limit the KIC to leucine conversion. The *in vitro* experiments in Chapter 3 demonstrated high rates of glutamate release by the cells into the media, suggesting that the intracellular concentration of glutamate in these cells would be expected to be maintained at a low level. In addition, BCAT1 knockdown in A11 cells led to an increase in the intracellular levels of glutamate, as measured by LCMS (Figure 67A). Therefore, it is possible that BCAT1 overexpression leads to reduced intracellular levels of glutamate and hence decreased interconversion of KIC and leucine. We performed ^{1}H spectroscopy experiments in tumour-bearing rats to compare glutamate levels in tumour voxels and contralateral healthy brain voxels. Glutamate concentrations were much lower in the tumour regions compared to the contralateral normal appearing brain (Figure 81D-F), suggesting that glutamate might be limiting the KIC to leucine conversion in the tumours.

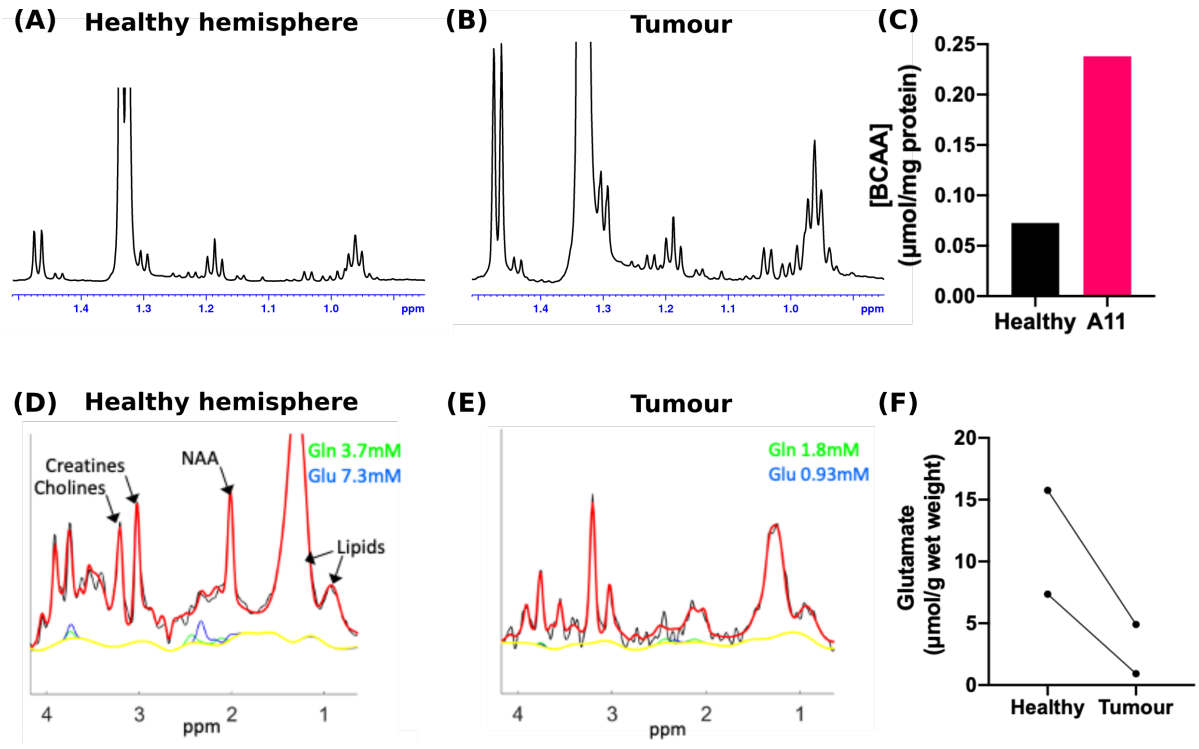

Figure 81 Co-substrate availability may be limiting for the exchange of label between KIC and leucine. *The concentrations of branched chain amino acids in an A11 tumour and in the contralateral healthy hemisphere were determined from ^{1}H NMR measurements on tissue extracts. The spectra of the healthy hemisphere sample (A) and the A11 tumour sample (B) are plotted, with the BCAAs peaks appearing between 0.9 and 1.1 ppm. The triplet at around 0.97 ppm corresponds to the leucine protons. Integration of the total BCAA signals and normalisation to protein content is shown in (C). ^{1}H spectroscopy experiment in two A11 tumour-bearing rats was performed to compare the concentration of glutamate in the healthy hemisphere and in tumours. Representative examples of the fitted spectra acquired from the healthy hemisphere (D) and a tumour region (E) from a 2.5 x 2.5 x 3 mm^{3} voxel. The phased spectra are shown in black, the fitted spectra in red, the baseline in yellow and the glutamine and glutamate peaks in green and blue respectively. (F) Calculated glutamate concentration in the regions sampled by ^{1}H spectroscopy.*

4.5 Discussion

Imaging the transamination reaction catalysed by BCAT using hyperpolarised [1-^{13}C]KIC has been demonstrated previously, both in healthy rat brain[190] and in EL4 tumours[189] as well as in cells *in vitro*[193]. More recently, hyperpolarised [1-^{13}C]KIC was used to compare the rate of oxidation of the ketoacid by measuring the generation of $H^{13}CO_3^-$ from injected [1-^{13}C]KIC in healthy livers and livers with hepatocellular carcinoma[185]. In this study, the potential for using hyperpolarised [1-^{13}C]KIC to image upregulated BCAT1 activity *in vivo* in glioblastoma was examined. The technique was optimised using subcutaneous EL4 lymphoma tumours, which show high levels of BCAT1 and the results obtained were in agreement with the literature. [1-^{13}C]KIC hyperpolarised relatively well and quickly, was well tolerated by the mice and was distributed around the body quickly. EL4 tumours were able to take up the substrate and the label was rapidly exchanged with the endogenous leucine pool. Imaging healthy rat brains demonstrated that [1-^{13}C]KIC could quickly cross the blood brain barrier, enabling the acquisition of sufficient signal from the brain.

Given the important role of BCAT1 in glioblastoma, as discussed in Chapter 3, a method to assess its activity *in vivo* non-invasively would be beneficial both for prognostic purposes and to detect response to the new therapies targeting BCAT1[202]. We investigated the ability of hyperpolarised ^{13}C KIC to image BCAT activity in glioblastoma patient derived orthotopic xenografts in rats. The images acquired showed no contrast between healthy rat brain and the tumours in terms of [1-^{13}C]leucine generation, with very similar leucine/KIC ratios measured in tumour regions and in the normal appearing contralateral brain hemisphere. In a clinical setting, however, there may be contrast between tumour and normal brain as BCAT activity of rat brain is higher than that in human brain, with rat brains having an average BCAT activity of 1944 ± 94 mU/g wet weight and human brains 510 ± 49 mU/g wet weight[203].

Imaging of hyperpolarised ^{13}C KIC metabolism has recently been attempted in a rat glioma model, where the authors reported much lower leucine to KIC ratios (0 to 0.008) than the ratios we observed in A11 tumours, with higher ratios in the contralateral normal appearing brain. The authors suggested that the tumour cells showed increased oxidation of the injected substrate, generating $H^{13}CO_3^-$ instead of transamination to ^{13}C leucine, and they explained this by showing that there was lower BCAT1 expression but higher Branched Chain Ketoacid Dehydrogenase (BCKDC) in the tumour compared to the normal brain. However, the ratio of

both ^{13}C leucine and $H^{13}CO_3^-$ signals to the KIC signal were very low (<0.005), and greatly affected by background noise. Additionally, given that human glioblastoma shows significant upregulation of BCAT1 when compared to healthy brain, whereas the cell line used in this study showed low expression of BCAT1, this result is not representative of human glioblastoma.

The [1-^{13}C]leucine signal generated in the brain (healthy and tumour-bearing) in this study was considerably lower than in the EL4 tumours. This was neither explained by the total BCAT activity nor the BCAT1 activity measured in tissue lysates, which were similar in EL4 tumours, healthy rat brain and in A11 gliomas. Also, A11 tumours overexpressing BCAT1, which had a three-fold higher total BCAT activity, still had very low [1-^{13}C]leucine signals, which were even lower than in the control A11 tumours. This suggests that BCAT activity is not limiting for the KIC to leucine conversion in these glioma tumours and instead it appears that overexpression of the enzyme further limits the conversion rate. For ^{13}C KIC to be converted to leucine, sufficient levels of BCAT should be present, but also sufficient concentrations of the glutamate co-substrate are required. The K_m of BCAT1 for KIC is 0.063 mM and of BCAT2 0.16 mM. The K_m for glutamate on the other hand is 13 mM for BCAT1 and 24 mM for BCAT2, therefore low glutamate concentrations could slow the reaction significantly[204]. GBM cells have been shown to excrete large amounts of glutamate *in vitro*, maintaining a very low intracellular glutamate concentration, which we also demonstrated in the A11 cells (Figure 39B)[51,205]. Using ^1H MRS, we showed that A11 PDOX GBM tumours had lower glutamate concentrations when compared to the contralateral healthy hemisphere. Moreover, as discussed in Chapter 3, BCAT1 knockdown in A11 cells led to a significant increase in the intracellular glutamate pool, possibly via increased flux through aminotransferase enzymes other than BCAT1. Therefore it is possible that BCAT1 overexpression leads to a reduction in the intracellular glutamate pool in these tumours, which would explain the lower transamination rate observed *in vivo*. Glutamate concentrations in EL4 tumours were assayed *ex vivo* in a previous study and were found to be 2.2 μmol/g tissue and significantly higher than adjacent muscle tissue (0.3 μmol/g) suggesting that glutamate availability was not limiting in hyperpolarised ^{13}C KIC imaging of EL4 tumours[189].

A potential solution to this problem would be to increase the glutamate levels in the tumours prior to imaging with hyperpolarised ^{13}C KIC. Injection of glutamate into tumour bearing animals would be challenging given that glutamate uptake into the brain is limited by the blood-brain barrier and that high levels of glutamate are excitotoxic[206]. Also, glioma cells show low

glutamate uptake, with a Vmax<10% of that of normal astrocytes[205]. A bolus injection of glutamine, instead, would in theory lead to a transient increase in intracellular glutamate levels owing to the high glutaminase activity in gliomas. Glioma cells show increased uptake of glutamine, as detected using ^{18}F-Fgln PET experiments, and upregulation of glutaminase, which converts glutamine to glutamate[207]. Alternatively, inhibition of glutamate release from glioma cells using a metabotropic glutamate receptor antagonist could lead to intracellular accumulation of glutamate facilitating the ^{13}C labelling of leucine from [1-^{13}C]KIC[205]. An increase in intracellular glutamate concentration in the tumour could potentially enable the *in vivo* assessment of BCAT activity and would also boost the leucine signal generated, which was very low in these imaging experiments. The rate of conversion of hyperpolarised [1-^{13}C]leucine to [1-^{13}C]KIC would not be limited by the concentration of glutamate and therefore, [1-^{13}C]leucine could be a better imaging substrate for this purpose. However, [1-^{13}C]leucine does not have favourable hyperpolarisation properties as it has a shorter T_1 than [1-^{13}C]KIC and would also need to be dissolved in a solvent before polarisation whereas [1-^{13}C]KIC can be used at its neat concentration as a liquid[208].

The unlabelled leucine pool could also be a limiting factor in the amount of ^{13}C leucine signal detected. However, studies on various cancer cell lines, including the rat C6 glioma cell line, have shown increased uptake of BCAAs via the upregulated LAT1 transporter[201]. In vivo MR spectroscopy experiments in a study by Suh et al showed that the leucine pool in a rat glioma model (F98) was significantly higher (0.278 ± 0.035 μmol/g wet tissue) than the contralateral healthy brain (0.075 ± 0.001 μmol/g wet tissue)[192]. These values are in agreement with the concentrations calculated here from *ex vivo* ^{1}H NMR analysis of A11 tumour and contralateral normal appearing brain extracts. This suggests that the endogenous leucine pool in the A11 tumours is not limiting for ^{13}C label exchange when compared to the contralateral hemisphere.

The presence of both isoenzymes and their contributions to the observed activity need to be taken into account. BCAT1 and BCAT2 have different activities, and in addition, the location of BCAT2 in the mitochondria might mean that it makes a different contribution to the signal observed compared to BCAT1, which is in the cytoplasm. In preliminary experiments in EL4 tumour bearing mice, we saw that BCAT1 inhibition by gabapentin led to a greatly reduced leucine to KIC ratio suggesting a large contribution of BCAT1 on the conversion of ^{13}C KIC to ^{13}C leucine in EL4 tumours. These experiments were limited by the high growth rate of the tumours, which led to changes in tumour size and possibly also metabolism between

consecutive days. Also, the need for repeated cannulation of these mice greatly limited the number of mice that were scanned on both days due to inability to cannulate an injured tail vein.

Imaging of hyperpolarised ^{13}C KIC is a promising technique and may prove useful in measuring BCAT1 upregulation non-invasively in some cancers. However, the dependence of label exchange between KIC and leucine on many factors, other than BCAT1 activity will need to be taken into account. In glioblastoma, more models need to be imaged using this technique in order to understand whether it provides useful prognostic information.

4.6 Conclusion

Hyperpolarised ^{13}C KIC is a promising substrate for studying BCAT activity in tumours and this was demonstrated in subcutaneous EL4 lymphoma tumours. However, the rate of label exchange in this reaction depends on multiple factors, including enzyme activity, the rate of substrate delivery, the activity of the MCT transporters and the sizes of the endogenous glutamate and leucine pools. In orthotopic patient derived glioma xenografts in rats, imaging of hyperpolarised ^{13}C KIC does not provide a direct measure of BCAT activity, which is most likely a result of a limiting glutamate concentration.

Chapter 5 - General Discussion

Metabolic imaging techniques are becoming essential tools for investigating cancer metabolism, particularly in the clinic, potentially enabling identification of new therapeutic targets and biomarkers of cancer. Some of these techniques, including hyperpolarised ^{13}C imaging, can be used clinically, to stage disease and monitor treatment response, which can be used to guide treatment.

In this thesis, the use of imaging with hyperpolarised [1-^{13}C]pyruvate imaging was cross-validated with MSI, another novel metabolic imaging technique. The two techniques generated positively correlated images of [1-^{13}C]lactate in subcutaneous murine lymphoma tumours following injection of hyperpolarised [1-^{13}C]pyruvate. The two techniques are complementary in the possibilities that they offer for imaging cancer metabolism, in that MSI enables the acquisition of high resolution images of a large number of metabolites, isotopically labelled or unlabelled, while ^{13}C MRSI with hyperpolarised [1-^{13}C]pyruvate generates only low resolution images of [1-^{13}C]lactate and [1-^{13}C]pyruvate, but these can be obtained non-invasively and in real time, thus providing kinetic information. In this study, using both techniques on the same tumours enabled an understanding of the factors influencing labelling kinetics.

Hyperpolarised [1-^{13}C]Ketoisocaproic acid is a novel substrate that has been demonstrated in a number of publications, where label flux between hyperpolarised [1-^{13}C]KIC and [1-^{13}C]leucine and $H^{13}CO_3^-$, catalysed by BCAT1/2 and BCKDC respectively, were measured following injection of hyperpolarised [1-^{13}C]KIC in mice and rats. This appears to be a promising technique given the recent interest in Branched Chain Amino Acid metabolism in cancer. However, as with any imaging substrate, it is important to understand what information it can provide and how useful it could be in a clinical scenario.

In this project, I have studied the role of BCAT1 in patient derived glioblastoma cells and xenografts in rodents, where I have shown that BCAT1 promotes cell proliferation via the regulation of HIF and FOXM1 transcriptional activity. BCAT1 knockdown in A11 glioblastoma cells led to a significantly different transcriptional profile, which could explain the reduced rate of cell proliferation as well as the reduced neurosphere forming ability of the cells. The proliferation defect in the cells could be mimicked by supplementation of the cells with dimethyl α-KG and could be rescued by DMOG. These results, in addition to changes in

the levels of 5-hydroxymethyl cytosine in the DNA of cells suggest that the effects of BCAT1 knockdown are mediated through activation of α-KG dependent dioxygenases. Therefore, the role of BCAT1 in these cells is to regulate the cytosolic pool of α-KG which has pleiotropic effects in the cells leading to a highly proliferative phenotype.

α-KG is a metabolic regulator of tumour fate owing to its central role in metabolic reactions as well as its role as a substrate for the α-KG dependent dioxygenases, in particular prolyl hydroxylase enzymes controlling HIF-1α degradation and the DNA and histone demethylase enzymes controlling gene expression[27]. α-KG can tightly control the degradation rate of HIF-1α, with a K_m of the prolyl hydroxylase for α-KG of about 50 μM, close to the physiological concentration of the metabolite, suggesting that even small changes in the levels of α-KG can have profound effects on the stability of HIF-1α and hence the hypoxic response of the cells[27]. The fact that all three TCA cycle intermediates which have oncogenic activity, succinate, fumarate and 2HG act through competitive inhibition of the α-KG dependent dioxygenases, highlights the role of α-KG as an obligate substrate of those enzymes controlling tumour fate. Owing to the regulatory role of α-KG, several attempts have been made to increase the intracellular levels of the metabolite as an anti-cancer agent[24,27]. For example, intraperitoneal injections of α-KG in a mouse model of breast cancer led to a significant reduction in primary tumour growth as well as the number of lung and lymph node metastases[209]. The problem with exogenous administration of α-KG is its low cell permeability, therefore the ketoacid is frequently attached to hydrophobic carriers in order to increase membrane permeability[39].

The identification of the processes regulating α-KG homeostasis in a cancer cell is thus an important step towards finding therapeutic targets for cancer and it is likely that targeting BCAT1 in glioblastoma, potentially in combination with inhibition of other α-KG regulating enzymes, can lead to the desired increase in α-KG levels in the tumour and hence arrest of tumour growth. A similar approach was followed by Atlante et al, where an inhibitor of α-KG dehydrogenase was administered to mice implanted orthotopically with breast cancer cells. This led to accumulation of α-KG and reduced incidence and area of lung metastases[210].

The ability to image the activity of BCAT1 non-invasively could be beneficial in terms of obtaining prognostic information about the tumour and in guiding treatment. However, hyperpolarised [1-^{13}C]KIC did not perform as well as we had hoped it would, in terms of measuring BCAT1 activity *in vivo*. In fact, overexpression of BCAT1 in patient derived orthotopic xenografts in rats led to reduced leucine signal in the tumour. This is a result of the

many factors that affect the rate of label exchange between [1-^{13}C]KIC and the endogenous leucine pool. The injected substrate needs to be delivered to the tumour, taken up by the cancer cells and converted to leucine. The concentration of the co-substrate, glutamate as well as the endogenous leucine pool will affect the rate of label exchange. In this case, we have evidence that the intracellular glutamate levels are limiting for the exchange of label between the injected [1-^{13}C]KIC and endogenous leucine pool. BCAT1 expression is associated with glutamate efflux from the cells, as documented before[51] and as shown here. It also appears that BCAT1 levels regulate the intracellular levels of glutamate, which would explain the decreased leucine signal observed when overexpressing BCAT1. This means that hyperpolarised [1-^{13}C]KIC cannot be used as a direct probe for BCAT1 activity in this case.

However, this limitation does not undermine the potential of the technique for imaging other tumours or pathologies. The changes in Branched Chain Amino Acid metabolism are very diverse in cancer and in human physiology and further research into the role of these metabolic pathways could identify potential scenarios where this imaging substrate might be useful. Additionally, as the hyperpolarised ^{13}C imaging field advances, the ability to hyperpolarise other substrates, such as [1-^{13}C]leucine, might prove more useful in providing a better measure of BCAT1 activity.

Metabolism plays a major role in cancer development, progression, resistance to therapy and recurrence following treatment. Further research into the role of BCAT1 as well as the rest of Branched Chain Amino Acid metabolism in glioblastoma could lead to a better understanding of its role in the pathophysiology of this cancer, which could open new opportunities for treatment. In particular, the differences between the roles of BCAT1 and BCAT2 in glioblastoma cells and how metabolic fluxes through the reactions catalysed by each of these isoforms is affected by flux in the reaction catalysed by the other isoform would be interesting to investigate given that knockdown of the two enzymes does not have the same effects on the cells. Additionally, the association between Branched Chain Amino Acid metabolism and fatty acid metabolism is an area that could be explored to identify metabolic vulnerabilities[211,212].

References

1 *Cancer Research UK*, <http://www.cancerresearchuk.org/health-professional/cancer-statistics/mortality#heading-Zero>

2 Hanahan, D. & Weinberg, R. A. The Hallmarks of Cancer. *Cell* **100**, 57-70 (2000).

3 Hanahan, D. & Weinberg, R. A. Hallmarks of cancer: The next generation. *Cell*, doi:10.1016/j.cell.2011.02.013 (2011).

4 Pavlova, N. N. & Thompson, C. B. The Emerging Hallmarks of Cancer Metabolism. *Cell Metabolism* **23**, 27-47, doi:10.1016/j.cmet.2015.12.006 (2016).

5 DeBerardinis, R. J. & Chandel, N. S. Fundamentals of cancer metabolism. *Science Advances* **2**, e1600200-e1600200, doi:10.1126/sciadv.1600200 (2016).

6 Koppenol, W. H., Bounds, P. L. & Dang, C. V. Otto Warburg's contributions to current concepts of cancer metabolism. *Nature Reviews Cancer* **11**, 325-337, doi:10.1038/nrc3038 (2011).

7 d'Amico, A. Review of clinical practice utility of positron emission tomography with 18F-fluorodeoxyglucose in assessing tumour response to therapy. *Radiologia Medica* **120**, 345-351, doi:10.1007/s11547-014-0446-4 (2015).

8 Heiden, M. G. V., Cantley, L. C. & Thompson, C. B. Understanding the Warburg Effect: The Metabolic Requirements of Cell Proliferation. *Science* **324**, 1029-1033, doi:10.1126/science.1160809 (2009).

9 Kishton, R. J. *et al.* AMPK Is Essential to Balance Glycolysis and Mitochondrial Metabolism to Control T-ALL Cell Stress and Survival. *Cell Metab* **23**, 649-662, doi:10.1016/j.cmet.2016.03.008 (2016).

10 Gao, C., Shen, Y., Jin, F., Miao, Y. & Qiu, X. Cancer Stem Cells in Small Cell Lung Cancer Cell Line H446: Higher Dependency on Oxidative Phosphorylation and Mitochondrial Substrate-Level Phosphorylation than Non-Stem Cancer Cells. *PLoS One* **11**, e0154576, doi:10.1371/journal.pone.0154576 (2016).

11 Yang, L., Venneti, S. & Nagrath, D. Glutaminolysis: A Hallmark of Cancer Metabolism. *Annu. Rev. Biomed. Eng* **19**, 163-194, doi:10.1146/annurev-bioeng-071516 (2017).

12 Lukey, M. J., Katt, W. P. & Cerione, R. A. Targeting amino acid metabolism for cancer therapy. *Drug Discovery Today* **22**, 796-804, doi:10.1016/j.drudis.2016.12.003 (2017).

13 Maus, A. & Peters, G. J. Glutamate and α-ketoglutarate: key players in glioma metabolism. *Amino Acids* **49**, 21-32, doi:10.1007/s00726-016-2342-9 (2017).

14 Stine, Z. E., Walton, Z. E., Altman, B. J., Hsieh, A. L. & Dang, C. V. MYC, metabolism, and cancer. *Cancer Discovery* **5**, 1024-1039, doi:10.1158/2159-8290.CD-15-0507 (2015).

15 Vander Heiden, M. G. & DeBerardinis, R. J. Understanding the Intersections between Metabolism and Cancer Biology. *Cell* **168**, 657-669, doi:10.1016/j.cell.2016.12.039 (2017).

16 Davidson, S. M. *et al.* Environment Impacts the Metabolic Dependencies of Ras-Driven Non-Small Cell Lung Cancer. *Cell Metab* **23**, 517-528, doi:10.1016/j.cmet.2016.01.007 (2016).

17 Yuneva, M. O. *et al.* The metabolic profile of tumors depends on both the responsible genetic lesion and tissue type. *Cell Metab* **15**, 157-170, doi:10.1016/j.cmet.2011.12.015 (2012).

18 Mardis, E. R. *et al.* Recurring Mutations Found by Sequencing an Acute Myeloid Leukemia Genome. *The New England Journal of Medicine* **361**, 1058-1066 (2009).

19 Parsons, D. W. *et al.* An Integrated Genomic Analysis of Human Glioblastoma Multiforme. *Science* **321**, 1807-1813, doi:10.1126/science.1164382 (2008).

20 Raineri, S. & Mellor, J. IDH1: Linking Metabolism and Epigenetics. *Frontiers in Genetics* **9**, 1-8, doi:10.3389/fgene.2018.00493 (2018).

21 Ricketts, C. *et al.* Germline SDHB mutations and familial renal cell carcinoma. *J Natl Cancer Inst* **100**, 1260-1262, doi:10.1093/jnci/djn254 (2008).

22 Castro-Vega, L. J. *et al.* Germline mutations in FH confer predisposition to malignant pheochromocytomas and paragangliomas. *Hum Mol Genet* **23**, 2440-2446, doi:10.1093/hmg/ddt639 (2014).

23 Isaacs, J. S. *et al.* HIF overexpression correlates with biallelic loss of fumarate hydratase in renal cancer: novel role of fumarate in regulation of HIF stability. *Cancer Cell* **8**, 143-153, doi:10.1016/j.ccr.2005.06.017 (2005).

24 Zdzisińska, B., Żurek, A. & Kandefer-Szerszeń, M. Alpha-Ketoglutarate as a Molecule with Pleiotropic Activity: Well-Known and Novel Possibilities of Therapeutic Use. *Archivum Immunologiae et Therapiae Experimentalis* **65**, 21-36, doi:10.1007/s00005-016-0406-x (2017).

25 Morris, J. P. *et al.* α-Ketoglutarate links p53 to cell fate during tumour suppression. *Nature* **573**, 595-599, doi:10.1038/s41586-019-1577-5 (2019).

26 Di Conza, G., Tsai, C. H. & Ho, P. C. Fifty Shades of α-Ketoglutarate on Cellular Programming. *Molecular Cell* **76**, 1-3, doi:10.1016/j.molcel.2019.09.002 (2019).

27 Abla, H., Sollazzo, M., Gasparre, G., Iommarini, L. & Porcelli, A. M. The multifaceted contribution of α-ketoglutarate to tumor progression: An opportunity to exploit? *Seminars in Cell and Developmental Biology*, 1-8, doi:10.1016/j.semcdb.2019.05.031 (2019).

28 Cummins, E. P. *et al.* Prolyl hydroxylase-1 negatively regulates IkappaB kinase-beta, giving insight into hypoxia-induced NFkappaB activity. *Proc Natl Acad Sci U S A* **103**, 18154-18159, doi:10.1073/pnas.0602235103 (2006).

29 TeSlaa, T. *et al.* α-Ketoglutarate Accelerates the Initial Differentiation of Primed Human Pluripotent Stem Cells. *Cell Metabolism* **24**, 485-493, doi:10.1016/j.cmet.2016.07.002 (2016).

30 Losman, J. A., Koivunen, P. & Kaelin, W. G., Jr. 2-Oxoglutarate-dependent dioxygenases in cancer. *Nat Rev Cancer* **20**, 710-726, doi:10.1038/s41568-020-00303-3 (2020).

31 Laukka, T. *et al.* Fumarate and Succinate Regulate Expression of Hypoxia-inducible Genes via TET Enzymes. *J Biol Chem* **291**, 4256-4265, doi:10.1074/jbc.M115.688762 (2016).

32 Xiao, M. *et al.* Inhibition of alpha-KG-dependent histone and DNA demethylases by fumarate and succinate that are accumulated in mutations of FH and SDH tumor suppressors. *Genes Dev* **26**, 1326-1338, doi:10.1101/gad.191056.112 (2012).

33 Figueroa, M. E. *et al.* Leukemic IDH1 and IDH2 mutations result in a hypermethylation phenotype, disrupt TET2 function, and impair hematopoietic differentiation. *Cancer Cell* **18**, 553-567, doi:10.1016/j.ccr.2010.11.015 (2010).

34 Turcan, S. *et al.* IDH1 mutation is sufficient to establish the glioma hypermethylator phenotype. *Nature* **483**, 479-483, doi:10.1038/nature10866 (2012).

35 Carey, B. W., Finley, L. W. S., Cross, J. R., Allis, C. D. & Thompson, C. B. Intracellular α-ketoglutarate maintains the pluripotency of embryonic stem cells. *Nature* **518**, 413-416, doi:10.1038/nature13981 (2015).

36 Hirsila, M., Koivunen, P., Gunzler, V., Kivirikko, K. I. & Myllyharju, J. Characterization of the human prolyl 4-hydroxylases that modify the hypoxia-inducible factor. *J Biol Chem* **278**, 30772-30780, doi:10.1074/jbc.M304982200 (2003).

37 Tennant, D. A. & Gottlieb, E. HIF prolyl hydroxylase-3 mediates alpha-ketoglutarate-induced apoptosis and tumor suppression. *J Mol Med (Berl)* **88**, 839-849, doi:10.1007/s00109-010-0627-0 (2010).

38 Rzeski, W. *et al.* Alpha-ketoglutarate (AKG) inhibits proliferation of colon adenocarcinoma cells in normoxic conditions. *Scand J Gastroenterol* **47**, 565-571, doi:10.3109/00365521.2012.660539 (2012).

39 MacKenzie, E. D. *et al.* Cell-permeating alpha-ketoglutarate derivatives alleviate pseudohypoxia in succinate dehydrogenase-deficient cells. *Mol Cell Biol* **27**, 3282-3289, doi:10.1128/MCB.01927-06 (2007).

40 Hensley, C. T., Wasti, A. T. & Deberardinis, R. J. Glutamine and cancer : cell biology , physiology , and clinical opportunities. *The Journal of Clinical Investigation* **123**, 3678-3684, doi:10.1172/JCI69600.3678 (2013).

41 van den Heuvel, A. P., Jing, J., Wooster, R. F. & Bachman, K. E. Analysis of glutamine dependency in non-small cell lung cancer: GLS1 splice variant GAC is essential for cancer cell growth. *Cancer Biol Ther* **13**, 1185-1194, doi:10.4161/cbt.21348 (2012).

42 Kung, H. N., Marks, J. R. & Chi, J. T. Glutamine synthetase is a genetic determinant of cell type-specific glutamine independence in breast epithelia. *PLoS Genet* **7**, e1002229, doi:10.1371/journal.pgen.1002229 (2011).

43 Ananieva, E. A. & Wilkinson, A. C. Branched-chain amino acid metabolism in cancer. *Current Opinion in Clinical Nutrition and Metabolic Care* **21**, 64-70, doi:10.1097/MCO.0000000000000430 (2018).

44 Zhang, L. & Han, J. Branched-chain amino acid transaminase 1 (BCAT1) promotes the growth of breast cancer cells through improving mTOR-mediated mitochondrial biogenesis and function. *Biochemical and Biophysical Research Communications* **486**, 224-231, doi:10.1016/j.bbrc.2017.02.101 (2017).

45 Mayers, J. R. *et al.* Tissue-of-origin Dictates Branched-Chain Amino Acid Metabolism in Mutant Kras -driven Cancers. *Science* **353**, 1161-1165, doi:10.1126/science.aaf5171.Tissue-of-origin (2017).

46 Yoshikawa, R. *et al.* ECA39 is a novel distant metastasis-related biomarker in colorectal cancer. *World Journal of Gastroenterology* **12**, 5884-5889, doi:10.3748/wjg.v12.i36.5884 (2006).

47 Chang, I. W. *et al.* BCAT1 overexpression is an indicator of poor prognosis in patients with urothelial carcinomas of the upper urinary tract and urinary bladder. *Histopathology* **68**, 520-532, doi:10.1111/his.12778 (2016).

48 Wang, Z.-Q. *et al.* BCAT1 expression associates with ovarian cancer progression: possible implications in altered disease metabolism. *Oncotarget* **6**, 31522-31543, doi:10.18632/oncotarget.5159 (2015).

49 Xu, Y. *et al.* Overexpression of BCAT1 is a prognostic marker in gastric cancer. *Human Pathology* **75**, 41-46, doi:10.1016/j.humpath.2018.02.003 (2018).

50 Hattori, A. *et al.* Cancer progression by reprogrammed BCAA metabolism in myeloid leukaemia. *Nature* **545**, 500-504, doi:10.1038/nature22314 (2017).

51 Tönjes, M. *et al.* BCAT1 promotes cell proliferation through amino acid catabolism in gliomas carrying wild-type IDH1. *Nature Medicine* **19**, 901-908, doi:10.1038/nm.3217 (2013).

52 Mayers, J. R. & Heiden, M. G. V. BCAT1 defines gliomas by IDH status. *Nature Medicine* **19**, 816-817, doi:10.1038/nm.3263 (2013).

53 Zhou, W. *et al.* Over-expression of BCAT1, a c-Myc target gene, induces cell proliferation, migration and invasion in nasopharyngeal carcinoma. *Molecular Cancer*, doi:10.1186/1476-4598-12-53 (2013).

54 Xu, M. *et al.* BCAT1 promotes tumor cell migration and invasion in hepatocellular carcinoma. *Oncology Letters* **12**, 2648-2656, doi:10.3892/ol.2016.4969 (2016).

55 Zheng, Y. H. *et al.* BCAT1, a key prognostic predictor of hepatocellular carcinoma, promotes cell proliferation and induces chemoresistance to cisplatin. *Liver International* **36**, 1836-1847, doi:10.1111/liv.13178 (2016).

56 Huet, E., Gabison, E. E., Mourah, S. & Menashi, S. Role of emmprin/CD147 in tissue remodeling. *Connective Tissue Research* **49**, 175-179, doi:10.1080/03008200802151722 (2008).

57 Nabeshima, K. *et al.* Emmprin (basigin/CD147): Matrix metalloproteinase modulator and multifunctional cell recognition molecule that plays a critical role in cancer progression. *Pathology International* **56**, 359-367, doi:10.1111/j.1440-1827.2006.01972.x (2006).

58 Liang, Q. *et al.* Inhibition of basigin expression in glioblastoma cell line via antisense RNA reduces tumor cell invasion and angiogenesis. *Cancer Biology and Therapy* **4**, 759-762, doi:10.4161/cbt.4.7.1828 (2005).

59 Yang, M. *et al.* Prognostic significance of CD147 in patients with glioblastoma. *Journal of Neuro-Oncology* **115**, 19-26, doi:10.1007/s11060-013-1207-2 (2013).

60 Papathanassiu, A. E. & Vu, H. A. Abstract 3216: Cytosolic leucine metabolism regulates the expression of prometastatic proteins: The genesis of a new druggable target. *Cancer Research* **72**, 3216 LP-3216 (2012).

61 Mayers, J. R. *et al.* Tissue of origin dictates branched-chain amino acid metabolism in mutant Kras-driven cancers. *Science* **353**, 1161-1165, doi:10.1126/science.aaf5171 (2016).

62 Li, J. T. *et al.* BCAT2-mediated BCAA catabolism is critical for development of pancreatic ductal adenocarcinoma. *Nature Cell Biology* **22**, 167-174, doi:10.1038/s41556-019-0455-6 (2020).

63 Clavell, L. A. *et al.* Four-agent induction and intensive asparaginase therapy for treatment of childhood acute lymphoblastic leukemia. *The New England Journal of Medicine* **315**, 657-663, doi:10.1249/00005768-199407000-00008 (1986).

64 Luengo, A., Gui, D. Y. & Vander Heiden, M. G. Targeting Metabolism for Cancer Therapy. *Cell Chemical Biology* **24**, 1161-1180, doi:10.1016/j.chembiol.2017.08.028 (2017).

65 Lindau, B. R., Laszlo, R., Stengle, J. & Burk, D. Certain Metabolic and Pharmacologic Effects in Cancer Patients Given Infusions of 2-Deoxy-D-Glucose. *Journal of the National Cancer Institute* **21**, 485-494 (1958).

66 Günter, H. The Physical Basis of the Nuclear Magnetic Resonance Experiment. Part I. *NMR Spectroscopy. Basic Principles, Concepts and Applications in Chemistry*, 13-28 (2013).

67 Cho, A., Lau, J. Y. C., Geraghty, B. J., Cunningham, C. H. & Keshari, K. R. Noninvasive interrogation of cancer metabolism with hyperpolarized 13C MRI. *Journal of Nuclear Medicine* **58**, 1201-1206, doi:10.2967/jnumed.116.182170 (2017).

68 Brateman, L. Chemical Shift Imaging: A Review. *American Journal of Roentgenology* **86** (1986).

69 Schär, M., Strasser, B. & Dydak, U. CSI and SENSE CSI. *eMagRes* **5**, 1291-1306, doi:10.1002/9780470034590.emrstm1454 (2016).

70 Ardenkjaer-Larsen, J. H. *et al.* Increase in signal-to-noise ratio of > 10,000 times in liquid-state NMR. *Proceedings of the National Academy of Sciences* **100**, 10158-10163, doi:10.1073/pnas.1733835100 (2003).

71 Galloway, D. A., Laimins, L. A., Division, B. & Hutchinson, F. Hyperpolarization MRI: Preclinical Models and Potential Applications in Neuroradiology. *Topics in Magnetic Resonance Imaging* **25**, 87-92, doi:10.1016/j.coviro.2015.09.001.Human (2016).

72 Rodrigues, T. B. *et al.* Magnetic resonance imaging of tumor glycolysis using hyperpolarized 13 C-labeled glucose. *Nature Medicine* **20**, 93-97, doi:10.1038/nm.3416 (2014).

73 Cabella, C. *et al.* In vivo and in vitro liver cancer metabolism observed with hyperpolarized [5-13C]glutamine. *Journal of Magnetic Resonance* **232**, 45-52, doi:10.1016/j.jmr.2013.04.010 (2013).

74 Chaumeil, M. M. *et al.* Hyperpolarized [1-13C] glutamate: A metabolic imaging biomarker of IDH1 mutational status in glioma. *Cancer Research* **74**, 4247-4257, doi:10.1158/0008-5472.CAN-14-0680 (2014).

75 Aggarwal, R., Vigneron, D. B. & Kurhanewicz, J. Hyperpolarized 1-[13C]-Pyruvate Magnetic Resonance Imaging Detects an Early Metabolic Response to Androgen Ablation Therapy in Prostate Cancer. *European Urology* **72**, 1028-1029, doi:10.1016/j.eururo.2017.07.022 (2017).

76 Gallagher, F. A. *et al.* Imaging breast cancer using hyperpolarized carbon-13 MRI. *Proceedings of the National Academy of Sciences of the United States of America* **117**, 2092-2098, doi:10.1073/pnas.1913841117 (2020).

77 Hesketh, R. L. & Brindle, K. M. Magnetic resonance imaging of cancer metabolism with hyperpolarized13C-labeled cell metabolites. *Current Opinion in Chemical Biology* **45**, 187-194, doi:10.1016/j.cbpa.2018.03.004 (2018).

78 Omuro, A. & DeAngelis, L. M. Glioblastoma and other malignant gliomas: A clinical review. *JAMA - Journal of the American Medical Association* **310**, 1842-1850, doi:10.1001/jama.2013.280319 (2013).

79 Fernandes, C. *et al. Glioblastoma*. (2017).

80 van Lith, S. A. M. *et al.* Glutamate as chemotactic fuel for diffuse glioma cells: Are they glutamate suckers? *Biochimica et Biophysica Acta - Reviews on Cancer* **1846**, 66-74, doi:10.1016/j.bbcan.2014.04.004 (2014).

81 Verhaak, R. G. W. *et al.* Integrated Genomic Analysis Identifies Clinically Relevant Subtypes of Glioblastoma Characterized by Abnormalities in PDGFRA, IDH1, EGFR, and NF1. *Cancer Cell* **17**, 98-110, doi:10.1016/j.ccr.2009.12.020 (2010).

82 Torsvik, A. *et al.* U-251 revisited: Genetic drift and phenotypic consequences of long-term cultures of glioblastoma cells. *Cancer Medicine* **3**, 812-824, doi:10.1002/cam4.219 (2014).

83 Allen, M., Bjerke, M., Edlund, H., Nelander, S. & Westermark, B. Origin of the U87MG glioma cell line: Good news and bad news. *Science Translational Medicine* **8**, doi:10.1126/scitranslmed.aaf6853 (2016).

84 Lenting, K., Verhaak, R., ter Laan, M., Wesseling, P. & Leenders, W. Glioma: experimental models and reality. *Acta Neuropathologica* **133**, 263-282, doi:10.1007/s00401-017-1671-4 (2017).

85 Jacobs, V. L., Valdes, P. A., Hickey, W. F. & de Leo, J. A. Current review of in vivo GBM rodent models: Emphasis on the CNS-1 tumour model. *ASN Neuro* **3**, 171-181, doi:10.1042/AN20110014 (2011).

86 Castle, K. D., Chen, M., Wisdom, A. J. & Kirsch, D. G. Genetically engineered mouse models for studying radiation biology. *Transl Cancer Res* **6**, S900-S913, doi:10.21037/tcr.2017.06.19 (2017).

87 Miyai, M. *et al.* Current trends in mouse models of glioblastoma. *J Neurooncol* **135**, 423-432, doi:10.1007/s11060-017-2626-2 (2017).

88 Ruiz-Rodado, V. *et al.* Metabolic Landscape of a Genetically Engineered Mouse Model of IDH1 Mutant Glioma. *Cancers (Basel)* **12**, doi:10.3390/cancers12061633 (2020).

89 Zou, P. *et al.* IDH1/IDH2 Mutations Define the Prognosis and Molecular Profiles of Patients with Gliomas: A Meta-Analysis. *PLoS ONE* **8**, 1-7, doi:10.1371/journal.pone.0068782 (2013).

90 Zhang, Y. *et al.* The p53 pathway in glioblastoma. *Cancers* **10**, doi:10.3390/cancers10090297 (2018).

91 Wang, J. *et al.* c-Myc is required for maintenance of glioma cancer stem cells. *PLoS ONE* **3**, doi:10.1371/journal.pone.0003769 (2008).

92 Zhang, S. *et al.* m6A Demethylase ALKBH5 Maintains Tumorigenicity of Glioblastoma Stem-like Cells by Sustaining FOXM1 Expression and Cell Proliferation Program. *Cancer Cell* **31**, 591-606.e596, doi:10.1016/j.ccell.2017.02.013 (2017).

93 H. Zheng, H. Y. H. Y. A. C. K. *et al.* Pten and p53 Converge on c-Myc to Control Differentiation , Self-renewal , and Transformation of Normal and Neoplastic Stem Cells in Glioblastoma. *Cold Spring Harbor Symposia on Quantitative Biology* **LXXIII**, 427-437 (2008).

94 Libby, C. J., Tran, A. N., Scott, S. E., Griguer, C. & Hjelmeland, A. B. The pro-tumorigenic effects of metabolic alterations in glioblastoma including brain tumor initiating cells. *Biochimica et Biophysica Acta - Reviews on Cancer* **1869**, 175-188, doi:10.1016/j.bbcan.2018.01.004 (2018).

95 Hu, Y. & Smyth, G. K. ELDA: Extreme limiting dilution analysis for comparing depleted and enriched populations in stem cell and other assays. *Journal of Immunological Methods* **347**, 70-78, doi:10.1016/j.jim.2009.06.008 (2009).

96 Kim, S. H. *et al.* EZH2 protects Glioma stem cells from radiation-induced cell death in a MELK/FOXM1-dependent manner. *Stem Cell Reports* **4**, 226-238, doi:10.1016/j.stemcr.2014.12.006 (2015).

97 Zhang, N. *et al.* FoxM1 Promotes β-Catenin Nuclear Localization and Controls Wnt Target-Gene Expression and Glioma Tumorigenesis. *Cancer Cell* **20**, 427-442, doi:10.1016/j.ccr.2011.08.016 (2011).

98 Schonberg, D. L. *et al.* Preferential Iron Trafficking Characterizes Glioblastoma Stem-like Cells. *Cancer Cell* **28**, 441-455, doi:10.1016/j.ccell.2015.09.002 (2015).

99 Iser, I. C., Pereira, M. B., Lenz, G. & Wink, M. R. The Epithelial-to-Mesenchymal Transition-Like Process in Glioblastoma: An Updated Systematic Review and In Silico Investigation. *Medicinal Research Reviews* **37**, 271-313, doi:10.1002/med.21408 (2017).

100 Sciacovelli, M. *et al.* Fumarate is an epigenetic modifier that elicits epithelial-to-mesenchymal transition. *Nature* **537**, 544-547, doi:10.1038/nature19353 (2016).

101 Vinci, M., Box, C. & Eccles, S. A. Three-dimensional (3D) tumor spheroid invasion assay. *Journal of Visualized Experiments* **2015**, 1-9, doi:10.3791/52686 (2015).

102 Hou, P. *et al.* Intermediary metabolite precursor dimethyl-2-ketoglutarate stabilizes hypoxia-inducible factor-1α by inhibiting prolyl-4-hydroxylase PHD2. *PLoS ONE* **9**, 1-17, doi:10.1371/journal.pone.0113865 (2014).

103 Tang, C. *et al.* Transcriptional regulation of FoxM1 by HIF-1α mediates hypoxia-induced EMT in prostate cancer. *Oncology Reports*, 1307-1318, doi:10.3892/or.2019.7248 (2019).

104 Eales, K. L., Hollinshead, K. E. R. & Tennant, D. A. Hypoxia and metabolic adaptation of cancer cells. *Oncogenesis* **5**, e190-e190, doi:10.1038/oncsis.2015.50 (2016).

105 Semenza, G. L. Defining the role of hypoxia-inducible factor 1 in cancer biology and therapeutics. *Oncogene* **29**, 625-634, doi:10.1038/onc.2009.441 (2010).

106 Xia, L. M. *et al.* Transcriptional up-regulation of FoxM1 in response to hypoxia is mediated by HIF-1. *Journal of Cellular Biochemistry* **106**, 247-256, doi:10.1002/jcb.21996 (2009).

107 Liu, M. *et al.* FoxM1B is overexpressed in human glioblastomas and critically regulates the tumorigenicity of glioma cells. *Cancer Research* **66**, 3593-3602, doi:10.1158/0008-5472.CAN-05-2912 (2006).

108 Wang, S. *et al.* CXCL12-induced upregulation of FOXM1 expression promotes human glioblastoma cell invasion. *Biochemical and Biophysical Research Communications* **447**, 1-6, doi:10.1016/j.bbrc.2013.12.079 (2014).

109 Maachani, U. B. *et al.* FOXM1 and STAT3 interaction confers radioresistance in glioblastoma cells. *Oncotarget* **7**, 77365-77377, doi:10.18632/oncotarget.12670 (2016).

110 Gouazé-Andersson, V. *et al.* FGFR1/FOXM1 pathway: A key regulator of glioblastoma stem cells radioresistance and a prognosis biomarker. *Oncotarget* **9**, 31637-31649, doi:10.18632/oncotarget.25827 (2018).

111 Land, H., Parada, L. F. & Weinberg, R. A. Tumorigenic conversion of primary embryo fibroblasts requires at least two cooperating oncogenes. *Nature* **304**, 596-602, doi:10.1038/304596a0 (1983).

112 Wong, D. J. *et al.* Module Map of Stem Cell Genes Guides Creation of Epithelial Cancer Stem Cells. *Cell Stem Cell* **2**, 333-344, doi:10.1016/j.stem.2008.02.009 (2008).

113 Herms, J. W., Von Loewenich, F. D., Behnke, J., Markakis, E. & Kretzschmar, H. A. C-MYC oncogene family expression in glioblastoma and survival. *Surgical Neurology* **51**, 536-542, doi:10.1016/S0090-3019(98)00028-7 (1999).

114 Chaurand, P., Schwartz, S. A., Reyzer, M. L. & Caprioli, R. M. Imaging Mass Spectrometry: Principles and Potentials. *Toxicologic Pathology* **33**, 92-101, doi:10.1080/01926230590881862 (2005).

115 Liu, J. & Ouyang, Z. Mass spectrometry imaging for biomedical applications. *Analytical and Bioanalytical Chemistry* **405**, 5645-5653, doi:10.1007/s00216-013-6916-z (2013).

116 Ifa, D. R., Wu, C., Ouyang, Z. & Cooks, R. G. Desorption electrospray ionization and other ambient ionization methods: current progress and preview. *The Analyst* **135**, 669-681, doi:10.1039/b925257f (2010).

117 Wiseman, J. M., Ifa, D. R., Song, Q. & Cooks, R. G. Tissue imaging at atmospheric pressure using Desorption Electrospray Ionization (DESI) mass spectrometry. *Angewandte Chemie - International Edition* **45**, 7188-7192, doi:10.1002/anie.200602449 (2006).

118 Haag, A. M. in *Modern Proteomics – Sample Preparation, Analysis and Practical Applications* Vol. 919 (eds H. Mirzaei & M. Carrasco) 157-169 (Springer International Publishing, 2016).

119 Samos, N. Mass Spectrometry Imaging of Biomolecular Information. *Analytical Chemistry*, 64-82 (2015).

120 McDonnell, L. A., Angel, P. M., Lou, S. & Drake, R. R. *Mass Spectrometry Imaging in Cancer Research: Future Perspectives*. 1 edn, Vol. 134 (Elsevier Inc., 2017).

121 Calligaris, D. *et al.* Application of desorption electrospray ionization mass spectrometry imaging in breast cancer margin analysis. *Proceedings of the National Academy of Sciences* **111**, 15184-15189, doi:10.1073/pnas.1408129111 (2014).

122 Santagata, S. *et al.* Intraoperative mass spectrometry mapping of an onco-metabolite to guide brain tumor surgery. *Proceedings of the National Academy of Sciences* **111**, 11121-11126, doi:10.1073/pnas.1404724111 (2014).

123 Ellis, S. R., Bruinen, A. L. & Heeren, R. M. A. A critical evaluation of the current state-of-the-art in quantitative imaging mass spectrometry. 1275-1289, doi:10.1007/s00216-013-7478-9 (2014).

124 Wang, Z. J. & Bok, A. Hyperpolarized 13C MRI : State of the Art and Future Directions. *Radiology* **291**, 273-284 (2019).

125 Granlund, K. L. *et al.* Hyperpolarized MRI of Human Prostate Cancer Reveals Increased Lactate with Tumor Grade Driven by Monocarboxylate Transporter 1. *Cell Metabolism* **31**, 105-114.e103, doi:10.1016/j.cmet.2019.08.024 (2019).

126 Nelson, S. J. *et al.* Metabolic imaging of patients with prostate cancer using hyperpolarized [1-13C]pyruvate. *Science Translational Medicine* **5**, doi:10.1126/scitranslmed.3006070 (2013).

127 Serrao, E. M. *et al.* Analysis of 13C and 14C labeling in pyruvate and lactate in tumor and blood of lymphoma-bearing mice injected with 13C- and 14C-labeled pyruvate. *NMR in Biomedicine* **31**, 1-10, doi:10.1002/nbm.3901 (2018).

128 Wang, J., Hesketh, R. L., Wright, A. J. & Brindle, K. M. Hyperpolarized 13C spectroscopic imaging using single-shot 3D sequences with unpaired adiabatic refocusing pulses. *NMR in Biomedicine* **31**, 1-12, doi:10.1002/nbm.4004 (2018).

129 Wang, J., Wright, A. J., Hu, D. E., Hesketh, R. & Brindle, K. M. Single shot three-dimensional pulse sequence for hyperpolarized 13C MRI. *Magnetic Resonance in Medicine* **77**, 740-752, doi:10.1002/mrm.26168 (2017).

130 Swales, J. G. *et al.* Quantitation of Endogenous Metabolites in Mouse Tumors Using Mass-Spectrometry Imaging. *Analytical Chemistry* **90**, 6051-6058, doi:10.1021/acs.analchem.7b05239 (2018).

131 Takáts, Z., Wiseman, J. M., Gologan, B. & Cooks, R. G. Mass spectrometry sampling under ambient conditions with desorption electrospray ionization. *Science* **306**, 471-473, doi:10.1126/science.1104404 (2004).

132 Adusumilli, R. & Mallick, P. in *Proteomics Methods and Protocols* Vol. 1550 (eds Lucio Comai, Parag Mallic, & E Jonathan Katz) 1-369 (Springer Protocols, 2017).

133 Race, A. M., Styles, I. B. & Bunch, J. Inclusive sharing of mass spectrometry imaging data requires a converter for all. *Journal of Proteomics* **75**, 5111-5112, doi:10.1016/j.jprot.2012.05.035 (2012).

134 Buck, A. *et al.* Round robin study of formalin-fixed paraffin-embedded tissues in mass spectrometry imaging. *Analytical and Bioanalytical Chemistry* **410**, 5969-5980, doi:10.1007/s00216-018-1216-2 (2018).

135 Watson, P. F. & Petrie, A. Method agreement analysis: A review of correct methodology. *Theriogenology* **73**, 1167-1179, doi:10.1016/j.theriogenology.2010.01.003 (2010).

136 Cohen, J. A coefficient of agreement for nominal scales. *Educational and Psychological Measurement* **XX**, 37-46 (1960).

137 Pinheiro, J. C. & Bates, D. M. *Mixed-Effects Models in S and S-plus*. (Springer, 2000).

138 Bivand, R. S., Pebesma, E. & Gómez-Rubio, V. *Applied Spatial Data Analysis with R: Second Edition*. (2013).

139 McDonnell, L. A., Van Remoortere, A., Van Zeijl, R. J. M. & Deelder, A. M. Mass spectrometry image correlation: Quantifying colocalization. *Journal of Proteome Research* **7**, 3619-3627, doi:10.1021/pr800214d (2008).

140 Charles, W. S. & Miles, C. Freezing Biological Samples. *Microscopy Today* **14**, 48-48, doi:10.1017/s1551929500055218 (2018).

141 Matsui, Y. *et al.* Adenylate Energy Charge of Rat and Human Cultured Hepatocytes. *In Vitro Cellular & Developmental Biology. Animal* **30A**, 609-614 (1994).

142 Landis, J. R. & Koch, G. G. The Measurement of Observer Agreement for Categorical Data. *Biometrics* **33**, 159-159, doi:10.2307/2529310 (1977).

143 Kettunen, M. I. *et al.* Magnetization transfer Measurements of exchange between hyperpolarized [1-13C]pyruvate and [1-13C]lactate in a murine lymphoma. *Magnetic Resonance in Medicine* **63**, 872-880, doi:10.1002/mrm.22276 (2010).

144 Josan, S. *et al.* Effects of isoflurane anesthesia on hyperpolarized 13C metabolic measurements in rat brain. *Magnetic Resonance in Medicine* **70**, 1117-1124, doi:10.1002/mrm.24532 (2013).

145 Witney, T. H., Kettunen, M. I. & Brindle, K. M. Kinetic modeling of hyperpolarized 13C label exchange between pyruvate and lactate in tumor cells. *Journal of Biological Chemistry* **286**, 24572-24580, doi:10.1074/jbc.M111.237727 (2011).

146 Kettunen, M. I., Kennedy, B. W. C., Hu, D. E. & Brindle, K. M. Spin echo measurements of the extravasation and tumor cell uptake of hyperpolarized [1-13C]lactate and [1-13C]pyruvate. *Magnetic Resonance in Medicine* **70**, 1200-1209, doi:10.1002/mrm.24591 (2013).

147 Singh, M. *et al.* Highly Multiplexed Imaging Mass Cytometry Allows Visualization of Tumor and Immune Cell Interactions of the Tumor Microenvironment in FFPE Tissue Sections. *Blood* **130**, 2751-2751, doi:10.1182/blood.V130.Suppl_1.2751.2751 (2017).

148 Burrage, L. C., Nagamani, S. C. S., Campeau, P. M. & Lee, B. H. Branched-chain amino acid metabolism: From rare Mendelian diseases to more common disorders. *Human Molecular Genetics* **23**, 1-8, doi:10.1093/hmg/ddu123 (2014).

149 Holeček, M. Branched-chain amino acids in health and disease: Metabolism, alterations in blood plasma, and as supplements. *Nutrition and Metabolism* **15**, 1-12, doi:10.1186/s12986-018-0271-1 (2018).

150 Sweatt, A. J. *et al.* Branched-chain amino acid catabolism: unique segregation of pathway enzymes in organ systems and peripheral nerves. *American journal of physiology. Endocrinology and metabolism* **286**, E64-E76, doi:10.1152/ajpendo.00276.2003 (2004).

151 Hutson, S. M. Structure and Function of Branched Chain Aminotransferases. *Progress in Nucleic Acid Research and Molecular Biology* **70**, 175-206 (2001).

152 Hutson, S. M., Lieth, E. & LaNoue, K. F. Function of leucine in excitatory neurotransmitter metabolism in the central nervous system. *The Journal of nutrition* **131**, 846S-850S (2001).

153 Pedroso, J. A. B., Zampieri, T. T. & Donato, J. Reviewing the effects of l-leucine supplementation in the regulation of food intake, energy balance, and glucose homeostasis. *Nutrients* **7**, 3914-3937, doi:10.3390/nu7053914 (2015).

154 Silva, L. S. *et al.* Branched-chain ketoacids secreted by glioblastoma cells via MCT1 modulate macrophage phenotype. *EMBO reports* **18**, e201744154-e201744154, doi:10.15252/embr.201744154 (2017).

155 McBrayer, S. K. *et al.* Transaminase Inhibition by 2-Hydroxyglutarate Impairs Glutamate Biosynthesis and Redox Homeostasis in Glioma. *Cell* **175**, 101-116.e125, doi:10.1016/j.cell.2018.08.038 (2018).

156 Goto, M. *et al.* Structural determinants for branched-chain aminotransferase isozyme-specific inhibition by the anticonvulsant drug gabapentin. *Journal of Biological Chemistry* **280**, 37246-37256, doi:10.1074/jbc.M506486200 (2005).

157 Papathanassiu, A. E. *et al.* BCAT1 controls metabolic reprogramming in activated human macrophages and is associated with inflammatory diseases. *Nature Communications* **8**, 16040-16040, doi:10.1038/ncomms16040 (2017).

158 Cooper, A. J. L., Conway, M. & Hutson, S. M. A continuous 96-well plate spectrophotometric assay for branched-chain amino acid aminotransferases. *Analytical Biochemistry* **308**, 100-105, doi:10.1016/S0003-2697(02)00243-9 (2002).

159 Moffat, J. *et al.* A lentiviral RNAi library for human and mouse genes applied to an arrayed viral high-content screen. *Cell* **124**, 1283-1298 (2006).

160 Wiederschain, D. *et al.* Single-vector inducible lentiviral RNAi system for oncology target validation. *Cell Cycle* **8**, 498-504 (2009).

161 Chen, G. & Deng, X. Cell Synchronization by Double Thymidine Block. *Bio Protoc.* **8**, doi:10.21769 (2018).

162 Chen, E. Y. *et al.* Enrichr: Interactive and collaborative HTML5 gene list enrichment analysis tool. *BMC Bioinformatics* **14**, doi:10.1186/1471-2105-14-128 (2013).

163 Kuleshov, M. V. *et al.* Enrichr: a comprehensive gene set enrichment analysis web server 2016 update. *Nucleic acids research* **44**, W90-W97, doi:10.1093/nar/gkw377 (2016).

164 Benvenisty, N., Leder, A., Kuo, A. & Leder, P. An embryonically expressed gene is a target for c-Myc regulation via the c-Myc-binding sequence. *Genes and Development* **6**, 2513-2523, doi:10.1101/gad.6.12b.2513 (1992).

165 Ben-Yosef, T., Eden, A. & Benvenisty, N. Characterization of murine BCAT genes: Bcat1, a c-Myc target, and its homolog Bcat2. *Mammalian Genome* **9**, 595-597 (1998).

166 Zhang, B. *et al.* Regulation of branched-chain amino acid metabolism by hypoxia-inducible factor in glioblastoma. *Cellular and Molecular Life Sciences*, doi:10.1007/s00018-020-03483-1 (2020).

167 Luger, A. L. *et al.* Doxycycline Impairs Mitochondrial Function and Protects Human Glioma Cells from Hypoxia-Induced Cell Death: Implications of Using Tet-Inducible Systems. *Int J Mol Sci* **19**, doi:10.3390/ijms19051504 (2018).

168 Ahler, E. *et al.* Doxycycline alters metabolism and proliferation of human cell lines. *PLoS One* **8**, e64561, doi:10.1371/journal.pone.0064561 (2013).

169 Conway, M. E., Coles, S. J., Islam, M. M. & Hutson, S. M. Regulatory Control of Human Cytosolic Branched-Chain Aminotransferase by Oxidation and S-Glutathionylation and Its Interactions with Redox Sensitive Neuronal Proteins. *Biochemistry* **47**, 5465-5479 (2008).

170 Conway, M. E. Emerging Moonlighting Functions of the Branched-Chain Aminotransferase Proteins. *Antioxid Redox Signal*, doi:10.1089/ars.2020.8118 (2020).

171 Coles, S. J. *et al.* S-Nitrosoglutathione Inactivation of the Mitochondrial and Cytosolic BCAT Proteins: S-Nitrosation and S-Thiolation. *Biochemistry* **48**, 645-656 (2009).

172 Liu, Z. *et al.* Systematic comparison of 2A peptides for cloning multi-genes in a polycistronic vector. *Sci Rep* **7**, 2193, doi:10.1038/s41598-017-02460-2 (2017).

173 Grankvist, N., Lagerborg, K. A., Jain, M. & Nilsson, R. Gabapentin Can Suppress Cell Proliferation Independent of the Cytosolic Branched-Chain Amino Acid Transferase 1 (BCAT1). *Biochemistry* **57**, 6762-6766, doi:10.1021/acs.biochem.8b01031 (2018).

174 Herman, M. A., She, P., Peroni, O. D., Lynch, C. J. & Kahn, B. B. Adipose tissue branched chain amino acid (BCAA) metabolism modulates circulating BCAA levels. *J Biol Chem* **285**, 11348-11356, doi:10.1074/jbc.M109.075184 (2010).

175 Sidhu, S. S., Mengistab, A. T., Tauscher, A. N., LaVail, J. & Basbaum, C. The microvesicle as a vehicle for EMMPRIN in tumor-stromal interactions. *Oncogene* **23**, 956-963, doi:10.1038/sj.onc.1207070 (2004).

176 P., K. *et al.* CD147 is tightly associated with lactate transporters MCT1 and MCT4 and facilitates their cell surface expression. *The EMBO Journal* **19**, 3896-3904 (2000).

177 Chirag, E. A., Patel, A. H., Drake, C. H., Powell, J. D. & Hutson, S. M. Cytosolic branched chain aminotransferase (BCATc) regulates mTORC1 signaling and glycolytic metabolism in CD4- T cells. *Journal of Biological Chemistry* **289**, 18793-18804, doi:10.1074/jbc.M114.554113 (2014).

178 Zhdanov, A. V., Okkelman, I. A., Collins, F. W., Melgar, S. & Papkovsky, D. B. A novel effect of DMOG on cell metabolism: direct inhibition of mitochondrial function precedes HIF target gene expression. *Biochim Biophys Acta* **1847**, 1254-1266, doi:10.1016/j.bbabio.2015.06.016 (2015).

179 Thewes, V. *et al.* The branched-chain amino acid transaminase 1 sustains growth of antiestrogen-resistant and ERα-negative breast cancer. *Oncogene* **36**, 4124-4134, doi:10.1038/onc.2017.32 (2017).

180 Wang, H.-G. *et al.* BCAT1 expression in hepatocellular carcinoma. *Clinics and Research in Hepatology and Gastroenterology* **40**, e55-e56, doi:10.1016/j.clinre.2016.03.003 (2016).

181 Lin, X., Tan, S., Fu, L. & Dong, Q. Bcat1 overexpression promotes proliferation, invasion, and wnt signaling in non-small cell lung cancers. *OncoTargets and Therapy* **13**, 3583-3594, doi:10.2147/OTT.S237306 (2020).

182 Mair, R. *et al.* Metabolic imaging detects low levels of glycolytic activity that vary with levels of c-Myc expression in patient-derived xenograft models of glioblastoma. *Cancer Research* **78**, canres.0759.2018-canres.0759.2018, doi:10.1158/0008-5472.CAN-18-0759 (2018).

183 Ben-Yosef, T., Yanuka, O. & Benvenisty, N. ECA39 is regulated by c-Myc in human and by a Jun/Fos homolog, Gcn4, in yeast. *Oncogene* **13**, 1859-1866 (1996).

184 Islam, M. M. *et al.* Branched-chain amino acid metabolon: Interaction of glutamate dehydrogenase with the mitochondrial branched-chain aminotransferase (BCATm). *Journal of Biological Chemistry* **285**, 265-276, doi:10.1074/jbc.M109.048777 (2010).

185 Ericksen, R. E. *et al.* Loss of BCAA Catabolism during Carcinogenesis Enhances mTORC1 Activity and Promotes Tumor Development and Progression. *Cell Metabolism* **29**, 1151-1165.e1156, doi:10.1016/j.cmet.2018.12.020 (2019).

186 Pistollato, F. *et al.* Hypoxia and succinate antagonize 2-deoxyglucose effects on glioblastoma. *Biochemical Pharmacology* **80**, 1517-1527, doi:10.1016/j.bcp.2010.08.003 (2010).

187 Raffel, S. *et al.* BCAT1 restricts αKG levels in AML stem cells leading to IDHmut-like DNA hypermethylation. *Nature* **551**, 384-388, doi:10.1038/nature24294 (2017).

188 Conway, M. E. *et al.* Decreased expression of the mitochondrial BCAT protein correlates with improved patient survival in IDH-WT gliomas. *Brain Pathology* **26**, 789-791, doi:10.1111/bpa.12385 (2016).

189 Karlsson, M. *et al.* Imaging of branched chain amino acid metabolism in tumors with hyperpolarized 13C ketoisocaproate. *International Journal of Cancer*, 729-736, doi:10.1002/ijc.25072 (2010).

190 Butt, S. A., Søgaard, L. V., Magnusson, P. O. & Lauritzen, M. H. Imaging cerebral 2-ketoisocaproate metabolism with hyperpolarized 13 C Magnetic Resonance Spectroscopic Imaging. *Journal of Cerebral Flow & Metabolism*, 1508-1514, doi:10.1038/jcbfm.2012.34 (2012).

191 Mac, M., Nehlig, A., NaÅ‚ecz, M. J. & NaÅ‚ecz, K. A. Transport of alpha-Ketoisocaproate in Rat Cerebral Cortical Neurons. *Archives of Biochemistry and Biophysics* **376**, 347-353, doi:10.1006/abbi.2000.1724 (2000).

192 Suh, E. H. *et al.* In vivo assessment of increased oxidation of branched-chain amino acids in glioblastoma. *Scientific Reports* **9**, 1-9, doi:10.1038/s41598-018-37390-0 (2019).

193 Billingsley, K. L. *et al.* The feasibility of assessing branched-chain amino acid metabolism in cellular models of prostate cancer with hyperpolarized [1-13C]-ketoisocaproate. *Magnetic Resonance Imaging* **32**, 791-795, doi:10.1016/j.mri.2014.04.015 (2014).

194 Haase, A., Frahm, J., Hanicke, W. & Matthaei, D. 1H NMR chemical shift selective (CHESS) imaging. *Physics in Medicine and Biology* **30**, 341-344, doi:10.1088/0031-9155/30/4/008 (1985).

195 Govindaraju, V., Young, K. & Maudsley, A. A. Proton NMR chemical shifts and coupling constants for brain metabolites. *NMR in Biomedicine* **13**, 129-153, doi:10.1002/1099-1492(200005)13:3<129::AID-NBM619>3.0.CO;2-V (2000).

196 De Graaf, A. A., Van Dijk, J. E. & BoéE, W. M. M. J. Quality: quantification improvement by converting lineshapes to the lorentzian type. *Magnetic Resonance in Medicine* **13**, 343-357, doi:10.1002/mrm.1910130302 (1990).

197 Pfeuffer, J., Tkac, I., Provencher, S. W. & Gruetter, R. Towards an In Vivo Neurochemical Profile : Quantification of 18 Metabolites in Short-Echo-Time 1H NMR Spectra of Rat Brain at TE = 2ms. *Journal of Magnetic Resonance* **120**, 55455-55455 (1999).

198 Lutz, N. W., Béraud, E. & Cozzone, P. J. Metabolomic Analysis of Rat Brain by High Resolution Nuclear Magnetic Resonance Spectroscopy of Tissue Extracts. *Journal of Visualized Experiments*, 1-12, doi:10.3791/51829 (2014).

199 Purvis, L. A. B. *et al.* OXSA: An open-source magnetic resonance spectroscopy analysis toolbox in MATLAB. *PLoS ONE* **12**, 1-10, doi:10.1371/journal.pone.0185356 (2017).

200 Bixel, G. M., Hutson, S. M. & Hamprecht, B. Cellular Distribution of Branched-chain Amino Acid Aminotransferase Isoenzymes Among Rat Brain Glial Cells in Culture. **45**, 685-694, doi:10.1177/002215549704500506 (1997).

201 Kim, D. K. *et al.* System L-amino acid transporters are differently expressed in rat astrocyte and C6 glioma cells. *Neuroscience Research* **50**, 437-446, doi:10.1016/j.neures.2004.08.003 (2004).

202 Panosyan, E. H., Lin, H. J., Koster, J. & Lasky, J. L. In search of druggable targets for GBM amino acid metabolism. *BMC Cancer* **17**, 162-162, doi:10.1186/s12885-017-3148-1 (2017).

203 Suryawan, A. *et al.* A molecular model of human branched-chain amino acid metabolism. *The American journal of clinical nutrition* **68**, 72-81 (1998).

204 Davoodi, J. *et al.* Overexpression and characterization of the human mitochondrial and cytosolic branched-chain aminotransferases. *Journal of Biological Chemistry* **273**, 4982-4989, doi:10.1074/jbc.273.9.4982 (1998).

205 Ye, Z. C. & Sontheimer, H. Glioma cells release excitotoxic concentrations of glutamate. *Cancer Research* **59**, 4383-4391 (1999).

206 Smith, Q. R. Transport of Glutamate and Other Amino Acids at the Blood-Brain Barrier. *The Journal of Nutrition* **130**, 1016S-1022S, doi:10.1093/jn/130.4.1016s (2000).

207 Márquez, J. *et al.* Glutamine Addiction In Gliomas. *Neurochemical Research* **42**, 1735-1746, doi:10.1007/s11064-017-2212-1 (2017).

208 Keshari, K. R. & Wilson, D. M. *Chemistry and biochemistry of 13 C hyperpolarized magnetic resonance using dynamic nuclear polarization*. Vol. 43 (2014).

209 Tseng, C. W. *et al.* Transketolase Regulates the Metabolic Switch to Control Breast Cancer Cell Metastasis via the alpha-Ketoglutarate Signaling Pathway. *Cancer Res* **78**, 2799-2812, doi:10.1158/0008-5472.CAN-17-2906 (2018).

210 Atlante, S. *et al.* alpha-ketoglutarate dehydrogenase inhibition counteracts breast cancer-associated lung metastasis. *Cell Death Dis* **9**, 756, doi:10.1038/s41419-018-0802-8 (2018).

211 Neinast, M. D. *et al.* Quantitative Analysis of the Whole-Body Metabolic Fate of Branched-Chain Amino Acids. *Cell Metab* **29**, 417-429 e414, doi:10.1016/j.cmet.2018.10.013 (2019).

212 White, P. J. *et al.* The BCKDH Kinase and Phosphatase Integrate BCAA and Lipid Metabolism via Regulation of ATP-Citrate Lyase. *Cell Metab* **27**, 1281-1293 e1287, doi:10.1016/j.cmet.2018.04.015 (2018).